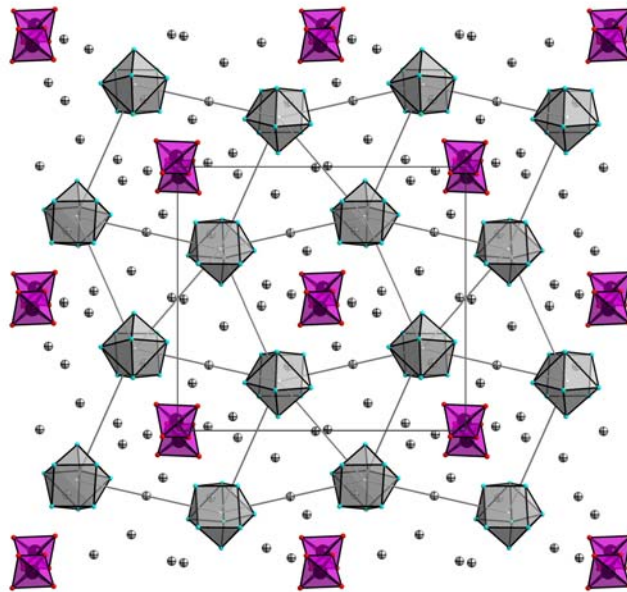


# Germanides, Germanide-Tungstate Double Salts and Substitution Effects in Zintl Phases



*Siméon Ponou*



**Technische Universität München**

Lehrstuhl für Anorganische Chemie  
mit Schwerpunkt Neue Materialien

August 2006

**Technische Universität München**

Lehrstuhl für Anorganische Chemie

**Germanides, Germanide-Tungstate Double Salts  
and  
Substitution Effects in Zintl Phases**

**Siméon Ponou**

Vollständiger Abdruck der von der Fakultät für Chemie der Technischen Universität  
München zur Erlangung des akademischen Grades eines

**Doktors der Naturwissenschaften**

genehmigten Dissertation.

Vorsitzender: Univ.-Prof. Dr. Michael Schuster  
Prüfer des Dissertation: 1. Univ.-Prof. Dr. Thomas Fässler  
2. Univ.-Prof. Dr. Ulrich K. Heiz  
3. Univ.-Prof. Dr. Rainer Niewa

Die Dissertation wurde am 07.07.2006 bei der Technischen Universität München eingereicht  
und durch die Fakultät für Chemie am 16.08.2006 angenommen.

*To my mother Domche Jeannette,  
my sisters Cathy, Fideline and Alyce*

*The Lord is my shepherd.  
I am never in need.*  
Psalm 23.1

To the memory of *Bertrand Seumo Meuleye*†

## Acknowledgements

To my Supervisor Prof. Thomas Fässler, my deepest gratitude for the supply of this interesting topics as well as all support and guidance. Thank you also for accepting me as PhD student, for your leniency and your great help, even on some rather personal problems;

To Prof. Sven Lidin, Stockholm University, for his assistance with solving crystal structures of the double-salts and for showing interest in my project;

Prof. Brigitte Eisenmann, TU Darmstadt, for the fruitful discussions on Zintl phases and for providing me with various literatures;

Prof. Lars Kloo and Dr. Martin Lindsjö, Royal Institute of Technology Stockholm, for the Raman spectroscopy;

Priv. Doz. Dr. Lorenz Kienle, Max-Planck-Institut für Festkörperforschung Stuttgart, for the Transmission Electron Microscopy study;

Dr. Mathias Opel, Walther-Meissner-Institut TU München, for SQUID magnetic measurements;

To Dr. Stefan Hoffmann (TU Darmstadt) for kindly introduce me to the general experimental techniques;

Dr. Stephan D. Hoffmann, Dr. Frank Dubois and Dr. Martin Schreyer for their valuable suggestions and assistance;

I am particularly indebted to Dipl.-Chem Sung-Jin Kim for reading my manuscript and for his suggestions and to Anna Margareth Fredricks for correcting the English language;

Also to all the members of the Fässler Research Group for their continuous encouragements, friendliness, care and company and whose comments were very helpful.

Finally, I would like to thank Mr. Henri Severin Kamgaing and Dipl.-Ing Paul René Ngandjui for moral supports.

**CONTENTS**

<b>1. Introduction</b> .....	<b>1</b>
<b>1.1 Probing the Zintl concept – Double salts with Zintl anions</b> .....	<b>2</b>
<b>1.2 Beyond the Zintl concept</b> .....	<b>4</b>
1.2.1 Bonding at the Zintl border.....	5
1.2.2 Beyond Electronic Effects .....	7
<b>1.3 Scope and aims of this work</b> .....	<b>7</b>
<b>1.4 Literature</b> .....	<b>9</b>
<b>2. Experimental and characterization methods</b> .....	<b>12</b>
<b>2.1 Starting materials and synthesis</b> .....	<b>12</b>
<b>2.2 X-ray diffraction study</b> .....	<b>14</b>
2.2.1 Powder X-ray diffraction.....	14
2.2.2 Single crystal X-ray diffraction .....	14
<b>2.3 Energy Dispersive X-ray analysis (EDX)</b> .....	<b>15</b>
<b>2.4 Differential Thermal Analysis (DTA)</b> .....	<b>16</b>
<b>2.5 Magnetic measurements</b> .....	<b>17</b>
<b>2.6 Theoretical band structure calculation</b> .....	<b>17</b>
<b>2.7 Literature</b> .....	<b>18</b>
<b>3. Alkali-metal Germanides and Germanide-Tungstate double salts</b> .....	<b>19</b>
<b>3.1 Introduction</b> .....	<b>19</b>
<b>3.2 Synthesis and characterization of the K and Rb germanide tungstates</b> <b><math>A_{10}[\text{Ge}_9]_2\text{WO}_4</math> (A = K, Rb, Cs)</b> .....	<b>21</b>
<b>3.2 Synthesis</b> .....	<b>21</b>
3.2.2 EDX analysis and X-ray powder diffraction.....	22
3.2.3 Characterization by Raman spectroscopy .....	22
<b>3.3 Crystal structure of the K germanide tungstates <math>\text{K}_{10}[\text{Ge}_9]_2\text{WO}_4</math></b> .....	<b>25</b>
3.3.1 Crystal structure determination .....	25
3.3.2 Description of the structure of $\text{K}_{10}[\text{Ge}_9]_2\text{WO}_4$ .....	26
<b>3.4 The Crystal structure of the Rb germanide tungstates <math>\text{Rb}_{10}[\text{Ge}_9]_2\text{WO}_4</math></b> .....	<b>38</b>
3.4.1 Crystal structure determination .....	38
3.4.2 Description of the structure of $\text{Rb}_{10}[\text{Ge}_9]_2\text{WO}_4$ .....	38
<b>3.5 Discussions on the double-salts</b> .....	<b>44</b>

---

<b>3.6 The crystal structure of <math>K_4Ge_9</math></b> .....	<b>48</b>
3.6.1 Synthesis and characterization .....	48
3.6.2 Crystal structure determination .....	48
3.6.3 Description of the structure of $K_4Ge_9$ .....	49
3.6.4 Discussions.....	56
<b>3.7 <math>Rb_8Hg_3Ge_{43}</math> – a Mercury substituted Germanium Clathrate-I</b> .....	<b>58</b>
3.7.1 Synthesis and characterization .....	58
3.7.2 Crystal structure determination .....	58
3.7.3 Structural description of $Rb_8Hg_3Ge_{43}$ .....	58
3.7.4 Discussions .....	62
<b>3.8 Literature</b> .....	<b>65</b>
<b>4. Influence of atomic properties on the structure and bonding of Zintl phases: Sb for Bi Homologous substitutions in <math>Ba_2Sb_3</math></b> .....	<b>67</b>
<b>4.1 Introduction</b> .....	<b>67</b>
<b>4.2 The Phase <math>Ba_2Bi_3</math>, its Coloring Variant <math>Ba_2BiSb_2</math> and the Solid Solutions <math>Ba_2Bi_{1+y}Sb_{2-y}</math> (<math>y &lt; 2</math>)</b> .....	<b>69</b>
4.2.1 Synthesis and characterization .....	69
4.2.2 Determination of the crystal structures.....	70
4.2.3 Structural descriptions of $Ba_2Bi_3$ and $Ba_2Bi_{1+y}Sb_{2-y}$ ( $y < 2$ ) .....	70
4.2.4 Electronic Structure and Discussions.....	80
4.2.5 Physical properties.....	84
<b>4.3 Further results – The crystal structure of <math>BaBi_2</math></b> .....	<b>86</b>
4.3.1 Source of the material and crystal structure determination .....	86
4.3.2 Description of the structure of $BaBi_2$ and discussions .....	88
<b>4.4 Literature</b> .....	<b>91</b>
<b>5. Substitution effects in Zintl phases of the Na/Sn phase system</b> .....	<b>92</b>
<b>5.1. Introduction</b> .....	<b>92</b>
<b>5.2. Synthesis and crystal structure refinement of the phase <math>Sr_8Na_{5+x}Sn_{13}</math></b> .....	<b>94</b>
5.2.1 Synthesis and characterization .....	94
5.2.2 Crystal structure refinement .....	94
5.2.3 Structural Description of $Sr_8Na_{5+x}Sn_{13}$ .....	99
<b>5.3. Multicenter bonding in the novel Zintl phase <math>Na_{13}Sn_{26}Bi</math></b> .....	<b>103</b>
5.3.1 Synthesis and characterization .....	103

5.3.2 Determination of the crystal structure .....	104
5.3.3 Structural description of $\text{Na}_{13}\text{Sn}_{26}\text{Bi}$ .....	104
<b>5.4 Discussions .....</b>	<b>112</b>
<b>5.5 Literature .....</b>	<b>115</b>
<b>6. Substitution effects on the Zintl phases of the Ba/Sn system.....</b>	<b>116</b>
<b>6.1 Overview .....</b>	<b>116</b>
<b>6.2 Sn for Bi partial substitution in <math>\text{Ba}_3\text{Sn}_5</math> – Synthesis and Characterization of the phases <math>\text{Ba}_3\text{Sn}_{4-y}\text{Bi}_{1+y}</math> (<math>y \leq 1</math>) .....</b>	<b>118</b>
6.2.1 Introduction .....	118
6.2.2 Synthesis and characterization .....	118
6.2.3 Crystal structure determination .....	119
6.2.4 Structural description of $\text{Ba}_3\text{Sn}_{4-y}\text{Bi}_{1+y}$ .....	121
6.2.5 Electronic Structure .....	124
6.2.6 Discussions .....	128
<b>6.3 Sn for Bi substitution effects in <math>\text{BaSn}_3</math> – The homologous series <math>\text{Ba}_{m+n}\text{Sn}_{3m+y}\text{Bi}_{3n-y}</math> .....</b>	<b>130</b>
<b>6.3.1 Introduction .....</b>	<b>130</b>
<b>6.3.2 Synthesis and Characterization .....</b>	<b>131</b>
6.3.2.1 Thermal analysis.....	131
6.3.2.2 HTREM observations and some implications .....	134
<b>6.3.3 <math>\text{Ba}_4\text{Sn}_{9+y}\text{Bi}_{3-y}</math> – The 8H structure of <math>\text{BaSn}_{3-x}\text{Bi}_x</math> (<math>x \sim 0.5</math>) .....</b>	<b>135</b>
6.3.3.1 Crystal structure determination .....	135
6.3.3.2 Structural description and relationship .....	137
<b>6.3.4 <math>\text{Ba}_{13}\text{Sn}_{30+y}\text{Bi}_{9-y}</math> – The 39R structure of <math>\text{BaSn}_{3-x}\text{Bi}_x</math> (<math>x \sim 0.5</math>) .....</b>	<b>141</b>
6.3.4.1 Crystal structure determination .....	141
6.3.4.2 Structural description and relationship .....	141
<b>6.3.5 Synthesis and Crystal structure of <math>\text{Ba}_5\text{Sn}_{9+y}\text{Bi}_{6-y}</math> – The 10H structure of <math>\text{BaSn}_{3-x}\text{Bi}_x</math> (<math>x \sim 0.75</math>) .....</b>	<b>148</b>
6.3.5.1 Synthesis .....	148
6.3.5.2 Crystal structure determination .....	148
6.3.5.3 Structural description and relationship .....	151
<b>6.3.6 Synthesis and Crystal Structure of <math>\text{Ba}_2\text{Sn}_{3+y}\text{Bi}_{3-y}</math> – The 12R structure of <math>\text{BaSn}_{3-x}\text{Bi}_x</math> (<math>x \sim 1</math>) .....</b>	<b>152</b>
6.3.6.1 Synthesis .....	152
6.3.6.2 Crystal structure determination .....	152

---

6.3.6.3 Structural description and relationship .....	154
<b>6.4 Discussions on the homologous series <math>Ba_{m+n}Sn_{3m+y}Bi_{3n-y}</math> .....</b>	<b>156</b>
<b>6.5 Literature .....</b>	<b>159</b>
<b>7. Heteronuclear Zintl Anions at the Border to Intermetallics – Synthesis, Characterization and Electronic Structure of <math>Ba_5In_4Bi_5</math> .....</b>	<b>160</b>
7.1 Introduction .....	160
7.2 Synthesis and Characterization.....	160
7.3 Crystal structure determination .....	161
7.4 Description of the Structure of $Ba_5In_4Bi_5$ .....	163
7.5 Electronic Structure of $Ba_5In_4Bi_5$ and Discussions .....	167
7.6 Literature .....	171
<b>8. Summary and Final Discussions .....</b>	<b>172</b>
<b>9. List of Publications .....</b>	<b>178</b>

**List of abbreviations**

A	alkali metal
Ae	alkaline-earth metal
ADPs	Atomic displacement parameters
CCD	Charge Coupling Device
COHP	Crystal Orbital Hamiltonian Population
ICOHP	integrated Crystal Orbital Hamiltonian Population
DTA	Differential Thermal Analysis
EDX	Energy Dispersive X-ray
E	p-block element
Tt	Tetrel, element of the group 14
Pn	Pnictogen, element of the group 15
Tr	Triel, element of the group 13
X	Halogen, element of the group 17
RE	Rare earth metal
VEC	Valence Electron Concentration
ICSD	Inorganic Crystal Structure Database
SQUID	Superconducting Quantum Interference Device
LMTO	Linear Muffin Tin Orbital
DOS	Density of States
ELF	Electron localization function
HOMO	Highest Occupied Molecular Orbital
LUMO	Lowest Unoccupied Molecular Orbital

## 1. Introduction

Intermetallic compounds are formed by two or more metals and represent a huge and important group of chemical compounds.<sup>[1]</sup> Today, the important research areas of intermetallic compounds are very broad and range from refractory high-strength super alloys,<sup>[2]</sup> magnetic compounds<sup>[3]</sup> and superconductors,<sup>[4]</sup> to metallic glasses for possible applications in fuels cells.<sup>[2]</sup> Furthermore, the possibility of functional intermetallic materials has been validated by several discoveries of polar intermetallics and Zintl phases that display complex combinations of structural, electronic, thermal, magnetic, and transport properties.<sup>[5-10]</sup> In the last 30 years, a large number of new intermetallic compounds have been synthesized, and their structural and electronic characterizations have given tremendous informations about their structure-property relationship.<sup>[11-13]</sup>

Among the classes of inorganic solids, the intermetallics remain the least understood with respect to their bonding properties.<sup>[14-15]</sup> This is mainly due to the fact that some of the features that primarily determine the chemical bonding, such as the degrees of valence-electron transfer and localization, vary widely and almost continuously with composition and the nature of the elements involved.<sup>[16-17]</sup> Several useful concepts for classifying the rich empirical knowledge on intermetallic systems have been developed. The most efficient ones are based on the degree of electron transfer which occurs during phase formation.<sup>[18-22]</sup>

Owing to the significant electronegativity differences between the components, the combination of main group p-block elements (E) – which can be metals, semimetals, or small-gap semiconductors – with electropositive s-block active metals (alkali A and alkaline-earth Ae metals) frequently leads to so called “polar intermetallic” compounds that contain polyanions of the post-transition elements. It is the merit of Zintl,<sup>[23-25]</sup> Klemm and others that some easily applicable rules exist for this subgroup of intermetallic compounds.

Mooser and Pearson<sup>[26-29]</sup> as well as Klemm and Busmann<sup>[30-33]</sup> found a correlation between the generalized 8-N rule and the possible anionic substructure in normal valence compounds (Zintl phases). The original definition of a Zintl phase was based on the concept of isostructural relationship of the reduced post-transition semimetal to structures of the elements with the same number of valences electrons. Schäfer and Eisenmann<sup>[34]</sup> developed an expansion of the definition:

*“(...) The limitation of the concept to the lattices of the elements may reasonably be dropped in favour of an extension of its validity to ensure the same number of bonds to neighbours of the same species, i.e. the  $(8 - N)$  rule should be fulfilled. The general valence rule of Pearson also leads to the same results”.*

With Eduard Zintl's interpretation of structures that are based on the NaTl <sup>[35]</sup> arrangement and his extensive studies of related compounds began the onslaught on the strict division between metallic and non-metallic compounds. The structural peculiarities of Zintl phases are explained by assuming the presence of both ionic and covalent parts in the bonding picture. Within the Zintl-Klemm-Busmann concept, all valence electrons can be assigned, at least formally, to the electronegative main group elements. The electrons are then localized either in two-center-two-electron (2c-2e) bonds between post-transition metal atoms or in the form of lone pairs located at these atoms. The applicability of the octet rule and the occurrence of anionic, homoatomic (or heteroatomic) analogues of some catenated nonmetals were first recognized among alkali-metal “salts” of the heavy post-transition metals and metalloids. <sup>[36-40]</sup> The electron transfer concept is strictly formal and has generated a great deal of misunderstanding. A major criticism of the Zintl concept is indeed the unreasonable assignment of ionic charges. The fact that the Zintl-Klemm concept works at all given the magnitudes of charge transfer is because we are counting occupied electronic states, not electrons as Nesper pointed out. <sup>[15]</sup>

Interest in the study of these valence compounds which are referred to as “Zintl phases” has increased markedly in recent decades, deriving mainly from the rich structural variety shown by these compounds, as well as the evident or prospective simplicity of their bonding schemes among polar intermetallic compounds. <sup>[39]</sup>

### **1.1 Probing the Zintl Concept – Double-salts with Zintl anions**

The chemical bond situation in Zintl phases should be characterized by closed shell atoms having, if necessary, covalent interactions in the anionic part of the structures, while ionic bonding governs the cation-anion interactions. From this picture, Zintl anions are chemical species whose existence is not bound to a specific crystal structure. Thus, they can form salts of various cations which can subsequently be combined with other salts (even those featuring classical anions) to form double salts in which two types of anions co-exist in stable salt-like compounds, providing

that a topological compatibility is achieved. [41] The resulting double-salts may be considered as further chemical proof for the validity of the term Zintl anion. Indeed, very recent exploratory investigations on double salts with Zintl anions have proven to be a very effective approach for the design of new classes of compounds. [42-43]

The first class of such double salts are the halogenide tetralide compounds like  $\text{Ba}_3\text{E}_2\text{I}$  ( $\text{E} = \text{Si}, \text{Ge}$ ), [44] which may be understood as double salts between the Zintl phases  $\text{Ba}_2\text{E}$  [45-46] and  $\text{BaI}_2$ . [47] Also,  $\text{Ba}_4\text{Si}_3\text{Br}_2$  [48] can be understood with respect to its stoichiometry as a double salt of  $\text{Ba}_3\text{Si}_3$  and  $\text{BaBr}_2$ , [47] where the silicon partial structure  $\text{Ba}_3\text{Si}_3$  completely differs from the infinite zigzag chain in  $\text{BaSi}$ , [49] instead a previously unknown finite variant in the form of a three-membered silicon ring  $[\text{Si}_3]^{6-}$  is formed.

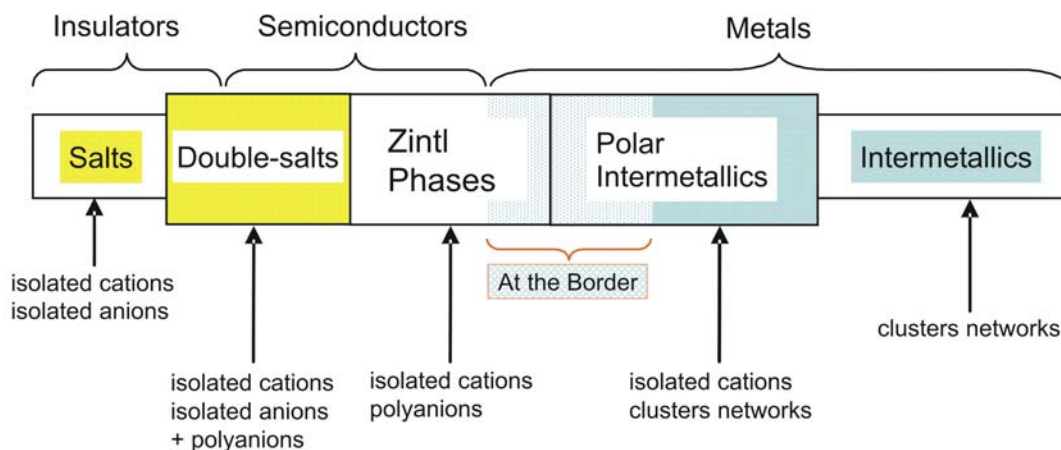
The second class of double salts with Zintl anions involves compounds containing oxides. They may also be considered as a specific subgroup of metal rich ternary or quaternary oxides where the bonding can be interpreted as polyanionic within the Zintl concept. They can further be divided in two groups. The first group involves ternary metal rich oxides (or suboxides) with Zintl anions and oxygen, and they can be classified as 'metallide oxides'. They contain isolated oxide ions coordinated by alkali or alkaline-earth cations combined with a wide variety of Zintl anions. These can range from simple noble gas isosteric metallide anions like  $\text{Ge}^{4-}$  in the anti-perovskites  $\text{Ca}_3\text{GeO}$ , [50] to dumbbells like  $\text{Sb}_2^{4-}$  in  $\text{Ba}_3\text{Sb}_2\text{O}$  [51] which are isoelectronic with the halogens and,  $\text{Ge}_4^{4-}$  tetrahedra in  $\text{Ba}_3\text{Ge}_4\text{O}$  [52] that are isosteric and isostructural with white phosphorus. Even more complex anions like the Wade's cluster anions  $[\text{Ti}_8]^{6-}$ , was described recently in  $\text{Cs}_8\text{Ti}_8\text{O}$ . [53] The second group of the double salts with oxides involves ternary or quaternary metal rich oxides with both Zintl and oxometallate anions. They form a rather unimaginable class of compounds. The most prominent examples of these are the recently reported 'tetrelide tetrelates' [54, 42] which (see § 3.1) contain the same group 14 element simultaneously in positive and negative oxidation states. Rare examples of solids containing an element in both positive and negative oxidation states are found in the auride aurate homologous series  $[\text{MAu}]_n[\text{M}_3\text{AuO}_2]$  ( $\text{M} = \text{Rb}, \text{Cs}$ ), which was systematically investigated by Jansen and co-workers. [55-56] Other classes of compounds that may be viewed as double salts with Zintl anions exist, like the

germanide carbide  $\text{Ba}_3[\text{Ge}_4][\text{C}_2]$  which contains the well known Zintl anion  $\text{Ge}_4^{4-}$  and acetylenide  $\text{C}_2^{2-}$ .<sup>[57-58]</sup>

Although there remain unresolved questions about the physical accuracy of the Zintl picture, the Zintl concept has particularly proven to be an effective tool in rationalizing structural properties and chemical bonding of salt-like materials along the border between metals and non-metals.

## 1.2 Beyond the Zintl concept

However, as soon as we leave the group of valence compounds and approach the variety of (inter)metallic compounds it becomes very difficult to work out simple bonding rules. In fact, the transition from valence compounds to typical metals is not abrupt and doesn't depend solely on the electronegativity difference (which determine the degree of charge transfer), but also on the valence electron concentration (VEC).<sup>[17]</sup> Zintl phases as valence compounds are expected to be diamagnetic and semiconducting. In the spectrum from insulators to valence compounds to intermetallic compounds, we observe a continuous transition in their chemical bonding going from ionic to metallic (see [Scheme 1](#)). At the border between classical Zintl phases and normal (inter)metallic phases, typical properties of Zintl phases diminish and metallic conductivity appears. Borderline cases of Zintl phases, that is, those exhibit "locally delocalized electrons" and not conforming to either 8-N rule or the Zintl-Klemm concept, marked the transition to the intermetallic phases. It is important to understand their chemical bonding and structure in order to establish relationships between stoichiometry, structure and physical properties.



Scheme 1.

## - Metallic Zintl Phases

The metallic conductivity of Zintl phases at the border to intermetallics can formally arise from:

- i) The significant occupation of the conduction bands, as illustrated with the idea of 'submerged continent' (valence band) by Nesper. <sup>[15]</sup>
- ii) The overlap of a formally filled valence band with an empty conduction band.
- iii) Thirdly, among 'electron-deficient' phases. This unusual condition exists, among formally electron-deficient phases (hypoelectronic), as having an open valence band. Here, elementary views of the bonding are based on precepts similar to those developed for molecular compounds which include newer and more complex aspects of "valence rules" and require extension of the Zintl classification to accommodate modern bonding concepts such as Wade's rules, multicenter two-electron bonding, and non-classical multicenter bonding also called 'hypervalent' bonding. <sup>[15]</sup>

Thus, extending the efficacy of the Zintl picture in understanding the chemical bonding of borderline Zintl phases is an important step in developing a useful general chemical understanding of compounds between metallic elements.

### 1.2.1 Bonding at the Zintl border

All the successive reformulations of Zintl concept proposed up to now aim at finding a "valence rule" for borderline polar intermetallics, using an analogy of any modern bonding concept known in molecular chemistry.

#### 1.2.1.1 Intermetallic $\pi$ -systems

As in molecular chemistry, an alternative path to compensate for electron-deficiency is the formation of multiple bonds, through  $\pi$ -interactions, as in unsaturated and aromatic molecular systems. The efficacy of the Zintl concept in rationalizing the stoichiometry, structure, and chemical bonding of complex  $\pi$ -bonded intermetallics has been probed successfully. The significance of Zintl phases exhibiting  $\pi$ -bonds has been emphasized by the discovery of high-T<sub>c</sub> superconductivity in the nominal Zintl phase MgB<sub>2</sub>.<sup>[6]</sup> Recently, Sn<sub>3</sub><sup>2-</sup> cyclopropenium-like trimers, were formulated to exist in the superconducting Zintl phase BaSn<sub>3</sub> (Ni<sub>3</sub>Sn-type), <sup>[59]</sup> where the isolated chains of face sharing octahedra may be viewed as stacked antiprismatic triangular

units, with strong interactions between the component  $\pi$ -systems along the chains, leading to metallic character. The observed superconductivity was therefore likened to the existence of pairing localization of conducting electrons. Extensive exploratory work by von Schnering and Nesper on ternary tetrelides (Si and Ge) resulted in the synthesis of arene-like  $\pi$ -systems, represented by  $\text{Ba}_4\text{Li}_2\text{Si}_6$  [60] featuring  $[\text{Si}_6]^{10-}$  units related to aromatic hydrocarbon rings such as benzene and,  $\text{Li}_8\text{MgSi}_6$  with quasi-aromatic Si five-membered rings,  $[\text{Si}_5]^{6-}$ . [61] Also, condensed systems consisting of hexagonal  $\text{Si}_6$  rings similar to arenes and conjugated polyaromatics have been isolated and characterized. [62-67]

### 1.2.1.2 Multi-center bonded deltahedral clusters

Certain group of compounds (mainly of the early main-group elements) containing isolated cluster with delocalized bond may be understood by the application of the Wade-Mingo's rules, which give a guide to the magic electron count developed for deltahedral boranes  $\text{B}_n\text{H}_n^{2-}$ . [68] These isolated clusters were originally categorized as Zintl ions because of the first broad investigation of them by Eduard Zintl in the 1930s through electrochemical studies on alkali-metal–post-transition metal (E) or metalloid systems in liquid ammonia. [69] While the occurrence of isolated clusters is well known for the group 13 (triel, Tr) elements, [70-71] large deltahedral clusters of group 14 (tetrel, Tt) elements in solid state systems have been fairly limited. Examples of phases with isolated cluster of the carbon group are the metallic  $\text{Ae}_3\text{Tt}_5$  (Tt = Sn, Pb; Ae = Sr, Ba), [72-73] which may be viewed as containing arachno-clusters of  $[\text{Tt}_5]^{6-}$ , and the  $\text{Rb}_4\text{Li}_2\text{Sn}_8$  [74] with arachno- $[\text{Sn}_8]^{6-}$  as well as  $\text{A}_4\text{Tt}_9$  and  $\text{A}_{12}\text{Tt}_{17}$  (A = alkali-metal) with nido- $[\text{Tt}_9]^{4-}$ . [75-78] More recent studies explored heteroatomic systems for clusters such as  $[\text{Tr}_4\text{Pn}_5]^{3-}$ , [79] which are isoelectronic with  $[\text{Tt}_9]^{4-}$ . The advantage of such clusters is that it might be possible to vary their charge by changing the ratio between the two elements without changing the total number of atoms of the cluster, for example  $[\text{Tr}_4\text{Pn}_5]^{3-}$  and  $[\text{Tr}_5\text{Pn}_4]^{5-}$  (Pn, pnictogen). Furthermore, of great interest is the possibility to bring the nine-atom clusters of the heavier tetrel group  $[\text{Tt}_9]$  into solution, and explore their reactivity towards a variety of ligands. [80] They are interesting in making semiconducting thin films and single-size nanoparticles from the dissolved clusters. Such particles exhibit size-dependent band gaps and large nonlinear optical effects that may lead to the next generation of optical devices.

### 1.2.1.3 *Non-classical electron-rich multicenter bonded networks*

Many polyanionic networks in intermetallic compounds built up from heavier late p-block elements show an unusual, non-classical local coordination. These include mainly, linear chains, two-dimensional square sheets and number of fascinating structures derived from these, like one-dimensional strips cut from square lattice.<sup>[81-82]</sup> The bonding theory for these systems, that arises from experimental studies,<sup>[16, 83-84]</sup> is constructed within a framework that makes a connection to well-understood multicenter bonding in small molecules such as  $\text{XeF}_4$ ,  $\text{XeF}_2$ , and  $\text{I}_3^-$  and, which is based on the fundamental 3c-4e bonding, independently introduced by Pimentel and Rundle.<sup>[85-86]</sup> This is similar in spirit to the analogy between the Zintl-Klemm treatment of classical polyanionic networks and octet rule for molecules. Non-classical bonding goes along with the relative absence of significant s-p interactions. The s-p mixing (or its absence) plays a critical role in the occurrence of these phases and in general, in determining their geometrical and electronic structures<sup>[87]</sup> (see §. 4). The electron-rich multicenter bonding may be viewed as delocalized, but directed bond. Meaning that it is intermediated between covalent bond (localized and directed) and metallic interaction (delocalized and non-directed).

## 1.2.2 Beyond electronic effects

Furthermore, a significant number of compounds between post-transition p-element and s-block metal have been found to show *metallic* properties with *open-shell* electron configurations, although they retain other characteristics long attributed to Zintl phases, especially salt like brittleness, stoichiometric formulations, and relatively high melting points.<sup>[88]</sup> It is implied that phase stability can be achieved not only through covalent bonding in the anionic lattice but also via other factors such as Madelung energy and packing efficiency. Unusual deviations from the classical closed-shell bonding scheme may then be tolerated when these other factors are equally important or even dominant in structure formation.<sup>[89]</sup> Thus, a new paradigm has emerged and is still being refined, one that accommodates modern bonding concepts and recognizes competitive factors in structural stabilization.

### 1.3 Scope and aims of this work

The work presented here should be considered within the framework of *compounds design within and beyond the Zintl-concept*. Our first goal is the design and synthesis of new double salts of Zintl anions involving soluble nine atoms clusters  $Tt_9^{4-}$  and oxometallate anions of transition metal like tungstates. Secondly, we are interested in the investigation of the transition from Zintl phases to intermetallics. The smooth transition of chemical bonding and electronic properties from electron-precise to electron-deficient Zintl phases, to nearly-free-electron intermetallic compounds provides a fertile area to search for materials with unique structural chemistry and novel electronic properties. It is well known that unusual structures and properties can be discovered at the transition between bond types.

In fact, the transition from Zintl phases to polar intermetallics can be investigated by systematic chemical combinations. Recent approaches have been based on the variation of the composition (thus of the VEC) in binary phases i.e., an increase of E/A ratio. Also mixed cations approaches have been explored. In the present work, we have embarked on exploring a new approach based on substitutions in the polyanionic substructure of some Zintl phases at the border to intermetallics.

One of the most prominent candidates to study the relationship between structure and physical properties is the element tin, since tin has the outstanding property that it exist in a metallic and nonmetallic allotropes almost equal in stability. The difference of the thermodynamically more stable  $\alpha$ -form compared to the  $\beta$ -form is only  $2 \text{ kJ mol}^{-1}$ . This fact manifests also in binary phases of tin and electropositive metals. On the tin-rich side compounds form structures that are typical for intermetallic compounds, but there exist also examples which form structures that are typical for valence compounds and furthermore compounds that are intermediate between the two classes and which possess both structural motives. <sup>[17]</sup>

Thus, the systematic study of the effects of Bi for Sn partial substitutions in some borderline Zintl phases of the Na/Sn and Ba/Sn phase systems are considered. In addition, the design of new phases with heteronuclear polyanion isoelectronic with borderline Zintl phases was investigated using the ternary system Ba/In/Bi. Last but not least, we have investigated the effects of analogous substitutions in the ternary system Ba/Bi/Sb to study the influence of some relevant atomic properties like electronegativity and relativistic effects on structure and bonding at the Zintl border.

## 1.4 Literature

- [1] Villars, P.; Calvert, L. D. *Pearsons Handbook of Crystallographic Data for Intermetallic Compounds*, 2nd ed.; ASM International: Materials Park, OH, 1991; Desk Edition, **1997**.
- [2] Sims, C. T.; Stoloff, N. S.; Hagel, W. C. *Superalloys II*, Wiley, New York, **1987**.
- [3] Herbst, J. F. in *Supermagnets* (Eds.: G. J. Long, F. Grandjean), **1991**.
- [4] Hillman, H. in *Superconductor Materials Science-Metallurgy, Fabrication and Applications* (Eds.: S. Foner, B. Schwartz), New York, **1981**, pp. 275.
- [5] Schwartz, R. B. in *Intermetallic Compounds, Vol. 3* (Eds.: J. H. Westbrook, R. L. Fleischer), Wiley, New York, **2002**, pp. 681.
- [6] Nagamatsu, J.; Nakagawa, N.; Muranaka, T.; Zenitani, Y.; Akimitsu, J. *Nature* **2001**, *410*, 6824.
- [7] Chan, J. Y.; Kauzlarich, S. M.; Klavins, P.; Shelton, R. N.; Webb, D. J. *Chem. Mater.* **1997**, *9*, 3132.
- [8] Campbell A. M. *Science* **2001**, *292*, 65.
- [9] Chung, D.-Y.; Hogan, T.; Brazis, P.; Rocci-Lane, M.; Kannerwurf, C.; Bastea, M.; Uher, C.; Kanatzidis, M. *Science* **2000**, *287*, 1024.
- [10] Kawaji H.; Horie H.; Yamanaka S.; Ishikawa M. *Phys. Rev. Lett.* **1995**, *74*, 1427.
- [11] Pearson, W. B. *The Crystal Chemistry and Physics of Metals and Alloys*; Wiley-Interscience: New York, **1972**.
- [12] Villars, P. In *Intermetallic Compounds Principles and Practice*; Westbrook, J. H., Fleischer, R. L., Eds.; John Wiley & Sons: Chichester, U.K., **1994**; Vol. 1, pp 227-275.
- [13] Hume-Rothery, W.; Smallman, R. E.; Haworth, C. W. In: *The Structure of Metal and Alloys*. 5<sup>th</sup> Ed. Anthony Rowe Ltd, Chippenham, Wilts, **1969**.
- [14] Pauling, L. In: *The Chemical bond – Structure and Dynamics*. Ed. Zewail, A., Boston Academic Press, Inc. **1992**, pp. 99.
- [15] Nesper, R. *Prog. Sol. St. Chem.* **1990**, *20*, 1.
- [16] Miller, G. J. In *Chemistry, Structure and Bonding of Zintl Phases and Ions*; Kauzlarich, S. M., Ed.; VCH Publishers: New York, **1996**.
- [17] Fässler, T. F.; Hoffmann, S. *Z. Kristallogr.* **1999**, *214*, 722.
- [18] Hume-Rothery, W. *J. Inst. Met.* **1926**, *35*, 313-367.
- [19] Frank, F. C.; Kasper, J. S. *Acta Crystallogr.* **1959**, *12*, 483-499.
- [20] Laves, F. *Naturwissenschaften* **1941**, *29*, 244.
- [21] Pearson, W.B. *J. Less-Common Met.* **1985**, *109*, L3-L6.
- [22] Nesper, R. *Angew. Chem.* **1991**, *103*, 805-834; *Angew. Chem., Int. Ed. Engl.* **1991**, *30*, 789-817.
- [23] Zintl, E.; Brauer, G. *Z. Phys. Chem. B* **1933**, *20*, 245-271.
- [24] Zintl, E.; Woltersdorf, P. *Z. Electrochem.* **1935**, *41*, 876-900.
- [25] Zintl, E. *Angew. Chem.* **1939**, *52*, 1.
- [26] Mooser, E.; Pearson, W. B. *Phys. Rev.* **1956**, *101*, 1608.
- [27] Mooser, E.; Pearson, W. B. *Acta Crystallogr.* **1959**, *12*, 1015.
- [28] Mooser, E.; Pearson, W. B. *Progress in Semiconductors. Vol. 5*, 103, Ed. Gibson, Kröger and Burgess, Wiley & Sons Inc. New York 1960.
- [29] Pearson, W. B. *Acta Crystallogr.* **1964**, *17*, 1.
- [30] Klemm, W. *Proc. Chem. Soc. London* **1958**, 329-341.
- [31] Busmann E. *Z. Anorg. Allg. Chem.* **1961**, *313*, 90.

- [32] Klemm, W. In *Festkoerperprobleme*; Sauter, F., Ed.; Vieweg: Braunschweig, Germany, **1963**; Vol. 3, pp 233-251.
- [33] Klemm, W.; Busmann, E. *Z. Anorg. Allg. Chem.* **1963**, 319, 297.
- [34] Schäfer, H.; Eisenmann, B.; Müller, W. *Angew. Chem.* **1973**, 85, 742.
- [35] Zintl, E.; Dullenkopf, W. *Z. Phys.Chem.B* **1932**, 16, 183.
- [36] Schäfer, H.; Eisenmann, B.; Müller, W. *Angew. Chem.* **1973**, 85, 742-760; *Angew. Chem., Int. Ed. Engl.* **1973**, 12, 694-712.
- [37] von Schnering, H. G. *Angew. Chem.* **1981**, 93, 44-63; *Angew. Chem., Int. Ed. Engl.* **1981**, 20, 33.
- [38] Corbett, J. D. *Chem. Rev.* **1985**, 85, 383-397.
- [39] *Chemistry, Structure and Bonding of Zintl Phases and Ions*; Kauzlarich, S. M., Ed.; VCH Publishers: New York, 1996.
- [40] Corbett, J. D. *Angew. Chem.* **2000**, 112, 682-704; *Angew. Chem., Int. Ed.* **2000**, 39, 670-690.
- [41] Zurcher, F.; Wengert, S.; Nesper, R. *Inorg. Chem.* **1999**, 38, 4567.
- [42] Frisch, G.; Hoch, C.; Röhr, C.; Zönnchen, P.; Becker, K.-D.; Niemeier D. *Z. Anorg. Allg. Chem.* **2003**, 629, 1661-1672
- [43] Wengert, S.; Nesper, R. *Inorg. Chem.* **2000**, 39, 2861.
- [44] Wengert, S.; Nesper, R. *J. Solid State Chem.* **2000**, 152, 460-465.
- [45] Bruzzone, G.; Franceschi, E. *J. Less Common Met.* **1978**, 57, 201
- [46] Turban, K.; Schäfer, H. *Z. Naturforsch. B* **1973**, 28, 220
- [47] Brackett, E. B.; Brackett, T. E. *J. Phys. Chem. A* **1963**, 67, 2132
- [48] Wengert, S.; Nesper, R.; Willems, J.B. *Chem. Eur. J.* **2001**, 7, No. 15, 3209-3213.
- [49] Rieger, W.; Parthé, E. *Acta Crystallogr.* 1967, 22, 919.
- [50] Röhr, C. *Z. Kristallogr.* **1995**, 210, 781.
- [51] M. Boss, F. Pickhard, C. Röhr, *Acta Crystallogr.* **2001**, C 57, 503.
- [52] Wengert S. Dissertation ETH Zurich Nr. 12070, **1997**.
- [53] Karpov, A.; Jansen, M. *Angew. Chem. Int. Ed. Engl.* **2005**, 44, 7639-7643.
- [54] Hoffmann, S.; Fässler, T. F.; Hoch, C.; C. Röhr, *Angew. Chem.* **2001**, 113, 4527; *Angew. Chem. Int. Ed.* **2001**, 40, 4398.
- [55] Mudring, A.-V.; Jansen, M. *Angew. Chem.* **2000**, 112, 3194-3196; *Angew. Chem. Int. Ed.* **2000**, 39, 3066-3069
- [56] Mudring, A.-V.; Nuss, J.; Wedig, U.; Jansen, M. *J. Solid State Chem.* **2000**, 155, 29-36
- [57] von Schnering, H. G.; Curda, J.; Carrillo-Cabrera, W.; Somer, M.; Peters, K. *Z. Kristallogr.* **1996**, 211, 634.
- [58] Curda, J.; Carrillo-Cabrera, W.; Somer, M.; Peters, K.; von Schnering, H. G. *Z. Anorg. Allg. Chem.* **1997**, 623, 929.
- [59] Fässler, T. F.; Kronseder, C. *Angew. Chem., Int. Ed. Engl.* **1997**, 36, 2683.
- [60] von Schnering, H. G.; Bolle, U.; Curda, J.; Peters, K.; Carillo-Cabrera, W.; Somer, M.; Schultheiss, W.; Wedig, U. *Angew. Chem., Int. Ed. Engl.* **1996**, 35, 984.
- [61] Nesper, R.; Curda, J.; von Schnering, H. G. *J. Solid State Chem.* **1986**, 62, 199.
- [62] Müller, W.; Schaefer, H.; Weiss, A. *Z. Naturforsch. B* **1970**, 25, 1371-1374.
- [63] Nesper, R.; Currao, A.; Wengert, S. *Chem. Eur. J.* **1998**, 4, 2251.
- [64] Currao, A.; Wengert, S.; Nesper, R.; Curda, J.; Hillebrecht, H. *Z. Anorg.Allg. Chem.* **1996**, 622, 501.

- [65] Currao, A.; Nesper, R. *Angew. Chem., Int. Ed. Engl.* **1998**, *37*, 841.
- [66] Wengert, S.; Nesper, R. *Inorg. Chem.* **2000**, *39*, 2861.
- [67] Wörle, M.; Nesper, R. *Angew. Chem., Int. Ed. Engl.* **2000**, *39*, 2349.
- [68] Wade, K. *Adv. Inorg. Chem. Radiochem.* **1976**, *18*, 1.
- [69] Zintl, E.; Gourbeau, J.; Dullenkoff, W. *Z. Phys. Chem.* **1931**, *154*, 1.
- [70] Belin, C.; Tillard-Charbonnel, A. *Prog. Sol. St. Chem.* **1993**, *22*, 59.
- [71] Corbett, J. D. *Angew. Chem., Int. Ed. Engl.* **2000**, *39*, 670.
- [72] Klem, M. T.; Vaughey, J. T.; Harp, J. G.; Corbett, J. D. *Inorg. Chem.* **2001**, *40*, 7020.
- [73] Zürcher, F.; Nesper, R.; Hoffmann, S.; Fässler, T. F. *Z. Anorg. Allg. Chem.* **2001**, *627*, 2211.
- [74] Bobev, S.; Sevov, S. C. *Angew. Chem.* **2000**, *112*, 4274; *Angew. Chem. Int. Ed.* **2000**, *39*, 4108.
- [75] Queneau, V.; Sevov, S. C. *Angew. Chem.* **1997**, *109*, 1818; *Angew. Chem. Int. Ed. Engl.* **1997**, *36*, 1754.
- [76] von Schnering, H.-G.; Baitinger, M.; Bolle, U.; Carrilo-Cabrera, W.; Curda, J.; Grin, Y.; Heinemann, F.; Llanos, J.; Peters, K.; Schmeding, A.; Somer, M. *Z. Anorg. Allg. Chem.* **1997**, *623*, 1037.
- [77] Queneau, V.; Todorov, E.; Sevov, S. C. *J. Am. Chem. Soc.* **1998**, *120*, 3263.
- [78] Hoch, C.; Wendorff, M.; Röhr, C. *J. Alloys Compd.* **2003**, *361*, 206.
- [79] Xu, L.; Sevov, S. C. *Inorg. Chem.* **2000**, *39*, 5383.
- [80] Fässler, T. F. *Coord. Chem. Rev.* **2001**, *215*, 347.
- [81] Papoian, G. A.; Hoffmann, R. *Angew. Chem., Int. Ed.* **2000**, *39*, 2408.
- [82] Papoian, G.; Hoffmann, R. *J. Am. Chem. Soc.* **2001**, *123*, 6600.
- [83] Brylak, M.; Jeitschko, W. *Z. Naturforsch. B* **1994**, *49*, 747.
- [84] Brylak, M.; Möller, M. H.; Jeitschko, W. *J. Solid State Chem.* **1995**, *115*, 305.
- [85] Pimentel, C. G. *J. Chem. Phys.* **1951**, *19*, 446.
- [86] Hach, R. J.; Rundle, R. E. *J. Am. Chem. Soc.* **1951**, *73*, 4321.
- [87] Munzarová, M. L.; Hoffmann, R. *J. Am. Chem. Soc.* **2002**, *124*, 4787-4795.
- [88] Corbett, J.D. in *Chemistry, Structure and Bonding of Zintl Phases and Ions*; Kauzlarich, S. M., Ed.; VCH Publishers: New York, **1996**.
- [89] Haussermann, U.; Amerion, S.; Eriksson, L.; Lee, C-S.; Miller G. J. *J. Am. Chem. Soc.* **2002**, *124*, 4371-4383.

## 2. Experimental and characterization methods

### 2.1 Starting materials and synthesis

The starting materials used for the synthesis in this work are all available as commercial products. They are listed in [Table 2.1](#) according to manufacturers form and purity. Almost all manipulations of reactants and products were done in a dry glove box (Mbraun, Garching) under argon atmosphere with O<sub>2</sub> and H<sub>2</sub>O level less than 1 ppm. Air stable reactants were dried under dynamic vacuum (10<sup>-3</sup> mbar) at 150°C over night prior to use. Air and moisture sensitive reactants were stored in the glove-box and were used as received. For alkali and alkaline-earth metal, surface impurities were removed with a scalpel immediately before loading. The syntheses were done in arc-welded niobium or tantalum crucibles. Pieces of 4 to 5 cm length tubes (external diameter 10 mm, wall width: 0.5 mm) were cut from a longer pipe, washed with distilled water and, subsequently dried in an oven at about 120°C over night. The metal tubes were then pressed together on one end with pliers and sealed with an arc-welder under argon atmosphere at reduced pressure (~ 400 mbar). The mixture of reactants was loaded in the container previously sealed on one end. The container was then pressed on the open side with pliers and sealed by arc-welding under argon. The ampoule containing the educts was finally enclosed in a schlenk-quartz tube which was subsequently evacuated and taken into the reaction ovens. No binary alloy of the alkali and alkaline-earth metals with niobium or tantalum is reported. However, Nb and Ta form variety of binary alloys with p-block elements like Ge, Sn, Sb ..., etc. The reactivity of the p-block elements with the tube material is nevertheless much lower than with the active metal at the applied temperature ranges.

**Reaction ovens:** The thermal treatment of the protecting quartz Schlenk-tubes (gas proof closed) containing the metal crucible were done in tubular computer-controlled ovens. The crucibles are enclosed in the quartz Schlenk tubes to prevent their oxidation at high temperature. Characteristics of the ovens (HTM Reetz GmbH, Berlin): Model LOBA, maximum temperature: 1200 °C, interior diameter: 45 mm, tube length: 300 mm, length of uniform temperature zone: 200 mm.

**Table 2.1** Starting material used in the synthesis

<b>Elements</b>	<b>Manufacturer</b>	<b>Form</b>	<b>Purity</b>
Na	Merck	rod under oil	99 %
K	Merck	rod under oil	99 %
Rb	Riedel-de-haën	ampoule	99.9%
Cs	Riedel-de-haën	ampoule	99.9%
Ca	Riedel-de-haën	chips	99.5%
Sr	Chempur	pieces	98 +%
Ba	Chempur	rod	99.3%
In	Aldrich	shot (tear shape)	99.99%
Si	Merck	powder	
Ge	Chempur	pieces	99.9999 +%
Sn	Chempur	granules	99.999%
Sb	Alfa aesar	ingot	99.99%
Bi	Chempur	granules	99.999%
W	Chempur	2.8 $\mu$ powder	99.95%
<b>Compounds</b>			
WO <sub>3</sub>	Aldrich	20 $\mu$ powder	99+%
Rb <sub>2</sub> WO <sub>4</sub>	Chempur	white powder	99.9%
GeO <sub>2</sub>	Chempur	white powder	99.999%
SnO	Aldrich	black powder	99+%
HgO	Alfa aesar	red powder	99.0%

**Thermal treatments:** The majority of the syntheses were performed according to the temperature program in [Figure 2.1](#). The normal heating rate  $r_1$  employed was between 120 and 180 K/h. The reaction time  $t_1$  at first reaction temperature  $T_1$ , and the cooling rate  $r_e$  were different for each synthesis. The cooling rate  $r_2$ , the second reaction temperature  $T_2$  and reaction time  $t_2$  were not in all case applied. All these parameters as well as specific deviations from this general procedure are discussed in more details in the preparative parts of each chapter.

The crucibles were subsequently opened in the glove-box under protecting argon atmosphere as the products are generally very sensitive to air and moisture. The outcome of all reactions was monitored by X-ray powder diffraction.

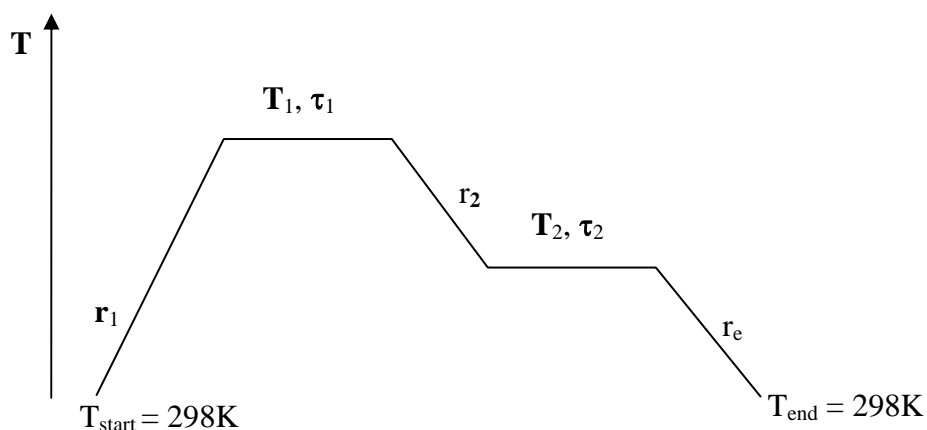


**Figure 2.1** Typical temperature program used for high temperature chemical synthesis

## 2.2 X-ray Diffraction Analysis

### 2.2.1 Powder X-ray diffraction

X-ray diffraction on powder was used for the phase analysis of our reaction products. The preparations of the samples were done in the glove box. The samples were finely ground in an agate mortar with a pestle to a homogeneous powder and then filled into a glass capillary which was previously dried under dynamic vacuum at  $150^\circ\text{C}$  over night (Markt-Röhrchen, length: 80 mm, diameter: 0.1-0.5 mm, Co. Hilgenberg). The capillary filled with the sample was sealed using a red-hot platinum wire.

The powder diagrams were collected on a powder diffractometer STADI P2 (Ge(111) monochromator for  $\text{Cu-K}\alpha_1$  radiation:  $\lambda = 1.54056 \text{ \AA}$ ) equipped with a linear position sensitive detector PSD with  $2\Theta_{\text{eff}} \sim 40^\circ$ , or with an image plate detector IP-PSD with  $2\Theta$  range of  $0\text{-}140^\circ$  (STOE, Darmstadt). Transmission geometry was used to characterize air-stable starting materials, but because the reaction products are very air sensitive only Debye-Scherrer geometry was appropriated.

Calculations of theoretical powder diagrams, as well as data processing of the experimental powder diagrams were performed with the STOE program package WinXPow.<sup>[1]</sup> Phase analyses can be done directly using a databank containing crystallographic data from original literatures or from the ICSD database.<sup>[2]</sup>

## 2.2.2 Single crystal X-ray diffraction

Single crystal X-ray diffraction is the bedrock structural technique in modern day chemistry. Single crystals were selected with a needle and mechanically isolated from the crushed samples in a glove box equipped with an optic microscope (Leica, Wetzlar- Germany), fixed at the top of a 0.1 mm capillary with dry silicon grease, which was in turn inserted into another 0.3 mm capillary and sealed with the hot-platinum wire or with melted wax. The capillaries were previously dried as for powder diffraction. The moisture was removed from the silicon grease by an eutectic mixture of Na and K metals.

The data collections were performed on various single crystal-diffractometers with image detector using monochromated Mo-K $\alpha$  radiation  $\lambda = 0.71073 \text{ \AA}$  (graphite monochromator). Before full data collection, the crystals were first checked for singularity and unit cell was determined from a limited number of diffraction pictures obtained by an appropriate routine. Only crystals with unreported unit cell were involved in full data collection. Among the devices used were the IPDS II with an image plate detector (STOE, Darmstadt) with active imaging plate diameter of 340 mm, max.  $2\Theta = 77^\circ$ , 2-circle goniometer,  $180^\circ \omega$  range, unlimited  $\phi$  range, which was also used at a window of a rotating anode (Nonius, FR591), as well as the Enraf-Nonius KappaCCD equipped with a CCD (charge coupling device) detector at the window of the same rotating anode. A cryostat (Cryostream Controller 700, Oxford Cryosystems) allows measurements at low temperature. Numerical (Xshape, Stoe)<sup>[3]</sup> or empirical absorption correction were applied to the data. The definitions of the parameters used in the crystal structure study by X-ray diffraction are summarized in [Table. 2.2](#).

The structure was solved by direct methods and refined by least-squares on  $F^2$  with the program package SHELXTL.<sup>[4]</sup> This contains, among other, the sub-programs XPREP for space group determination, SHELXS for structure solution and SHELXL for structure refinement. Graphical visualization of the structure can be done using the program XP. For the pictorial representation of the crystal structures, the program DIAMOND<sup>[5]</sup> was used.

### 2.3 Energy Dispersive X-ray (EDX) analysis

Chemical composition of the products was investigated with a scanning electron microscope equipped with an integrated energy dispersive X-ray system. Compositional analysis by this method is semi-quantitative. All synthesized materials were investigated in a JEOL 5900LV operating at 20 kV and equipped with a LINK AN 10000 detector system for EDX analysis.

**Table 2.2** Definitions of different parameters in X-ray diffraction study of single crystal

Error	$\Delta_1 = \ F_o\  - \ F_c\ $ and $\Delta_2 =  F_o^2 - F_c^2 $ $F_o$ = observed structure amplitude (experimental) $F_c$ = structure amplitude calculated from the structure model
Conventional R-factor or residual factor on F	$R_1 = \frac{\sum_{hkl} \Delta_1}{\sum_{hkl} F_o}$ $h, k, l$ Miller indices
Weighted agreement factor	$wR_2 = \sqrt{\frac{\sum_{hkl} w \Delta_2^2}{\sum_{hkl} w (F_o^2)^2}}$ $a$ and $b$ are weighting coefficient $\sigma(F_o)$ = Standard uncertainty on $F_o$ $w = \frac{1}{\sigma^2(F_o^2) + (a \cdot \mathbf{P})^2 + b \cdot \mathbf{P}}$ $\mathbf{P} = \frac{1}{3} \max(0, F_o^2) + \frac{2}{3} F_c^2$
Goodness of Fit for the model	$S = \sqrt{\frac{\sum_{hkl} w \Delta_2^2}{m - n}}$ $m$ = number of Reflections $n$ = number of refined parameters
Internal agreement factor of the data	$R_{int} = \frac{\sum_{hkl} (F_o^2 - \overline{F_o^2})}{\sum_{hkl} F_o^2}$
Standard deviation of the data	$R_\sigma = \frac{\sum_{hkl} \sigma(F_o^2)}{\sum_{hkl} F_o^2}$
Isotropic displacement parameter U	$f' = f \cdot \exp\left(-8\pi^2 \mathbf{U} \frac{\sin^2 \theta}{\lambda^2}\right)$ $f$ atomic scattering factor $f'$ corrected atomic scattering factor (to include atomic vibration)
Anisotropic displacement parameter $U_{ij}$	$f' = f \cdot \exp\left(-2\pi^2 (U_{11}h^2 \mathbf{a}^{*2} + U_{22}k^2 \mathbf{b}^{*2} + U_{33}l^2 \mathbf{c}^{*2} + 2U_{23}kl \mathbf{b}^* \mathbf{c}^* + 2U_{13}hl \mathbf{a}^* \mathbf{c}^* + 2U_{12}hk \mathbf{a}^* \mathbf{b}^*)\right)$ $\mathbf{a}^*, \mathbf{b}^*, \mathbf{c}^*$ reciprocal unit cell vector

### 2.4 Differential Thermal analysis (DTA)

The thermal behaviour of our products was studied by differential thermal analysis with the help of a differential scanning calorimeter NETZSCH DSC 404 c (NETZSCH, Germany). D.T.A is based on the spontaneous temperature difference

between a sample and a thermally inert reference heated in the same oven. This temperature difference arises when a thermal event (exothermic or endothermic) occurred in the sample. This method therefore allows the determination of reaction temperatures, and melting or decomposition points. As reference we used an empty crucible similar to the one containing the sample. Nearly 200 mg of sample was introduced in a Nb crucible which was sealed by arc-welding under argon. The DTA curves were collected under continuous argon flux (TU München) or under static argon atmosphere (TU Darmstadt) to prevent the corrosion of crucible at high temperature. In most cases two cycles of heating and cooling were performed. After the DTA experiments, the crucibles are open in the glove box and the product is again analyzed by x-ray diffraction.

## 2.5 Magnetic measurements

Magnetic susceptibility measurements of some samples were performed using a SQUID magnetometer (Quantum Design MPMS 5S). The samples were cooled in the absence of a magnetic field checked before by an external Hall probe. After the introduction of a magnetic field, data were recorded while the sample was warmed (“shielding”) and then cooled (“Meissner”).

## 2.6 Theoretical calculation of the electronic structures

The quantum mechanical band structures calculation of some of our compounds have been performed with the TB-LMTO-ASA method (Tight Binding Linear Muffin Tin Orbital) using the LMTO program package of Andersen *et al.* [6] in order to point out structure–properties relations. In the LMTO approach, the density functional theory is used with the local density approximation (LDA) for the exchange correlation energy.<sup>[7]</sup> The calculations are done within the atomic spheres approximation (ASA) which includes correction for the neglect of interstitial region and the partial waves of higher order. To reduce the overlap between the atomic spheres as much as possible, empty interstitial spheres were added to the potential. The construction of the ASA radii was performed by an automatic procedure of the program package using the method proposed by Andersen. [8] As a measure of the bonding strengths we computed the crystal orbital Hamiltonian population (COHP)<sup>[9]</sup> function which is the Hamiltonian population weighted density of states. Integrated COHP values of selected atom pair interactions were extracted from the energy-

partitioning crystal orbital Hamilton population scheme <sup>[10]</sup> to gain information about the bond strengths, comparable to the longer established Mulliken overlap populations <sup>[11]</sup> deduced from the crystal orbital overlap populations (COOP).<sup>[12]</sup> Bonding properties were also investigated by analyzing the electron localization function (ELF) <sup>[13]</sup> topologically.<sup>[14]</sup> The ELF results from a comparison of the local Pauli repulsion in the compound with that in a uniform electron gas of the respective electron density at a given point. It can take on values between 0 and 1. High ELF values are found in core shells, covalent bonds, and lone pairs. The ELF may be graphically represented either as 2D slices or by isosurfaces of a certain ELF value enveloping regions of higher ELF. The latter are called domains of the ELF that are considered irreducible if they contain only one attractor (maximum). The topological analysis of the ELF leads to basins, which are the spatial regions containing all points whose gradient paths end at the same attractor. Basins may be grouped into basin sets if the ELF at the interconnection point exceeds a certain value. The ELF proved to be a valuable tool to identify covalent substructures even in intermetallic compounds. <sup>[15-16]</sup>

---

## 2.7 Literature

- [1] Stoe WinxPow, version 2.08, Stoe & Cie GmbH, Darmstadt, **2003**.
- [2] ICSD/Retrieve, version 1.4.1, FIZ Karlsruhe, **2005**.
- [3] X-SHAPE, Stoe & Cie GmbH: Crystal optimization program for numerical absorption correction, based on the program HABITUS by W. Herrendorf and H. Bärnighausen, Karlsruhe (1993), Gieben, 1996, Darmstadt, **1997**.
- [4] Diamond, version 3.1a, K. Brandenburg, Crystal Impact GbR, Bonn, **2005**.
- [5] SHELXTL, version 5.1 UNIX, Bruker Analytical X-ray Systems, 1997.
- [6] Tank, R. W.; Jepsen, O.; Burkhardt, A.; Andersen, O. K. *TB-LMTO-ASA 4.7*; Max-Planck-Institut für Festkörperforschung: Stuttgart, Germany, 1998.
- [7] von Barth, U.; Hedin, L. *J. Phys. C* **1972**, *5*, 1629-1642.
- [8] Jepsen, O.; Andersen, O.K. *Z. Physik B* **1995**, *97*, 35.
- [9] Dronskowski, R.; Blöchl, P. E. *J. Phys. Chem.* **1993**, *97*, 8617-8624.
- [10] Boucher, F.; Rousseau, R. *Inorg. Chem.* **1998**, *37*, 2351.
- [11] Mulliken, R.S. *J. Chem. Phys.* 1955, *23*, 2343.
- [12] Hughbanks, T.; Hoffmann, R. *J. Am. Chem. Soc.* **1983**, *105*, 3528.
- [13] Becke, A.D.; Edgecombe, K.E. *J. Chem. Phys.* **1990**, *92*, 5397.
- [14] Silvi, B.; Savin, A. *Nature* **1994**, *371*, 683-686.
- [15] Savin, A.; Nesper, R.; Wengert, S.; Fässler, T. F. *Angew. Chem., Int. Ed. Engl.* **1997**, *36*, 2683; **1997**, *109*, 1892.
- [16] Fässler, T. F. *Chem. Soc. Rev.* **2003**, *32*, 80-86.

### 3. Alkali-metal Germanides and Germanide-Tungstate double salts

#### 3.1. Introduction

The possibility to combine Zintl anions with other classical anions in formally double salts was first demonstrated quite recently in some halogenide silicides by Simon and co-workers using rare-earth metals as counterions.<sup>[1-2]</sup> The systematic investigation of silicide halogenide double salts using alkaline-earth metal by Nesper and co-workers results in further examples of such type of materials, sometimes with unprecedented Zintl anions like cyclotrisilicide.<sup>[3-4]</sup> The real breakthrough in the synthesis of this emerging class of composite materials was the discovery of the rather unexpected tetrelide-tetrelate compounds where the same group 14 elements co-exist with negative and positive oxidation states in the two different anions of the structure.<sup>[5]</sup> This class of double salts features tetrelate anions and the ubiquitous Zintl anions  $[\text{Tt}_4]^{4-}$  (Tt = element of the group 14). The latter are isosteric with white phosphorus and are known from the binary Zintl phases  $\text{ATt}$  and  $\text{A}_{12}\text{Tt}_{17}$  (A = alkali metal). They co-exist in the latter with Wade nido-clusters  $[\text{Tt}_9]^{4-}$  in the ratio  $\text{Tt}_4:\text{Tt}_9 = 2:1$ . In the tetrelide-silicate  $\text{Cs}_{10}[\text{Si}_4][\text{Si}_3\text{O}_9]$ <sup>[5]</sup> the Zintl anion  $[\text{Si}_4]^{4-}$  exists along with the cyclotrisilicate ion  $[\text{Si}_3\text{O}_9]^{6-}$ , known from silicates of the form  $\text{A}_6\text{Si}_3\text{O}_9$ .<sup>[6]</sup> The two isotopic rubidium compounds  $\text{Rb}_{14}[\text{Si}_4]\text{Si}_6\text{O}_{17}$  and  $\text{Rb}_{14}[\text{Ge}_4]\text{Si}_6\text{O}_{17}$  can also be formally separated into ions in the same way. Beside the tetrelide anions  $[\text{E}_4]^{4-}$ , they feature the anion  $[\text{Si}_6\text{O}_{17}]^{10-}$ , previously unknown for the silicates and composed of two condensed cyclotrisilicate rings.<sup>[5]</sup> It is amazing that in those compounds, Ge or Si atoms have a the formal oxidation state  $-I$  in the anions  $[\text{E}_4]^{4-}$ , whereas in the silicate unit  $[\text{Si}_6\text{O}_{17}]^{10-}$  Si has the formal oxidation state  $+IV$ . Moreover, the stannide silicate  $\text{Cs}_{20}[\text{Sn}_4]_2[\text{SiO}_4]_3$  and stannide germanate  $\text{A}_{12}[\text{Sn}_4]_2[\text{GeO}_4]$  (A = Rb, Cs) have been reported.<sup>[7]</sup> Even some 'metallide metallate oxides' compounds featuring the anions  $[\text{Sn}_4]^{4-}$  beside  $[\text{SnO}_3]^{4-}$  as well as isolated oxygen anions have been discussed.<sup>[8]</sup>

The tetrelate-tetrelide mixed materials have great potential as precursors for the synthesis of nanoparticles of the tetrel elements. Nanostructured materials featuring

metal or semiconductor clusters of well defined sizes are tunable light-emitting materials due to quantum size effects and they often display catalytic properties that can be modified by the particle size. [9-11] Therefore the next logical step is to look for double salts with the larger Zintl anions  $[\text{Tt}_9]^{4-}$  which may have several advantages compared to the smaller  $[\text{Tt}_4]^{4-}$  anions. The former are molecules of captivating beauty and simplicity, which can be regarded as small charged element particles that open new possibilities for chemical reactions and the development of nano-scaled materials. In fact, they are soluble in diverse organic solvents, providing further possibilities of synthetic strategies of nanoscaled materials in liquid media. Furthermore, they can be functionalized and interconnected through controlled oxidation, allowing an effective tuning of cluster size and properties. [12-14]

Also, of great fundamental and technological interests is the preparation of double salts between Zintl anions and oxometallate of transition metal. The semiconducting transition metal oxides are important wide band gap semiconductors that have distinctive properties. [15] Among the numerous transition metal semiconducting oxides, tungsten oxides are of intense interests and have been investigated extensively for their outstanding electrochromic, optochromic, and gaschromic properties. Tungsten oxides have been used to construct flat panel displays, photoelectrochromic "smart" windows, optical modulation devices, writing-reading-erasing optical devices, gas sensors, humidity and temperature sensors, and so forth. [16] Recently, some non-stoichiometric tungsten oxides  $\text{WO}_{3-x}$  have attracted considerable attention in physics, chemistry and materials areas for their interesting electronic properties, especially the superconductivity and charge carrying abilities. [17-18] However, studies on nanoscale tungsten oxides were comparatively rare because of lack of preparation methods for such materials. In attempting to meet the needs of the development of display systems, catalysts, and sensors, the preparation of  $\text{WO}_3$  nanostructures with small crystals and superior surface properties is still a primary challenge for scientists. [19-21] Thus, the preparation of soluble mixed salts of tetrelide tungstate is of trivial importance. In addition, outstanding electronic configurations may arise from the relative energy levels of the transition metal oxometallate LUMO on one hand, and those of the tetrelide clusters HOMO and LUMO on the other, which can lead to interesting electronic or even opto-electronic properties.

### 3.2. Synthesis and characterizations of the alkali metal germanide tungstates $A_{10}[\text{Ge}_9]_2\text{WO}_4$ (A = K, Rb, Cs)

#### 3.2.1 Synthesis

Several synthesis approaches were implemented for the preparation of germanide tungstates. Reactions were carried out in niobium ampoules using various synthesis routes with different starting mixtures.

(i) The double salts could be obtained from reactions using the tungstates  $A_2\text{WO}_4$ , elemental Ge and alkali metal. Mixtures with the composition  $A:\text{Ge}:A_2\text{WO}_4 = 3:5:1$  were used. The mixtures were heated at the rate of 120K/h first to 600°C for 24 hours (to prevent evaporation of the alkali-metal), then to 950°C for 5 hours, cooled down at the rate of -6°C/h to 750°C, annealed for five days, and subsequently cooled down to room temperature at the same rate. Crystals with quite big size could be obtained by this method.

(ii) The compounds could also be prepared directly from simple elements and oxide. Starting mixtures comprise elemental K or Rb, Ge and W as well as  $\text{GeO}_2$ . Mixtures of the composition  $A:\text{Ge}:W:\text{GeO}_2 = 5:3:1:2$  were submitted to thermal treatment similar to point (i). This results in the best crystal quality for  $\text{Rb}_{10}[\text{Ge}_9]_2\text{WO}_4$  which forms ruby red translucent crystals with rod-like or needle-like shape. Nevertheless, the crystals of the Rb based compound are of lower crystalline quality and poorly diffracting compared to the K analogue.

(iii) In the third method, mixtures of elemental alkali metal and Ge as well as the oxides  $\text{WO}_3$  and  $\text{HgO}$  (added as a mere oxygen provider) in the ratio  $A:\text{Ge}:\text{WO}_3:\text{HgO} = 5:5:1:1$  were heated at the rate of 120K/h first to 600°C for 24 hours, then to 800°C for 120 hours and subsequently cooled down to room temperature at the rate of -6°C/h. This results in the best single crystal quality for the  $\text{K}_{10}[\text{Ge}_9]_2\text{WO}_4$  which forms also ruby red transparent crystals with rod- or needle-like shape.

In all three methods described above, the A/Ge ratio in the starting mixtures also appears to be important for the quality of the crystal and even for the obtaining of the desired phases. It should be close to 1 for a successful synthesis. Attempts to prepare the phase from stoichiometric mixtures always failed as the presence of an excess of tungsten oxide seems to be necessary to obtain single crystals of good quality suitable for X-ray diffraction study. The tungstate surface likely contains the

nucleation sites of the mixed salt crystal. Indeed, a careful observation of the reaction products with the optical microscope suggests that mixed salt crystals growth in an epitaxial fashion on the surface of the tungstate phase.

### 3.2.2 EDX analysis and powder X-ray diffraction

Single crystals extracted from the reaction products were analyzed using energy dispersive X-ray spectroscopy. The measurements confirmed the presence of all four elements (K or Rb, Ge, W and O). A quantitative estimation of the atomic ratio was difficult to perform due to the extreme sensitivity of the compounds to moisture. However, an atomic ratio A:Ge close to 1:2 (A = K, Rb) could be observed for most of the analyzed crystals, as well as Ge:W atomic ratio close or larger than 10:1. Because the preparation of the mixed salts from stoichiometric mixtures always failed, all reactions were designed to yield an excess of  $K_2WO_4$ . The X-ray diagrams of the reaction products (Figure 3.1) show reflections corresponding to the double salt (calculated from single crystal structure solution data), along with some other major peaks which are assigned to unreacted elemental tungsten and the tungstate  $K_2WO_4$ .

### 3.2.3 Characterization by Raman spectroscopy

The transparency of the double salt crystals allowed their characterization by Raman spectroscopy. The Raman spectrum of a single crystalline solid of the Rb based phase was recorded at room temperature on single crystals (sealed in a 1mm  $\emptyset$  capillary) from a with a Bio-Rad Fourier transformed Raman system, employing the 1024 nm radiation of an infrared Nd:YAG laser. It should be noted that the Notchfilter cut the signal for wave numbers  $< 130 \text{ cm}^{-1}$ . At least three measurements were made on different crystals and were highly reproducible.

Intensive studies by Raman spectroscopy of the Nine-atom nido-clusters of the group 14 have been done by von Schnering et al. [22] for both the  $A_{12}Tt_{17}$  and the  $A_4Tt_9$  phases. The  $E_9$  clusters show typical lines in the Raman spectrum. For a nine-atom species with  $C_{4v}$  symmetry one expects 21 fundamentals with 20 Raman active modes. Generally four to five broad bands are observed, a phenomenon that was attributed to accidental coincidences and low intensities. Therefore, solid state Raman spectroscopy cannot be used for an analysis of small cluster distortions as

they are observed using X-ray diffraction methods, but they can prove the presence of various clusters in the single crystals, powders, in non-crystalline samples and in solutions. [22]

The Raman spectrum of the  $[\text{Ge}_9]^{4-}$  anion in the alkali metal compounds  $A_4\text{Ge}_9$  ( $A = \text{K, Rb, Cs}$ ) [22] exhibits the breathing mode at  $222 \text{ cm}^{-1}$ , beside two bands of medium intensity at  $147$  and  $164 \text{ cm}^{-1}$  and two additional very weak intensities at  $188$  and  $241 \text{ cm}^{-1}$ , respectively. The “cluster breathing” modes ( $\text{Ge}_9$ ) at  $222 \text{ cm}^{-1}$  is often considered as fingerprints because this mode is the most intense and doesn't overlap. The three fundamentals of  $\text{WO}_4^{2-}$  ( $\text{cm}^{-1}$ ) are Raman active,  $A_1$  ( $\nu_1 = 925$ ),  $B_2$  ( $\nu_3 = 833.5$ ) and  $E$  ( $\nu_2 = 325$ ). For the anion tungstate, the frequencies of solid samples are generally lower than those of vapor or solution samples (see Table 3.1). [23-24]

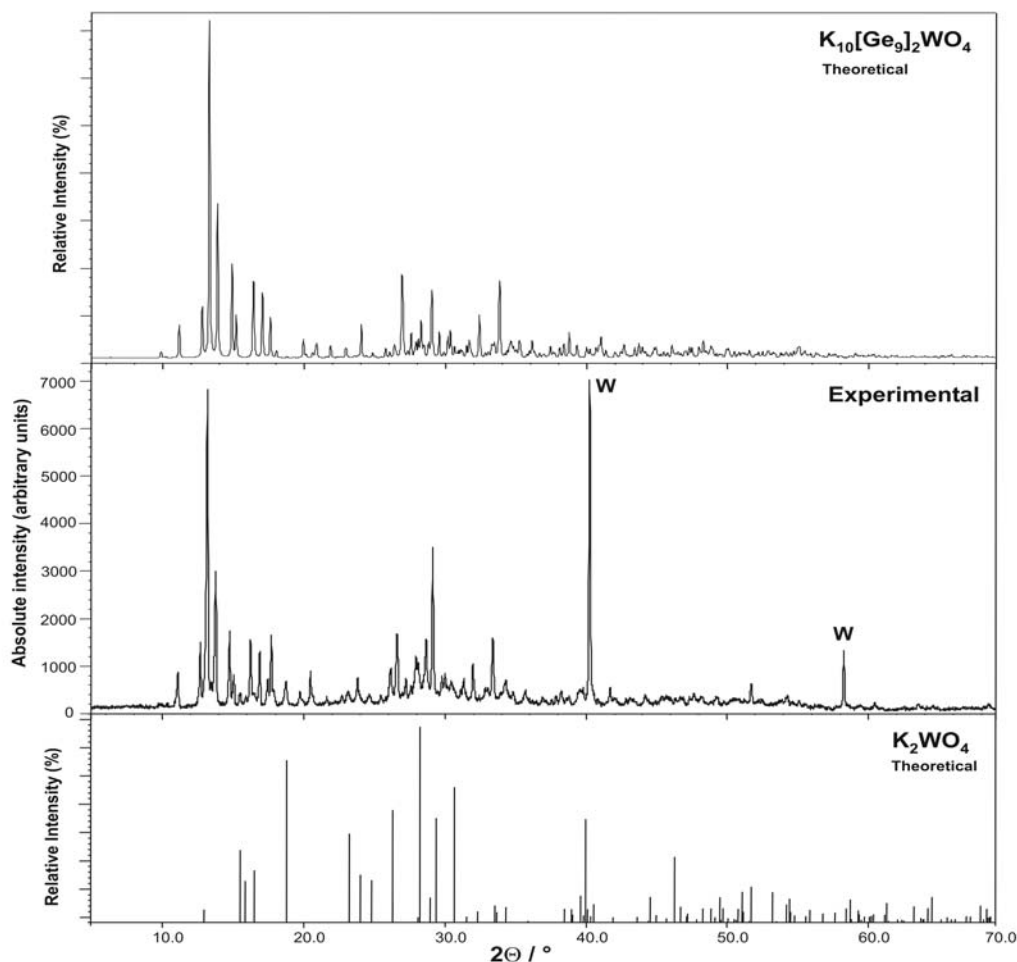


**Figure 3.1** Powder diagram of the reaction products K:Ge:W:GeO<sub>2</sub> (ratio 5:5:1:2) at 750°C; (above) calculated diagrams of  $\text{K}_{10}[\text{Ge}_9]_2\text{WO}_4$ ; (below) peak positions of  $\text{K}_2\text{WO}_4$ . Peaks marked with W correspond to unreacted tungsten metal.

An automatic peak search using the instrument program reveals the following peak positions ( $\text{cm}^{-1}$ ) with the corresponding assignment: 915 ( $\text{WO}_4$ ,  $A_1$ ), 807 ( $\text{WO}_4$ ,  $B_2$ ), 325 ( $\text{WO}_4$ ,  $E$ ), 221 ( $\text{Ge}_9$ ) and 164 ( $\text{Ge}_9$ ). Very weak peaks could possibly be present at 203 (shoulder for  $\text{Ge}_9$ ) and 830 ( $\text{WO}_4$ ,  $F_2$ ). The experimental peaks assigned to the  $\text{WO}_4^{2-}$  anion are in good agreement with those reported in the literature (Table 3.1). Only two peaks can clearly be assigned to the  $\text{Ge}_9$  cluster. The most intense band of the spectrum appears at  $222 \text{ cm}^{-1}$  and correspond to the breathing mode of the  $[\text{Ge}_9]^{4-}$  cluster.<sup>[22]</sup> Considering the characteristic peak of  $\text{Ge}_9$  at  $222 \text{ cm}^{-1}$ , the Raman spectrum confirms, thus, the presence of two different anions  $[\text{Ge}_9]^{4-}$  and  $\text{WO}_4^{2-}$  with very specific intensity patterns and characteristic wave numbers.

**Table 3.1** Raman frequencies ( $\text{cm}^{-1}$ ) of  $\text{WO}_4^{2-}$

	$\nu_1 (A_1)$	$\nu_3 (F_2)$	$\nu_2 (E)$
Solution <sup>[23]</sup>	931 – 928 – 925	$838 \pm 4$	325
Solid state samples <sup>[24]</sup>	901 – 909	836 – 830	
Experimental	916	807 and 830*	325

\* very weak peak

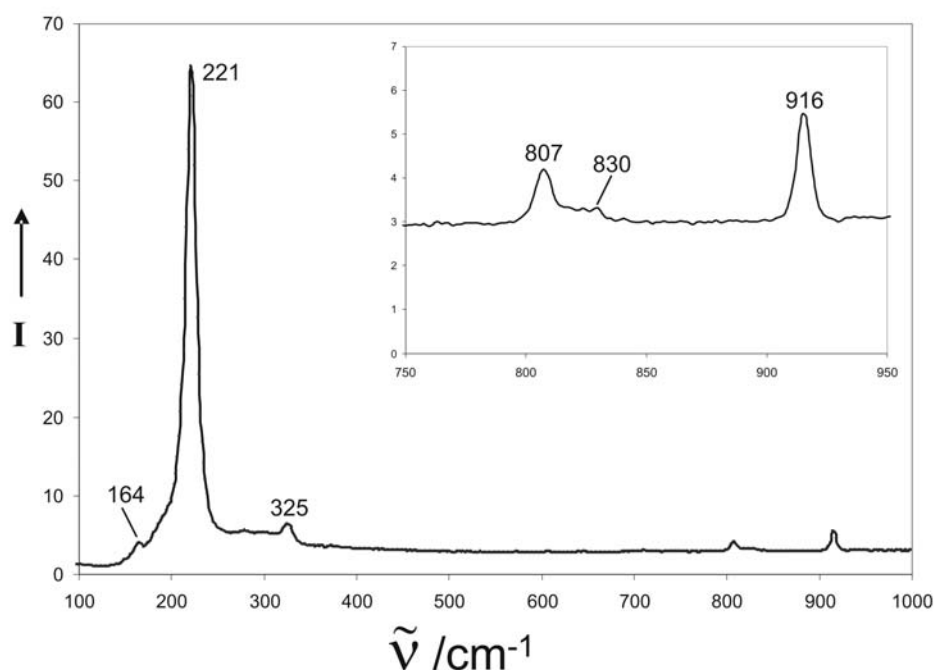


**Figure 3.2** Raman spectra of the double salt  $\text{Rb}_{10}[\text{Ge}_9]_2\text{WO}_4$ . The inset focuses in the region from  $750$  to  $950 \text{ cm}^{-1}$ ; see text and Table 3.1 for the proposed assignment.

### 3.3 Crystal structure of the potassium germanide tungstates $K_{10}[Ge_9]_2WO_4$

#### 3.3.1 Crystal structure determination

A transparent ruby-red crystal with needle-like shape was selected and mounted on top of a glass stick. Full data collection was carried out on the Oxford diffractometer XCalibur3. The unit cell angles are all close to  $90^\circ$ , but on the basis of systematic extinction, the structure was solved in the space group  $P2_1/c$ . The crystallographic data as well as details for structure solution and refinement are summarized in [Table 3.2](#) and [Tables 3.3](#). The structure was solved using the Patterson method and allowed the localization of the W atoms. Ge and Rb positions were successively determined by the difference Fourier method based on the atomic distances and the previously known geometry of the  $Ge_9$  clusters. All atoms, but O were refined with anisotropic thermal parameters. The O positions were localized on the residual electron density map around the W position and refined isotropically. One over two  $Ge_9$  cluster of the structure is disordered.

The displacement ellipsoids of the K9 and K10 atoms which are located within the layer of the disordered cluster B are elongated along the direction to Ge atoms with largest ADPs. This feature seems to indicate a correlation with the disorder of the cluster B. Nevertheless, we were not able to find an acceptable splitting model, as the orientational disorder of the cluster seems to have a rather complex model with more than two orientations of the clusters.

The refinement based on the non-split average model was at first unsatisfactory with a high residual with  $R_1$  of about 25%. But in fact, the monoclinic cell here is pseudo-orthorhombic with a  $\beta$  angle of  $90.05^\circ$ . This is a typical case of twinning by pseudo-merohedry, known to occur when the lattice of the individual has a metric close to that of a higher holohedry. The appropriated twinning matrix was found to be  $\begin{pmatrix} -100 & & \\ 010 & & \\ 001 & & \end{pmatrix}$ , and this is indeed the most important factor, lowering the residuals to acceptable levels. Thus, we considered only the non-split average model and the final residuals, when applying the twinning law, were  $R_1 = 0.080$  and  $wR_2 = 0.198$  for all data and  $R_1 = 0.073$  and  $wR_2 = 0.191$ , for observed reflections [ $I > 2\sigma(I)$ ]. No significant peaks in the residual density map are visible. In fact, when the disorder is only partially refined (two over nine atoms of the disordered Ge cluster B), the residuals drop significantly to  $R_1 = 0.073$  and  $wR_2 = 0.186$  for all data.

**Table 3.2** Crystallographic data and details of structure refinement parameters for  $K_{10}[Ge_9]_2WO_4$ 

Chemical formula	$K_{10}Ge_{18}WO_4$
Formula weight	1945.47
Temperature	293(2) K
Crystal size	0.1×0.15×0.25 mm <sup>3</sup>
Crystal colour and habit	Ruby-red platy rod
Diffractometer	Oxford XCalibur CCD
Crystal system	Monoclinic
Space group	P 1 2 <sub>1</sub> /c 1 (Nr. 14)
Unit cell parameters	a = 13.908(1) Å b = 15.909(1) Å; β = 90.050(6)° c = 17.383(1) Å
Unit cell Volume	3846.03(5) Å <sup>3</sup>
Z	4
Density calculated	3.369 g/cm <sup>3</sup>
Absorption coefficient (Mo K <sub>α</sub> )	17.90 mm <sup>-1</sup> (λ = 0.71073 Å)
Absorption correction	Semi empirical
F(000)	3488.0
Theta range	3.47° - 20.30°
Resolution range	5.87 - 1.02 Å
Index range	-13 ≤ h ≤ 10, -15 ≤ k ≤ 15, -16 ≤ l ≤ 16
Data completeness	100.0%
Integrated reflections	15358 (R <sub>σ</sub> = 0.061)
Independent reflections	3726 (R <sub>int</sub> = 0.077)
Refinement method	Full-matrix least-squares on F <sup>2</sup>
Parameters	279
Goodness of fit on F <sup>2</sup>	1.060
Observed reflections [ >2σ(I)]	3251
Final R indices [ >2σ(I)]	R <sub>1</sub> = 0.073, wR <sub>2</sub> = 0.191
Final R indices (all data)	R <sub>1</sub> = 0.080, wR <sub>2</sub> = 0.198
Twin law	-1 0 0 0 1 0 0 0 1
Twin ratio	0.506
Largest diff. peak and hole	Highest peak 2.96 [2.77 Å from O2] Deepest hole -1.51 [0.86 Å from W1]

$$w=1/[\sigma^2(Fo^2) + (0.121 \times P)^2 + 85.41 \times P] \text{ where } P = (Fo^2 + 2Fc^2)/3$$

### 3.3.2 Description of the Structure of $K_{10}[Ge_9]_2WO_4$

The crystal structure of  $K_{10}[Ge_9]_2WO_4$  is represented in [Figures 3.3](#). It shows discrete  $WO_4$  units and  $Ge_9$  clusters that are separated by isolated K atoms. This is consistent with the ionic formulation as  $10 K^+ (WO_4)^{2-} [(Ge_9)^{4-}]_2$  with the Wade's *nido-cluster*  $Ge_9^{4-}$ . The structure contains two crystallographically independent  $Ge_9^{4-}$  clusters (A and B) and one  $WO_4^{2-}$  anion (C). The anions form alternated layers that are stacked in the [100] direction with the sequence ACBC... ([Figures 3.3a](#)).

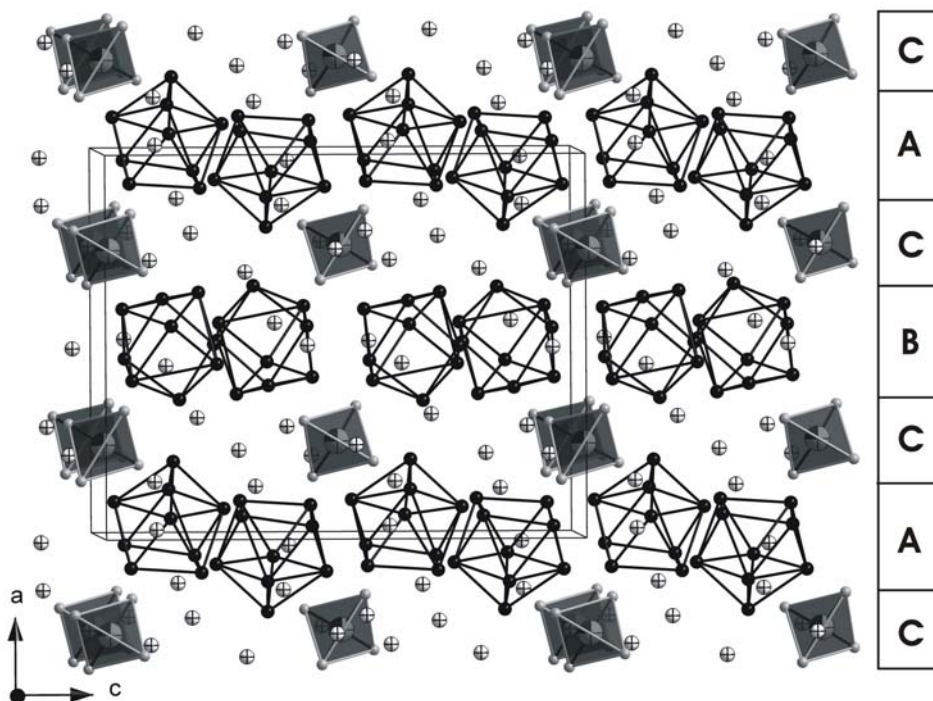


**Figure 3.3 (a)** Structure projection of  $K_{10}[Ge_9]_2WO_4$  in  $[010]$  direction showing alternating layers of germanide clusters (A and B) and tungstate tetrahedra (C) with the sequence ACBC. The  $WO_4^{2-}$  anions are shown as polyhedra, the black spheres are Ge atoms in the  $Ge_9^{4+}$  clusters and isolated crossed spheres are  $K^+$  cations.

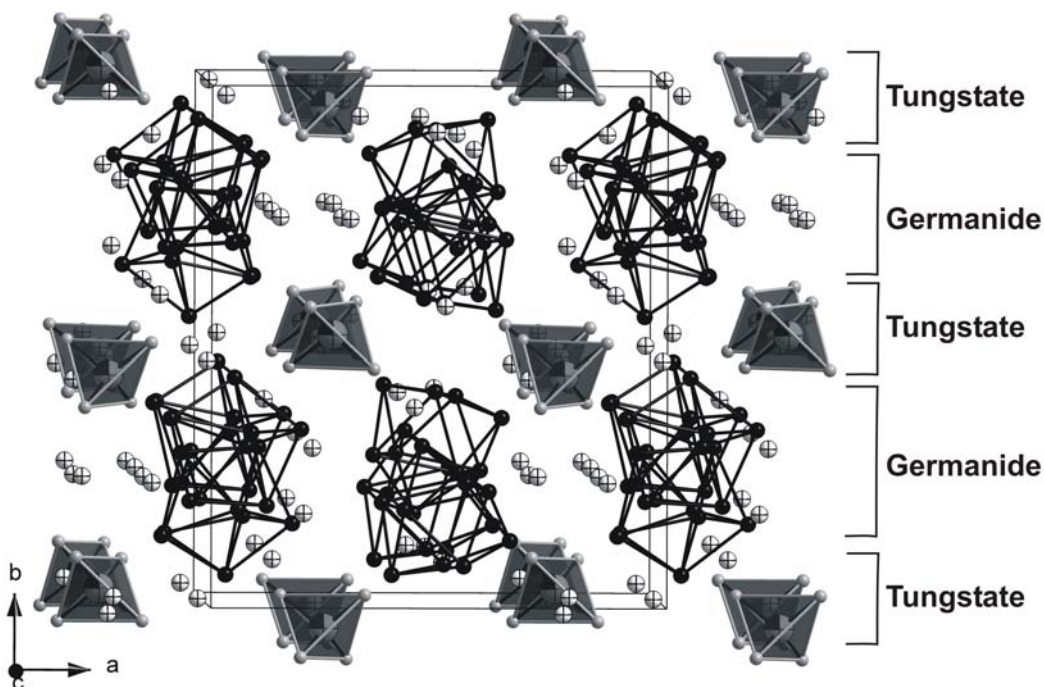


**Figure 3.3 (b)** Projection of the crystal structure of the  $K_{10}[Ge_9]_2WO_4$  in  $[001]$  direction showing alternating layers of germanide clusters and tungstate tetrahedra with the ratio  $Ge_9^{4+} : WO_4^{2-} = 2:1$ .

**Table 3.3a** Atomic coordinates and equivalent displacement parameters for the compound  $K_{10}[Ge_9]_2WO_4$ 

Atom	Wyck.	x	y	z	$U_{eq}/\text{\AA}^2$
W1	4e	0.7537(1)	0.0383(1)	0.0047(1)	0.0473(5)
O1	4e	0.846(2)	0.976(2)	0.053(2)	0.050(6)
O2	4e	0.664(2)	0.974(2)	0.962(2)	0.066(8)
O3	4e	0.700(2)	0.099(2)	0.075(1)	0.048(6)
O4	4e	0.806(2)	0.093(1)	0.930(1)	0.046(6)
Ge1A	4e	0.1906(2)	0.3476(2)	0.1604(3)	0.051(1)
Ge2A	4e	0.0863(3)	0.3371(2)	0.0373(2)	0.045(1)
Ge3A	4e	0.0447(3)	0.4463(2)	0.1515(3)	0.050(1)
Ge4A	4e	0.0675(3)	0.3182(2)	0.2662(2)	0.044(1)
Ge5A	4e	0.1156(3)	0.2010(2)	0.1552(2)	0.045(1)
Ge6A	4e	0.9133(3)	0.3684(3)	0.0710(2)	0.052(1)
Ge7A	4e	0.9019(3)	0.3699(3)	0.2179(2)	0.049(1)
Ge8A	4e	0.0561(3)	0.7111(3)	0.2915(2)	0.051(1)
Ge9A	4e	0.0285(3)	0.7117(2)	0.4374(2)	0.048(1)
Ge1B	4e	0.4483(8)	0.3219(5)	0.3574(6)	0.195(6)
Ge2B	4e	0.5915(6)	0.2372(9)	0.4363(7)	0.236(7)
Ge3B	4e	0.4059(5)	0.2022(5)	0.4554(3)	0.121(3)
Ge4B	4e	0.3628(4)	0.2117(7)	0.2974(6)	0.171(5)
Ge5B	4e	0.5484(4)	0.2471(4)	0.2602(3)	0.092(2)
Ge6B	4e	0.5369(6)	0.0940(7)	0.4478(6)	0.190(5)
Ge7B	4e	0.3819(5)	0.0753(6)	0.3681(6)	0.159(4)
Ge8B	4e	0.4999(5)	0.0920(4)	0.2618(3)	0.106(2)
Ge9B	4e	0.6427(3)	0.1395(4)	0.3354(4)	0.097(2)
K1	4e	0.1458(6)	0.7515(5)	0.1086(5)	0.051(2)
K2	4e	0.1205(7)	0.1039(5)	0.3392(5)	0.064(3)
K3	4e	0.2453(6)	0.5032(5)	0.0209(5)	0.061(2)
K4	4e	0.2043(8)	0.3201(5)	0.4489(7)	0.082(3)
K5	4e	0.7113(6)	0.2557(6)	0.1156(6)	0.069(3)
K6	4e	0.0256(5)	0.5151(6)	0.6049(6)	0.060(2)
K7	4e	0.6844(7)	0.4474(8)	0.3085(5)	0.087(4)
K8	4e	0.2224(9)	0.5276(7)	0.2912(5)	0.094(4)
K9	4e	0.4397(8)	0.389(1)	0.1447(7)	0.118(5)
K10	4e	0.504(1)	0.090(2)	0.0668(9)	0.19(1)

$U_{eq}$  is defined as one third of the trace of the orthogonalized  $U^j$  tensor

The geometry of the anions and their coordination by the alkali metal cations strongly resemble that of the respective parent compounds, the Zintl phase  $K_4Ge_9$  and, the tungstate  $K_2WO_4$ .

The cluster B is strongly disordered resulting in a pathological shape of the thermal ellipsoids of the corresponding Ge atoms. The disorder neither vanishes nor reduces if the data are collected at low temperature (100 K). An acceptable splitting model was difficult to find as the most disordered atoms seem to be distributed in more than two positions. Therefore a non-split average model was chosen for its

description. The distortions due to orientational disorder are very often observed in the structure of different phases featuring  $E_g$  *nido*-clusters and this seems to be mainly a consequence of the incomplete orientational ordering of the clusters and results in relative large conventional  $R$ -values with several alkali metal positions disclosing large values of atomic displacement parameters (ADPs). Sometimes, the disorder can be modeled in terms of statistical occupation by two or more overlapping clusters with different orientations coinciding with only some of the atom positions. In fact, a threefold orientational disorder was found in the binary phase  $K_4Ge_9$  for one of the two crystallographically different clusters (see § 3.6).

**Table 3.3b** Atomic displacement parameters ( $\text{\AA}^2$ ) for the compound  $K_{10}[Ge_9]_2WO_4$

Atom	$U_{11}$	$U_{22}$	$U_{33}$	$U_{12}$	$U_{13}$	$U_{23}$
W1	0.047(1)	0.052(1)	0.043(1)	-0.0013(7)	0.001(1)	0.0024(7)
Ge1A	0.030(2)	0.053(2)	0.070(3)	-0.008(2)	-0.002(2)	0.002(2)
Ge2A	0.049(2)	0.056(2)	0.031(2)	-0.005(2)	0.015(2)	-0.002(2)
Ge3A	0.049(2)	0.035(2)	0.067(3)	0.001(2)	-0.004(2)	-0.011(2)
Ge4A	0.051(2)	0.057(3)	0.024(2)	0.003(2)	-0.007(2)	-0.003(2)
Ge5A	0.042(2)	0.039(2)	0.054(3)	0.008(2)	-0.005(2)	-0.002(2)
Ge6A	0.039(2)	0.075(3)	0.041(2)	0.013(2)	-0.015(2)	0.004(2)
Ge7A	0.043(2)	0.068(3)	0.037(2)	0.015(2)	0.014(2)	-0.000(2)
Ge8A	0.049(2)	0.057(3)	0.046(2)	0.015(2)	0.015(2)	-0.006(2)
Ge9A	0.061(3)	0.044(2)	0.039(2)	0.011(2)	-0.013(2)	0.002(2)
Ge1B	0.27(1)	0.112(5)	0.20(1)	0.073(7)	0.177(9)	0.034(6)
Ge2B	0.109(6)	0.38(2)	0.22(1)	-0.022(8)	-0.024(7)	-0.23(1)
Ge3B	0.118(5)	0.19(1)	0.058(3)	0.081(5)	0.052(3)	0.043(4)
Ge4B	0.061(4)	0.26(1)	0.195(9)	0.006(5)	-0.038(5)	0.135(8)
Ge5B	0.116(4)	0.085(3)	0.074(4)	0.016(4)	0.057(4)	0.026(3)
Ge6B	0.148(6)	0.108(5)	0.063(4)	-0.037(4)	-0.010(4)	-0.036(3)
Ge7B	0.037(2)	0.151(5)	0.102(5)	0.020(3)	0.017(3)	0.000(4)
Ge8B	0.134(6)	0.23(1)	0.21(1)	0.099(7)	0.048(6)	0.158(9)
Ge9B	0.087(5)	0.176(8)	0.21(1)	-0.057(5)	0.040(6)	0.024(7)
K1	0.065(5)	0.044(5)	0.043(5)	-0.001(4)	0.006(4)	0.005(4)
K2	0.081(6)	0.057(6)	0.052(6)	-0.002(5)	-0.026(5)	0.003(5)
K3	0.066(6)	0.046(5)	0.071(6)	-0.008(4)	-0.018(5)	0.017(4)
K4	0.097(8)	0.033(5)	0.116(9)	0.002(5)	0.046(7)	-0.001(5)
K5	0.061(5)	0.065(6)	0.080(7)	-0.012(5)	0.016(5)	-0.005(5)
K6	0.041(5)	0.070(6)	0.068(6)	0.007(4)	-0.007(4)	-0.018(5)
K7	0.065(6)	0.16(1)	0.034(6)	0.041(6)	-0.010(5)	-0.010(6)
K8	0.12(1)	0.115(9)	0.044(6)	-0.064(7)	0.020(6)	-0.023(6)
K9	0.063(7)	0.21(2)	0.081(9)	0.061(8)	-0.008(6)	0.004(9)
K10	0.09(1)	0.38(3)	0.10(1)	-0.14(1)	-0.011(9)	0.02(2)

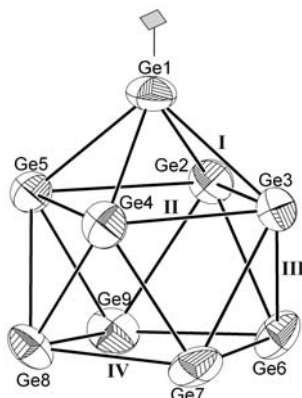
Some relevant interatomic distances are listed in Table 3.4. Considering the idealized  $C_{4v}$  symmetry (i.e. neglecting the deviation from  $4mm$  symmetry), the intracuster Ge–Ge contacts can be sorted into four groups where atoms at equivalent positions are expected to have similar bond distances (Scheme 2):

distances to the capping Ge1 atom (group **I**), within the capped square (group **II**), between the two square (group **III**), and finally within the open basal square (group **IV**). In fact, there are only two types of effective bond lengths in cluster A (ordered). The distances of the group **I** and **III** and **IV** are shorter (from 2.526(5) Å to 2.625(6) Å) than those of the group **II** between five-bonded atoms (from 2.700(5) Å to 3.009(5) Å). This corresponds to the bond pattern found for all fully isolated  $E_9$  *nido*-cluster. Similar distribution of bond distances is observed in the ordered  $Ge_9^{4-}$  cluster of the binary  $K_4Ge_9$ , (see § 3.6) with Ge–Ge distances ranging from 2.517(6) Å to 2.906(6) Å.

The Ge–Ge intracluster distances are also similar to those in e.g.  $Cs_4Ge_9$  (2.522(8) Å – 3.008(11) Å) [25] and to those in  $Ge_9$  clusters of the K-crypt salt crystallized from solution (from 2.538(5) Å to 2.962(7) Å). [26]

The bond distances in the disordered cluster B are roughly in the same range (between 2.360 Å and 3.123 Å) but, because of the strong distortion, the usual bond pattern of  $E_9$  *nido* cluster can not be rigorously observed. The contacts of the group **I** range from 2.36(1) Å to 2.77(2) Å, with some rather short distances like Ge1B–Ge4B (2.36(2) Å) and, also quite long bond distances like group **IV** Ge2B–Ge5B = 3.12(1) Å, which do not correspond to the real distances but result from the non-split average model.

For comparison, the intracluster Ge–Ge distances of the Zintl cluster  $Ge_4^{4-}$  which correspond to 2c–2e bond, are between 2.506(3) Å and 2.556(3) Å in the double salt  $Rb_{14}Ge_4Si_6O_{17}$ , [5] but a bit longer in the Zintl phase  $RbGe$  (from 2.557(1) Å to 2.584(1) Å). [27] Similar Ge–Ge bond distances from 2.496(3) Å to 2.501(3) Å are also found in the germanium type I clathrate (see § 3.7), while in the element the Ge–Ge distance is shorter 2.445 Å.



**Scheme 2.** Ortep view of the  $Ge_9$  cluster A (50% probability level) with labeling of the bond lengths in four groups (I, II, III, IV) according to approximate  $C_{4v}$  point-group symmetry.

**Table 3.4** Ge–Ge and W–O distances of  $\text{Ge}_9^{4+}$  clusters and  $\text{WO}_4^{2-}$  anion respectively, in  $\text{K}_{10}[\text{Ge}_9]_2\text{WO}_4$  (standard deviations are in parentheses)

<b>Cluster A</b>			<b>Cluster B (disordered)</b>		
Atomic pair		distance /Å	Atomic pair		distance /Å
Ge1	—Ge5	2.556(5)	Ge1B	—Ge4B	2.36(2)
	—Ge4	2.556(6)		—Ge5B	2.49(1)
	—Ge3	2.570(5)		—Ge2B	2.77(2)
	—Ge2	2.589(6)		—Ge3B	2.62(1)
Ge2	—Ge6	2.526(5)	Ge2B	—Ge9B	2.45(1)
	—Ge9	2.593(5)		—Ge6B	2.41(2)
	—Ge3	2.700(5)		—Ge3B	2.66(1)
	—Ge5	3.009(5)		—Ge5B	3.12(1)
Ge3	—Ge6	2.611(6)	Ge3B	—Ge6B	2.51(1)
	—Ge7	2.599(6)		—Ge7B	2.55(1)
	—Ge4	2.868(6)		—Ge4B	2.81(1)
Ge4	—Ge7	2.585(5)	Ge4B	—Ge7B	2.51(1)
	—Ge8	2.618(5)		—Ge5B	2.72(1)
	—Ge5	2.765(5)		—Ge8B	2.77(1)
Ge5	—Ge9	2.576(5)	Ge5B	—Ge9B	2.52(1)
	—Ge8	2.567(5)		—Ge8B	2.56(1)
Ge6	—Ge7	2.557(5)	Ge6B	—Ge9B	2.55(1)
	—Ge9	2.625(6)		—Ge7B	2.58(1)
Ge7	—Ge8	2.598(6)	Ge7B	—Ge8B	2.49(1)
Ge8	—Ge9	2.566(6)	Ge8B	—Ge9B	2.46(1)
Ge6	—Ge8	3.485(5)*	Ge6B	—Ge8B	3.28(1)*
Ge7	—Ge9	3.818(5)*	Ge7B	—Ge9B	3.81(1)*

\* corresponding to the diagonal of the open basal square of the clusters

Atomic pair		distance /Å	<i>O–O distances (/Å) at the edges of <math>\text{WO}_4^{2-}</math> tetrahedra</i>		<i>Corresponding <math>\text{O}_i\text{–W–O}_j</math> angles (°)</i>
W1	—O4	1.72(2)	O1—O2	2.99(4)	111.9(11)
	—O3	1.72(2)	O1—O3	2.84(3)	106.4(11)
	—O2	1.78(3)	O1—O4	2.88(3)	108.8(10)
	—O1	1.83(2)	O2—O3	2.84(4)	108.5(11)
			O2—O4	2.79(4)	106.0(12)
			O3—O4	2.91(3)	115.4(11)

The distortion of the clusters from ideal  $C_{4v}$  symmetry can be assessed by the ratio of the two diagonals ( $d_1$  and  $d_2$ ) of the open basal square which should be equal to one in an ideal geometry. The cluster A with  $d_1/d_2$  ratio of 1.1 has the shape of a distorted monocapped square antiprism close to  $C_{2v}$  symmetry. The cluster B ( $d_1/d_2 = 1.16$ ) is more distorted because of the incomplete orientational ordering and may be viewed as hybrid between a monocapped square antiprism and a tricapped trigonal prism ( $D_{3h}$ ) in the non-split average model. For comparison, the two clusters (A and B) are represented in [Figure 3.4](#) with {1,4,4} setting.

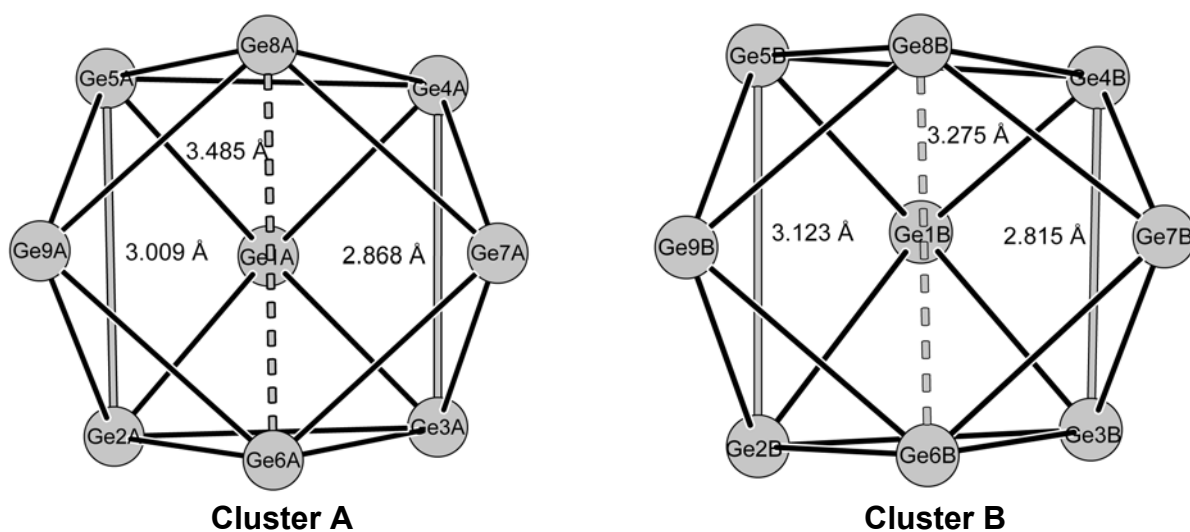


**Figure 3.4** Ball and stick representation of the cluster A (left) and cluster B (right). Grey lines denote heights of eventual tricapped trigonal prism geometry with the fragmented representing the longest height.

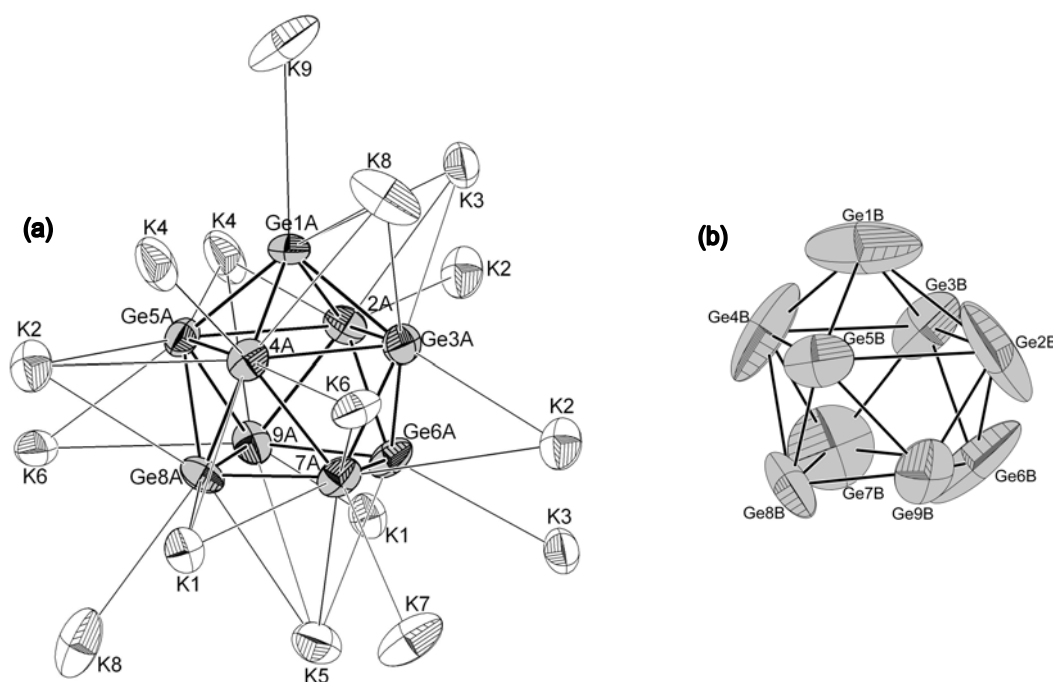


**Figure 3.5** (a) Ortep plot of the coordination of  $\text{Ge}_9^{4+}$  (cluster A) by  $\text{K}^+$  cations (up to 3.9 Å) with several of them capping the polyhedron faces (left) (b) Non-split average model of Cluster B (disordered) with pathological shapes of thermal ellipsoids (at 50% probability level)

Due to the above mentioned distortion of the clusters, it is often difficult to distinguish between a nine-atom closo species (a tricapped trigonal prism) and a nine-atom nido species (a monocapped square antiprism), even for clusters that crystallized from

solution.<sup>[12]</sup> However the two clusters in the present compound are unambiguously *nido*-clusters according to their formal charge and their interatomic distances, although they are strongly distorted with one edged (Ge2–Ge5) of the waist that is significantly longer (3.009(5) Å in cluster A and 3.123 Å in cluster B) than other equivalent contacts.

The Ge<sub>9</sub> clusters are surrounded by 16 closest K<sup>+</sup> neighbours (Figure 3.5) in a quite similar way than in the binary phase K<sub>4</sub>Ge<sub>9</sub> (see §3.6) with several of the cations capping the polyhedron faces. The K–Ge interaction distances in cluster A vary from 3.37(1) Å to 3.87(1) Å, and in cluster B from 3.38(1) Å to 3.97(2) Å. The shortest intercluster distance of 4.01(1) Å observed between cluster A and cluster B is slightly longer than in Cs<sub>4</sub>Ge<sub>9</sub> (3.956(8) Å) although the latter contains bigger Cs<sup>+</sup> cations. The shortest interaction distance between K<sup>+</sup> cations is 3.70(5) Å.

The coordination of the central W atom by the four surrounding oxygen atoms yields a tetrahedra structure. The W–O distances in the WO<sub>4</sub><sup>2-</sup> anion of the mixed-salt range from 1.72(2) Å to 1.83(2) Å and are comparable with those in K<sub>2</sub>WO<sub>4</sub> (from 1.76(4) Å to 1.81(2) Å).<sup>[28]</sup> As illustrated in Figure 3.6, the WO<sub>4</sub><sup>2-</sup> anionic units are surrounded by 9 K<sup>+</sup> cations which is less than the 11 K<sup>+</sup> neighbours found in K<sub>2</sub>WO<sub>4</sub>, but there are strong similarities for the coordination in the two phases as five over six tetrahedron edges are capped by K<sup>+</sup> in both cases.

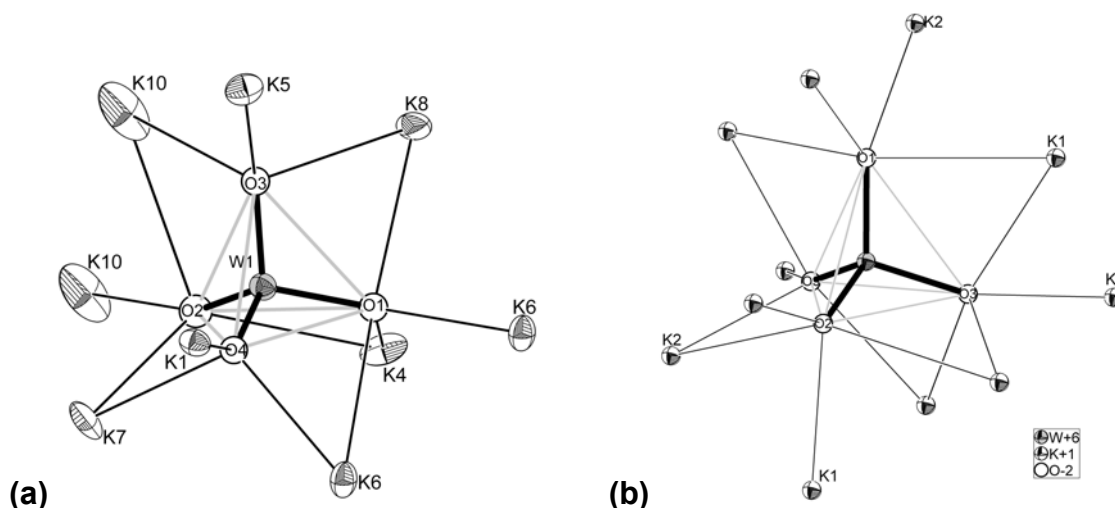


**Figure 3.6** (a) Ortep view of the coordination of WO<sub>4</sub><sup>2-</sup> anion by K<sup>+</sup> in K<sub>10</sub>[Ge<sub>9</sub>]<sub>2</sub>WO<sub>4</sub> with several of them capping the tetrahedron edges (the thermal ellipsoids are at 50% probability level). (b) Coordination of the same anions in K<sub>2</sub>WO<sub>4</sub>.

**Table 3.5** Some relevant O–K and Ge–K interaction distances (< 3.95 Å) in  $K_{10}[Ge_9]_2WO_4$  (standard deviations are in parentheses)

Atomic pair	distance /Å	Atomic pair	distance /Å
O1 —K4	2.58(2)	K4 —Ge3B	3.38(1)
—K6	2.65(3)	—Ge2A	3.36(1)
—K8	2.98(3)	—Ge1B	3.75(1)
—K6	3.34(3)	—Ge4A	3.70(1)
O2 —K10	2.60(3)	—Ge5A	3.81(1)
—K7	2.97(3)	—Ge9A	3.83(1)
—K10	3.42(3)	—Ge4B	3.84(1)
—K4	3.42(4)	K5 —Ge6A	3.42(1)
O3 —K5	2.59(2)	—Ge5B	3.39(1)
—K10	2.74(3)	—Ge2B	3.53(2)
—K8	2.81(3)	—Ge7A	3.67(1)
O4 —K1	2.66(2)	—Ge8A	3.68(1)
—K6	2.72(2)	—Ge9A	3.80(1)
—K7	2.78(3)	K6 —Ge5A	3.76(1)
K1 —Ge9A	3.44(1)	—Ge7A	3.72(1)
—Ge8A	3.48(1)	—Ge9A	3.76(1)
—Ge9B	3.57(1)	—Ge4A	3.71(1)
—Ge7A	3.62(1)	K7 —Ge7A	3.63(1)
—Ge2B	3.75(1)	—Ge5B	3.80(2)
—Ge6A	3.75(1)	—Ge7B	3.80(2)
—Ge4A	3.83(1)	—Ge8B	3.66(1)
K2 —Ge3A	3.41(1)	—Ge1B	3.94(2)
—Ge5A	3.55(1)	K8 —Ge9B	3.40(1)
—Ge2A	3.60(1)	—Ge3A	3.70(1)
—Ge7B	3.70(1)	—Ge1A	3.68(1)
—Ge4A	3.71(1)	—Ge8A	3.73(1)
—Ge4B	3.85(1)	K9 —Ge5B	3.38(1)
—Ge8A	3.76(1)	—Ge1A	3.54(1)
—Ge7A	3.86(1)	—Ge3B	3.62(2)
K3 —Ge6A	3.40(1)	—Ge6B	3.65(2)
—Ge6B	3.40(1)	—Ge8B	3.72(2)
—Ge2A	3.46(1)	—Ge1B	3.85(2)
—Ge1A	3.55(1)	—Ge7B	3.88(2)
—Ge7B	3.50(1)	—Ge6B	3.69(2)
—Ge9B	3.66(1)	K10 —Ge8B	3.39(2)
—Ge3A	3.71(1)	—K10	3.70(5)
		—Ge2B	3.76(2)

The interaction distances between K and the oxygen atoms of the tungstate (Table 3.5) vary from 2.58(2) Å to 2.81(3) Å in  $K_{10}[Ge_9]_2WO_4$  which is a bit shorter compared to those in the simple tungstate  $K_2WO_4$  (between 2.68(3) Å and 2.97(3) Å). In the double salt, the shortest distance between two W centers of the tungstate anions is 6.961(2) Å, much longer than in  $K_2WO_4$  (4.201(5) Å).

Regarding only the packing of the anions, the structure can be described as a hierarchical cluster replacement derivative of the  $\text{Al}_2\text{Cu}$  structure type. <sup>[29]</sup> As shown in [Figure 3.7](#),  $\text{Ge}_9$  clusters substitute Al atoms and the  $\text{WO}_4$  tetrahedra occupy the Cu position, while the  $\text{K}^+$  cations occupy the resulting tetrahedral voids of the structure. The relationship between the basic structure  $\text{Al}_2\text{Cu}$  and the hierarchical derivative structure by atom-by-cluster replacement plus filling of 10 over 16 tetrahedral voids can be written as  $\square_{16}\text{Al}_2\text{Cu} \cong \square_6\text{K}_{10}[\text{Ge}_9]_2[\text{WO}_4]$  ( $\square$  denoted tetrahedral hole).

As a consequence, the structure of  $\text{K}_{10}[\text{Ge}_9]_2\text{WO}_4$  may be described as an antisymmetrical stacking in the [100] direction of almost planar  $3^2434$  nets (A and B) formed by isolated  $\text{Ge}_9$  clusters, that are separated by a larger planar  $4^4$  net of tungstate (C), resulting in the stacking sequence ACBC.... Subsequently, the staggered alternating  $\text{Ge}_9$  layers are penetrated in their quadrangles based channels by strings of isolated  $\text{WO}_4^{2-}$  anions running in the [100] direction in the way that the latter are positioned above and below the layers of the former and are coordinated by eight  $\text{Ge}_9$  clusters in a square antiprismatic geometry ([Figure 3.8](#)).

Apart from the effect of the unfilled tetrahedral holes, the deformation of the formally tetragonal unit cell of the aristotyp ( $\text{Al}_2\text{Cu}$ ) to a monoclinic one is mainly a result of the site colouring due to the different orientations of the 'non-spherical'  $\text{Ge}_9$  clusters for a better packing in the crystal. The distribution of the  $\text{Ge}_9$  clusters here differs clearly with that in the  $\text{K}_4\text{Ge}_9$  phases where the clusters form interpenetrated linear chains in a  $\text{Cr}_3\text{Si}$  like hierarchical derivative.

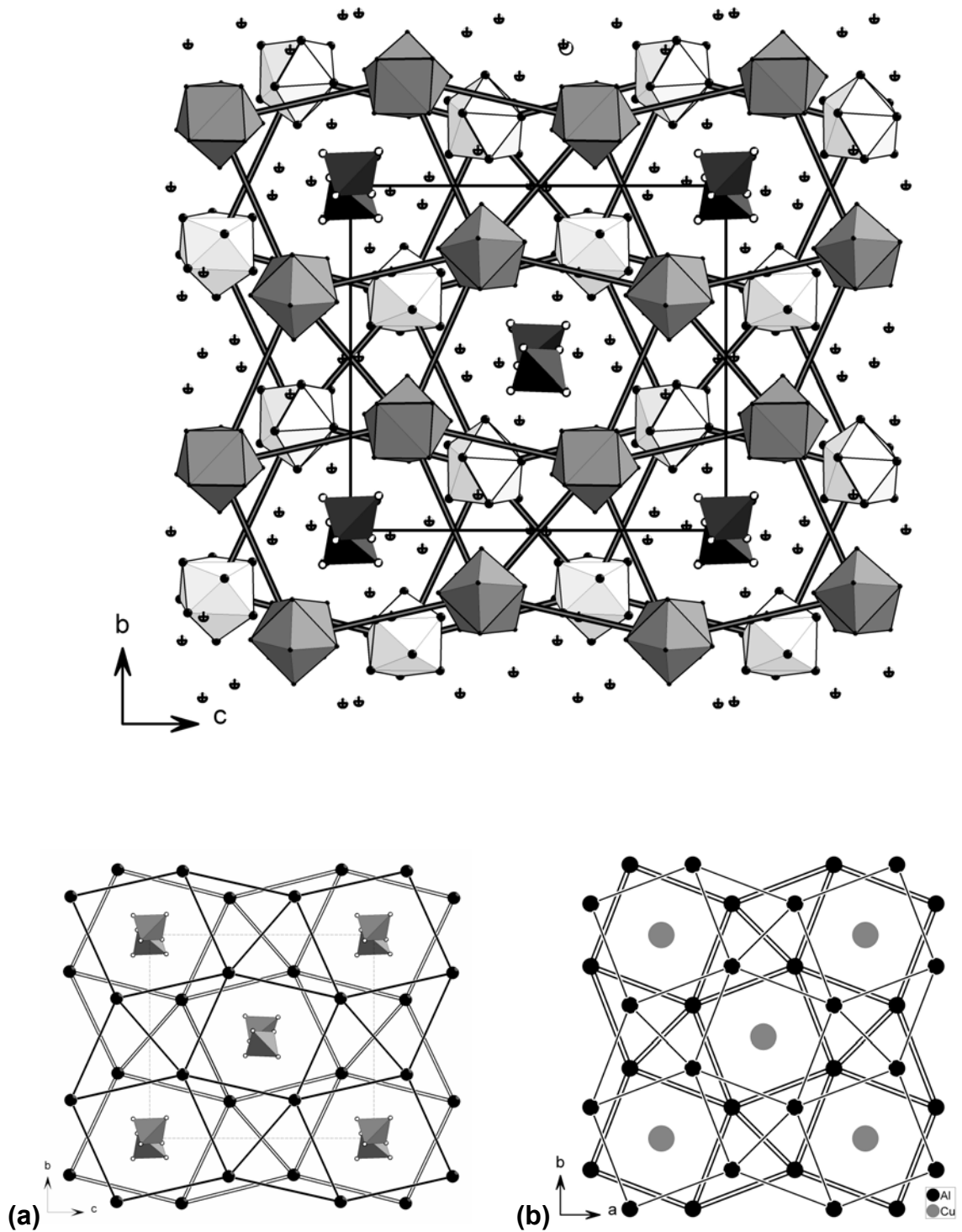


**Figure 3.7** (Top) Projection of the structure of  $K_{10}[Ge_9]_2WO_4$  in  $[100]$  direction.  $Ge_9$  clusters in polyhedral representation; different alternating A and B layers are grey ( $x = 0$ ) or light grey ( $x = 1/2$ ). (a) The  $Ge_9$  clusters are replaced by their centre of gravity for clarity revealing the hierarchical replacement relation with the  $Al_2Cu$ -type (b).

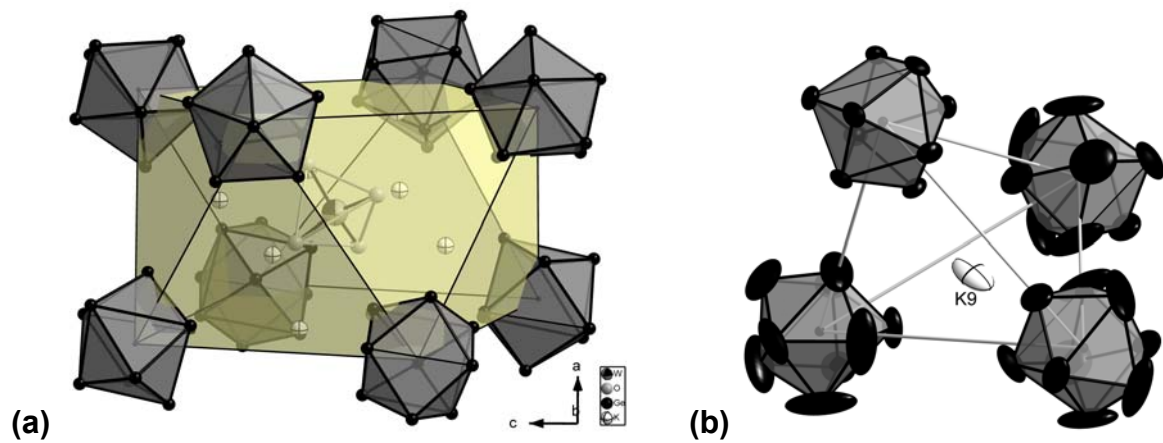


**Figure 3.8** Some details of the  $K_{10}[Ge_9]_2WO_4$  structure. (a) Square antiprismatic coordination of  $WO_4^{2-}$  anion by eight  $Ge_9^{4+}$  clusters with (b)  $K^+$  cations located in the voids of the resulting face sharing tetrahedral.

### 3.4 The Crystal structure of the rubidium germanide tungstates $\text{Rb}_{10}[\text{Ge}_9]_2\text{WO}_4$

#### 3.4.1 Crystal structure determination

The structure solution of the Rb phase which is isostructural to the K compound was straightforward and reveals the similarity of the two crystal structures. A ruby-red transparent crystal with needle shape was selected and mounted on a top of a glass stick. Full data collection was carried out on the Stoe IPDS II diffractometer with an image plate detector which turns to be more appropriated as the crystals of the Rb phase were very poor diffracting. The monoclinic unit cell is again pseudo-orthorhombic, with larger cell edges consistent with the bigger atomic size of the Rb cation compared to K. On the basis of systematic extinctions, the structure solution was done in the space group  $P2_1/c$ , confirming the isotypism with the previous phase  $\text{K}_{10}[\text{Ge}_9]_2\text{WO}_4$ . The crystallographic data as well as details for structure solution and refinement are summarized in [Table 3.6](#), and the atomic parameters in [Tables 3.7](#). The structure model of the K phase was successful used as starting model in the refinement. All atoms, but O were refined with anisotropic thermal parameters. One over two  $\text{Ge}_9$  cluster of the structure is disordered. The refinement based on a split model was still unsatisfactory. Using the same twinning matrix  $-100\ 010\ 001$  the residuals were lowered to better levels of  $R_1 = 0.145$  and  $wR_2 = 0.312$  for all data [ $R_1 = 0.118$ ,  $wR_2 = 0.289$  for  $I > 2\sigma(I)$ ] with no significant residual density map. The poor crystalline quality of the crystal is reflected in the residuals.

#### 3.4.2 Description of the Structure of $\text{Rb}_{10}[\text{Ge}_9]_2\text{WO}_4$

The compound  $\text{Rb}_{10}[\text{Ge}_9]_2\text{WO}_4$  is isotyp to the previously described K homologue. There is one ordered cluster A and one disordered cluster B. The interatomic distances in the  $\text{Ge}_9^{4-}$  clusters and the  $\text{WO}_4^{2-}$  anion are listed in [Table 3.8](#). The Ge–Ge intracluster contacts in cluster A are between 2.555(8) Å and 2.985(7) Å which indicated that this cluster here is overall less distorted than the corresponding one in the K analogue, probably due to packing effects. In the clusters of type B the Ge–Ge contacts are between 2.47(3) Å and 3.04(2) Å. The shape of the  $\text{Ge}_9$  clusters ([Figure 3.9](#)) keeps the two types of bond lengths. For the cluster A, the bond distances to the capping Ge1 atoms (group I) and within the basal open square (group IV) range from 2.555(8) Å to 2.626(8) Å and those of group III (between atoms of the two

different squares) from 2.533(7) Å to 2.623(8) Å. The group **II** distances within the capped square range from 2.727(7) Å to 2.985(7) Å.

Similar distribution of the bond distances can not rigorously be found in the second cluster B due to the strong distortion. The intracluster bond distances of group **I** range from 2.47(3) Å to 2.69(2) Å and those of group **III** from 2.50(1) Å to 2.73(2) Å. The bond distances of group **II** which should all be longer vary from 2.68(1) Å to 3.04(2) Å. At least one bond distance of the group **II** is shorter than some of the first type, but the general trend remains.

**Table 3.6** Crystallographic data and details of structure refinement parameters for  $\text{Rb}_{10}[\text{Ge}_9]_2\text{WO}_4$

Chemical formula	$\text{Rb}_{10}\text{Ge}_{18}\text{WO}_4$
Formula weight	2409.17
Temperature	293(2) K
Crystal size	0.1×0.1×0.3 mm <sup>3</sup>
Crystal colour and habit	Ruby-red needle
Diffractometer	STOE IPDS II
Crystal system	Monoclinic
Space group (No.)	$P 1 2_1/c 1$ (14)
Unit cell parameters	$a = 14.361(3)$ Å $b = 16.356(3)$ Å; $\beta = 90.01(3)^\circ$ $c = 17.839(4)$ Å
Unit cell Volume	4190.3(2) Å <sup>3</sup>
Z	4
Density calculated	3.910 g/cm <sup>3</sup>
Absorption coefficient (Mo $K_\alpha$ )	27.62 mm <sup>-1</sup> ( $\lambda = 0.71073$ Å)
Absorption correction	none
F(000)	4208.0
Theta range	3.32° - 23.94°
Resolution range	6.17 - 0.88 Å
Index range	$-15 \leq h \leq 16$ , $-18 \leq k \leq 18$ , $-20 \leq l \leq 20$
Data completeness	95.3%
Integrated reflections	27051 ( $R_\sigma = 0.129$ )
Independent reflections	6255 ( $R_{\text{int}} = 0.228$ )
Refinement method	Full-matrix least-squares on $F^2$
Parameters	279
Goodness of fit on $F^2$	1.050
Observed reflections [ $I > 2\sigma(I)$ ]	4726
Final R indices [ $I > 2\sigma(I)$ ]	$R_1 = 0.118$ , $wR_2 = 0.289$
Final R indices (all data)	$R_1 = 0.145$ , $wR_2 = 0.312$
Twin matrix	-1 0 0 0 1 0 0 0 1
Twin ratio	0.523
Residual map (e <sup>-</sup> /Å <sup>3</sup> )	5.67 /-4.21

$$w = 1/[\sigma^2(\text{Fo}^2) + (0.1449 \times \text{P})^2 + 300.6819 \times \text{P}] \text{ where } \text{P} = (\text{Fo}^2 + 2\text{Fc}^2)/3$$

**Table 3.7a** Atom coordinates and equivalent isotope atomic displacement parameters for the compound  $\text{Rb}_{10}[\text{Ge}_9]_2\text{WO}_4$  (standard deviations are in brackets)

Atom	Wyck.	x	y	z	$U_{\text{eq}}/\text{\AA}^2$
W1	4e	0.7557(2)	0.0400(1)	0.0048(1)	0.0511(5)
O1	4e	0.844(2)	0.980(2)	0.051(2)	0.05(1)
O2	4e	0.671(3)	0.980(3)	0.961(2)	0.08(1)
O3	4e	0.707(3)	0.108(3)	0.075(3)	0.09(1)
O4	4e	0.801(3)	0.100(2)	0.934(2)	0.07(1)
Ge1A	4e	0.1831(4)	0.3479(3)	0.1615(3)	0.057(1)
Ge2A	4e	0.0841(4)	0.3377(3)	0.0406(2)	0.048(1)
Ge3A	4e	0.0428(4)	0.4440(3)	0.1535(3)	0.053(1)
Ge4A	4e	0.0639(4)	0.3183(3)	0.2644(2)	0.051(1)
Ge5A	4e	0.1109(4)	0.2053(3)	0.1537(3)	0.052(1)
Ge6A	4e	0.9166(4)	0.3698(4)	0.0739(3)	0.054(1)
Ge7A	4e	0.9028(4)	0.3682(4)	0.2175(3)	0.055(1)
Ge8A	4e	0.0557(4)	0.7140(3)	0.2923(3)	0.057(1)
Ge9A	4e	0.0273(4)	0.7172(3)	0.4345(3)	0.050(1)
Ge1B	4e	0.445(1)	0.314(1)	0.355(1)	0.208(9)
Ge2B	4e	0.579(1)	0.246(1)	0.430(1)	0.231(9)
Ge3B	4e	0.398(1)	0.191(1)	0.448(1)	0.167(6)
Ge4B	4e	0.369(1)	0.199(1)	0.290(1)	0.185(8)
Ge5B	4e	0.546(1)	0.242(1)	0.262(1)	0.090(2)
Ge6B	4e	0.535(1)	0.097(1)	0.451(1)	0.139(5)
Ge7B	4e	0.390(1)	0.065(1)	0.366(1)	0.148(5)
Ge8B	4e	0.509(1)	0.089(1)	0.265(1)	0.131(4)
Ge9B	4e	0.640(1)	0.143(1)	0.339(1)	0.108(3)
Rb1	4e	0.1412(3)	0.7472(3)	0.1077(2)	0.050(1)
Rb2	4e	0.1283(4)	0.1028(4)	0.3375(3)	0.065(1)
Rb3	4e	0.2437(4)	0.5041(3)	0.0221(3)	0.058(1)
Rb4	4e	0.2039(5)	0.3200(4)	0.4486(5)	0.102(3)
Rb5	4e	0.7084(4)	0.2589(5)	0.1117(4)	0.083(2)
Rb6	4e	0.0269(3)	0.5099(4)	0.6060(3)	0.064(1)
Rb7	4e	0.6783(5)	0.4393(6)	0.3098(3)	0.094(2)
Rb8	4e	0.2189(5)	0.5293(4)	0.2899(3)	0.086(2)
Rb9	4e	0.4324(5)	0.3826(8)	0.1465(5)	0.137(4)
Rb10	4e	0.5076(7)	0.0859(13)	0.0669(6)	0.213(9)

$U_{\text{eq}}$  is defined as one third of the trace of the orthogonalized  $U^{\text{II}}$  tensor

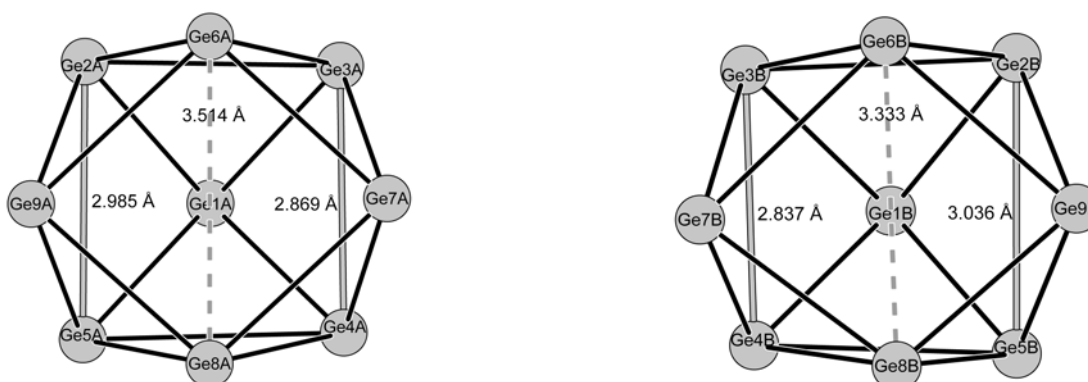


**Figure 3.9** Ball and stick model of the cluster A (left) and cluster B (right), the stronger distortion of cluster B is emphasized by higher bond fluctuation at the heights (draw as grey lines). The shorter diagonal is shown as dashed line.

**Table 3.7b** Anisotropic displacement parameters ( $\text{\AA}^2$ ) for  $\text{Rb}_{10}[\text{Ge}_9]_2\text{WO}_4$ 

Atom	$U_{11}$	$U_{22}$	$U_{33}$	$U_{12}$	$U_{13}$	$U_{23}$
W1	0.053(1)	0.062(1)	0.038(1)	-0.007(1)	0.007(1)	0.001(1)
Ge1A	0.044(3)	0.059(3)	0.067(3)	-0.007(2)	-0.002(3)	0.002(3)
Ge2A	0.054(3)	0.056(3)	0.032(2)	-0.011(2)	0.015(2)	-0.005(2)
Ge3A	0.048(3)	0.046(3)	0.064(3)	-0.002(2)	-0.003(3)	-0.013(2)
Ge4A	0.057(3)	0.069(3)	0.025(2)	-0.001(3)	-0.004(2)	-0.004(2)
Ge5A	0.049(3)	0.048(3)	0.060(3)	0.013(2)	-0.005(3)	0.000(2)
Ge6A	0.048(3)	0.076(3)	0.038(2)	0.017(3)	-0.017(2)	0.006(2)
Ge7A	0.049(3)	0.081(4)	0.035(2)	0.014(3)	0.012(2)	0.006(2)
Ge8A	0.068(4)	0.061(3)	0.043(3)	0.024(3)	0.017(3)	0.000(2)
Ge9A	0.065(3)	0.053(3)	0.032(2)	0.014(2)	-0.014(2)	0.001(2)
Ge1B	0.26(2)	0.19(1)	0.17(1)	0.14(1)	0.16(1)	0.08(1)
Ge2B	0.26(2)	0.25(2)	0.19(1)	-0.02(2)	-0.065(14)	-0.16(1)
Ge3B	0.16(1)	0.26(1)	0.080(5)	0.14(1)	0.089(6)	0.079(7)
Ge4B	0.046(4)	0.31(2)	0.20(1)	-0.038(7)	-0.048(6)	0.16(1)
Ge5B	0.102(5)	0.109(6)	0.060(4)	-0.003(5)	0.039(4)	0.027(4)
Ge6B	0.18(1)	0.139(8)	0.076(5)	-0.082(8)	0.028(6)	-0.043(5)
Ge7B	0.044(3)	0.166(8)	0.113(6)	0.020(4)	0.013(4)	0.020(6)
Ge8B	0.097(6)	0.22(1)	0.100(6)	0.060(7)	0.009(5)	0.089(7)
Ge9B	0.075(5)	0.23(1)	0.137(8)	-0.042(7)	0.012(6)	0.051(9)
Rb1	0.059(3)	0.060(3)	0.031(2)	0.000(2)	0.005(2)	-0.004(2)
Rb2	0.061(3)	0.083(4)	0.051(3)	-0.002(3)	-0.015(2)	0.003(3)
Rb3	0.063(3)	0.054(3)	0.055(3)	-0.007(2)	-0.018(2)	0.011(2)
Rb4	0.100(5)	0.043(3)	0.162(7)	0.007(3)	0.051(5)	0.008(4)
Rb5	0.066(3)	0.109(5)	0.073(4)	-0.007(3)	0.015(3)	-0.003(4)
Rb6	0.049(3)	0.079(4)	0.063(3)	0.006(3)	-0.004(2)	-0.023(3)
Rb7	0.075(4)	0.170(7)	0.036(3)	0.041(4)	-0.012(3)	-0.004(3)
Rb8	0.102(5)	0.113(5)	0.043(3)	-0.043(4)	0.011(3)	-0.019(3)
Rb9	0.070(4)	0.26(1)	0.079(4)	0.066(6)	-0.007(4)	-0.004(6)
Rb10	0.099(7)	0.44(3)	0.099(6)	-0.13(1)	0.006(5)	0.01(1)

Just like in the K analogue, the cluster A with  $d_1/d_2$  ratio of 1.08 has the shape of a distorted monocapped square antiprism close to  $C_{2v}$  symmetry (Figure 3.9). The cluster B ( $d_1/d_2 = 1.15$ ) with orientational disorder is a hybrid between a monocapped square antiprism and a tricapped trigonal prism in non-split average model.

The Ge clusters are coordinated by  $\text{Rb}^+$  cations with the shortest Rb–Ge distance of 3.49(1) Å (Table 3.9). The shortest intercluster distance is 4.28(2) Å, whereas the interaction distances between the  $\text{Rb}^+$  cations are all longer than 3.69(3) Å (Rb10–Rb10).

**Table 3.8** Interatomic distances within  $\text{Ge}_9^{4-}$  clusters and the anion  $\text{WO}_4^{2-}$  in  $\text{Rb}_{10}[\text{Ge}_9]_2\text{WO}_4$  (standard deviations are in parentheses)

<b>Cluster A</b>			<b>Cluster B (disordered)</b>		
Atomic pair		distance /Å	Atomic pair		distance /Å
Ge1	—Ge5	2.555(8)	Ge1B	—Ge4B	2.47(3)
	—Ge4	2.557(8)		—Ge5B	2.50(1)
	—Ge3	2.559(8)		—Ge2B	2.59(3)
	—Ge2	2.587(8)		—Ge3B	2.69(2)
Ge2	—Ge6	2.533(7)	Ge2B	—Ge9B	2.51(2)
	—Ge9	2.577(7)		—Ge6B	2.54(3)
	—Ge3	2.727(7)		—Ge3B	2.77(2)
	—Ge5	2.985(7)		—Ge5B	3.04(2)
Ge3	—Ge6	2.603(7)	Ge3B	—Ge6B	2.50(1)
	—Ge7	2.623(8)		—Ge7B	2.53(2)
	—Ge4	2.869(8)		—Ge4B	2.84(2)
Ge4	—Ge7	2.591(8)	Ge4B	—Ge7B	2.59(2)
	—Ge8	2.623(8)		—Ge5B	2.68(1)
	—Ge5	2.787(7)		—Ge8B	2.73(2)
Ge5	—Ge9	2.540(7)	Ge5B	—Ge9B	2.52(1)
	—Ge8	2.583(8)		—Ge8B	2.56(1)
Ge6	—Ge7	2.569(7)	Ge6B	—Ge7B	2.46(1)
	—Ge9	2.626(8)		—Ge9B	2.51(1)
Ge7	—Ge8	2.597(8)	Ge7B	—Ge8B	2.62(1)
Ge8	—Ge9	2.569(7)	Ge8B	—Ge9B	2.63(2)
Ge6	—Ge8	3.514(8)*	Ge6B	—Ge8B	3.33(1)*
Ge7	—Ge9	3.803(8)*	Ge7B	—Ge9B	3.84(1)*

\* corresponding to the diagonals of the basal open square

Atomic pair	Distance /Å	
W1	—O4	1.73(4)
	—O2	1.75(4)
	—O1	1.80(3)
	—O3	1.82(5)

O—O distances (/Å) at the edges of $\text{WO}_4^{2-}$ tetrahedra	Corresponding $\text{O}_i\text{—W—O}_j$ angles (°)	
O1—O2	2.95(5)	113.1(17)
O1—O3	2.90(5)	106.9(18)
O1—O4	2.92(5)	112.2(17)
O2—O3	2.96(7)	112.9(20)
O2—O4	2.75(6)	104.6(19)
O3—O4	2.86(6)	107.1(20)

The structure of the tungstate anion and its coordination by  $\text{Rb}^+$  cations are similar to those in the parent compound  $\text{Rb}_2\text{WO}_4$  (Figure 3.10).<sup>[30]</sup> The W—O distances in the double salt (Table 3.8) are between 1.73(4) Å and 1.82(5) Å, generally shorter than in  $\text{Rb}_2\text{WO}_4$  (from 1.82(4) Å to 1.88(2) Å). The shortest distance between two W atoms is 7.140(3) Å longer than in the structure of  $\text{Rb}_2\text{WO}_4$  (4.35(2) Å). The closest Ge atom to W (Ge9A) is at about 4.391(6) Å which means that the  $\text{WO}_4^{2-}$  anions are closer to the  $\text{Ge}_9^{4-}$  cluster than to other equivalent anions; nevertheless, the  $\text{Ge}_9^{4-}$

clusters and the  $\text{WO}_4^{2-}$  anion don't see each other directly, but through a screen of  $\text{Rb}^+$  cations. The interaction distances between O and the 9 closest  $\text{Rb}^+$  cations range from 2.55(5) Å to 2.97(4) Å and is reasonably comparable to the corresponding interactions in  $\text{Rb}_2\text{WO}_4$  (from 2.75(4) Å to 3.10(4) Å) in which  $\text{WO}_4^{2-}$  anion is coordination by 11  $\text{Rb}^+$  cations.

**Table 3.9** Some relevant O–Rb and Rb–Ge interaction distances (< 4.0 Å) in  $\text{Rb}_{10}[\text{Ge}_9]_2\text{WO}_4$  (standard deviations are in parentheses)

<i>Atomic pair</i>	<i>distance /Å</i>	<i>Atomic pair</i>	<i>distance /Å</i>
O1 —Rb4	2.71(3)	Rb4 —Ge3B	3.49(1)
—Rb6	2.81(3)	—Ge2A	3.51(1)
—Rb8	3.09(3)	—Ge1B	3.85(1)
—Rb6	3.39(3)	—Ge4A	3.85(1)
O2 —Rb10	2.83(5)	—Ge5A	3.92(1)
—Rb7	3.00(4)	—Ge9A	3.97(1)
—Rb10	3.48(5)	Rb5 —Ge6A	3.56(1)
—Rb4	3.57(4)	—Ge5B	3.57(1)
O3 —Rb5	2.55(5)	—Ge2B	3.74(2)
—Rb10	2.90(5)	—Ge7A	3.82(1)
—Rb8	2.93(5)	—Ge8A	3.86(1)
O4 —Rb1	2.73(4)	—Ge9A	3.94(1)
—Rb7	2.90(4)	Rb6 —Ge5A	3.82(1)
—Rb6	2.97(4)	—Ge7A	3.86(1)
Rb1 —Ge9A	3.55(1)	—Ge9A	3.86(1)
—Ge8A	3.56(1)	—Ge4A	3.86(1)
—Ge7B	3.70(1)	Rb7 —Ge7A	3.80(1)
—Ge7A	3.75(1)	—Ge5B	3.84(1)
—Ge6A	3.85(1)	—Ge9B	3.87(2)
—Ge4A	3.90(1)	—Ge6B	3.87(1)
Rb2 —Ge3A	3.58(1)	Rb8 —Ge7B	3.58(1)
—Ge5A	3.69(1)	—Ge3A	3.78(1)
—Ge2A	3.81(1)	—Ge1A	3.79(1)
—Ge9B	3.84(1)	—Ge8A	3.82(1)
—Ge4A	3.87(1)	Rb9 —Ge5B	3.49(1)
—Ge4B	3.89(1)	—Ge1A	3.64(1)
—Ge8A	3.96(1)	—Ge3B	3.78(1)
—Ge7A	3.99(1)	—Ge8B	3.81(1)
Rb3 —Ge6A	3.53(1)	—Ge6B	3.82(2)
—Ge8B	3.56(1)	—Ge1B	3.89(2)
—Ge2A	3.57(1)	—Ge9B	3.93(2)
—Ge1A	3.67(1)	—Ge8B	3.94(2)
—Ge9B	3.67(1)	Rb10 —Ge6B	3.53(1)
—Ge7B	3.75(1)	—Rb10	3.69(4)
—Ge3A	3.85(1)	—Ge2B	3.81(2)

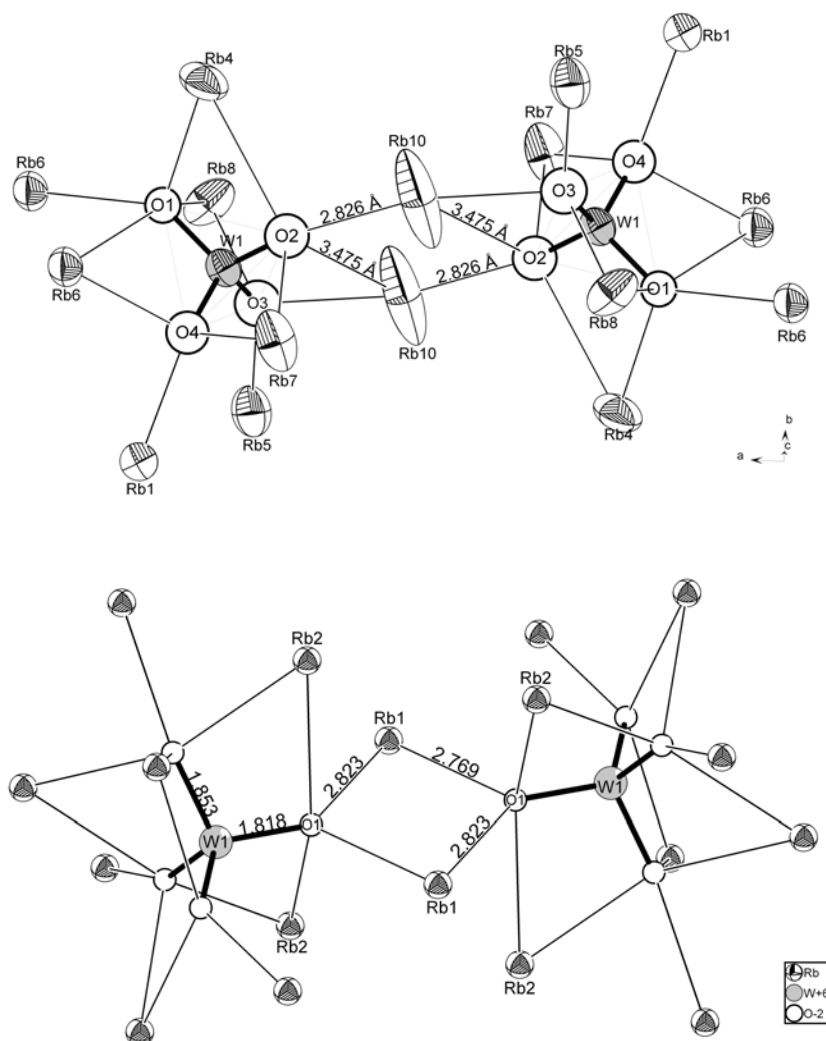


**Figure 3.10** Comparison of the coordination of  $\text{WO}_4^{2-}$  by  $\text{Rb}^+$  in  $\text{K}_{10}[\text{Ge}_9]_2\text{WO}_4$  (**top**) with several of them capping the tetrahedron edges (the thermal ellipsoids are at 50% probability level) and in  $\text{Rb}_2\text{WO}_4$  (**bottom**) showing some clear similarities.

### 3.5 Discussions on the double-salts $\text{A}_{10}[\text{Ge}_9]_2[\text{WO}_4]$

The  $\text{A}_{10}[\text{Ge}_9]_2[\text{WO}_4]$  ( $\text{A} = \text{K}, \text{Rb}, \text{Cs}$ ) compounds crystallize in a new structure type. For the isostructural Cs phase, the unit cell parameters was  $a = 14.944(1)$ ,  $b = 16.472(1)$ ,  $c = 18.498(2)$ ,  $\beta = 91.48(1)^\circ$  and  $V = 4551.7(7)$ , but the crystals were not good enough for satisfactory structure refinements. The topological analysis of the structure shows that they are hierarchical derivatives of the *initiator*  $\text{Al}_2\text{Cu}$  ( $\text{I4/mcm}$ ) with  $\text{Ge}_9^{4-}$  clusters at Al positions and  $\text{WO}_4^{2-}$  anions at Cu positions. Their structure may be viewed as an interpenetration of the two simple parent structures  $\text{A}_4\text{Ge}_9$  and  $\text{A}_2\text{WO}_4$  with the ratio 2:1, i.e.  $2\text{A}_4[\text{Ge}_9] \cdot \text{A}_2[\text{WO}_4]$  ( $\text{A} = \text{K}, \text{Rb}, \text{Cs}$ ). At first glance, the

formation of composite materials between two parent compounds, comprising an almost binary intermetallic phase  $A_4Ge_9$  (with alkali metal, A and a semi-metal, Ge) and an oxometallate of a transition metal (W) may be explained by the topological compatibility of the two parent compounds structures. It is most likely that the main factor behind the existence of the composite compounds is the most favorable Madelung energy. The volume per formula unit of the composite materials, is bigger than the sum of the volumes of the two simple parent compounds:  $V(Rb_{10}[Ge_9]_2[WO_4]) = 1048 \text{ \AA}^3$  bigger than  $2V(Rb_4Ge_9) + V(Rb_2WO_4) = 1027 \text{ \AA}^3$  and, for the K phase  $V(K_{10}[Ge_9]_2[WO_4]) = 961.5 \text{ \AA}^3$  also bigger than the sum of the volumes  $2V(K_4Ge_9) + V(K_2WO_4) = 943.16 \text{ \AA}^3$ . Indeed, in the structure of the composite materials, all the anions involved are more distant to each other than in the corresponding simple compounds. This is particularly true for  $WO_4^{2-}$  anions which are farther in the double salt (7.140(3) Å) than in the structure of  $Rb_2WO_4$  (4.35(2) Å). In  $K_{10}[Ge_9]_2[WO_4]$  the shortest Ge–Ge intercluster distance is 4.01(1) Å, significantly longer than in the binary  $K_4Ge_9$  (3.656(5) Å). In the case of the Rb double salt, the shortest  $Ge_9$  intercluster distance is 4.28(2) Å, longer than in the binary  $Cs_4Ge_9$  structure (3.956(8) Å) though the latter features the bigger  $Cs^+$  cation. Consequently, the formation of the double salt is followed by an increase of volume along with weaker interactions between the different anions of the compounds. This is in agreement with ionic nature of these salt-like compounds.

The preparation of naked  $Ge_9^{4-}$  cluster in 'neat' solid was reported only recently. The difficulty to obtain large cluster of group 14 in the solid state is attributed to the large ratio of nuclearity to charge. Wade's rules for counting bonding electron states in given classes of clusters (*closo*, *nido* ...etc) indicate that deltahedral tetrel clusters will have charges that are independent of their nuclearity, so that large clusters would carry relatively small negative charges. This can presumably set up situations in which the number of cations is insufficient to separate the large clusters. The most common way to crystalline products of Group 14 clusters is therefore the extraction of binary or ternary alloys with ethylenediamine (en) followed by the addition of the sequestering agents [2.2.2]crypt<sup>[26]</sup> or 18-crown-6.<sup>[31]</sup> Only few examples show that crystalline products can be obtained from solution without such sequestering agents. Among these, the inclusion of ethylene diamine (*en*) into the structure of  $Rb_4Ge_9$  was reported and the solvated phase  $Rb_4[Ge_9][en]$  crystallizes in a hierarchical derivative

of the  $\text{Al}_4\text{YbMo}_2$  structure type and has an orange colour indicating an increase of the band gap. [32]

The use of salt melts instead of organic solvents as reaction media for Zintl anion was at the origin, one of the basic ideas behind the investigations of double salts with Zintl anions. The existence of the  $\text{A}_{10}[\text{Ge}_9]_2[\text{WO}_4]$  composite compounds shows that, similarly to organic solvents and to diverse tetrelates, the inclusion of transition metal oxometallate into the structure of the almost pure binary intermetallic phases  $\text{A}_4\text{Ge}_9$  is possible. Interestingly, the synthesis can be done, not only through the reaction between the two simple parent compounds, but also from the simple elements and oxides, yielding the double salt as the major product with no detectable binary intermetallic  $\text{A}_4\text{Ge}_9$ . This may indicate that the crystallization of the composite material is easier than the corresponding simple binary phases. The presence of an excess tungstate phase in the reaction product is in agreement the starting mixtures.

Beyond topological compatibility, the stability of the anion tungstate in a strongly reductive medium should be vital for the existence of the compound. This may explain why attempts to prepare the molybdate analogues have not been successful so far. As a matter of fact, the structure of  $\alpha\text{-SnWO}_4$  contains octahedral coordinated  $\text{W}^{6+}$  ( $\text{WO}_2\text{O}_{4/2}$ ) and was prepared by direct reaction below  $600^\circ\text{C}$  between the oxides  $\text{SnO}$  and  $\text{WO}_3$ , but not the corresponding  $\text{SnMoO}_4$ . Any attempt using  $\text{SnO}$  and  $\text{MoO}_3$  leads to a mixture of  $\text{SnO}_2$  and  $\text{MoO}_2$  indicating that the  $\text{MoO}_3$  is reduced by  $\text{SnO}$ . [33] This is in agreement with the fact that the tungsten bronzes are generally more stable than the corresponding molybdenum bronze.

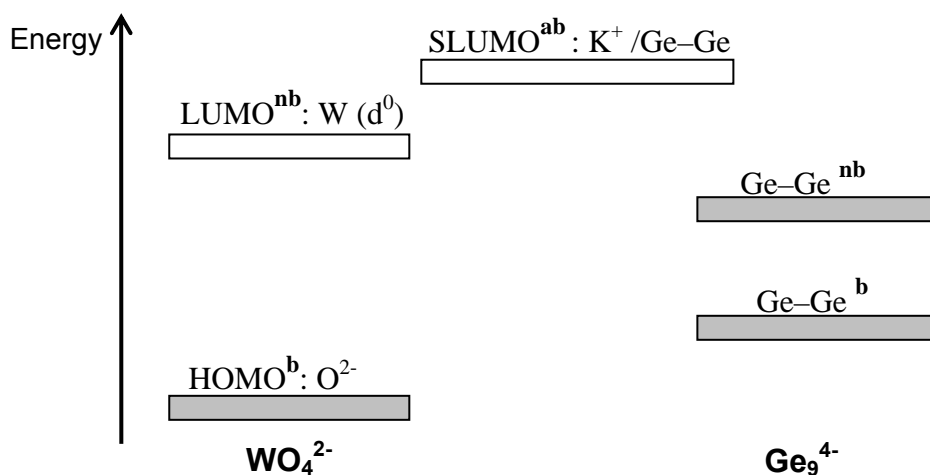
The composite compounds are ruby-red transparent, whereas the semiconducting binary phases  $\text{A}_4\text{Ge}_9$  are deep red. This may also indicate a change of the band gap in the double salt. Indeed, the dark red colour of  $\alpha\text{-SnWO}_4$  has been attributed to the charge transfer from  $\text{Sn}^{2+}$  to octahedral coordinated  $\text{W}^{6+}$  in, whereas the colourless  $\beta\text{-SnWO}_4$  with discrete  $\text{WO}_4$  tetrahedra show significant absorption only in the ultraviolet region because this charge transfer band has been moved to higher energies. [33] The  $\text{A}_2\text{WO}_4$  phases ( $\text{A} = \text{K}, \text{Rb}, \text{Cs}$ ) which contain also isolated  $\text{WO}_4$  tetrahedra are colourless.

Although it is more difficult to transfer an electron to  $\text{W}^{6+}$  in tetrahedral coordination, the energy level of highest occupied molecular orbital (HOMO) of the  $\text{Ge}_9^{4-}$  cluster is higher than that of  $\text{Sn}^{2+}$  cation and this should lower the energy gap. Thus, a charge

transfer from the HOMO of the  $\text{Ge}_9^{4-}$  cluster to the LUMO of the  $\text{WO}_4^{2-}$  anion can not be ruled out as suggested by the plausible electronic states schematically drawn below (Scheme 3).

The phases  $\text{A}_{10}[\text{Ge}_9]_2[\text{WO}_4]$  represent an intriguing class of material in which an oxometallate anion with unfilled non-bonding states ( $\text{W}^{6+}$ ,  $d^0$ ) co-exist beside polynuclear units of a semimetal (Ge) in its negative oxidation state. It is well established that such Zintl anions are very easy to oxidize and this is the main reason why they are air and moisture sensitive.

It would be an exciting challenge to prepare similar composite materials with magnetic transition metal oxide like rhenium or even f-block elements like uranium whose chemical reactivity is often very similar with that of tungsten. This may lead to a new class of materials with dispersed magnetic d-elements. In such system, the long-distant magnetic *d*-electrons can interact with each other through nano-scale spacing and may lead to unique spontaneous spin ordering. Thus, the investigations of optical and electronic properties as well as the preparation of novel composite materials with magnetic d-elements are suitable.



**Scheme 3.** Schematic drawing of the most likely electronic states of the composite material  $\text{A}_{10}[\text{Ge}_9]_2[\text{WO}_4]$ : b = bonding, nb = non bonding, ab = antibonding

### 3.6 The crystal structure of $K_4Ge_9$

#### 3.6.1 Synthesis and characterization

During the preparation of the double salt, simple binaries were often obtained instead, depending on the temperature treatment. Single crystals of the binary phase  $K_4Ge_9$  whose crystal structure is still missing, were obtained from the reaction with the composition  $W:GeO_2:Ge:K = 1:2:4.5:6$ . The mixture, loaded in a niobium ampoule, was heated at the rate of 2K/min to 600°C, hold for 24 hours, then heated up again at 1K/min to 950°C, hold for 5h and, subsequently cooled down to room temperature at -0.1K/min. Some deep red brittle crystals with irregular shape could be extracted from the reaction mixture. EDX analysis reveals the presence of only K and Ge elements, indicating a K/Ge binary phase.

#### 3.6.2 Crystal structure determination of $K_4Ge_9$

Several crystals were selected and first checked for singularity. The best crystal was used for full data collection on the Oxford Xcalibur3 diffractometer at room temperature. Three series of 138 frames were collected with an exposure time of 45 sec each with a crystal-detector distance of 50 mm. The reflection intensities were integrated and a semi-empirical absorption correction was applied. The cell parameters of the rhombohedra lattice were determined and refined using all the integrated peaks. Then, the structure was successfully solved by direct methods in the noncentrosymmetric space group  $R3c$  for a fairly large cell (ca.  $21 \times 21 \times 25 \text{ \AA}^3$ ). Eleven apparent Ge positions were assigned on the basis of peak heights and six K positions judging from bond distances and peak heights. Subsequent least-squares refinements and difference Fourier syntheses quickly located five other weak peaks atoms assigned to defect Ge positions. The occupancies of these positions were allowed to vary, and they converge successively to approximately 1/3, in agreement with the expected stoichiometry. The occupancies at those five positions were therefore fixed to 1/3 and they were refined isotropically. To obtain acceptable residuals, the twin matrix  $\bar{1}000\bar{1}000\bar{1}$  was applied because of the obverse/reverse twinning which is typical in acentric phase with rhombohedra symmetry. The final refinement on  $F^2$  yields the residual factors  $R_1 = 0.073$  and  $wR_2 = 0.203$  for all data [ $R_1 = 0.070$  and  $wR_2 = 0.199$  for  $I > 2\sigma(I)$ ]. The residual Fourier map was essentially featureless. Relevant crystallographic and refinement details are listed in [Table 3.10](#) and, [Tables 3.11](#) contains the atomic positions and displacement parameters.

**Table 3.10** Crystallographic data and details of structure refinement parameters for  $K_4Ge_9$ 

Chemical formula	$K_4Ge_9$
Formula weight	809.71
Temperature	293(2) K
Crystal size	0.2×0.2×0.25 mm <sup>3</sup>
Crystal colour and habit	deep-red block
Diffractometer	Oxford Xcalibur 3
Crystal system	Rhombohedral
Space group	R3c (Nr. 161)
Unit cell parameters	a = 21.208(1) Å c = 25.096(2) Å
Unit cell Volume	9775.4(8) Å <sup>3</sup>
Z	24
Density calculated	3.301 g/cm <sup>3</sup>
Absorption coefficient (Mo, K $\alpha$ )	17.338 mm <sup>-1</sup> ( $\lambda = 0.71073$ Å)
Absorption correction	empirical
F(000)	8736
Theta range	3.33° - 20.30°
Index range	-20 ≤ h ≤ 19, -20 ≤ k ≤ 20, -19 ≤ l ≤ 24
Integrated reflections	12106 ( $R_\sigma = 0.076$ )
Independent reflections	1780 ( $R_{int} = 0.158$ )
Data completeness	99.4%
Refinement method	Full-matrix least-squares on F <sup>2</sup>
Parameters / restraints	168 / 1
Goodness of fit on F <sup>2</sup>	1.173
Observed reflections [ $I > 2\sigma(I)$ ]	1684
Final R indices [ $I > 2\sigma(I)$ ]	$R_1 = 0.070$ , $wR_2 = 0.199$
Final R indices (all data)	$R_1 = 0.073$ , $wR_2 = 0.203$
Twin law	-100 0-10 00-1
Twin ratio	0.883
Residual map [e/Å <sup>3</sup> ]	1.14 / -1.29

$$w = 1/[\sigma^2(F_o^2) + (0.1303 \times P)^2 + 132.17 \times P] \text{ where } P = (F_o^2 + 2F_c^2)/3$$

### 3.6.3 Description of the structure of $K_4Ge_9$

The phase  $K_4Ge_9$  crystallizes in the polar space group R3c and its structure can be described as built of isolated nine-atom clusters of germanium surrounded by potassium cations (Figure 3.12). This is consistent with the ionic formulation as  $4K^+$ ,  $(Ge_9)^{4-}$  in accordance with Wade's rules, electron precise *nido* clusters with 22 skeleton electrons. There are two crystallographically independent  $Ge_9$  clusters in the structure: type A cluster (ordered) and type B cluster (disordered) in a ratio A:B = 3:1. The type A cluster adopts a monocapped square antiprism with only small deviations from the ideal  $C_{4v}$  symmetry (Figure 3.13). The type B cluster approximately represents threefold orientational disorder around the threefold

axis. This means that the site is statistically occupied by three overlapping clusters with different orientations coinciding only with four over nine atomic positions.

Regarding only the packing of the  $Ge_9$  clusters, the crystal structure of  $K_4Ge_9$  represents a hierarchical atom-to-cluster replacement structure of  $Cr_3Si$  in which Cr atoms are replaced by the type A  $Ge_9$  clusters and Si atoms by the disordered type B  $Ge_9$  clusters (Figure 3.14). The  $K^+$  cations occupy 16 of the 24 tetrahedral holes of the pseudo cubic packing. The hierarchical relation can be written as:  $\square_{24}[Cr]_3[Si]_1 \cong \square_8K_{16}[Ge_9]_3[Ge_9]_1$  ( $\square$  represent tetrahedral holes)

**Table 3.11a** Atom coordinates and equivalent isotropic atomic displacement parameters for the compound  $K_4[Ge_9]$  (standard deviation are in parentheses)

Atom	Wyck.	s.o.f	x	y	z	$U_{eq}/\text{\AA}^2$
Ge1	18b	1	0.8684(2)	0.0487(2)	0.2024(2)	0.058(1)
Ge2	18b	1	0.7763(2)	0.0802(2)	0.1620(2)	0.052(1)
Ge3	18b	1	0.7688(2)	0.9416(2)	0.1500(2)	0.055(1)
Ge4	18b	1	0.7896(2)	0.9357(2)	0.2588(2)	0.053(1)
Ge5	18b	1	0.7937(2)	0.0666(2)	0.2756(2)	0.050(1)
Ge6	18b	1	0.6550(2)	0.9576(2)	0.1521(2)	0.054(1)
Ge7	18b	1	0.6638(2)	0.8632(2)	0.2136(2)	0.058(1)
Ge8	18b	1	0.6775(2)	0.9434(2)	0.2944(2)	0.055(1)
Ge9	18b	1	0.6715(2)	0.0368(2)	0.2316(2)	0.053(1)
Ge1B	6a	1	0	0	0.0422(3)	0.063(2)
Ge2B	18b	1	0.4094(2)	0.6798(3)	0.0565(2)	0.067(2)
Ge3B	18b	1/3	0.017(1)	0.906(1)	0.9879(5)	0.043(3)
Ge4B	18b	1/3	0.062(1)	0.949(1)	0.9732(6)	0.058(4)
Ge5B	18b	1/3	0.973(1)	0.890(1)	0.9927(6)	0.059(4)
Ge6B	18b	1/3	0.119(1)	0.041(1)	0.9780(6)	0.050(3)
Ge7B	18b	1/3	0.096(1)	0.997(2)	0.9656(7)	0.063(5)
K1	18b	1	0.5999(6)	0.8059(5)	0.0740(4)	0.071(3)
K2	6a	1	0	0	0.2563(7)	0.071(5)
K3	18b	1	0.7590(5)	0.0123(5)	0.0283(4)	0.072(3)
K4	18b	1	0.6544(6)	0.1172(7)	0.1053(8)	0.136(7)
K5	18b	1	0.8453(6)	0.8412(6)	0.0975(4)	0.080(3)
K6	18b	1	0.8172(6)	0.2386(5)	0.2323(5)	0.083(3)

$U_{eq}$  is defined as one third of the trace of the orthogonalized  $U^j$  tensor

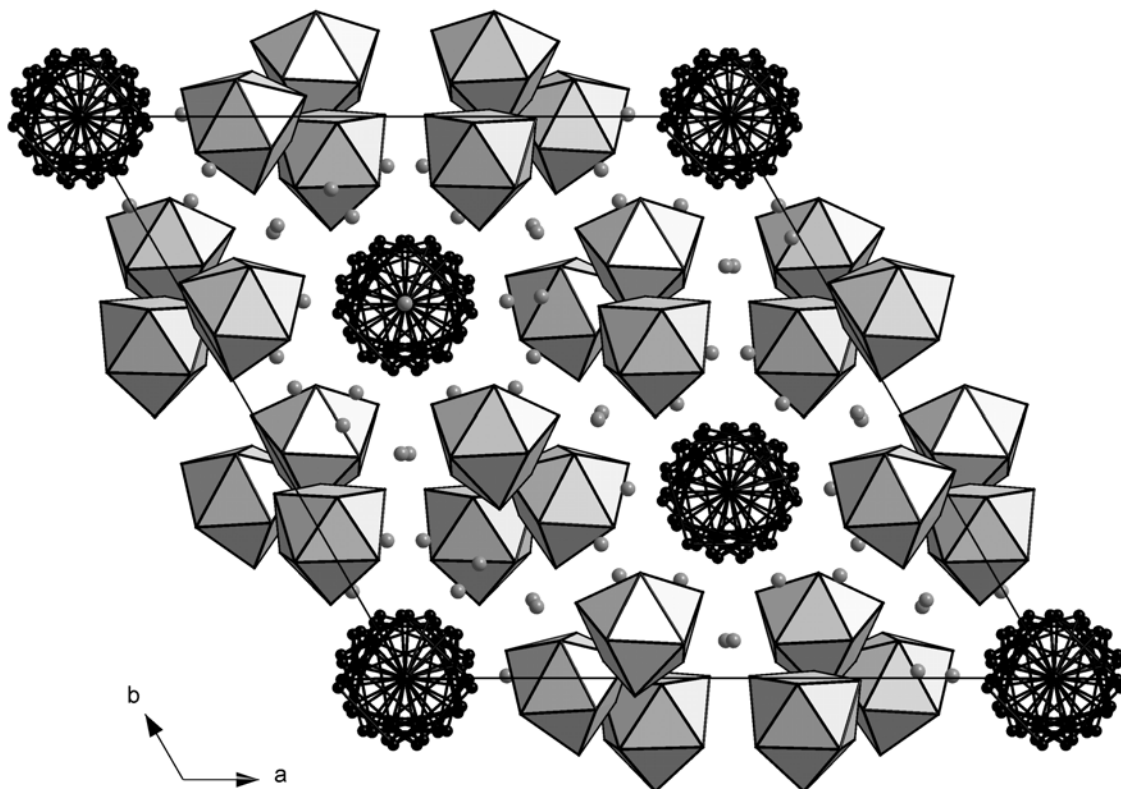


**Figure 3.12** Projection of the crystal structure of  $K_4Ge_9$  in the  $c$ -direction. The ordered  $Ge_9$  clusters (type A) are shown as polyhedra. Black spheres are Ge atoms in the disordered cluster (type B) and K atoms are isolated grey spheres.

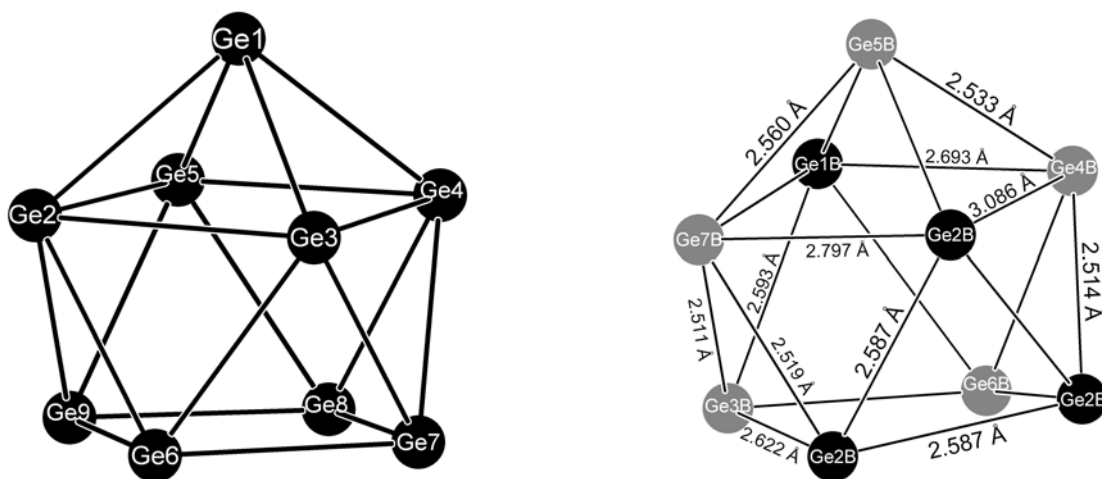


**Figure 3.13** View of the two types of  $Ge_9$  clusters in  $K_4Ge_9$  with a monocapped square antiprism: left type A and right type B. Cluster B has the same geometry in its three symmetry related orientations. The numbering system here serves for the assignment of the atoms in Table 3.12.

**Table 3.11b** Anisotrope atomic displacement ( $\text{\AA}^2$ ) parameters for the compound  $K_4[Ge_9]$  (standard deviations are in parentheses)

Atom	$U_{11}$	$U_{22}$	$U_{33}$	$U_{12}$	$U_{13}$	$U_{23}$
Ge1	0.036(2)	0.066(3)	0.069(3)	0.023(2)	0.003(2)	0.001(2)
Ge2	0.064(3)	0.041(2)	0.050(3)	0.026(2)	0.001(2)	0.013(2)
Ge3	0.070(3)	0.067(3)	0.047(2)	0.048(2)	-0.003(2)	-0.012(2)
Ge4	0.060(3)	0.058(3)	0.055(3)	0.040(2)	0.002(2)	0.011(2)
Ge5	0.047(2)	0.046(2)	0.055(3)	0.020(2)	-0.008(2)	-0.016(2)
Ge6	0.049(2)	0.053(2)	0.057(3)	0.023(2)	-0.016(2)	-0.009(2)
Ge7	0.068(3)	0.034(2)	0.055(3)	0.013(2)	-0.004(2)	-0.002(2)
Ge8	0.061(3)	0.051(2)	0.051(3)	0.027(2)	0.015(2)	0.009(2)
Ge9	0.062(3)	0.076(3)	0.045(2)	0.051(2)	0.001(2)	-0.004(2)
Ge1B	0.070(3)	0.070(3)	0.047(5)	0.035(2)		
Ge2B	0.054(3)	0.096(4)	0.055(3)	0.040(3)	0.004(2)	0.005(2)
Ge4B	0.047(9)	0.08(1)	0.068(9)	0.05(1)	0.004(8)	-0.014(9)
K1	0.101(8)	0.051(5)	0.066(6)	0.040(5)	0.000(5)	0.004(5)
K2	0.068(7)	0.068(7)	0.08(1)	0.034(3)		
K3	0.081(6)	0.057(6)	0.049(5)	0.013(5)	-0.008(5)	-0.010(5)
K4	0.069(7)	0.094(9)	0.22(2)	0.024(7)	-0.030(9)	0.09(1)
K5	0.107(9)	0.063(6)	0.077(8)	0.048(6)	0.018(6)	0.004(5)
K6	0.096(8)	0.055(6)	0.091(8)	0.034(6)	0.018(6)	0.002(6)

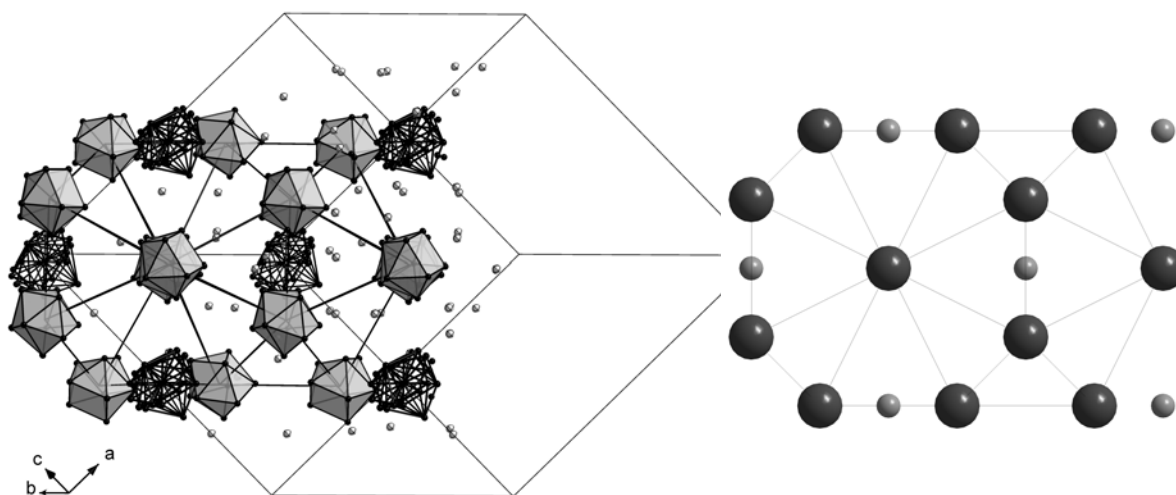


**Figure 3.14** Some details of the crystal structure of  $K_4Ge_9$  showing the hierarchical relationship with the initiator  $Cr_3Si$  structure (right): Cr, large dark grey spheres and Si, small light grey spheres

**Table 3.12** Interatomic distances within  $Ge_9^{4-}$  cluster in  $K_4Ge_9$  (standard deviations are in parentheses)

<b>Cluster A</b>			<b>Cluster B disordered</b>		
	<i>Atomic pair</i>	<i>distance / Å</i>		<i>Atomic pair</i>	<i>distance / Å</i>
Ge1	—Ge4	2.555(6)	Ge5B	—Ge1B	2.45(1)
	—Ge3	2.560(6)		—Ge4B	2.54(2)
	—Ge2	2.568(6)		—Ge7B	2.56(3)
	—Ge5	2.574(6)		—Ge2B	2.66(2)
Ge2	—Ge6	2.599(6)	Ge1B	—Ge4B	2.69(1)
	—Ge9	2.605(6)		—Ge3B	2.59(1)
	—Ge3	2.878(6)		—Ge6B	2.75(1)
Ge3	—Ge5	2.906(6)	Ge2B	—Ge7B	2.83(2)
	—Ge7	2.563(6)		—Ge2B	2.586(7) ×2
	—Ge6	2.699(6)		—Ge7B	2.80(2)
Ge4	—Ge4	2.778(6)	Ge3B	—Ge4B	3.09(3)
	—Ge7	2.582(6)		—Ge6B	2.60(2)
	—Ge8	2.620(6)		—Ge2B	2.62(1)
Ge5	—Ge5	2.766(5)	Ge4B	—Ge7B	2.51(3)
	—Ge8	2.586(6)		—Ge6B	2.56(2)
	—Ge9	2.589(6)		—Ge2B	2.51(2)
Ge6	—Ge9	2.517(6)	Ge2B	—Ge2B	2.586(7)
	—Ge7	2.607(6)	Ge6B	—Ge2B	2.52(2)
Ge7	—Ge8	2.568(6)	Ge7B	—Ge2B	2.52(2)
Ge8	—Ge9	2.585(6)	Ge6B	—Ge2B	3.46(2)*
Ge6	—Ge8	3.634(6)*	Ge3B	—Ge2B	3.82(2)*
Ge7	—Ge9	3.631(7)*			

(\*) corresponding to the diagonals of the basal (open) square

Interatomic contacts (Table 3.12) within cluster A range from 2.517(6) Å to 2.906(6) Å with two types of effective bond lengths, applying the bond classification according to Scheme 2. Shorter bonding distances are found in group I (2.555(6) Å to 2.574(6) Å), group III (2.563(6) Å to 2.699(6) Å) and group IV (2.517(6) Å to 2.607(6) Å). The bond distances of group II are significantly longer and range from 2.766(5) Å to 2.906(6) Å. In agreement with the general pattern of the bond distances distribution observed for all similar nine-atom *nido*-cluster of the tetrel group  $E_9^{4-}$ . The ratio of the two diagonals  $d_1/d_2$  for cluster A is 1.00, indicating very small deviation from the ideal  $C_{4v}$  symmetry of a monocapped square antiprism.

Cluster B, on the other hand, is disordered around the threefold axis giving three orientations which coincides with four of its nine atomic positions. These fixed positions are Ge1B at special position (6a) on the  $C_3$  rotation axis and, Ge2B at general position (18b) with three positions that are related by the  $C_3$  symmetry. The five other atomic positions (general position, 18b) are virtually repeated by the

symmetry operations of the threefold axis, leading to 1/3 occupancy. The orientational disorder is ascribed to the resulting three possible symmetry equivalent orientations of the cluster B. The analysis of the electron density distribution around the disordered atoms suggests that some of them are slightly offset from the ideal (symmetry equivalent) positions, probably due to packing effects. These atoms (Ge3B, Ge5B, Ge6B, Ge7B) could therefore be refined only isotropically. Consequently, the three symmetry equivalent orientations of the cluster B are just average orientations and further splitting of the disordered atomic positions may be needed for a more precise description of the cluster B. In the average model, the cluster orientations are constrained to be symmetrically equivalent, and corollary the structure of the cluster in the three different orientations is the same (Figure 3.15).

The intracuster bonds in the disordered cluster B vary from 2.449(14) Å to 3.086(25) Å with nearly the same bond distribution pattern as for cluster A. Shorter bonding distances are found in group I (2.45(1) Å to 2.66(1) Å), group III (2.52(1) Å to 2.62(1) Å) and group IV (2.51(3) Å to 2.59(1) Å). The bond distances in group II that involve five-bonded atoms are generally longer and range from 2.693(13) Å to 3.086(25) Å. The strong distortion of cluster B is mirrored by the rather long distances like 3.086(25) Å at the waist (Ge2B–Ge4B, group II) and like 2.75(1) Å for Ge1B–Ge6B (group III) which is longer than some bond distances of group II. Also, the ratio of the basal square diagonals for cluster B,  $d_1/d_2 = 1.10$ , diverges from the ideal value of 1, indicating much stronger deviation from the ideal  $C_{4v}$  symmetry of the expected monocapped square antiprism. Nevertheless, although the incomplete orientational ordering leads to strongly distorted cluster B, the model of the disorder as three symmetrically related orientations appears to be quite satisfactory as the resulting geometry of the cluster remains close to that observed for similar cluster in other phase. Stronger distortions have been described also for the  $Ge_9$  clusters in the double salt  $A_{10}[Ge_9]_2WO_4$ .

Thus, the Ge–Ge intracuster distances are close to those in the Cs homologue  $Cs_4Ge_9$  (2.522(8) Å to 3.008(11) Å) and also close to those of the K-crypt salt crystallized from solution (2.538(5) Å to 2.962(7) Å).

The  $K^+$  cations are coordinated by 6 to 11 Ge atoms. Relatively large ADPs are found for the least coordinated K4 atom which is surrounded by only 6 Ge atoms. The  $Ge_9$  clusters A and B are surrounded by 16 and 13 closest  $K^+$  neighbours

respectively (up to 4.0 Å), with several of the cations capping the polyhedron faces (Figure 3.16). The K–Ge interaction distances (Table 3.13) vary from 3.42(1) Å to 3.91(1) Å for cluster A, and from 3.11(2) Å to 3.95(2) Å for cluster B. The shortest intercluster distance is 3.656(5) Å between two clusters A and is shorter than in  $Cs_4Ge_9$  (3.956(8) Å) with bigger  $Cs^+$  cations. The shortest interaction distance between  $K^+$  cations is 3.97(1) Å.

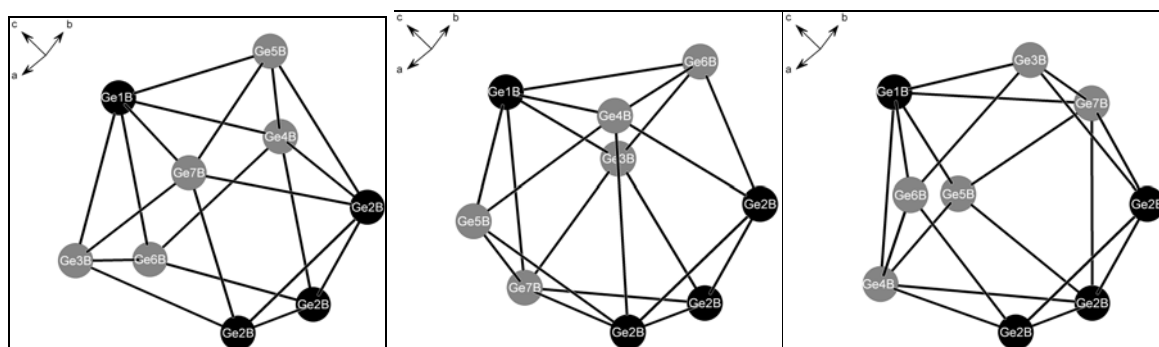


**Figure 3.15** Representation of the three orientations of the disordered  $Ge_9$  cluster type B in the crystal structure of  $K_4Ge_9$ . The defect positions are in grey,  $Ge1B$  and  $Ge2B$  positions (black spheres) coincide in all orientations; Capping atom,  $Ge5B$ .

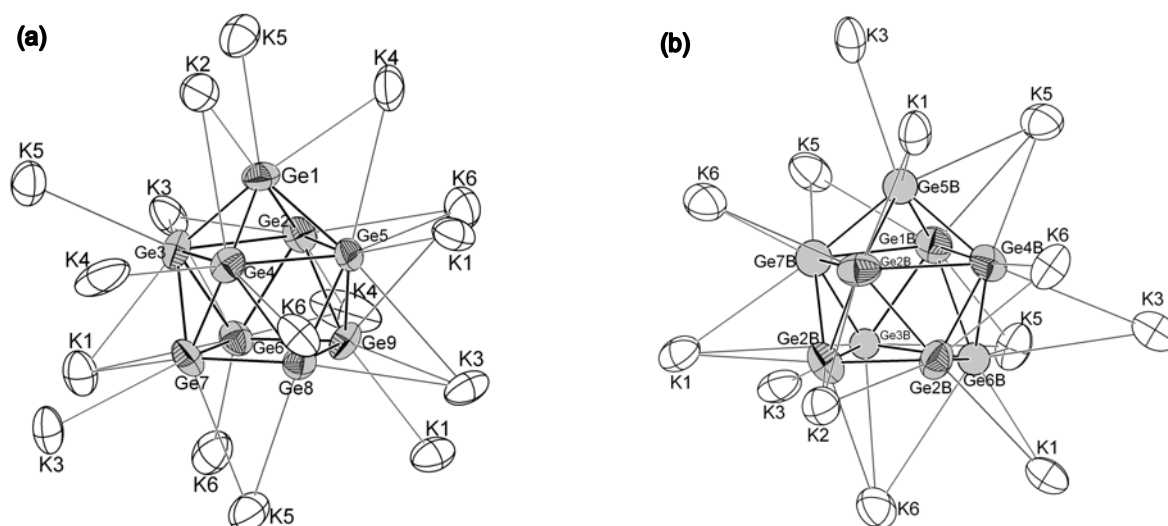


**Figure 3.16** Coordination of  $Ge_9$  cluster by  $K^+$  cations in  $K_4Ge_9$  (up to 4 Å): (a) The ordered type A  $Ge_9$  cluster with 16 closest  $K^+$  neighbours; (b) The disordered type B  $Ge_9$  cluster with 13 closest  $K^+$  neighbours clusters (thermal ellipsoids at 50% probability level). Grey spheres denoted Ge atoms refined isotropically.

**Table 3.13** Some relevant K–Ge interaction distances ( $< 4.0 \text{ \AA}$ ) in  $K_4[Ge_9]$  (standard deviations are in parentheses)

Atomic pair		distance /Å
K1	—Ge6B	3.25(2)
	—Ge9	3.42(1)
	—Ge6	3.44(1)
	—Ge5	3.58(1)
	—Ge7B	3.58(3)
	—Ge2B	3.59(1)
	—Ge5B	3.65(2)
	—Ge7	3.73(1)
	—Ge3	3.80(1)
	—K3	3.97(1)
	K2	—Ge2B
—Ge1		3.68(1) ×3
—Ge4		3.961(4) ×3
K6	—Ge4B	3.11(2)
	—Ge7B	3.19(2)
	—Ge8	3.40(1)
	—Ge2	3.50(1)
	—Ge4	3.59(1)
	—Ge5	3.59(1)
	—Ge3B	3.61(2)
	—Ge2B	3.69(1)
	—Ge6B	3.83(2)
	—Ge9	3.83(1)
	—Ge6	3.91(1)
Atomic pair		distance /Å
K3	—Ge3B	3.27(2)
	—Ge5B	3.32(2)
	—Ge7	3.43(1)
	—Ge3	3.46(1)
	—Ge9	3.46(1)
	—Ge8	3.59(1)
	—Ge2	3.60(1)
	—Ge6	3.65(1)
	—Ge5	3.78(1)
	—Ge6B	3.95(2)
	K4	—Ge4
—Ge2		3.37(1)
—Ge1		3.46(1)
—Ge6		3.59(1)
—Ge5		3.67(1)
K5	—Ge9	3.70(2)
	—Ge6B	3.32(2)
	—Ge3	3.52(1)
	—Ge7	3.53(1)
	—Ge5B	3.54(2)
	—Ge7B	3.54(2)
	—Ge8	3.54(1)
	—Ge4B	3.60(2)
	—Ge1B	3.60(1)
	—Ge1	3.64(1)
—Ge3B	3.83(2)	

### 3.6.4 Discussions

$K_4Ge_9$  crystallizes in a rhombohedra (pseudo cubic) polar space group  $R3c$ , in agreement with the unit cell parameters previously found by von Schnering and co-workers. <sup>[22]</sup> Its structure represents the much symmetrical  $Cr_3Si$ -analogous packing of  $E_9$  clusters of the group 14, with only two types of  $Ge_9$  clusters. In the structure of other germanides  $Cs_4Ge_9$  and  $Rb_4Ge_9$  which have the same  $Cr_3Si$  hierarchical packing of the clusters, four crystallographically independent clusters are found, whereas up to 16 different types of  $Sn_9$  clusters exist in the structure of the stannide  $Rb_4Sn_9$ .

The orientational disorder of one  $Ge_9$  cluster in  $K_4Ge_9$  structure can be explained by the existence in the crystal lattice of three symmetrically equivalent orientations (related by a  $C_3$  axis) which are successively adopted by the cluster with the same

frequency. The strong distortion of the disordered cluster may originate from the weak number of coordinating  $K^+$  cations which creates some kind of local instabilities. The subsequent relaxation provokes a slight ‘crack of symmetry’, and results in more than three ‘real’ orientations for the cluster which are no more perfectly symmetrically related.

The isolated clusters  $[E_9]^{4-}$  ( $E = Si, Ge, Sn, Pb$ ) are well known in solution and have been stabilized with a variety of counterions and solvates. In solid state, they are found in simple binary intermetallic phases  $A_4E_9$  and  $A_{12}E_{17}$ , but their crystal structures are made difficult by problems with crystal quality, multiple twinning, structural disorder or large unit cells. [34]

In case of the germanide  $A_4Ge_9$ , reliable data are available to the best of our knowledge only for the crystal structure of  $Cs_4Ge_9$ . [25] Unit cell parameters suggest  $Rb_4Ge_9$  to be isostructural with the Cs analogue, but the poor crystallinity of the single crystal prevents a satisfactory refinement of the data. [25]

No silicium phase with the formulation  $A_4Si_9$  is known. Generally speaking, in the structures of the  $A_4E_9$  phases ( $A = K, Rb, Cs; E = Ge, Sn, Pb$ ), two type of clusters arrangements are reported so far (Table 3.14). The plumbides  $A_4Pb_9$  ( $A = K, Rb, Cs$ ) have been structurally characterized with a hexagonal close packing arrangement of  $[Pb_9]^{4-}$  clusters. [35-37] For the stannide, only the structure of  $K_4Sn_9$  is reported with also a hexagonal close packing arrangement of the  $[Sn_9]^{4-}$  clusters. [38] In the course of the present work, we have structurally characterized the  $Rb_4Sn_9$  phase with a  $Cr_3Si$  hierarchical cluster replacement. In contrast to the structures of solvated phases where the dimensionality of the arrangement of  $[E_9]^{4-}$  cluster ( $E = Ge, Sn$ ) depends on the kind and size of the counter ions, [39-40] in ‘neat’ solid  $A_4E_9$ , the packing mode of the clusters varies only for the tin phases.

**Table 3.14** Different Arrangements of  $E_9^{4-}$  Clusters in  $A_4E_9$  crystal structures

Element (Property)	<b>K</b>	<b>Rb</b>	<b>Cs</b>
<b>Ge</b> (Semi-conductor)	$Cr_3Si$	$Cr_3Si$	$Cr_3Si$
<b><math>\alpha</math>-Sn</b> (Semi-metal) <b><math>\beta</math>-Sn</b> (Metallic)	hcp	$Cr_3Si$	$Cr_3Si$ (?)
<b>Pb</b> (Metallic)	hcp	hcp	hcp

hcp: hexagonal close packing

### 3.7 $\text{Rb}_8\text{Hg}_3\text{Ge}_{43}$ a Mercury substituted Germanium Clathrate-I

#### 3.7.1 Synthesis and characterization

During the preparation of the double salt, a type I clathrate of germanium was obtained from the reaction with the composition  $\text{HgO}:\text{WO}_3:\text{Ge}:\text{Rb} = 1:1:5:3.5$ . The mixture loaded in a niobium ampoule was heated at the rate of 2K/min to 750°C for 120 hours, cooled down at -0.1K/min to 400°C, then annealed for several days and subsequently cooled down to room temperature by switching off the oven. Some reddish crystals with very regular polyhedral shape could be extracted from the reaction mixture as by-product. EDX analysis indicates the presence of only Rb, Ge and Hg elements with the Ge/Hg ratio roughly in agreement with the refine value.

#### 3.7.2 Crystal Structure determination

The best crystal was used for full data collection on the Stoe IPDS diffractometer at room temperature. The crystal-detector distance was 100 mm. The crystallographic data as well as the structure refinement data are summarized in [Table 3.15](#) and the atomic positions and equivalent isotropic displacement parameters are listed in [Tables 3.16](#). The cubic primitive lattice parameters were determined and refined using 13043 integrated peaks from the 360 collected images. Systematical absence reflection was consistent with the space group  $\text{Pm}\bar{3}\text{n}$ . The structure was successfully solved by direct method. Ge/Hg mixed occupancy was found at one position (site 6d). The refinement on  $F^2$  yield the satisfactory residual factor  $R_1 = 0.053$  and  $wR_2 = 0.099$  for all data with essentially featureless residual map.

#### 3.7.3 Description of the structure of $\text{Rb}_8\text{Hg}_3\text{Ge}_{43}$

As represented in [Figure 3.17](#),  $\text{Rb}_8\text{Hg}_3\text{Ge}_{43}$  has a structure of a type I germanium clathrate which is substituted by a group 12 metal (Hg) in the host framework. The compound crystallizes in primitive cubic lattice (space group  $\text{Pm}\bar{3}\text{n}$ , No. 223). The crystallographic sites of the (tetrahedral) framework atoms are 6c, 16i and 24k, and those of the (endohedral) guest atoms are 2a and 6d. The 6c site is a Ge/Hg mixed occupied position.

**Table 3.15** Crystallographic data and refinement parameters for Rb<sub>8</sub>Hg<sub>3</sub>Ge<sub>43</sub>

Empirical formula	<b>Rb<sub>8</sub>Hg<sub>2.9</sub>Ge<sub>43.1(1)</sub></b>
Formula weight	4406.90
Temperature	293(2) K
Crystal size	0.2×0.2×0.2 mm <sup>3</sup>
Crystal color and habit	Reddish with polyhedral shape
Diffractometer	Stoe IPDS II
Crystal system	cubic
Space group	Pm $\bar{3}$ n (Nr. 223)
Unit cell parameters	a = 10.882(2) Å
Unit cell Volume	1288.73(3) Å <sup>3</sup>
Z	1
Density calculated	5.678 g/cm <sup>3</sup>
Absorption coefficient (Mo K $\alpha$ )	41.028 mm <sup>-1</sup> ( $\lambda$ = 0.71073 Å)
Absorption correction	semi-empirical
F(000)	1912.0
Theta range	3.74° - 29.11°
Resolution range	5.44 - 0.73 Å
Index range	0 ≤ h ≤ 10, 0 ≤ k ≤ 10, 2 ≤ l ≤ 14
Data completeness	100.0%
Integrated reflections	529 (R $_{\sigma}$ = 0.031)
Independent reflections	317 (R $_{int}$ = 0.027)
Refinement method	Full-matrix least-squares on F <sup>2</sup>
Parameters	17
Goodness of fit on F <sup>2</sup>	1.286
Observed reflections [ $I > 2\sigma(I)$ ]	276
Final R indices	R <sub>1</sub> = 0.044, wR <sub>2</sub> = 0.097
Final R indices (all data)	R <sub>1</sub> = 0.053, wR <sub>2</sub> = 0.099
Extinction coefficient	0.0030(4)
Residual map	2.08 / -3.15

$$w = 1/[\sigma^2(Fo^2) + (0.05 \times P)^2 + 0.00 \times P]$$

**Table 3.16a** Atomic coordinates and equivalent isotropic displacement parameters for Rb<sub>8</sub>Hg<sub>3</sub>Ge<sub>43</sub>

Atom	Site	x	y	z	s.o.f	U <sub>eq</sub> / Å <sup>2</sup>
Ge(1)	6c	½	¼	0	0.51(2)	0.0076(6)
Hg(1)	6c	½	¼	0	0.49(2)	0.0076(6)
Ge(2)	16i	0.1838(1)	x	x	1	0.0048(5)
Ge(3)	24k	0.3048(1)	0.1176(1)	0	1	0.0055(4)
Rb(1)	2a	0	0	0	1	0.0123(9)
Rb(2)	6d	¼	½	0	1	0.0224(7)

U<sub>eq</sub> is defined as one third of the trace of the orthogonalized U<sup>ij</sup> tensor

**Table 3.16b** Anisotropic displacement parameters (Å<sup>2</sup>) for Rb<sub>8</sub>Hg<sub>3</sub>Ge<sub>43</sub>

Atom	U <sub>11</sub>	U <sub>22</sub>	U <sub>33</sub>	U <sub>23</sub>	U <sub>13</sub>	U <sub>12</sub>
Ge(1)/Hg(1)	0.0050(6)	U <sub>11</sub>	0.0128(8)	–	–	–
Ge(2)	0.0048(5)	U <sub>11</sub>	U <sub>11</sub>	U <sub>12</sub>	U <sub>12</sub>	-0.0004(3)
Ge(3)	0.0054(7)	U <sub>11</sub>	U <sub>11</sub>	–	–	0.0003(5)
Rb(1)	0.0123(9)	U <sub>11</sub>	U <sub>11</sub>	–	–	–
Rb(2)	0.026(1)	0.014(1)	U <sub>11</sub>	–	–	–

The prototypes of the clathrate-I structure are the gas hydrates with stoichiometry  $G_8(\text{H}_2\text{O})_{46}$ , where  $G = \text{Ar}, \text{Kr}, \text{Xe}, \text{H}_2\text{S}, \text{Cl}_2, \text{CH}_4$ , etc. The 46 clathrand atoms (Ge and Ge/Hg atoms in this case) are all in tetrahedra coordinated and their arrangement in the unit cell is such that one can define two type polyhedra of different sizes: one is a 20-atom pentagonal dodecahedron  $[5^{12}]$ , and the other is a 24-atom tetrakaidecahedron  $[5^{12}6^2]$  (the symbol  $[5^{12}6^2]$  denotes a polyhedron with 12 pentagonal and 2 hexagonal faces). They are eight cages per formula unit, two smaller and six larger. The guest atoms (Rb in this case) are encapsulated into these cages (i.e.  $\text{Rb1@Ge}_{20}$  and  $\text{Rb2@Ge}_{24}$ ). Another feature of this structure is that the tetrakaidecahedra are condensed into “channels” by sharing common hexagonal faces. A system of three pairs of mutually perpendicular and nonintersecting “channels” of tetrakaidecahedra result and it encloses the smaller pentagonal dodecahedra which are separated from each other, as shown in [Figure 3.18](#).

The shortest Ge–Ge separations ([Table 3.17](#)) are 2.496(3) Å and 2.501(3) Å. Similar Ge–Ge distances are found in the type II germanium clathrate (2.486(1) Å to 2.503(1) Å).<sup>[41]</sup> Somewhat longer Ge3–Ge3 bond distance of 2.559(1) Å is observed and, the longest interatomic separation (2.567(1) Å) is between the same Ge(3) and the Hg substituted Ge1. The slightly increase of interatomic distance here may therefore be correlated with the Ge/Hg substitution in agreement with the bigger atomic size of Hg compared to the lighter Ge atom. Rb1 (site 2a) is enclosed in the smaller cage with Rb–Ge distance ranging from 3.464(2) Å to 3.555(1) Å whereas Rb2 (site 6d) occupy the largest cage with longer Rb–Ge distances that range from 3.681(1) Å to 3.847(1) Å. Because the sizes of the cages are significantly different, the Rb2 is freer to rattle and, subsequently, its  $U_{\text{eq}}$  is nearly twice that of Rb1. On the other hand, the Ge atoms in the rigid framework with strong covalent bonds have relatively very small ADPs. This is typical for the clathrate structures.

**Table 3.17** Some relevant Interatomic distances

Atomic pair	distance /Å	Atomic pair	distance /Å
Ge(1)/Hg(1) – Ge(3)	2.567(1) ×4	Rb(1) – Ge(2)	3.464(2) ×8
Ge(2) – Ge(2)	2.496(3)	– Ge(3)	3.555(1) ×4
– Ge(3)	2.501(1) ×3	Rb(2) – Ge(3)	3.681(1) ×8
Ge(3) – Ge(2)	2.501(1) ×2	– Ge(1)/Hg(1)	3.848(1) ×2
– Ge(3)	2.559(3)		
– Ge(1)/Hg(1)	2.567(1)		

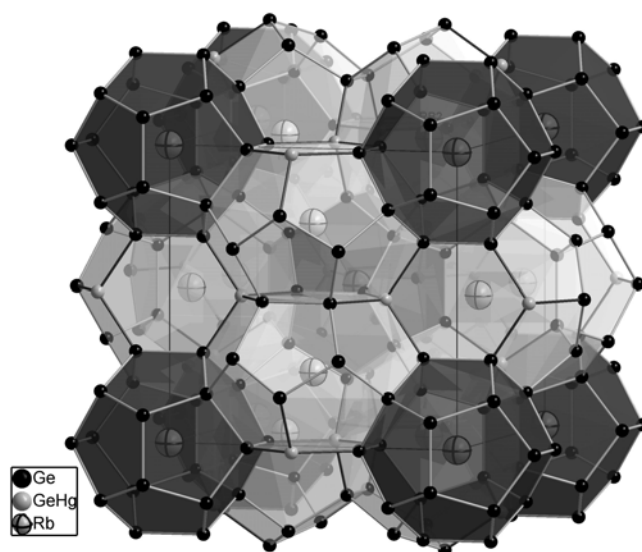


**Figure 3.17** Polyhedral representation of type-I clathrate with the pentagonal dodecahedra in black and the tetrakaidecahedra in grey.

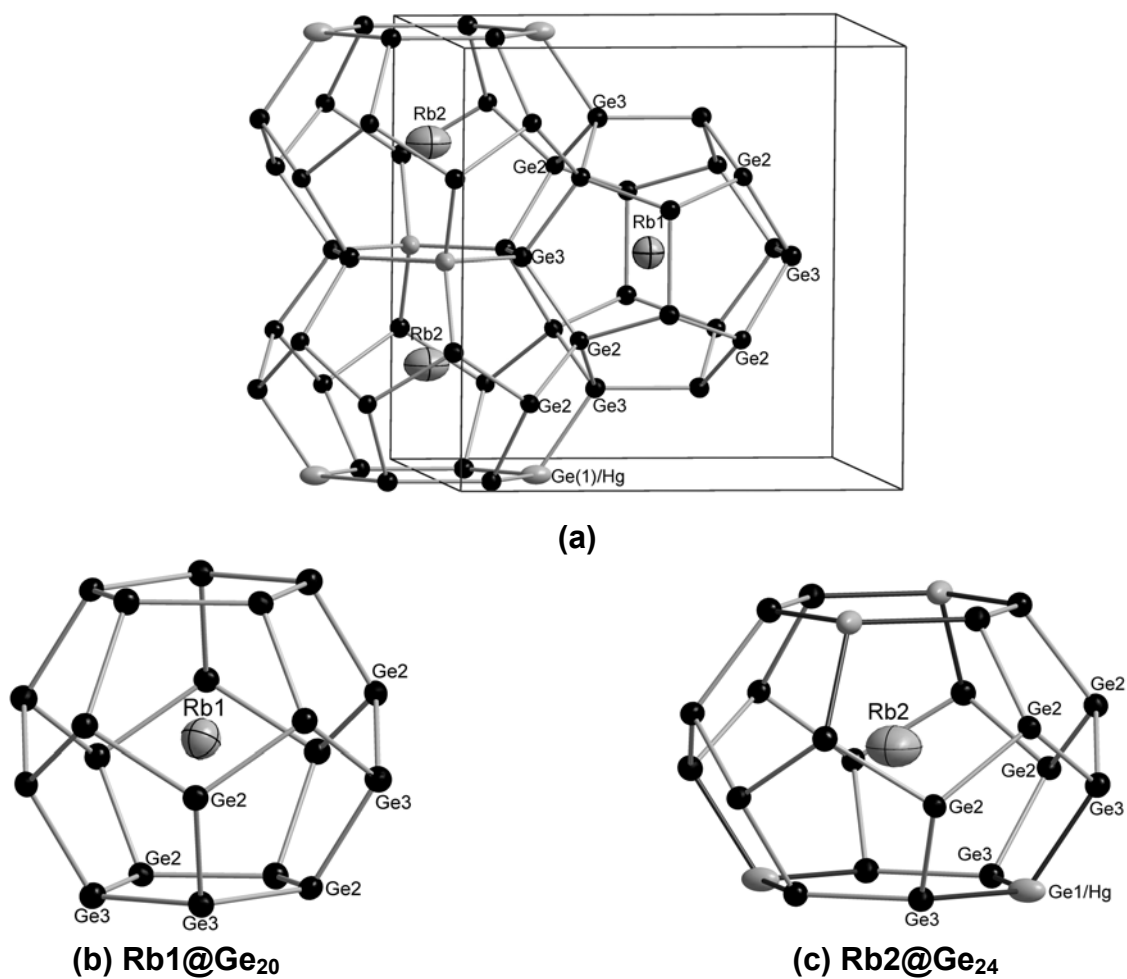


**Figure 3.18** Structural details of the clathrate-I  $\text{Rb}_8\text{Hg}_3\text{Ge}_{43}$  (a) View of the two types of germanium polyhedra ( $\text{Ge}_{20}$  and  $\text{Ge}_{24}$ ) in the unit cell (with thermal ellipsoids at 99% probability level), linked by sharing pentagonal faces. (b) The pentagonal dodecahedron is centered by Rb1 and (c) the tetrakaidecahedron by Rb2.

In the simple clathrate-I structure of  $\text{Rb}_8\text{Ge}_{46}$ , all Ge atoms of the framework are in tetrahedral coordination with four neighbouring Ge atoms and the octet is satisfied. In other words, the Ge covalent network can be completed without using electron from guest metals (Rb).

Nevertheless, there are different ways to achieve electronically balance clathrates, i.e. to stabilize true Zintl phases.<sup>[42-43]</sup> One way is to form vacancies in the framework like in  $\text{Rb}_8\text{Sn}_{44}\square_2$  ( $\square$  = vacancy) in which partial ordering of these vacancies was recently observed.<sup>[44-45]</sup> A missing Tt atom will leave the four neighbouring atoms with incomplete valence shells; i.e. four extra electrons will be needed to complete their octet configurations with lone pairs. Two vacancies per formula will translate to  $2 \times (-4) = -8$  charges and, this equals the number of donated electrons by the 8 alkali metals. Another way to balance the extra electrons from the alkali metals is to substitute group 14 atoms with an electron-poorer element, from group 13 (Tl, Tr) or group 12 for example. This idea has been widely utilized for making novel ternary phases with the clathrate-I structure. The corresponding ideal stoichiometries will be  $\text{A}_8\text{Tr}_8\text{Tt}_{38}$  and  $\text{A}_8\text{M}_4\text{Tt}_{42}$ , where (Tr, group 13 element and M, group 12 metal). Many clathrates with these compositions exist, and their compliance with the Zintl concept has been proven.<sup>[46]</sup>

Hg (group 12) has two electrons less than Ge. Therefore, the three Hg atoms of the framework need only six electrons, resulting in two unaccounted electrons from the guest metal Rb. This means that the compound  $\text{Rb}_8\text{Hg}_3\text{Ge}_{43}$  is a 'metallic Zintl phase'. But, we should keep in mind that Hg has two stable oxidation states and, in case of mixed-valent Hg, the charge optimization of the system can be achieved by two monovalent ( $2\text{Hg}^{\text{I}}$ ) and one divalent ( $1\text{Hg}^{\text{II}}$ ) mercury giving a charge balance (Zintl) phase. The reddish colour of the compound crystals pledges in favour of an electronic picture with mixed valent Hg atoms. But this ought to be confirmed by theoretical calculations and appropriated physical measurements.

### 3.7.4 Discussions

The title compound  $\text{Rb}_8\text{Hg}_3\text{Ge}_{43}$  crystallizes in a type-I clathrate structure and can be viewed as mercury substituted germanium clathrate doped with Rb. The first single-crystal refinements of the structures of clathrate-I doped with alkali metal appeared in 1969 for the potassium compounds  $\text{K}_8\text{Tt}_{46}$  (Tt = Si, Ge, Sn), using data collected

on a Weissenberg camera.<sup>[47]</sup> The accuracy of the structure has been questioned ever since.<sup>[45]</sup> Four-bonded atoms of group 14 should have zero formal charge, and therefore the ideal clathrates should be ‘metallic Zintl phases’ considering a full charge transfer from the guest metal to the framework atoms. This stoichiometry for  $\text{Na}_8\text{Si}_{46}$ <sup>[48-49]</sup> has been confirmed by Rietveld analysis and  $^{29}\text{Si}$  NMR work, in agreement with the ideal stoichiometric ratio and the measured metallic-like electric resistivity.<sup>[50]</sup> Some reported structure refinements have claimed vacancies at guest position in  $\text{K}_{8-x}\text{Si}_{46}$ .<sup>[51]</sup> But, it is still not clear whether the Ge compound is  $\text{K}_8\text{Ge}_{46}$ ,  $\text{K}_8\text{Ge}_{44}\square_2$  or  $\text{K}_{8-x}\text{Ge}_{46}$ , or anything between, since no better structure determination has been published. Moreover, unlike the silicon phase  $\text{Ba}_{8-x}\text{Si}_{46}$ ,<sup>[54]</sup> the germanium analogue occurs only with framework vacancies, i.e.  $\text{Ba}_8\text{Ge}_{43}\square_3$ .<sup>[55]</sup> A full ordering of the vacancies in the latter has been described recently.<sup>[56]</sup>

To the best of our knowledge, only two alkali metal doped Sn clathrate-I structures, substituted with group 12 metal  $\text{Cs}_8\text{M}_4\text{Sn}_{42}$  ( $\text{M} = \text{Zn}, \text{Cd}$ )<sup>[57-58]</sup> have been reported so far and, no mercury substituted compound is known overall. The compound  $\text{Rb}_8\text{Hg}_3\text{Ge}_{43}$  represents the first mercury substituted group 14 clathrate-I and the first alkali metal doped germanium clathrate-I substituted with a group 12 element. The advantage of using Hg is that, unlike the lighter Zn or Cd homologues which both have only one stable oxidation state +II, Hg has two stable oxidation states +I and +II. This opens new possibilities for the control of the number of charge carrier (therefore controlling the metallic property) in these materials by adjusting the concentration of the electron donor with that of the electron acceptor atoms in the substituted framework.<sup>[59]</sup> According to the Zintl concept,  $\text{Rb}_8\text{Hg}_3\text{Ge}_{43}$  may be either a semiconducting clathrate-I with mix-valent mercury ( $2\text{Hg}^{\text{I}}$  and  $1\text{Hg}^{\text{II}}$ ), or a ‘metallic Zintl phase’ with 2 ‘extra’ electrons. A phase range  $\text{Rb}_8\text{Ge}_{46-x}\text{Hg}_x$  ( $2 < x \leq 4$ ) originates from the mercury ability for mix-valency may be expected, with the limit phase  $\text{Rb}_8\text{Hg}_4\text{Ge}_{42}$  ( $x = 4$ ) containing exclusively divalent  $\text{Hg}^{\text{II}}$ .

The interest in clathrates jumped abruptly even higher after the unexpected discovery of superconductivity in the clathrate-I compounds  $\text{Ba}_y\text{Na}_x\text{Si}_{46}$  and  $\text{Ba}_{8-x}\text{Si}_{46}$ .<sup>[52-53]</sup> It was unprecedented because no other examples of superconductivity were known for phases with covalent  $sp^3$  bonding. In addition, it was hypothesized that variable physical properties such as the Seebeck coefficient or thermopower ( $S$ ) and the electrical ( $\sigma$ ) and thermal ( $\lambda$ ) conductivities may be tuned by altering the

guest atoms in the cages. This brought new motivations for clathrate studies as potential thermoelectric materials. The stability of the clathrates, the fact that they conduct electricity relatively well, and the possibility of “rattling” guest cations in the cavities bring the clathrates closer to the ultimate thermoelectric PGEC (“phonon-glass and an electron crystal”) material, a concept introduced by *Slack* in 1979.<sup>[60]</sup> Si and Ge clathrates are considered promising candidates for thermoelectric applications since their relatively large unit cells with voids and rattlers inside them are important prerequisites for scattering of the heat-carrying phonons and thereby for low phonon-contributed thermal lattice conductivity. All this interest has led to the search for reliable and reproducible ways for the synthesis of all clathrates in high yields and with well defined stoichiometry. Furthermore, *Cordier and Woll*<sup>[61]</sup> have shown that some transition metal atoms like Ni, Cu, Pd, Ag, Pt or Au can partially substitute the clathrand atoms in Si and Ge compounds having a type-I clathrate structure. Ferromagnetism was reported for compounds with composition  $\text{Ba}_8\text{Mn}_x\text{Ge}_{46-x}$  ( $x = 1-3$ ).<sup>[62]</sup> It is speculated that these novel clathrates-based ferromagnetic semiconductor might be utilized as an alternative to the conventional magnetic-doped semiconductors made by epitaxial growth for applications in spintronics.<sup>[63]</sup>

### 3.8 Literature

- [1] Simon, A.; Mattausch, H. *Angew. Chem.* **1998**, *110*, 498
- [2] Mattausch, H.; Oeckler, O.; Simon, A. *Z. Anorg. Allg. Chem.* **1999**, *625*, 1.
- [3] Wengert, S.; Nesper, R. *J. Solid State Chem.* **2000**, *152*, 460-465.
- [4] Wengert, S.; Nesper, R.; Willems, J. B. *Chem. Eur. J.* **2001**, *7*, 3209-3213
- [5] Hoffmann, S.; Fässler, T. F.; Hoch, C.; Röhr, C. *Angew. Chem.* **2001**, *113*, 4527; *Angew. Chem. Int. Ed.* **2001**, *40*, 4398.
- [6] Hoch, C.; Röhr, C. *Z. Naturforsch.* **2001**, *B56*, 423 - 430.
- [7] Hoch, C.; Röhr, C. *Z. Anorg. Allg. Chem.* **2002**, *628*, 1541-1548
- [8] Frisch, G.; Hoch, C.; Röhr, C.; Zönnchen, P.; Becker, K.-D.; Niemeier D. *Z. Anorg. Allg. Chem.* **2003**, *629*, 1661-1672
- [9] Stucky, G. D.; MacDougall, J. E. *Science* **1990**, *247*, 669-678.
- [10] Behrens, P.; Stucky, G. D. *Angew. Chem.* 1993, *105*, 729-732; *Angew. Chem. Int. Ed. Engl.* **1993**, *32*, 696.
- [11] Schöllhorn, R. *Chem. Mater.* **1996**, *8*, 1747-1757.
- [12] Fässler, T. F. *Coord.Chem. Rev.* **2001**, *215*, 377.
- [13] Yong, L.; Hoffman, S. D.; Fässler, T. F. *Z. Anorg. Allg. Chem.* **2004**, *630*, 1977-1981.
- [14] Nienhaus, A.; Hauptmann, R.; Fässler, T. F. *Angew. Chem., Int. Ed.* **2002**, *41*, 3213.
- [15] (a) Grandqvist, C. G. *Handbook of Inorganic Electrochromic Materials*, Elsevier, Amsterdam, 1995. (b) *Large Area Chromogenics: Materials and Devices for Transmittance Control*, Lampert C. M. Grandqvist, C. G. Eds, vol. IS4, SPIE Press, 1988
- [16] Kolytyn, Yu.; Nikitenko, S. I.; Gedanken, A. *J. Mater. Chem.* **2002**, *12*, 1107.
- [17] Aird, A.; Domeneghetti, M. C.; Mazzi, F.; Tazzoli, V.; Salje, E. K. H. *J. Phys.: Condens. Matter* **1998**, *10*, L569.
- [18] Polaczek, A.; Pekata, M.; Obuszko, Z. *J. Phys.: Condens. Matter* **1994**, *6*, 7909.
- [19] Hu, J.; Odom, T. W.; Lieber, C. M. *Acc. Chem. Res.* **1999**, *32*, 435.
- [20] Huang, M. H.; Mao, S.; Feick, H.; Yan, H. Q.; Wu, Y. Y.; Kind, H.; Weber, E.; Russo, R.; Yang, P. D. *Science* **2001**, *292*, 1897.
- [21] Duan, X.; Huang, Y.; Cui, Y.; Wang, J.; Lieber, C. M. *Nature* **2000**, *409*, 66.
- [22] von Schnering, H. G.; Baitinger, M.; Bolle, U.; Carrillo-Cabrera, W.; Curda, J.; Grin, Yu.; Heinemann, F.; Llanos, J.; Peters, K.; Somer, M. *Z. Anorg. Allg. Chem.* **1997**, *623*, 1037.
- [23] Weinstock N.; Schulze, H.; Müller, A. *J. Chem. Phys.* **1973**, *59*(9), 5063-5067.
- [24] Nagarathna, H. M.; Bencivenni, L.; Gingerich K.A. *J. Chem. Phys.* **1984**, *81*(2), 591-598.
- [25] Quénéau, V.; Sevov, S. C. *Angew. Chem.* 1997, *109*, 1818; *Angew. Chem. Int. Ed. Engl.* **1997**, *36*, 1754.
- [26] Belin, C.H.E.; Corbett, J. D.; Cisar, A. *J. Amer. Chem. Soc.* **1977**, *99*, 7163.
- [27] Llanos, J. Dissertation, Universität Stuttgart, 1984.
- [28] Kools, F.X.; Koster, A. S.; Rieck, G. D. *Acta Cryst. B*, **1969**, *25*, 1704-1708.
- [29] Havinga, E. E.; Damsma, H.; Hokkeling, P. *J. Less-Common Met.* **1972**, *27*, 169-186.
- [30] Kools, F.X.N.M., Koster, A.S., Rieck, G. D. *Acta Cryst. B*, **1970**, *26*, 1974-1977.
- [31] Fässler, T. F.; Hoffmann, R. *J. Chem. Soc. Dalton Trans.* **1999**, 3339.
- [32] Somer, M.; Carrillo-Cabrera, W.; Peters, E. M.; Peters, K.; von Schnering, H. G. *Z. Anorg. Allg. Chem.* **1998**, *624*, 1915.

- [33] Jeitschko, W.; Sleight, A. W. *Acta Cryst.* **1974**, B30, 2088.
- [34] Fässler, T. F.; Hoffmann, S. *Z. Kristallogr.* **1999**, 214, 722.
- [35] Queneau, V.; Sevov, S. C. *Inorg. Chem.* **1998**, 37, 1358-1360.
- [36] Todorov, E.; Sevov, S. C. *Inorg. Chem.* **1998**, 37, 3889-3891.
- [37] Hoch, C.; Wendorff, M.; Röhr, C. *J. Alloys Comp.* **2003**, 361, 206-221.
- [38] Hoch, C.; Wendorff, M.; Röhr, C. *Acta. Cryst.* **2002**, C58, i45-i46.
- [39] Hauptmann, R.; Hoffmann, R.; Fässler, T. F. *Z. Anorg. Allg. Chem.* **2001**, 627, 2220.
- [40] Hauptmann, R.; Fässler, T. F. *Z. Anorg. Allg. Chem.* **2002**, 628, 1500.
- [41] Bobev, S.; Sevov, S. C. *J. Am. Chem. Soc.* **1999**, 121, 3795.
- [42] (a) von Schnering, H.-G. *Nova Acta Leopold.* **1985**, 59, 168. (b) von Schnering, H.-G. *Bol. Soc. Chil. Quim.* **1988**, 33, 41.
- [43] Nesper, R.; von Schnering, H.-G. *Tschermaks Mineral. Petrogr. Mitt.* **1983**, 32, 195.
- [44] Dubois, F.; Fässler, T. F. *J. Am. Chem. Soc.* **2005**, 127, 3264-3265
- [45] Zhao, J.-T.; Corbett, J. D. *Inorg. Chem.* **1994**, 33, 5721-5726
- [46] Bobev, S.; Sevov, S.C. *J. Solid State Chem.* **2000**, 153, 92-105
- [47] Gallmeier, J.; Schäfer, H.; Weiss, A. *Z. Naturforsch. B* **1969**, 24, 665.
- [48] Cros, C.; Pouchard, M.; Hagenmuller, P. *Acad. Sci., Paris, C. R.* **1965**, 260, 4764.
- [49] Kasper, J.; Hagenmuller, P.; Pouchard, M.; Cross, C. *Science* **1965**, 150, 1713
- [50] Ramachandran, G.K.; Dong, J.; Diefenbacher, J.; Gryko, J.; Marzke, R.F.; Sankey, O.F.; McMillan, P.F. *J. Solid State Chem.* **1999**, 145, 716
- [51] Ramachandran, G.K.; McMillan, P.F.; Diefenbacher, J.; Gryko, J.; Dong, J.; Sankey, O. F. *Phys. Rev. B* **1999**, 60, 12294.
- [52] Yamanaka, S.; Horie, H.; Nakano, H.; Ishikawa, M. *Fullerene Sci. Technol.* **1995**, 3, 21.
- [53] Kawaji, H.; Horie, H.; Yamanaka, S.; Ishikawa, M. *Phys. Rev. Lett.* **1995**, 74, 1427.
- [54] Yamanaka, S.; Enishi, E.; Fukuoka, H.; Yasukawa, M. *Inorg. Chem.* **2000**, 39, 56.
- [55] Carrillo-Cabrera, W.; Curda, J.; Peters, K.; Paschen, S.; Baenitz, M.; Grin, Yu.; von Schnering, H. *G. Z. Kristallogr. NCS* **2000**, 215, 321.
- [56] Carrillo-Cabrera, W.; Budnyk, S.; Prots, Y.; Grin, Yu. *Z. Anorg. Allg. Chem.* **2004**, 630, 2267-2276
- [57] Nolas, G.; Weakley, T.; Cohn, J. L. *Chem. Mater.* **1999**, 11, 2470.
- [58] Wilkinson, A. P.; Lind, C.; Young, R. A.; Shastri, S. D.; Lee, P.L.; Nolas, G. S. *Chem. Mater.* **2002**, 14, 1300.
- [59] Pacheco, V.; Bentien, A.; Carrillo-Cabrera, W.; Paschen, S.; Steglich, F.; Grin Yu. *Phys. Rev.* **2005**, B71, 165205.
- [60] Slack, G. A. *Solid State Phys.* **1979**, 34, 1.
- [61] Cordier G.; Woll, P. *J. Less-Common Met.* **1991**, 169, 291.
- [62] Kawaguchi, K. Tanigaki, M. Yasukawa, *Appl. Phys. Lett.* **2000**, 77, 3438
- [63] Ohno, H.; Chiba, D.; Matsukura, F.; Omiya, T.; Abe, E.; Dietl, T.; Ohno, Y.; Ohtani, K. *Nature* **2000**, 408, 944.

## 4. Influence of atomic properties on the structure and bonding of Zintl phases: Homologous substitutions in $\text{Ba}_2\text{Sb}_{3-x}\text{Bi}_x$

### 4.1 Introduction

The simple electron counting relationships developed for Zintl phases generally overestimate the extent of charge transfer from the electropositive s-block metal to the anionic network. The effective charge transfer depends on both the electronegativity difference between the anions and cations as well as the structure (or composition), which influences the valence states of the component atoms (VEC in the anionic network).<sup>[1]</sup> Another important characteristic that influences structure and bonding is the atomic core states.<sup>[2]</sup> Related to the atomic core states is the relativistic contraction of *s* orbitals as the atomic number increases. This contraction renders the *s*-orbitals essentially inert toward significant interatomic overlap (*lone pair* effect) and, this goes together with the expansion of the valence *p*, *d*, and so on, orbitals as a result of a shielding phenomenon. The relativistic effects are greatest for the sixth period elements Au, Hg, Tl, Pb, Bi and Po. They have a marked tendency for low valence states and, as a result, their structures often differ significantly from those of their earlier analogues.<sup>[2]</sup> This can be pursued when comparing the structures and bonding of binary antimonides and bismuthides. NaSb follows the classical Zintl-Klemm concept by forming spiral chains of Sb atoms:  $\text{Na}^+\text{Sb}^-$  gives  $\frac{1}{\infty}[\text{Sb}^-]$ .<sup>[3]</sup> On the other hand, NaBi contains planar square nets of Bi atoms:  $\text{Na}^+\text{Bi}^-$  gives  $\frac{2}{\infty}[\text{Bi}^-]$ .<sup>[4]</sup> However, if the Klemm pseudo-atom concept is generalized to include the differences in elemental structure with period, then the square net of  $\text{Bi}^-$  corresponds to a piece of the simple cubic structure of  $\alpha$ -Po.<sup>[2]</sup>

Similar differences are found in compounds on the pnictogen rich side of alkaline-earth antimonides and bismuthides binary systems, respectively. On the antimony-rich side, all structurally characterized binary phases with alkaline-earth metal can be described as classical Zintl phases. In contrast, they are relatively few known polybismuthides, i.e. compounds in which Bi formally assumes a negative oxidation state and engages in homonuclear Bi–Bi bonding.

In the structure of  $\text{BaSb}_3$  which is so far the antimony richest phase,<sup>[5]</sup> one third of Sb atoms in the formula unit is three bonded and the remaining two third atoms are two bonded resulting in a typical Zintl phase formulated by  $(\text{Ba}^{2+})[(2\text{b-Sb}^-)_2(3\text{b-Sb}^0)]$ . On

the other hand, the Bi analogues,  $\text{SrBi}_3$  (AuCu<sub>3</sub>-type) and  $\text{BaBi}_3$  (AuCu-type) [4] are pure intermetallic compounds. Increasing the alkaline-earth content, the structures of the compounds  $\text{AeSb}_2$  (Ae = Ca, Sr) [6] contain infinite zigzag chains  ${}_{\infty}^1[\text{Sb}^-]$  of two bounded Sb atoms in agreement with the Zintl concept. The Bi analogue,  $\text{CaBi}_2$  [7] was characterized by powder diffraction and its structure was assumed to be isomorphous with  $\text{YbSb}_2$ , [8] with a  $\text{ZrSi}_2$  structure type, meaning that it features both classical zigzag infinite chains  ${}_{\infty}^1[\text{Bi}^-]$  and, non-classical planar square nets  ${}_{\infty}^2[\text{Bi}^-]$  in its structure. The bonding in  $\text{CaBi}_2$  can be rationalized using a reformulation of the Zintl concept which includes the concept of electron-rich multicenter bonding also referred to as ‘hypervalent bonding’. [9] By further increase of the alkaline-earth content, the structures of the phases  $\text{Ae}_2\text{Sb}_3$  (Ae = Sr, Ba) [10] contain six members zigzag chains of Sb atoms corresponding to classical Zintl phases  $(\text{Ae}^{2+})_2[(1b\text{-Sb}^{2-})_1(2b\text{-Sb}^-)_2]$ . In contrast to  $\text{Sr}_2\text{Sb}_3$ , the Bi homologue  $\text{Sr}_2\text{Bi}_3$  [7] cannot be classified as a Zintl phase. The latter contains hexagon-based helicoidal chains of Bi atoms that are interconnected by a longer bond, to form two-dimensional networks of three- and two-bonded Bi atoms that are separated by Sr cations.

On the alkaline-earth rich side, the isostructural compounds  $\text{Ae}_{11}\text{Pn}_{10}$  (Ae = Ca, Sr, Ba; Pn = Sb, Bi) [7, 11-12] are formally Zintl phases featuring isolated  $\text{Pn}^{3-}$  anions,  $\text{Pn}_2^{4-}$  dumbbells and square planar  $\text{Pn}_4^{4-}$  units giving  $(\text{A}^{2+})_{22}[\text{2b-Pn}^{1-}]_4[\text{1b-Pn}^{2-}]_8[\text{Pn}^{3-}]_8$ . The structural shift between bismuthides and antimonides appears simultaneously with the occurrence of polymeric units in the anionic sublattice of the antimonides. The Pauling’s electronegativities are almost similar for Bi ( $\chi = 2.02$ ) and Sb ( $\chi = 2.05$ ) but, after Allred and Rochow Sb ( $\chi = 1.82$ ) is slightly more electronegative than Bi ( $\chi = 1.67$ ). Therefore, the observed difference in structure and chemical bonding, between bismuthides and antimonides on the pnictogen-rich side may be ascribed mainly to the greater relativistic effects in bismuth.

To ascertain this, we have investigated in the ternary system Ba/Sb/Bi, the phases  $\text{Ba}_2\text{Sb}_{3-x}\text{Bi}_x$  ( $0.5 \leq x \leq 3$ ) in a bid to observe at constant VEC, the structural and bonding transitions from the valence (Zintl) phase  $\text{Ba}_2\text{Sb}_3$  to the yet unknown  $\text{Ba}_2\text{Bi}_3$  phase, which is predicted to be a borderline polar intermetallic like the Sr analogue  $\text{Sr}_2\text{Bi}_3$ . The structural changes would be, presumably directly related to the difference in atomic properties between Sb and the heavier Bi, therefore giving a direct way to probe the limit of the Zintl concept.

## 4.2 The Phase $\text{Ba}_2\text{Bi}_3$ , its Coloring Variant $\text{Ba}_2\text{BiSb}_2$ and the Solid Solutions $\text{Ba}_2\text{Bi}_{1+y}\text{Sb}_{2-y}$ ( $y < 2$ )

### 4.2.1 Synthesis and Characterization

The phase  $\text{Ba}_2\text{Bi}_3$  and substituted variant  $\text{Ba}_2\text{Bi}_{1+y}\text{Sb}_{2-y}$  ( $y < 2$ ) that are all air sensitive and isostructural, were synthesized from the elements at high temperature. Mixtures of the elements, barium, bismuth and antimony with nominal composition  $\text{Ba}_2\text{Sb}_{3-x}\text{Bi}_x$  where used with  $x = 1.0, 1.5, 2.0, 2.5$  and  $3.0$ . The reaction mixtures were heated at  $850^\circ\text{C}$  for 5 hours, then annealed at  $750^\circ\text{C}$  for at least 48 hours and cooled to room temperature at  $60^\circ\text{C}/\text{hour}$  rate. The starting mixtures with  $x < 1$  yield the already known  $\text{Ba}_2\text{Sb}_3$  structure type meaning that noticeable substitution effects occur only for  $x \geq 1$ . Almost pure phases were obtained for  $x < 2$ , as revealed by the X-ray powder patterns (Figure 4.1). But, for  $\text{Ba}_2\text{Bi}_3$  and other mixtures with  $x > 1$ , the presence of other yet unidentified phases was undisputable. The products of all reactions are grey but with metallic luster. EDX analysis showed that Ba, Bi and eventually Sb were present. No detectable amount of any contaminant (Nb or other element) was observed.

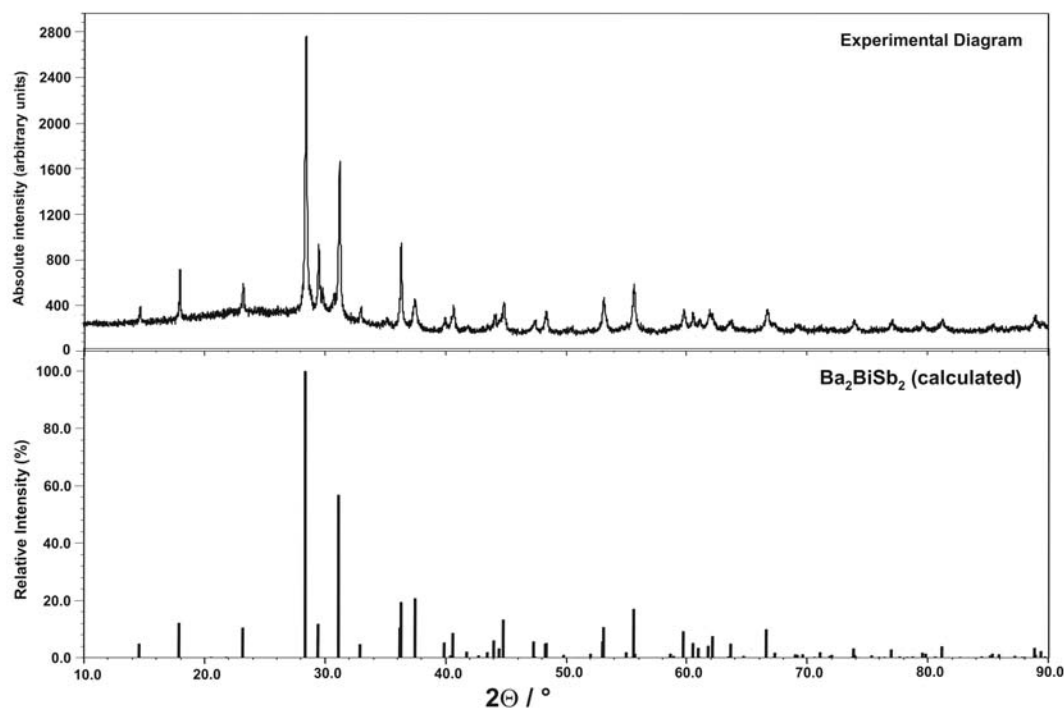


**Figure 4.1** Experimental powder diagram of the reaction product (top)  $\text{Ba}_2\text{BiSb}_2$  and theoretical (bottom) powder diagram calculated from single crystal structure.

### 4.2.2 Determination of the Crystal structures

For the single crystal diffraction, few crystals from different reaction products were selected and checked for singularity. For the best ones, full diffraction data were collected on a Stoe IPDS II ( $\omega$ - scan,  $\Delta\omega = 1^\circ$ ) or on a Nonius CCD diffractometers at room temperature. The crystalline quality of the crystals decreases with increasing substitution rate, giving crystals of poorest quality for  $\text{Ba}_2\text{Bi}_3$ . For the latter, the same single crystal was measured on both diffractometers to compare the two machines. Final cell parameters were refined from least-squares analysis of all integrated reflections. Intensity data were processed and numerical absorption corrections were applied with the use of the program X-Shape (STOE). Based on the intensity statistics, the satisfactory averaging and the successful structure solution, the centrosymmetric space group *Immm* was chosen. All the structures were solved by direct methods and refined by least-squares methods on  $F^2$ . In  $\text{Ba}_2\text{Bi}_3$  the sites *4h* and *2a* were assigned to bismuth. In the substituted phases  $\text{Ba}_2\text{Bi}_{1+y}\text{Sb}_{2-y}$  ( $y < 2$ ), this model results in high atomic displacement parameters (ADPs) and electron density hole at atomic site *4h*, suggesting the presence of a lighter atom. This site was refined with Bi/Sb mixed occupancy after the presence of Sb was confirmed in those compounds by EDX analysis. The ADPs of the two elements were constrained to be the same in the mixed occupied site. Similar treatment on the *2a* site didn't yield any Sb occupancy. The final compositions obtained from single crystal refinements are in good agreement with those of corresponding starting mixtures. The important crystallographic and refinements data are summarized in [Tables 4.1](#) and, the atomic parameters obtained from the measurements on the same Stoe IPDS II diffractometer are listed in [Tables 4.2](#). Strong absorption problems are often reflected in the final residuals.

### 4.2.3 Structural descriptions of $\text{Ba}_2\text{Bi}_3$ and $\text{Ba}_2\text{Bi}_{1+y}\text{Sb}_{2-y}$ ( $y < 2$ )

$\text{Ba}_2\text{Bi}_3$  and the isostructural phases  $\text{Ba}_2\text{Bi}_{1+y}\text{Sb}_{2-y}$  ( $y < 2$ ) crystallize in the  $\text{W}_2\text{CoB}_2$  <sup>[13]</sup> structure type, orthorhombic space group *Immm* with Ba at W position (site *4j*), Bi at Co position (site *2a*) and Bi and/or Sb at B position (site *4h*). A projection of the structure is shown in [Figure 4.2](#). Two crystallographically and structurally different pnictogen positions are observed (three- and four-bonded). In the non substituted phase  $\text{Ba}_2\text{Bi}_3$ , the four-bonded Bi1 (site *2a*) has a square planar environment of Bi2

atoms and the three-bonded Bi2 (site *4h*) a trigonal planar coordination. In the substituted phases the four-bonded position is occupied exclusively by Bi1 atoms, but the three bonded position (site *4h*) can be partially substituted by Sb in the solid solutions Ba<sub>2</sub>Bi<sub>1+y</sub>Sb<sub>2-y</sub> ( $y < 2$ ). Full substitution of the site *4h* occurs in the ordered pseudo-binary phase Ba<sub>2</sub>BiSb<sub>2</sub> ( $y = 0$ ), thus confirming the structural and chemical analogies with W<sub>2</sub>CoB<sub>2</sub> and related compounds.

The structure of the phases Ba<sub>2</sub>Bi<sub>1+y</sub>Sb<sub>2-y</sub> ( $y \leq 2$ ) contains rigorously planar layers of (4.6.4.6)(4.6<sup>2</sup>)<sub>2</sub> nets of interconnected Bi or Bi/Sb respectively, that are separated by Ba atoms. As a result of the ABAB stacking sequence of the 2D planar layers, the Ba atoms (*W* position in W<sub>2</sub>CoB<sub>2</sub>) are located above and below the six- and four-membered rings of the Bi/Sb net (Figure 4.2).

**Table 4.1a** Selected details of Crystallographic data and Structure Refinement for Ba<sub>2</sub>Bi<sub>3</sub>

Chemical formula	Ba <sub>2</sub> Bi <sub>3</sub>	Ba <sub>2</sub> Bi <sub>3</sub>
Formula weight	901.62	901.62
Temp (°C)	293(2) K	293(2) K
Diffractometer	Stoe IPDS II	Brucker CCD
Crystal size mm <sup>3</sup>	0.15×0.15×0.20	0.15×0.15×0.20
Space group	<i>Immm</i> (N° 71)	<i>Immm</i> (N° 71)
Unit cell parameters (Å)	a = 4.819(2) ; b = 7.989(4) c = 9.982(3)	a = 4.819(2); b = 7.997(2) c = 9.992(3) Å
Unit cell volume, Z = 2	384.3(3) Å <sup>3</sup>	385.1(2) Å <sup>3</sup>
ρ <sub>calc</sub> (g/cm <sup>3</sup> )	7.792	7.775
μ /cm <sup>-1</sup> Mo, K <sub>α</sub> )	784.4	782.7
F(000)	722	722
2θ range	6.5 – 59.9°	6.52 – 57.95°
Index ranges	-6 ≤ h ≤ 6, -10 ≤ k ≤ 10, -13 ≤ l ≤ 13	-6 ≤ h ≤ 5; -10 ≤ k ≤ 10 -12 ≤ l ≤ 13
data completeness	95.1 %	99%
Integrated Reflins	2044 (R <sub>σ</sub> = 0.067)	1614 (R <sub>σ</sub> = 0.043)
Indpt reflections	333 (R <sub>int</sub> = 0.153)	319 (R <sub>int</sub> = 0.054)
Parameters	13	13
Absorption correction	numerical	empirical
Min / max Trans.	0.0024 / 0.0232	/
GOF on F <sup>2</sup>	1.079	1.179
Observed rflns [ $I > 2\sigma(I)$ ]	210	289
R <sub>1</sub> /wR <sub>2</sub> , $I > 2\sigma_1$	0.0702 / 0.1959	0.0638 / 0.1631
R <sub>1</sub> /wR <sub>2</sub> , all data	0.0898 / 0.2047	0.0678 / 0.1646
weighting scheme ( <i>a</i> / <i>b</i> )*	<i>a</i> = 0.112 / <i>b</i> = 14.22	<i>a</i> = 0.100 / <i>b</i> = 38.84
Residual map (e <sup>-</sup> /Å <sup>3</sup> )	5.88 / -4.12	8.03 / -5.54

(\*)  $w = 1/[\sigma^2(F_o^2) + (a.P)^2 + b.P]$

**Table 4.1b** Selected details of Crystallographic data and Structure Refinement for Ba<sub>2</sub>Bi<sub>1+y</sub>Sb<sub>2-y</sub> (y = 0.5 and y = 0.1)

Chemical formula	Ba <sub>2</sub> Bi <sub>1.50(4)</sub> Sb <sub>1.50(4)</sub>	Ba <sub>2</sub> Bi <sub>1.10(4)</sub> Sb <sub>1.90(4)</sub>
Formula weight	770.78	727.16
Temp (°C)	293(2) K	293(2) K
Diffractometer	STOE IPDS II	STOE IPDS II
Crystal size mm <sup>3</sup>	0.10×0.15×0.15	0.10×0.10×0.20
Space group	<i>Immm</i>	<i>Immm</i>
Unit cell parameters (Å)	a = 4.821(1); b = 7.750(2) c = 9.919(2)	a = 4.803(1); b = 7.688(2) c = 9.900(2)
Cell Volume, Z = 2	370.6(2) Å <sup>3</sup>	365.5(1) Å <sup>3</sup>
ρ <sub>calc</sub> (g/cm <sup>3</sup> )	6.908	6.607
μ /cm <sup>-1</sup> Mo, K <sub>α</sub> )	512.33	417.7 (λ= 0.71073 Å)
F(000)	626	594
2θ range	6.7 – 60.2°	6.7 – 58.8°
Index range	-6 ≤ h ≤ 5; -10 ≤ k ≤ 10; -13 ≤ l ≤ 14	-6 ≤ h ≤ 6; -10 ≤ k ≤ 10; -13 ≤ l ≤ 13
data completeness	95.9 %	99.7 %
Integrated Reflns	2435 (R <sub>σ</sub> = 0.020)	1817 (R <sub>σ</sub> = 0.021)
Indpt reflections	326 (R <sub>int</sub> = 0.104)	316 (R <sub>int</sub> = 0.083)
Absorption correction	numerical	numerical
Min. / max. Transmission	0.0081 / 0.0511	0.0258 / 0.1039
Parameters	14	14
G.O.F on F <sup>2</sup>	1.147	1.117
Observed rflns [I>2σ(I)]	286	266
R <sub>1</sub> /wR <sub>2</sub> , I > 2σ <sub>I</sub>	0.01 / 0.103	0.051 / 0.137
R <sub>1</sub> /wR <sub>2</sub> , all data	0.048 / 0.147	0.054 / 0.139
weighting scheme	a = 0.105 / b = 0.00	a = 0.0999 / b = 0.00
Residual map (e <sup>-</sup> /Å <sup>3</sup> )	2.36 / -3.48	2.74 / -2.23

(\*)  $w = 1/[\sigma^2(F_o^2) + (a.P)^2 + b.P]$

The pnictogens sheet can also be regarded as made up by one-dimensional three-atom-wide Bi or Bi/Sb ribbons that extend along the *a*-direction and are interconnected by a shorter bond distance in the *b*-direction. The central Bi1 atoms in the strips have a square planar environment, which is unusual for classical compounds of main-group elements. Here, weak electron-rich multicenter bonding is undoubtedly occurring besides localized 2c-2e bonds. The three-atom-wide ribbons are the narrowest strip of vertex-sharing squares that can be cut out from a square lattice (Figure 4.3). They are described in many non-classical bonded pnictides and more recently in LaGaBi<sub>2</sub>.<sup>[14]</sup> Sidewise connection of the three-atom-wide Sb- or Bi-ribbons has been observed in α-ZrSb<sub>2</sub><sup>[15]</sup> and HfBi<sub>2</sub>,<sup>[16]</sup> respectively. Wider antimony strips are found for instance in the binaries Zr-Sb and Hf-Bi phases.<sup>[15-17]</sup>

**Table 4.1c** Selected details of Crystallographic data and Structure Refinement for Ba<sub>2</sub>Bi<sub>1+y</sub>Sb<sub>2-y</sub> (y = 1 and y = 1.25)

Chemical formula	Ba <sub>2</sub> Bi <sub>1.98(5)</sub> Sb <sub>1.02(5)</sub>	Ba <sub>2</sub> Bi <sub>2.23</sub> Sb <sub>0.77(4)</sub>
Formula weight	814.4	833.58
Temp (°C)	293(2) K	293(2) K
Diffractometer	Stoe IPDS II	Nonius CCD
Crystal size mm <sup>3</sup>	0.10×0.10×0.15	0.10×0.15×0.20
Space group	<i>Immm</i> (N° 71)	<i>Immm</i> (N° 71)
Unit cell parameters (Å)	a = 4.822(2) ; b = 7.820(3) c = 9.944(3)	a = 4.822(1) ; b = 7.809(2) c = 9.964(2)
Cell Volume, Z = 2	375.0(2) Å <sup>3</sup>	375.2(1) Å <sup>3</sup>
ρ <sub>calc</sub> (g/cm <sup>3</sup> )	7.213	7.379
μ /cm <sup>-1</sup> (Mo, K <sub>α</sub> )	605.47	648.76
F(000)	658	672
2θ range	6.6 – 62.7°	6.62 – 56.50°
Index range	-6 ≤ h ≤ 6; -11 ≤ k ≤ 11; -12 ≤ l ≤ 14	0 ≤ h ≤ 6; 0 ≤ k ≤ 10 0 ≤ l ≤ 13
Data completeness	94.7 %	100%
Integrated Reflns	1631 (R <sub>σ</sub> = 0.033)	3994 (R <sub>σ</sub> = 0.019)
Indpt reflections	357 (R <sub>int</sub> = 0.146)	292 (R <sub>int</sub> = 0.098)
Absorption correction	numerical	empirical
Min. / max. Transmission	0.0038 / 0.0269	/
Parameters	14	14
GOF on F <sup>2</sup>	1.082	1.135
Observed rflns [I > 2σ(I)]	274	280
R <sub>1</sub> /wR <sub>2</sub> , I > 2σ <sub>1</sub>	0.044 / 0.119	0.070 / 0.185
R <sub>1</sub> /wR <sub>2</sub> , all data	0.056 / 0.157	0.072 / 0.190
weighting scheme	a = 0.0897 / b = 26.6	a = 0.1555 / b = 6.01
Residual map (e <sup>-</sup> /Å <sup>3</sup> )	4.31 / -3.80	8.67 / -6.53

(\*)  $w = 1/[\sigma^2(F_o^2) + (a.P)^2 + b.P]$

In Ba<sub>2</sub>Bi<sub>3</sub>, the Bi2–Bi2 distance (corresponding to the interconnection of the ribbons) of 3.247(6) Å is close to those found in the non-classical bonded three-atom-wide Bi ribbon in LaGaBi<sub>2</sub> (3.2366(5) Å),<sup>[14]</sup> but also close to Bi–Bi bond distances in the binaries Ae<sub>11</sub>Bi<sub>10</sub> (Ae = Sr, Ba) (3.152(3) Å – 3.286(4) Å)<sup>[11-12]</sup> where they are considered to be localized. The Bi2–Bi2 bond distance in Ba<sub>2</sub>Bi<sub>3</sub> is also long compared to the one in elemental bismuth (3.072 Å). Nevertheless, the Bi–Bi bond lengths are highly variable and not easily correlated with bond strength; in some case, matrix effects may be important. The Bi1–Bi2 contact within the ribbons is quite long (3.380(2) Å), but comparable to those in Sr<sub>2</sub>Bi<sub>3</sub> (3.13 – 3.39 Å) or in the Bi<sub>3</sub><sup>7-</sup> linear trimers (3.397 Å) found in Zintl phases like Eu<sub>14</sub>MnBi<sub>11</sub>.<sup>[18]</sup> In HfBi<sub>2</sub>, the Bi–Bi distances from 3.210 Å to 3.289 Å are found within similar three-atom-wide Bi ribbons that are inter-connected by pair, through shorter bonds (3.072 Å).<sup>[16]</sup> The longest interatomic distances in Ba<sub>2</sub>Bi<sub>3</sub> (see Table 4.3) are found between Ba and Bi

atoms (from 3.631 Å to 3.669 Å) and this is consistent with the predominantly ionic nature of the Ba–Bi interactions.

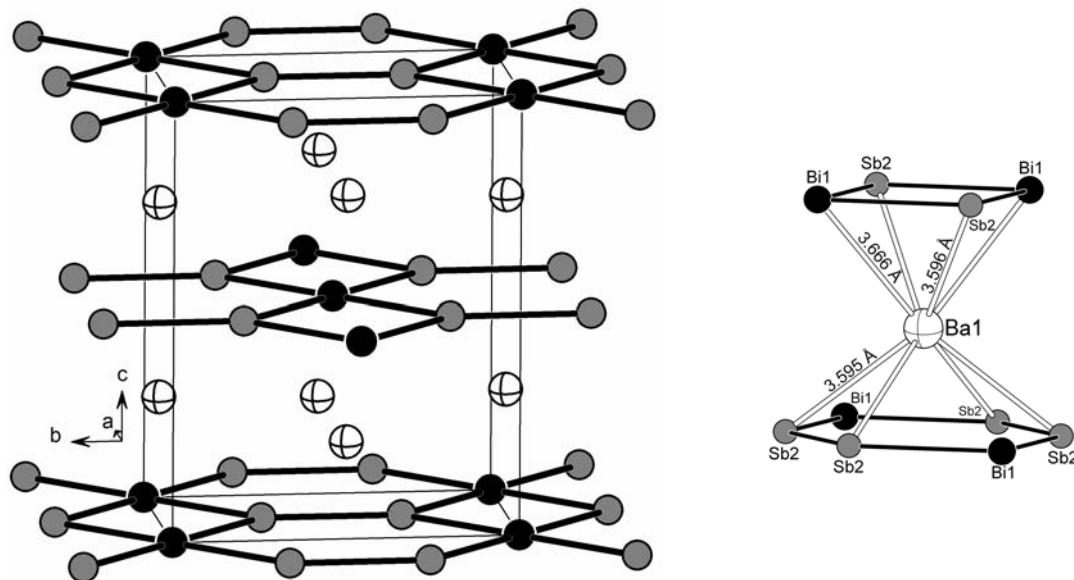


**Figure 4.2** Projection of the Crystal Structure of the phases  $\text{Ba}_2\text{Bi}_{1+y}\text{Sb}_{2-y}$ . Bi, black sphere, the Bi/Sb mixed occupied position (site  $4h$ ) is shown in grey. The site  $4h$  is occupied exclusively by Sb atoms in  $\text{Ba}_2\text{BiSb}_2$  ( $y = 0$ ) or by Bi atoms in  $\text{Ba}_2\text{Bi}_3$  ( $y = 2$ ). **Right:** The coordination geometry around Ba1 atoms with interaction distances as found in  $\text{Ba}_2\text{BiSb}_2$

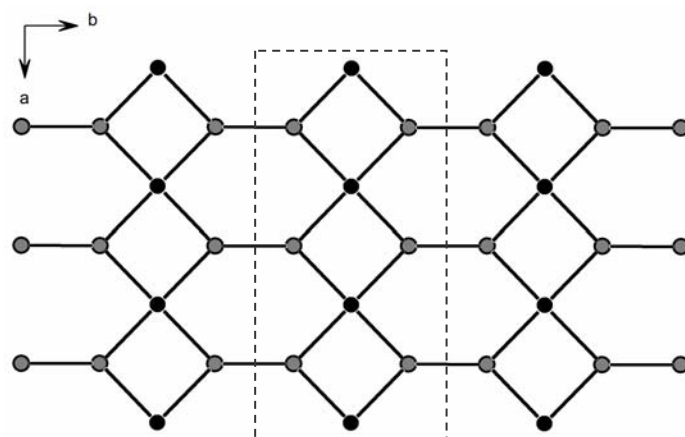


**Figure 4.3** Projection of the anionic layer, emphasizing the interconnection of the three-atom-wide ribbons (outlined by the box). Bi black, Sb/Bi grey

In Ba<sub>2</sub>BiSb<sub>2</sub>, the Bi1–Sb2 distance of 3.322(1) Å remain too long to be considered a localized single bond. The Sb2–Sb2 distance of 3.098 Å is also longer than those found in Zintl phases, like Ba<sub>2</sub>Sb<sub>3</sub> (2.866 – 3.005 Å) or Ba<sub>11</sub>Sb<sub>10</sub> (2.955 – 3.047 Å) and Ba<sub>3</sub>Na<sub>2</sub>Sb<sub>4</sub> (2.907(2) Å)<sup>[19]</sup> which contain Sb<sub>2</sub><sup>4-</sup> dumbbells. Comparable bond lengths are observed in many non-classical geometries in rare-earth antimonides like Sb quadratic square nets in YbSb<sub>2</sub> (3.120 Å)<sup>[8]</sup> or Sb<sub>5</sub> five-atom-wide ribbons in the ternary compounds La<sub>13</sub>Ga<sub>8</sub>Sb<sub>21</sub> (from 3.093(1) Å to 3.134(2) Å)<sup>[20]</sup> and Pr<sub>12</sub>Ga<sub>4</sub>Sb<sub>23</sub> (3.109(1) Å).<sup>[21]</sup>

As expected and due to the substitution of Bi by smaller Sb, the cell Volume reduces by approximately 5% going from Ba<sub>2</sub>Bi<sub>3</sub> to Ba<sub>2</sub>BiSb<sub>2</sub> (Figure 4.4a). This shrinking is highly anisotropic as it can be seen from the change of lattice parameters: a, b and c are reduced by 0.3%, 3.8% and 0.8% respectively (Figure 4.4b).

**Table 4.2a** Atomic coordinates and equivalent isotopic thermal displacement parameters ( $U_{eq}$ )<sup>\*</sup> for Ba<sub>2</sub>Bi<sub>1+y</sub>Sb<sub>2-y</sub> (y = 2, 1, 0.5, 0)

Atom	Site	s.o.f	x	y	z	$U_{eq} / \text{Å}^2$
<b>Ba<sub>2</sub>Bi<sub>3</sub> (y = 2)</b>						
Ba1	4j	1	½	0	0.7245(4)	0.0126(6)
Bi1	2a	1	0	0	0	0.0224(7)
Bi2	4h	1	½	0.7032(4)	0	0.0137(5)
<b>Ba<sub>2</sub>Bi<sub>2</sub>Sb<sub>1</sub> (y = 1)</b>						
Ba1	4j	1	½	0	0.7212(3)	0.0282(7)
Bi1	2a	1	0	0	0	0.0369(7)
Bi2	4h	0.49(2)	½	0.7031(3)	0	0.0303(7)
Sb2	4h	0.51(2)	½	0.7031(3)	0	0.0303(7)
<b>Ba<sub>2</sub>Bi<sub>1.5</sub>Sb<sub>1.5</sub> (y = 0.5)</b>						
Ba1	4j	1	½	0	0.7203(2)	0.0223(6)
Bi1	2a	1	0	0	0	0.0296(6)
Bi2	4h	0.24(2)	½	0.7023(2)	0	0.0245(7)
Sb2	4h	0.76(2)	½	0.7023(2)	0	0.0245(7)
<b>Ba<sub>2</sub>Bi<sub>1</sub>Sb<sub>2</sub> (y = 0)</b>						
Ba1	4j	1	½	0	0.7202(2)	0.0281(6)
Bi1	2a	1	0	0	0	0.0360(6)
Bi2	4h	0.05(2)	½	0.7016(2)	0	0.0263(6)
Sb2	4h	0.95(2)	½	0.7016(2)	0	0.0263(6)

<sup>(\*)</sup>  $U_{eq}$  is defined as one third of the trace of the orthogonalized  $U^j$  tensor

**Table 4.2(b)** Anisotropic Atomic Displacement Parameters for  $\text{Ba}_2\text{Bi}_{1+y}\text{Sb}_{2-y}$  ( $y = 2, 1, 0.5, 0$ )

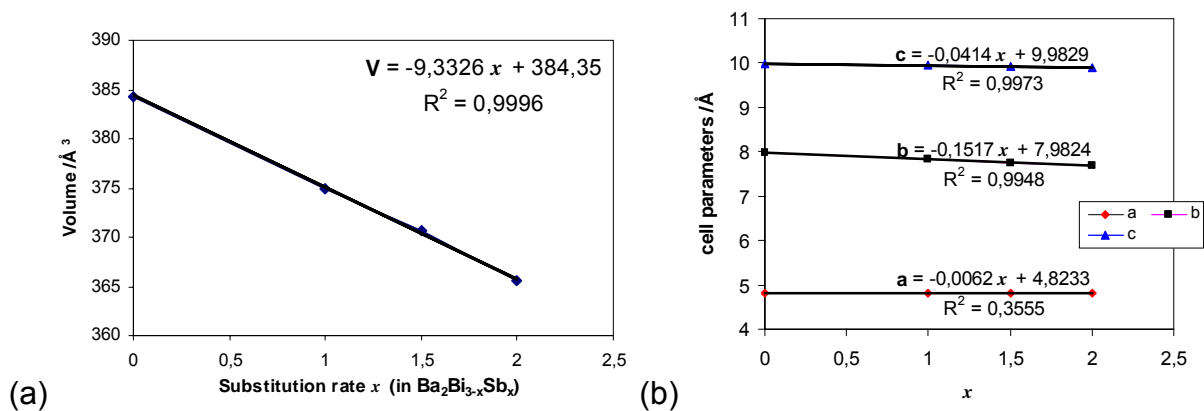
Atom	$\text{Ba}_2\text{BiSb}_2$			$\text{Ba}_2\text{Bi}_3$		
	$U_{11}$	$U_{22}$	$U_{33}$	$U_{11}$	$U_{22}$	$U_{33}$
Bi1	0.039(1)	0.044(1)	0.024(1)	0.033(2)	0.070(3)	0.025(2)
Bi2/Sb2	0.033(1)	0.032(1)	0.024(1)	0.041(2)	0.038(2)	0.024(1)
Ba1	0.0278(8)	0.0274(8)	0.0225(8)	0.031(2)	0.041(2)	0.027(2)

Atom	$\text{Ba}_2\text{Bi}_2\text{Sb}_1$			$\text{Ba}_2\text{Bi}_{1.5}\text{Sb}_{1.5}$		
	$U_{11}$	$U_{22}$	$U_{33}$	$U_{11}$	$U_{22}$	$U_{33}$
Bi1	0.0344(9)	0.045(1)	0.0241(8)	0.026(1)	0.060(2)	0.0241(9)
Bi2/Sb2	0.0325(9)	0.0287(9)	0.0244(9)	0.0270(9)	0.039(1)	0.0251(9)
Ba1	0.0276(8)	0.0296(8)	0.0244(8)	0.0202(9)	0.042(1)	0.0224(9)

**Table 4.3** Selected interatomic distances (Å) and bonds angles (°) in  $\text{Ba}_2\text{Bi}_{1+y}\text{Sb}_{2-y}$  ( $y = 2, 1, 0.5, 0$ )

Atom pair	$\text{Ba}_2\text{Bi}_3$	$\text{Ba}_2\text{Bi}_2\text{Sb}_1$	$\text{Ba}_2\text{Bi}_{1.5}\text{Sb}_{1.5}$	$\text{Ba}_2\text{BiSb}_2$
Bi(1)–Pn(2)	3.380(2)	3.347(2)	3.335(2)	3.322(1)
Pn(2)–Pn(2)	3.247(6)	3.178(4)	3.141(3)	3.098(3)
Ba(1)–Bi(1)	3.656(3)	3.673(2)	3.672(2)	3.665(1)
Ba(1)–Pn(2)	3.631(4)	3.615(2)	3.604(2)	3.595(2)
Ba(1)–Pn(2)	3.669(3)	3.631(2)	3.615(2)	3.596(2)
Pn(2)–Pn(2)–Bi(1)	134.54(4)°	133.91(3)°	133.71(2)°	133.70(2)°
Bi(1)–Pn(2)–Bi(1)	90.91(8)°	92.19(6)°	92.57(4)°	92.59(4)°

**Figure 4.4** Linear model of the variation of unit cell volume (a) and unit cell parameters (b) with Bi to Sb substitutions rate ( $x$ ).

Using only the cell parameters obtained from the same diffractometer (Stoe IPDS II), a linear decrease of the unit cell volume with the substitutions rate is observed with a very good reliability factor ( $R = 99.96\%$ ). The lattice parameters  $b$  and  $c$  decrease quasi linearly with the substitution rate  $x$  also with good reliability factors ( $R > 99.5\%$ ), but the  $a$ -parameter varies irregularly ( $R = 35.6\%$ ). As revealed by the gradient of the trend lines, the substitutions have strongest effects on the  $b$ -parameter which is in the direction of the interconnection of the ribbons. In comparison, this effect is nearly four times less in  $c$ -direction which is the direction of interaction between anionic layers and barium cations, meaning that the interactions between Ba atoms and the anionic network are only slightly influenced by the substitutions. In  $a$ -direction which is the direction of the ribbons, the reduction due to substitutions is neither significant nor regular.

The anisotropy of the lattice compression correlates directly to changes in interatomic distances when going from the Bi to the Sb-Bi sub-lattice. Complete substitution of Bi2 by Sb consequently leads to shorter Bi1–Sb contacts, compared to Bi1–Bi2 contacts. However, on one hand the Bi1–Sb contact ( $3.322(1) \text{ \AA}$ ) reduces by only 1.7% and remains still longer than some reported Bi–Bi contacts mentioned above, and on the other hand the Sb–Sb contact in  $\text{Ba}_2\text{BiSb}_2$  ( $3.098 \text{ \AA}$ ) is reduced by 4.6 %, if compared to the Bi2–Bi2 contact in  $\text{Ba}_2\text{Bi}_3$ . In contrast, the Ba–Bi1 interaction distances vary irregularly; it increases from  $\text{Ba}_2\text{Bi}_3$  to  $\text{Ba}_2\text{Bi}_2\text{Sb}$  ( $3.656 \text{ \AA}$  to  $3.673 \text{ \AA}$ ), but decrease from  $\text{Ba}_2\text{Bi}_{1.5}\text{Sb}_{1.5}$  to  $\text{Ba}_2\text{BiSb}_2$  ( $3.672 \text{ \AA}$  to  $3.665 \text{ \AA}$ ) whereas the Ba–Pn2 (Pn2 = Bi2/Sb2) decrease regularly from  $3.669(3) \text{ \AA}$  in  $\text{Ba}_2\text{Bi}_3$  to  $3.595(2) \text{ \AA}$  in  $\text{Ba}_2\text{BiSb}_2$ , indicating that the variations of the Ba–Pn interaction distances are mainly due to matrix effects, which is consistent with the ionic nature of these interactions.

Non-classical coordination geometries of atoms have been described in many rare-earth pnictides (Pn), mostly antimonides. Bonding in those non-classical structures can be rationalized using a reformulation of the Zintl concept to account for partial bond order by interpreting longer Pn–Pn bonds as one-electron-two-center ( $1e^-2c$ ) bonds or half-bonds, to a first approximation. Longer Sb–Sb bond distances ( $3.0 - 3.3 \text{ \AA}$ ) are found as indicators.<sup>[22-23]</sup> The  $\frac{1}{\infty}[\text{Bi}_3]$  one-dimensional ribbon can be regarded as being excised from an infinite two-dimensional square net of Bi atoms or fused from finite linear triatomic rods containing  $3c-4e^-$  bonds like  $\text{X}_3^-$  anions.<sup>[9]</sup> As proposed by Hoffmann and co-workers,<sup>[9-24]</sup> the molecular bonding model of the ribbon can be constructed starting from the square-planar hypervalent molecule  $\text{XeF}_4$

(Figure 4.5a) in which the Xe atom is hypervalent while F atoms are classical (an octet can be completed around each F atom). In order to build a dimer of  $\text{XeF}_4$ , the bridging F atoms have to be replaced by oxygen atoms in order to preserve their classical electron count (Figure 4.5b). Thus, in the hypothetical  $\text{XeO}_2$  polymer (Figure 4.5c) both O and Xe atoms are classical. The electron in extended  $\text{XeO}_2$  is  $8 + 2 \times 6 = 20$  electrons per unit. A neutral  ${}^1[\text{Pn}_3]$  strip contains only 15 electrons per  $\text{Pn}_3$ , which necessitates an addition of a charge of -5 to match the electronic requirement i.e.  $[\text{Pn}_3]^{5-}$ .

Applying the Zintl-Klemm-Bussmann concept for the title compounds leads to the formula  $(\text{Ba}^{2+})_2[\text{Bi}_3]^{4-}$  or  $(\text{Ba}^{2+})_2[\text{BiSb}_2]^{4-}$ . According to the above described electron counting rule, the isolated infinite three-atom-wide ribbon, is stable for an electron count of  $20 e^-$  per trimer (i.e.,  $[\text{Bi}_3]^{5-}$  or  $[\text{BiSb}_2]^{5-}$ ). Then, the interconnection of two ribbons like in the structure of  $\alpha\text{-ZrSb}_2$  implies that each atom at the border loses one electron (if we assumed that the interconnection of ribbons is realized through classical  $2c-2e$  bonds) giving  $[\text{Bi}_3]^{4-}$  (Figure 4.5d). This means that a one side interconnection of the ribbons like in  $\alpha\text{-ZrSb}_2$  would have lead to electronically stable phases in which the three-bonded Bi or Sb atoms and the four-bonded Bi atoms will be assigned the same formal charge of  $\text{Pn}^{1-}$ . But, in the title phases, the ribbons are connected at both sides and the same implementation leads to an electron count of  $[\text{Bi}_3]^{3-}$  (or  $[\text{SbBiSb}]^{3-}$ ) resulting in  $(\text{Ba}^{2+})_2[\text{Bi}_3]^{3-}(e^-)$ . In contrast to  $\alpha\text{-ZrSb}_2$  where the interconnection distance between Sb ribbons of 2.88 Å is in the range of a single bond distance, in  $\text{Ba}_2\text{BiSb}_2$  the Sb-Sb distance is 3.098 Å, indicating that the additional electron fills the antibonding states. Nevertheless, the observed Sb-Sb long bond distance has a higher degree of bond shrinking compared to Sb-Bi bonds, which can be understood as a higher degree of electron localization.

Corollary, partitioning the shared electrons evenly between pairs of Pn atoms, each atom conforms the octet rule if the Pn-Pn bond is considered to be fractional  $1e^-2c$  bonding, on average. This gives rise to a formal charge of -1 for the four-coordinated Bi1 and -1.5 formal charge for the three-coordinated Bi2 or Sb2 atoms. Each Bi1 atom is assigned a count of six electrons: in four-bonded Bi1 two lone pairs occupy the s- and  $p_z$ -orbitals perpendicular to the sheet (or  $sp_z$  hybrids thereof), and the remaining two electrons are distributed over the in-plane  $p_x$  and  $p_y$  orbitals which overlap with those on neighboring three-bonded Bi2 (or Sb2) atoms (bearing two lone

pairs) to form delocalized Bi1–Bi2/Sb2 bonds. The Bi2 atoms (or Sb2) are connected by classical 2c-2e covalent bonds and, the unaccounted electron occupies the antibonding states. In agreement with the model, the bond angles are close to  $90^\circ$ . This means that in the compound  $\text{Ba}_2\text{Bi}_3$  and its substituted variant  $\text{Ba}_2\text{Bi}_{1+y}\text{Sb}_{2-y}$ , the planar anionic layers possess a new intermediate degree of hypervalency which is consistent with the strict site preference of Sb atoms.

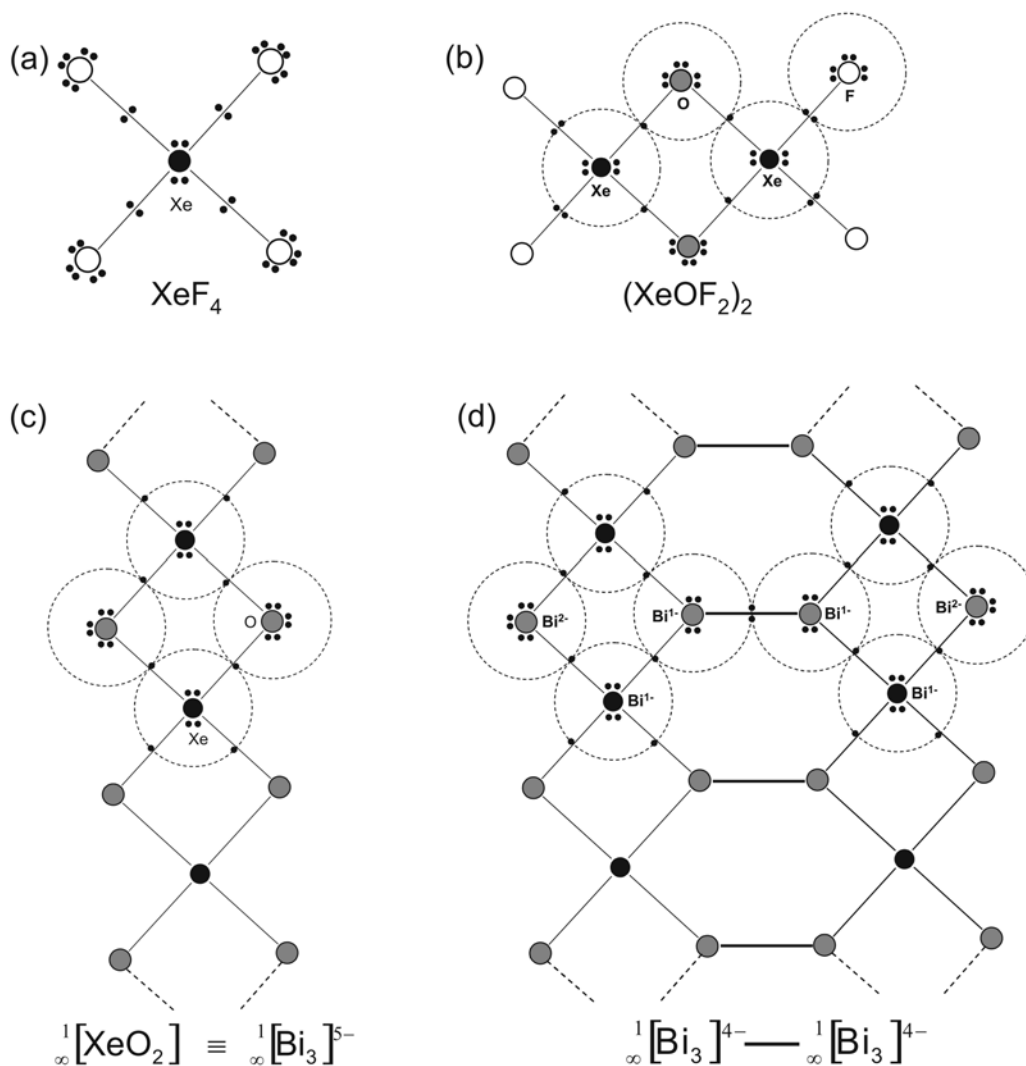


**Figure 4.5** Electron counting scheme in three-atom-wide ribbons with electron-rich multicenter bonding; the lines are not classical electron pair bonds, but just connectivity. (a) Starting molecular model  $\text{XeF}_4$  with classical F and hypervalent Xe atoms, respectively; (b) the hypothetical dimer  $(\text{XeF}_2\text{O})_2$  forms by condensation of two  $\text{XeF}_4$  molecules after the replacement of the two bridging F atoms by Oxygen; (c) the hypothetical one dimensional  $(\text{XeO}_2)_n$  polymer, which is isoelectronic with  ${}^1_{\infty}[\text{Bi}_3]^{5-}$ ; (d) Interconnection of two  ${}^1_{\infty}[\text{Bi}_3]^{4-}$  strips by classical 2c-2e covalent bonds (represented by thicker lines) after removal of one electron per lone-pair.

#### 4.2.4 Electronic Structure and Discussions

To examine the properties of  $\text{Ba}_2\text{Bi}_3$  and the substituted phases  $\text{Ba}_2\text{Bi}_{1+y}\text{Sb}_{2-y}$  as well as the overall electronic properties, the bands structures of  $\text{Ba}_2\text{Bi}_3$  and  $\text{Ba}_2\text{BiSb}_2$  were obtained from LMTO calculations. The DOS plots of  $\text{Ba}_2\text{Bi}_3$  and  $\text{Ba}_2\text{BiSb}_2$  with the projected DOS for Ba, Bi1 and Bi2 (or Sb2) are shown in [Figure 4.6](#). The orbitals are filled up to the Fermi level  $E_F$  and no band gap is visible around  $E_F$  meaning that the compound is metallic. The DOS at the Fermi level attains a high value, predicting the compound to be highly conductive. A distinctive feature in the electronic structure of both  $\text{Ba}_2\text{Bi}_3$  and  $\text{Ba}_2\text{BiSb}_2$  is the sharp singularity flanking the Fermi energy, which indicates an electronic instability, making these compounds good candidates for interesting physical properties like e.g. superconductivity.<sup>[25]</sup> The density-of-states exhibit a clear separation between the bands with s- and p-orbitals of Bi (about 5 eV in  $\text{Ba}_2\text{Bi}_3$ ). For  $\text{Ba}_2\text{Bi}_3$ , the bands with Bi s-orbitals character are at lower energy levels between -12 eV and -9 eV while the occupied states in the valence band between -4 eV and the Fermi level are mainly of Bi1 and Bi2 p-orbitals character, but with strong contributions from Ba states.

The dispersion of the bands along the high symmetry lines as shown in [Figure 4.7](#) reveals relatively flat bands with saddle points, crossing the Fermi level in the directions  $R \rightarrow W$  and  $W \rightarrow S$ , which are parallel to the anionic layer. These flat bands are responsible for the sharp peak at  $E_F$  observed in the DOS plot. The importance of saddle points and the associated van Hove singularities in the DOS was discussed for the cuprate superconductors.<sup>[26]</sup> In our case, fat band analysis – where bands are drawn with a thickness representative of their corresponding orbital contribution – shows that these flat bands originate from the Bi1 and Bi2  $p_x$ - and  $p_y$ -orbitals, emphasizing the high electronic correlation within the Bi layer. Another noteworthy feature is the band with large dispersion crossing the Fermi level along the symmetry path  $\Gamma \rightarrow X$  which is perpendicular to the anionic layers. This band is contributed from Bi1  $p_z$ -orbital in  $\text{Ba}_2\text{Bi}_3$  and is strongly mixed with Ba orbitals. This suggests that the metallic conductivity may be three-dimensional, albeit anisotropic, where the unexpected conductivity in the c-direction is induced by the significant covalent character of Ba–Bi interactions.

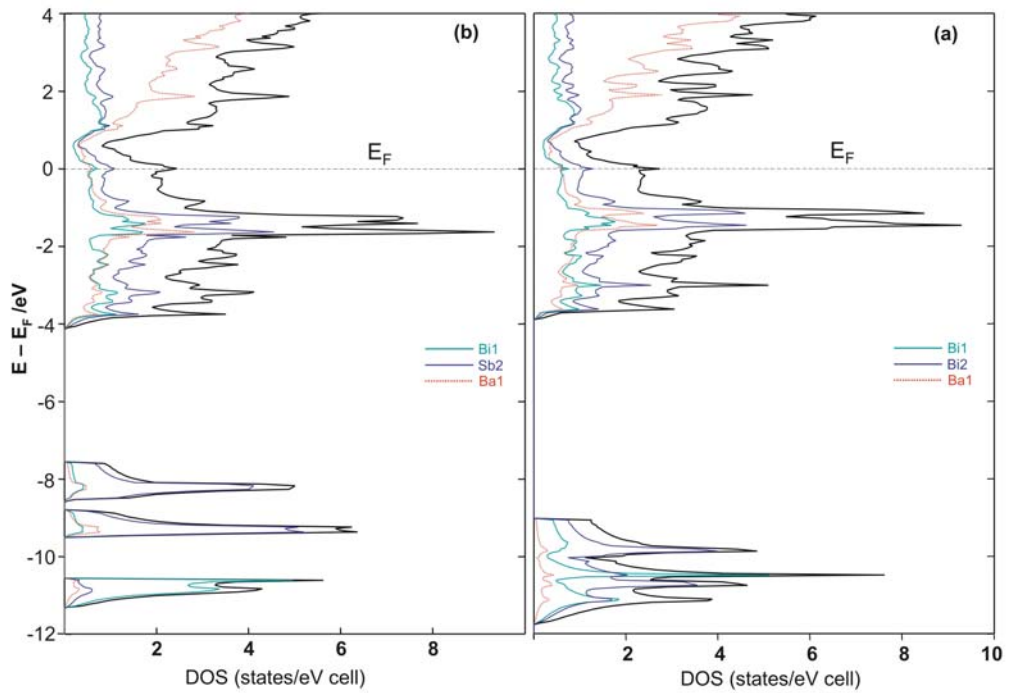
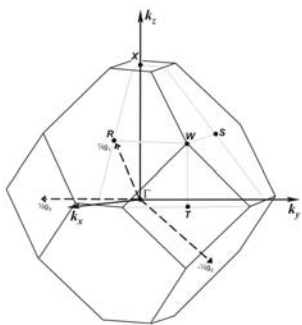


**Figure 4.6** Total and projected Density of State (DOS) plot for  $\text{Ba}_2\text{Bi}_3$  (a) and  $\text{Ba}_2\text{BiSb}_2$  (b).



The first Brillouin zone of Orthorhombic I lattice with  $c > b > a$ :  $\Gamma(0,0,0)$ ,  $X(\frac{1}{2}, \frac{1}{2}, -\frac{1}{2})$ ,  $R(\frac{1}{2}, 0, 0)$ ,  $S(\frac{1}{2}, 0, -\frac{1}{2})$ ,  $T(\frac{1}{2}, -\frac{1}{2}, 0)$ ,  $W(\frac{3}{4}, -\frac{1}{4}, -\frac{1}{4})$

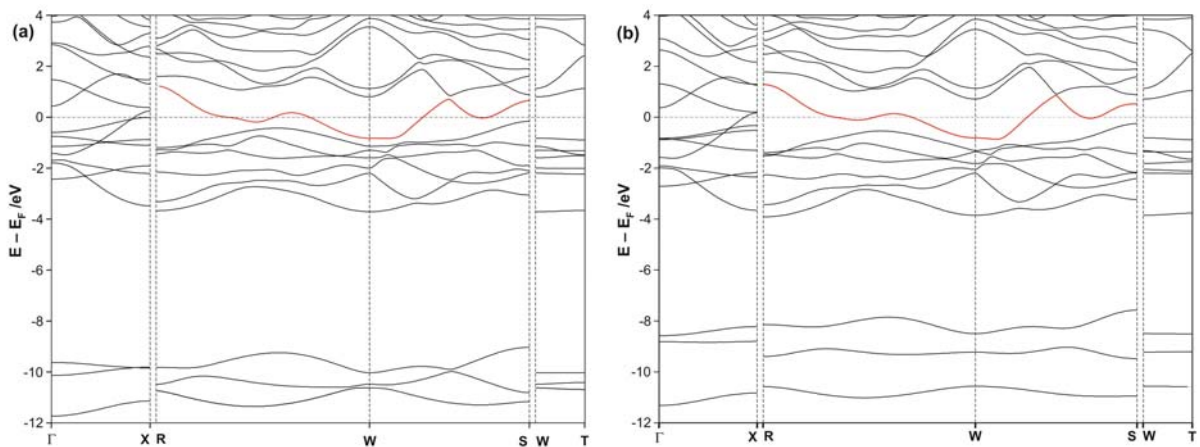


**Figure 4.7** Band dispersion for  $\text{Ba}_2\text{Bi}_3$  (a) and  $\text{Ba}_2\text{BiSb}_2$  (b). The bands crossing the  $E_F$  in The direction  $R \rightarrow W \rightarrow S$  are plotted in red. The Fermi level is taken as point of zero energy.

The band dispersion of the substituted phase  $\text{Bi}_2\text{BiSb}_2$  is virtually identical to that of  $\text{Ba}_2\text{Bi}_3$ . The outstanding differences are mainly due to the separation of Sb2 states in  $\text{Bi}_2\text{BiSb}_2$  with respect to Bi2 states in  $\text{Bi}_2\text{Bi}_3$ . This is visible in the DOS plots (Figure 4.7) where the states with essentially Bi and Sb s-orbital character (between -12 eV and -9 eV in  $\text{Ba}_2\text{Bi}_3$ ) clearly separate into three states. The band with mainly Bi 6s-orbital character is situated below the Sb 5s bands, due to the relativistic contraction. Furthermore, we can see in the band structure of  $\text{Ba}_2\text{Bi}_3$  a relatively flat band in  $G \rightarrow X$  which just touches the Fermi level at X and that is contributed from  $p_x$ -orbital of Bi2 (lone pair); in  $\text{Bi}_2\text{BiSb}_2$  the corresponding band which is contributed from  $p_x$ -orbital of Sb2 is clearly below the Fermi level. Therefore, in the highest occupied bands, the states deriving from Sb2 orbitals lie lower in energy compared to the Bi2 states, so that the structure may be stabilized under Sb for Bi substitutions.

To explain the strict site preference for Sb atoms, the COHP curves are more informative (Figure 4.8). For  $\text{Ba}_2\text{Bi}_3$  the average integrated cohp (-icohp) up to  $E_F$  for Bi1–Bi2 (3.380 Å) and Bi2–Bi2 (3.247 Å) are 0.75 eV/bond and 0.95 eV/bond respectively, which indicate significant bonding interactions. However, around the Fermi level the interactions are antibonding indicating that the bonds are weakened by the occupation of antibonding states. The Bi1–Bi2 bond would be optimized at the energy level of about -1.50 eV (below  $E_F$ ) with a -icohp = 1.05 eV/bond, whereas the Bi2–Bi2 would be optimized at the energy level of about -1.25 eV (below  $E_F$ ) with a -icohp value of 0.136 eV/bond. For  $\text{Ba}_2\text{BiSb}_2$ , the cohp curves are also quite similar to those of  $\text{Ba}_2\text{Bi}_3$ . The Bi1–Sb2 bond has a -icohp value of 0.75 eV/bond and would be optimized at the energy level of -1.65 eV with a -icohp of 1.05 eV/bond just like the Bi1–Bi2 bond in  $\text{Ba}_2\text{Bi}_3$ . This means that there is no strengthening of this bond due to substitutions. In contrast, the Sb2–Sb2 bond has a -icohp value of 1.10 eV/bond, and would be optimized at the energy level of -1.40 eV with a -icohp of 1.60 eV/bond, indicating stronger interactions compared to Bi2–Bi2 in  $\text{Ba}_2\text{Bi}_3$ , thus this bond is significantly strengthened upon substitution.

Therefore, the substitution gives indication of atomic sites with enhanced property for electron localization, in agreement with the model of the interconnection of the weakly bonded three-atom-wide ribbons by stronger 2c-2e covalent bond.

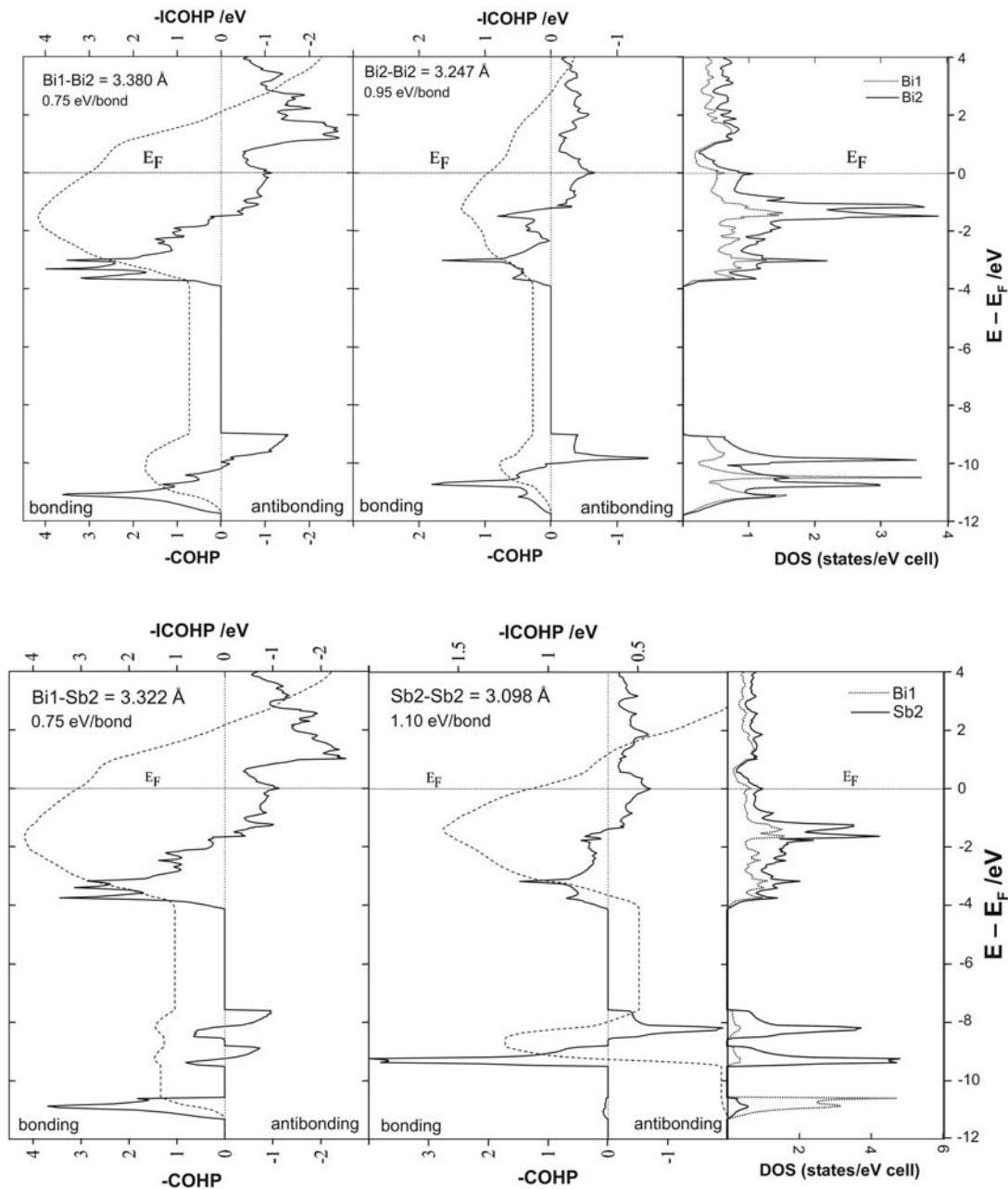


**Figure 4.8** Crystal Orbital Hamiltonian Population (cohp) curves (solid lines) and their integration (dashed lines) for Bi–Bi the interactions in  $\text{Ba}_2\text{Bi}_3$  (top) and Bi–Bi/Sb interactions in  $\text{Ba}_2\text{BiSb}_2$  (bottom) with the corresponding projected DOS.

However, because of the orbital mixing in the extended anionic layer in  $\text{Ba}_2\text{Bi}_3$ , the extra electron is delocalized in the whole substructure. Hence, the strict site preference of Sb in the coloring variant  $\text{Bi}_2\text{BiSb}_2$  is unexpected and it indicates that the energies of the atomic sites and/or the bonds are significantly different enough within the anionic layer to be able to discriminate between two chemically very close elements like Sb and Bi. This is likely to enlighten us about some aspects of coloring

problem in the solid state.<sup>[27]</sup> The strict site preference for Sb atoms may be ascribed to the higher electronegativity of Sb, but also to the reluctance of the Bi atom for covalent bonding due to stronger relativistic effects. Indeed, the electron-rich multicenter bonding goes along with the relative absence of significant s-p interaction, which is due to the contraction of the less-screened s orbitals relative to p orbitals down the groups in the Periodic Table.

Because of the continuous distribution of states with essentially non-bonding or anti-bonding character near the Fermi level, non-classical bonded networks are able to tolerate some degree of oxidation or reduction without undergoing severe distortion. They have the capacity to act as an electron sink, able to accept additional electrons to an extent that Pn–Pn bonds are weakened only slightly. Thus, the occurrence of such networks may be linked to the electron transfer process from the electro-positive active metal to the electronegative p-element according to the Zintl-Klemm-Busmann concept.<sup>[22]</sup> This can be seen in the electronic structures which show a relatively strong covalent character of the Ba–Bi interactions. When the electron transfer is not effective enough because the difference of electronegativity is shallow, or in case of electron excess (e.g. doping) the main group component may adopt a non-classical geometry to deaden (act as damper) the charge fluctuation. This can nicely be pursued in the present study on the series  $\text{Ba}_2\text{Bi}_x\text{Sb}_{3-x}$  where a transition from a typical Zintl phase  $\text{Ba}_2\text{Sb}_3$  to electron-rich multicenter bonded phases  $\text{Ba}_2\text{Bi}_{1+y}\text{Sb}_{2-y}$  is observed at increasing Bi content.

$\text{Ba}_2\text{Bi}_3$  and its coloring variant  $\text{Ba}_2\text{BiSb}_2$  present a great fundamental interest because they are mixed valence compounds of the same atom Bi or of two chemically very close atoms Bi and Sb. During the past years, charge, spin, and orbital ordering have attracted increasing attention because such collective processes seem to be strongly related to the occurrence of, e.g., superconductivity or magneto resistance. Prerequisites are mixed valency and markedly correlated electrons.<sup>[27]</sup>

#### 4.2.5 Physical properties

A sample with the composition  $\text{Ba}_2\text{Bi}_{1.95}\text{Sb}_{1.05}$  (as refined from single crystal diffraction), was prepared by annealing of a mixture Ba:Bi:Sb = 2:2:1 at 750°C for 2 weeks. The magnetic measurements were performed on that sample in the

temperature range from 1.8 K to 300 K using a SQUID magnetometer. The sample was cooled in the absence of a magnetic field; data were recorded after the introduction of a 1 G field, while sample was warmed (“shielding”) and the cooled (“Meissner”). A superconducting state below  $T_c = 3.4$  K was observed by a sharp transition from a negative to positive value of the magnetization. The only previously known superconducting phase in the Ba/Bi/Sb system is the binary  $\text{BaBi}_3$  ( $T_c = 5.7$  K). Ongoing measurements on the sample with composition  $\text{Ba}_2\text{BiSb}_2$  suggest that the  $T_c$  may vary strongly with the substitution rate. We believe that more attention should be pay on the magnetic properties of these phases.

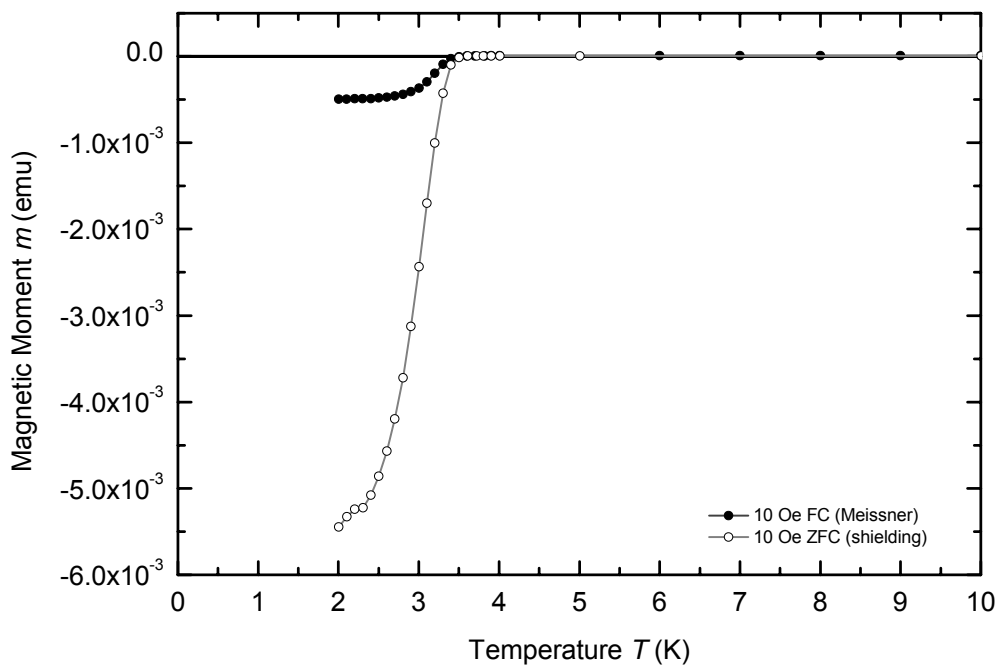


**Figure 4.9** SQUID magnetic measurement of  $\text{Ba}_2\text{Bi}_{1.95}\text{Sb}_{1.05}$ . Diamagnetic shielding (O) and Meissner effect (●) as a function of temperature

### 4.3 Further results – The crystal structure of BaBi<sub>2</sub>

#### 4.3.1 Source of the material and crystal structure determination

During the thermal analyze of the phase Ba<sub>2</sub>Bi<sub>3</sub>, a single crystal was extracted from the DTA sample – a mixture with nominal composition Ba:Bi = 2:3 – which was previously heated at 900°C for 5 hours and quenched at room temperature. After the DTA experiment was performed on this sample, the single crystal was isolated and the crystallographic investigations reveal a tetragonal unit cell, with parameters that differ clearly from the expected orthorhombic cell parameters of the phase Ba<sub>2</sub>Bi<sub>3</sub>. The structure solution yields the composition BaBi<sub>2</sub> with the unit cell parameters,  $a = b = 5.0167(7)$  Å and  $c = 35.870(7)$  Å, space group I4<sub>1</sub>/amd (Nr. 141). The phase BaBi<sub>2</sub> could not be detected in the powder diagram of the sample, indicating that it represents a by-product. EDX analysis confirms the presence of only Ba and Bi elements.

**Table 4.4** Crystallographic data and structure refinement of BaBi<sub>2</sub>

Chemical formula	BaBi <sub>2</sub>
Formula weight	555.30
Space group	I4 <sub>1</sub> /amd (Nr. 141)
Diffractometer	Stoe IPDS II
Temperature	293(2)K
Unit cell parameters	$a = 5.0167(7)$ Å; $c = 35.870(7)$ Å
Unit cell volume	$902.8(3)$ Å <sup>3</sup> , $Z = 8$
$\rho_{\text{calc}}$ (g/cm <sup>3</sup> )	8.171
$\mu$ (mm <sup>-1</sup> ) (Mo-K $\alpha$ )	86.181( $\lambda = 0.71073$ Å)
F(000)	1776
crystal size (mm <sup>3</sup> )	0.10 × 0.15 × 0.15
2 $\theta$ range for data collection	4.6° – 52.2°
index ranges	$-6 \leq h \leq 6$ , $-5 \leq k \leq 6$ , $-43 \leq l \leq 40$
Collected reflections	3205
Independent reflections	328
Observed reflections [ $I > 2\sigma$ ]	218
$R_{\text{int}} / R_{\sigma}$	0.135 / 0.035
Absorption correction	numerical
min /max Transmission	0.0031 / 0.0165
Nr. of parameters	14
goodness-of-fit on $F^2$	1.112
$R_1/wR_2^{[*]}$ , $I > 2\sigma$	0.079 / 0.217
$R_1/wR_2$ , all data	0.100 / 0.227
extinction parameter	0.0002(2)
Residual map (e <sup>-</sup> /Å <sup>3</sup> )	8.62 / -3.54

$$[*] w = 1/[\sigma^2 (F_o^2) + (0.1422 \times P)^2 + 23.74 \times P]$$

The single crystal diffraction was performed on the Stoe IPDS II. A total of 360 frames were recorded with exposure time of 6 min/frame with  $\omega$ -scan,  $\Delta\omega = 1^\circ$ . The crystal detector distance was 130 mm. Numerical absorption correction was applied using the program X-shape from Stoe. The tetragonal space group  $I4_1/amd$  was found to be correct based on intensity statistics and successful structure solution. All the five atomic positions of the structure were found during structure solution by direct methods and no mixed-occupancy was found, indicating a fully ordered phase. A summary of the crystallographic and refinement data is given in Table 4.4 and the atomic parameters in Tables 4.5. The last Fourier difference map indicated high residual peaks in electron density of  $8.62 \text{ e}^-/\text{\AA}^3$  and the electron hole  $-3.54 \text{ e}^-/\text{\AA}^3$  in the near vicinity of the Bi2 position which has fairly high ADPs. This may be ascribed to some anharmonicity in the atomic thermal displacement. But errors during absorption corrections or the poor crystalline quality are other possible explanations.

**Table 4.5(a)** Atomic Coordinates and Isotropic Equivalent Displacement Parameters for BaBi<sub>2</sub>

Atom	site	x	y	z	$U_{\text{eq}}/\text{\AA}^2$
Ba1	8e	0	$\frac{3}{4}$	0.0521(1)	0.023(1)
Bi1	8e	$\frac{1}{2}$	$\frac{1}{4}$	0.0290(1)	0.031(1)
Bi2	8e	0	$\frac{3}{4}$	0.1233(1)	0.077(2)

**Table 4.5(b)** Anisotropic Displacement Parameters ( $\text{\AA}^2$ ) for BaBi<sub>2</sub>

Atom	$U_{11}$	$U_{22}$	$U_{33}$	$U_{23}$	$U_{13}$	$U_{12}$
Ba1	0.025(2)	0.024(2)	0.020(2)	–	–	–
Bi1	0.022(1)	0.034(2)	0.038(1)	–	–	–
Bi2	0.031(2)	0.173(5)	0.029(2)	–	–	–

**Table 4.6** Selected interatomic distances ( $\text{\AA}$ ) and bonds angles ( $^\circ$ ) in BaBi<sub>2</sub>

Atom pair	distances / $\text{\AA}$	
Bi1 –Bi1	3.257(3)	×2
Bi1 –Ba1	3.643(1)	×4
Bi2 –Bi2	3.549(1)	
Bi2 –Ba1	3.580(3)	×2
Bi1–Bi1–Bi1	100.7(1) $^\circ$	
Bi2–Bi2–Bi2	89.93(1) $^\circ$	

Atom pair	distances / $\text{\AA}$	
Ba1 –Bi2	3.580(3)	×2
–Bi1	3.643(1)	×4
–Bi2	3.666(3)	×2
–Bi1	3.841(2)	×2
Bi2–Bi2–Bi2	176.1(1) $^\circ$	

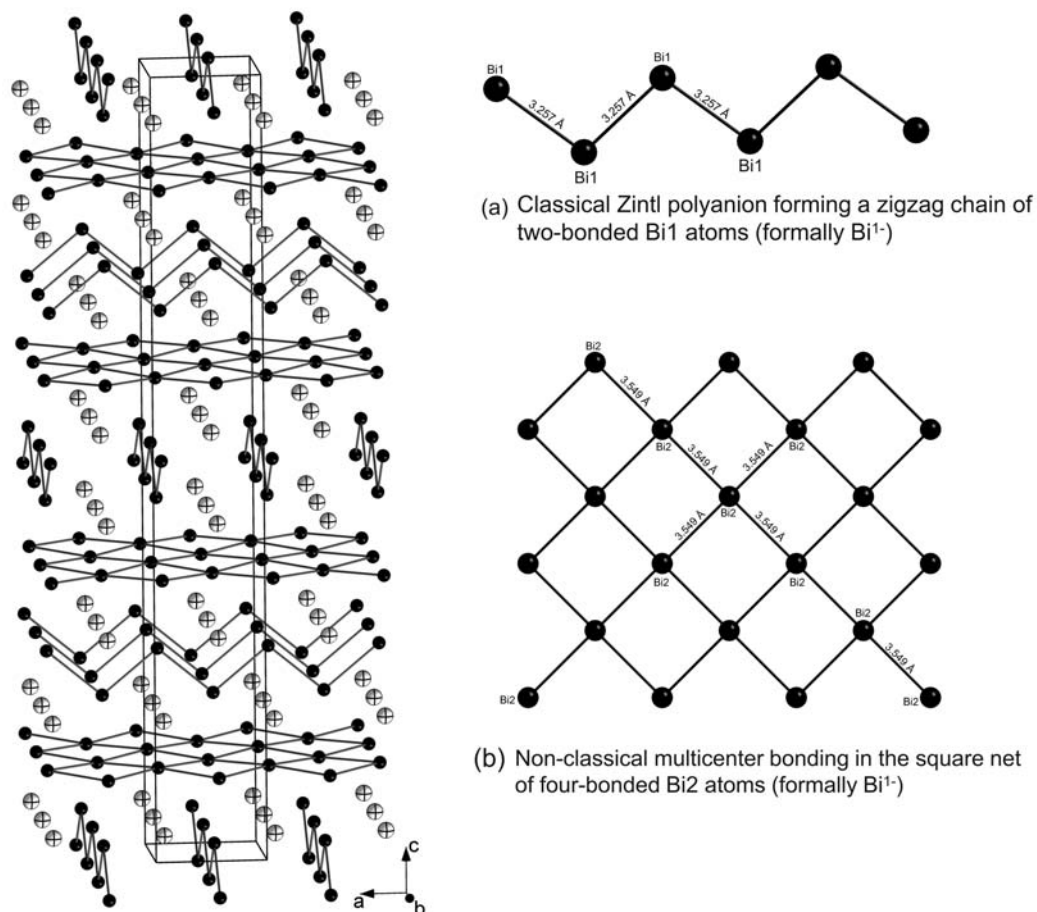


**Figure 4.10** Projection of the structure of BaBi<sub>2</sub> (Bi atoms as black spheres; Ba atoms white crossed spheres). (a) Closer view of the 1D zigzag chains of Bi1 atoms and (b) of the 2D square net of Bi2 atoms.

### 4.3.2 Description of the structure of BaBi<sub>2</sub> and discussions

The intermetallic compound BaBi<sub>2</sub> crystallizes in the tetragonal system, space group  $I4_1/amd$  (No. 141). Similarly to that EuBi<sub>2</sub> and YbSb<sub>2</sub>, the structure of BaBi<sub>2</sub> (Figure 4.10) is composed of 1D zigzag chains of two-bonded Bi atoms (formally Bi<sup>1-</sup>) and 2D square sheet of four-bonded Bi atoms in square planar environment, (thus formally to Bi<sup>1-</sup>) having non-classical coordination geometry. The BaBi<sub>2</sub> structure is different from that of YbSb<sub>2</sub> ( $Cmcm$ , ZrSi<sub>2</sub> type) [8] and belong actually to the HfGa<sub>2</sub> structure type, [4] but it can also be seen as a distorted variant of the ZrSi<sub>2</sub> structure type. [4] Another example of bismuthide with HfGa<sub>2</sub> structure type is EuBi<sub>2</sub>. [29] There are two and one independent Bi and Ba positions, respectively. The Ba atoms are positioned as spacers between two zigzag chains and the four membered rings of the square sheet.

Within the 1D zigzag chains formed by Bi1 atoms (Figure 4.10a), the Bi1–Bi1 contacts of 3.257(3) Å are in the range of a single bond distance. Bi–Bi bond lengths of 3.286(4) Å and 3.152(3) Å were reported for Bi<sub>4</sub><sup>4-</sup> square and Bi<sub>2</sub><sup>4-</sup> dumbbell of Ba<sub>11</sub>Bi<sub>10</sub>, respectively. The Bi–Bi–Bi bond angle within the 1D zigzag chain is 100.7(1)°, which is smaller than 109.9° expected for an ideal tetrahedron (Table 4.6). This is due to the presence of two lone pairs per Bi<sup>-</sup> anion.

The 2D Bi square nets normal to the c-axis are formed by Bi2 atoms (Figure 4.10b). The Bi–Bi separation of 3.549(1) Å is too long to be considered as single bond distance. It is even longer than the Bi–Bi distance in other square net like in the isostructural EuBi<sub>2</sub> (3.344 Å). The Bi–Bi distance of 3.380(2) Å for the four-bonded Bi in Ba<sub>2</sub>Bi<sub>3</sub> and 3.397 Å in the linear trimer Bi<sub>3</sub><sup>7-</sup> in Eu<sub>14</sub>MnBi<sub>11</sub> [18] are also significantly shorter; but in BaBi<sub>3</sub> where the interactions are assumed to be metallic, somewhat longer bond distances are found (3.658(1) Å and 3.668(1) Å). [4] Nevertheless, the Bi–Bi interactions within the square nets in BaBi<sub>2</sub> may be electron-rich multicenter bonding with unusual long Bi–Bi distance which is due to a mere packing effects. Also the large ADPs of Bi2 atoms may arise from bond frustrations originated from the same packing effects. The Bi–Bi–Bi angles are 89.93(1)° and 176.1(1)°, respectively, which diverge from those for an ideal 2D square net, indicating that the sheets are slightly puckered. Similar square sheets have been reported in EuBi<sub>2</sub> and many Sb analogues are known in, e.g. YbSb<sub>2</sub>.

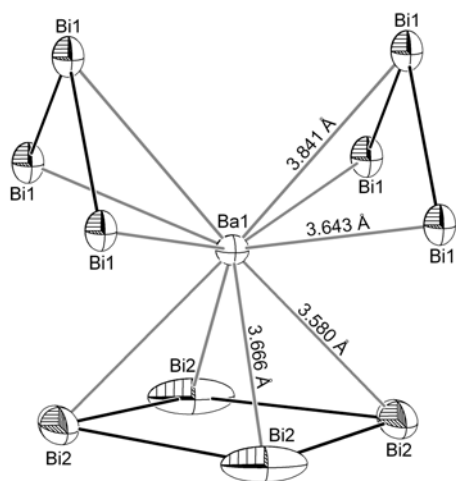


**Figure 4.11** The coordination geometry around Ba atom in BaBi<sub>2</sub> (the thermal ellipsoids at 50% probability level)

The Ba coordination by the ten closest Bi atoms (up to 4 Å) is represented in [Figure 4.11](#) and it shows the Ba1 atoms capping the Bi2 square of the 2D net and, being sandwiched between two Bi1 chains.

Interestingly, the orientation of the 1D Bi zigzag chains in the structure of CaBi<sub>2</sub> [\[7, 30\]](#) (ZrSi<sub>2</sub>-type, Cmcm) is only along one direction (c-axis of the orthorhombic lattice) whereas the corresponding Bi zigzag chains in BaBi<sub>2</sub> have two orientations, along a- and b-axis, alternatively; this is due to the higher symmetry for HfGa<sub>2</sub>-type of BaBi<sub>2</sub>. The electron count scheme for BaBi<sub>2</sub> can be easily developed by using both the classical Zintl concept in 1D units and the electron-rich multicenter bonding in the 2D square nets. Hence, BaBi<sub>2</sub> can be formulated as Ba<sup>2+</sup>(2b-Bi<sup>1-</sup>)<sub>chain</sub>(4b-Bi<sup>1-</sup>)<sub>square</sub> (2b- and 4b- denote two- and four-connected atom, respectively).

The compound BaBi<sub>2</sub> nicely illustrates the bonding type transition from localized 2c-2e covalent bond in the zigzag chain with two-bonded (Bi1)<sup>1-</sup> atoms as predicted by the Zintl concept, to electron-rich multicenter bonding in the 2D square net with four-bonded (Bi2)<sup>1-</sup> atoms in a non-classical square planar environment. Here, two bond types (localized and delocalized) occur in two different subunits of the structure. In the previously described phase Ba<sub>2</sub>Bi<sub>3</sub> the same atom interacts simultaneously with its different neighbours with either localized or delocalized bonds.

## 4.4 Literature

- [1] Fässler, T. F.; Hoffmann, S. *Z. Kristallogr.* **1999**, *214*, 722.
- [2] Miller, G. J. In *Chemistry, Structure and Bonding of Zintl Phases and Ions*; Kauzlarich, S. M., Ed.; VCH Publishers: New York, 1996.
- [3] Cromer, D.T. *Acta Cryst.* **1959**, *12*, 41-45.
- [4] Villars, P.; Calvert, L. D. *Pearsons Handbook of Crystallographic Data for Intermetallic Compounds*, 2nd ed.; ASM International: Materials Park, OH, 1991; Desk Edition, 1997.
- [5] Deller, K.; Eisenmann, B. *Z. Naturforsch. B*, **1978**, *33*, 676.
- [6] (a) Deller, K.; Eisenmann, B. *Z. Naturforsch. B*, **1976**, *31*, 1146. (b) Deller, K.; Eisenmann, B. *Z. Anorg. Allg. Chem.*, **1976**, *425*, 104.
- [7] Merlo, F.; Fornasini, M. L. *Mater. Res. Bull.* **1994**, *29*, 149.
- [8] Wang, R.; Bodnar, R.; Steinfink, H. *Inorg. Chem.* **1966**, *5*, 1468.
- [9] Papoian, G. A.; Hoffmann, R. *Angew. Chem. Int. Ed.* **2000**, *39*, 2408.
- [10] (a) Eisenmann, B. *Z. Naturforsch. B*, **1979**, *34*, 1162. (b) Eisenmann, B.; Jordan, H.; Schäfer, H. *Naturforsch. B*, **1985**, *40*, 1603.
- [11] Deller, K.; Eisenmann, B. *Z. Naturforsch. B*, **1976**, *31*, 29.
- [12] Derrien, G.; Tillard-Charbonnel, M.; Manteghetti, A.; Monconduit, L.; Belin, C. *J. Solid State Chem.* **2002**, *164*, 169.
- [13] Rieger, W.; Nowotny, H.; Benesovsky, F. *Monatshefte für Chemie* **1966**, *97*, 378.
- [14] Morgan, M. G.; Wang, M.; Chan, W. Y.; Mar, A. *Inorg. Chem.* **2003**, *42*(5), 1549.
- [15] (a) Kjekshus, A. *Acta Chem. Scand.* **1972**, *26*, 1633. (b) Garcia, E.; Corbett, J.D. *J. Solid State Chem.* **1988**, *73*, 440. (c) Garcia, E.; Corbett, J. *J. Solid State Chem.* **1988**, *73*, 452.
- [16] Eberle, D.; Schubert, K. *Z. Metallkd.* **1968**, *59*, 306.
- [17] Haase, M. G.; Block, H.; Jeitschko, W. *Z. Anorg. Allg. Chem.* **2001**, *627*, 1941.
- [18] Chan, J. Y.; Wang, M. E.; Rehr, A.; Kauzlarich, S. M.; Webb, D. J. *Chem. Mater.* **1997**, *9*, 2131.
- [19] Chi, L.; Corbett, J.D. *J. Solid State Chem.* **2001**, *162*, 327.
- [20] Mills, A. M.; Mar, A. *Inorg. Chem.* **2000**, *39*, 4599.
- [21] Mills, A.M.; Deakin, L.; Mar, A. *Chem. Mater.* **2001**, *13*, 1778.
- [22] Nesper, R. *Prog. Sol. St. Chem.* **1990**, *20*, 1.
- [23] Mills, A. M.; Lam, R.; Ferguson, M. J.; Deakin, L.; Mar, A. *Coord. Chem. Rev.* **2002**, *233-234*, 207.
- [24] Papoian, G.; Hoffmann, R. *J. Am. Chem. Soc.* **2001**, *123*, 6600.
- [25] (a) Fässler, T. F. *Chem. Soc. Rev.* **2003**, *32*, 80-86. (b) Fässler, T. F.; Kronseder, C. *Angew. Chem.* **1997**, *109*, 2800. *Angew. Chem. Int. Ed. Engl.* **1997**, *36*, 2683
- [26] Newns, D.M.; Krishnamurthy, H.R.; Pattnaik, P.C.; Tsuei, C.C.; Chi, C.C.; Kane C.L. *Physica B* **1993**, *801*, 186.
- [27] Miller, G. J. *Eur. J. Inorg. Chem.* **1998**, 523-536.
- [28] Mudring, A-V.; Nuss, J.; Wedig, U.; Jansen, M. *J. Solid State Chem.* **2000**, *155*, 29-36
- [29] Sun, Z.-M.; Mao J.-G. *J. Solid State Chem.* **2004**, *177*, 3752-3756
- [30] Ponou, S.; Fässler, T.F. GDCh-Jahrestagung, München, Oktober **2003**, Abstract book, p.168.

## 5. Substitution effects in Zintl phases of the Na/Sn phase system

### 5.1. Introduction

Depending on the atomic ratio Na/Sn, the dimensionality of the tin network in binary phases can vary from 0-D to 3-D (see Table 5.1), and the Sn-Sn bonding ranges from localized two-center-two-electron (2c-2e) bonds to purely metallic bond. In the Na/Sn binary phases, the discrete tin units (0-D) are observed in the compounds  $\text{Na}_4\text{Sn}$  [1] and  $\text{Na}_{15}\text{Sn}_4$  [2] containing isolated Sn atoms,  $\text{Na}_9\text{Sn}_4$  [2] with dimeric  $\text{Sn}_2$ -dumbbells, and  $\beta\text{-Na}_4\text{Sn}_4$  [3] with tetrahedral  $[\text{Sn}_4]^{4-}$  anions. Two-dimensional tin networks are found for the phases  $\text{Na}_7\text{Sn}_{12}$  [4] and  $\text{NaSn}_2$  [5] featuring the polyanions  ${}_{\infty}^2[\text{Sn}_{12}]^{7-}$  and  ${}_{\infty}^2[\text{Sn}_8]^{4-}$ , respectively, which are separated by layers of sodium cations. Finally, a three-dimensional tin network is found in  $\text{Na}_5\text{Sn}_{13}$  [6] and in the Sn richest phase  $\text{NaSn}_5$ . [7] The Zintl-Klemm concept can be applied to the low dimensional phases (0D to 2D) to describe their electronic structure. But the three dimensional phase,  $\text{Na}_5\text{Sn}_{13}$  [6] can be described as a Zintl phase only if the one assumes that the long Sn-Sn contact of 3.61 Å is consistent with covalent bonding. However, many structural descriptions of polymeric tin frameworks as well as very recent quantum calculations suggest that covalent Sn-Sn distances ought to be less than 3.1 Å. [8-10] In elemental tin, the Sn-Sn contact in semi-conducting  $\alpha\text{-Sn}$  is about 2.810 Å and in metallic  $\beta\text{-Sn}$  they are two different contacts at 3.016 Å and 3.175 Å. Therefore the classification of the compounds  $\text{Na}_5\text{Sn}_{13}$  as Zintl phase remains questionable. The second 3D phase,  $\text{NaSn}_5$  [7] features planar quadratic Sn-net and pentagon-dodecahedra fragment as main structural motifs. Here, the Zintl-Klemm concept is not applicable, but both covalent and metallic contacts are encountered in the Sn substructure. The structural motifs of both the covalent bonded  $\alpha\text{-Sn}$  and the metallic  $\beta\text{-Sn}$  occur in units of four-fold covalently bonded Sn with Sn-Sn distances as in  $\alpha\text{-Sn}$ , and in quadratic nets of five-fold coordinated Sn atoms with Sn-Sn distances as in  $\beta\text{-Sn}$ , respectively.

Table 5.1 Summary of the important crystallographic data and structural motif of sodium stannides known up to date with emphasis on atomic distances

Compounds	Space Group	Unit cell parameters /Å; Volume /Å <sup>3</sup>	Type	Pearson symbol	Structural motif	d(Sn-Sn) /Å	d(Na-Sn) /Å	d(Na-Na) /Å	Litt.
<b>Na<sub>4</sub>Sn</b>	Pnam	a = 9.744(3); b = 22.751(10); c = 5.539(2) V = 1227.92, Z = 8	own	oP40	Isolated Sn-anions		≥ 3.130(7)	≥ 3.086(7)	[1]
<b>Na<sub>3.7</sub>Sn</b>	Prma	a = 9.82(2); b = 5.57(1) c = 22.79(4) V = 1246.55(43), Z = 8	own	oP40-2.42	Isolated Sn-anions		≥ 3.16	≥ 3.06	[2]
<b>Na<sub>15</sub>Sn<sub>4</sub></b>	I43d	a = 13.14(2) V = 2268.75(45), Z = 4	Cu <sub>15</sub> Si <sub>4</sub>	cl76	Isolated Sn-anions		≥ 3.24	≥ 3.26	[2]
<b>Na<sub>9</sub>Sn<sub>4</sub></b>	Cmcm	a = 5.42(1); b = 9.39(2) c = 29.62(6) V = 1507.47(53), Z = 4	Li <sub>9</sub> Ge <sub>4</sub>	oC52	Sn <sub>2</sub> -Dumbbells	2.83 and 2.86	≥ 3.18	≥ 3.01	[2]
<b>β-Na<sub>4</sub>Sn<sub>4</sub></b>	I4 <sub>1</sub> /acd	a = 10.46(2) c = 17.39(3) V = 1902.7(5), Z = 8	NaPb	tl64	Sn <sub>4</sub> <sup>4-</sup> -Tetrahedra	2.967(2)	≥ 3.35(2)	≥ 3.62(2)	[3]
<b>Na<sub>7</sub>Sn<sub>12</sub> (NaSn<sub>1.7</sub>)</b>	P2/h	a = 13.375(3) b = 9.329(2); β = 90.15(3)° c = 17.976(4) V = 2243.0(8), Z = 4	own	mP78	2D-polyanions 2 [Sn <sub>12</sub> <sup>7-</sup> ] <sub>∞</sub>	2.827(2) to 3.088(2)	≥ 2.91(2) <sup>[b]</sup> ≥ 3.14(2) <sup>[b]</sup> and ≥ 3.19(1)	≥ 3.49(2)	[4]
<b>NaSn<sub>2</sub></b>	C2/m	a = 13.423(3) b = 6.870(2); β = 102.56(3)° c = 15.566(3) V = 1401.1(5), Z = 16	own	mC48	2D Polyanions of Realgar-Type Units [Sn <sub>8</sub> <sup>4-</sup> ]	2.832(1) to 2.9750(8)	≥ 3.121(3)	≥ 3.44(1)	[5]
<b>Na<sub>5</sub>Sn<sub>13</sub> (NaSn<sub>2.6</sub>)</b>	Cmcm	a = 8.979(1); b = 19.448(6) c = 50.43(2) V = 8806(2), Z = 16	own	oC288	3D-network from planar units of pentagonal rings and As <sub>4</sub> S <sub>5</sub> analogue $3 \left[ \text{Sn}^0 \right]_8 \left( \text{Sn}^{1-} \right)_5$	2.80 to 2.98 and 3.61 <sup>[a]</sup>	≥ 3.16	≥ 3.38(4)	[6]
<b>NaSn<sub>5</sub></b>	P4 <sub>2</sub> /m	a = 6.2850(1) c = 8.794(2) V = 347.4(1), Z = 2	own	tP12	3D-network from quadratic Sn-net and dodecahedra fragments	2.810 to 3.143	≥ 3.35(2)	≥ 3.62(2)	[7]

[a] This long distance is considered to be bonding to allow the description of the compound as Zintl-phase; [b] distance involving a Na split position

Thus, a transition from classical Zintl phases to polar intermetallic compounds in the Na/Sn systems is observed at increasing tin content and the border seems to correspond to Sn:Na atomic ratio larger than that of the phase  $\text{Na}_5\text{Sn}_{13}$  (Sn/Na = 2.6) which itself can be virtually considered to be a borderline compound. Therefore to gain a deeper insight into the transition from valence compounds to intermetallics in this system, we have embarked on accessing the structural stability of  $\text{Na}_5\text{Sn}_{13}$  toward an increase of  $x$  using partial substitutions. Two different approaches have been used in which the substitutions are made in cationic or in anionic substructures, respectively. Attempts were made firstly to substitute one Na with Sr in nominal composition  $\text{SrNa}_4\text{Sn}_{13}$  and, secondly to substitute one Sn with Bi according to the nominal composition  $\text{Na}_5\text{Sn}_{12}\text{Bi}$ .

## 5.2. Synthesis and crystal structure refinement of the phase $\text{Sr}_\delta\text{Na}_{5+x}\text{Sn}_{13}$

### 5.2.1 Synthesis and characterization

The compound  $\text{Sr}_\delta\text{Na}_{5+x}\text{Sn}_{13}$  was obtained from a mixture of elements Sr:Na:Sn with the composition of 1:4:13. The reaction was designed to optimize the electron count in the Zintl phase  $\text{Na}_5\text{Sn}_{15}$  which may alternatively be considered to be formally one electron deficient. The mixture was heated up to 800°C at the rate of 120°C/h, kept there for 12 h, then quenched at room temperature and subsequently annealed at 270°C for 14 days. The product is air and moisture sensitive and crystallized as irregular silvery crystals with needle shape.

### 5.2.2 Crystal structure refinement

Needle shape single crystals were selected from the product and checked for singularity. The best one was used for full data collection on the Enraf-Nonius CCD at room temperature with a crystal detector distance of 40 mm. The crystallographic data as well as the structure refinement data are summarized in [Table 5.2](#) and the atomic positions and thermal displacement parameters (ADPs) are listed in [Tables 5.3](#). The unit cell parameters and systematically absent reflections were consistent with the orthorhombic unit cell, space group *Cmcm*, similar to those reported by Corbett.<sup>[6]</sup> After the structure was solved by direct method, Sn and Na atomic positions were assigned on the basis of peak height and atomic distances. The

resulting model was roughly in agreement with the previous. Two additional maxima of electron density were visible on the residual map, but with quite small peak heights. The two positions were assigned to Na and the occupancies were refined. This resulted in under-occupancy of about 45% at one position (site 8f) and 43% at the other (site 16h). The distance between the two sites is very short, about 1.744 Å, meaning they can't be simultaneously occupied. Thus, the occupancies at those two positions were fixed to 50% resulting in relatively large ADPs for both. In addition, another Na position shows very small anisotropic ADPs and was refined as a Na/Sr mixed-occupied site, giving nearly 8% Sr occupancy. No significant Sr occupancy was observed at other Na positions. The final residual factor were  $R_1 = 0.027$  and  $wR_2 = 0.047$  for all data, with an essentially featureless residual map.

**Table 5.2** Crystallographic data and refinement parameters for  $\text{Sr}_{0.08(1)}\text{Na}_{5.67}\text{Sn}_{13}$

Empirical formula	$\text{Sr}_{0.08(1)}\text{Na}_{5.67}\text{Sn}_{13}$
Formula weight	1680.41
Temperature	293(2) K
Crystal size	0.05×0.1×0.2 mm <sup>3</sup>
Diffractometer	Nonius Kappa CCD
Crystal system	Orthorhombic
Space group	Cmcm (Nr. 63)
Unit cell parameters	a = 8.995(1) Å, b = 19.453(1) Å c = 50.433(2) Å
Unit cell Volume	8824.8(5) Å <sup>3</sup>
Z	16
Density calculated	5.059 g/cm <sup>3</sup>
Absorption coefficient (Mo K $\alpha$ )	14.715 mm <sup>-1</sup> ( $\lambda = 0.71073$ Å)
Absorption correction	empirical
F(000)	11447
Theta range	1.62° ≤ $\theta$ ≤ 19.11°
Resolution range	5.00 - 0.83 Å
Index range	-6 ≤ h ≤ 6, -16 ≤ k ≤ 16, -45 ≤ l ≤ 45
Integrated reflections	7140 ( $R_\sigma = 0.029$ )
Independent reflections	2625 ( $R_{\text{int}} = 0.015$ )
Refinement method	Full-matrix least-squares on F <sup>2</sup>
Parameters / restraints	210 / 0
Goodness of fit on F <sup>2</sup>	1.139
Observed reflections [ $I > 2\sigma(I)$ ]	1390
Final R indices	$R_1 = 0.022$ , $wR_2 = 0.045$
Final R indices (all data)	$R_1 = 0.027$ , $wR_2 = 0.047$
Weighting schema	a = 0, b = 208.63
Residual map [ $e^- / \text{Å}^3$ ]	0.68 and -0.65

**Table 5.3a** Atomic coordinates and equivalent isotropic displacement parameters ( $U_{\text{eq}}$ )\* for  $\text{Sr}_\delta\text{Na}_{5+x}\text{Sn}_{13}$  (standard deviation in parentheses)

Atom	Wyck.	s.o.f.	x	y	z	$U_{\text{eq}}/\text{\AA}^2$
Sn1	8f	1	0	0.09831(7)	0.55063(3)	0.0217(5)
Sn2	8f	1	$\frac{1}{2}$	0.00012(7)	0.65221(3)	0.0208(5)
Sn3	8f	1	0	0.22021(7)	0.58176(3)	0.0217(5)
Sn4	8f	1	$\frac{1}{2}$	0.22829(7)	0.53900(3)	0.0249(5)
Sn5	8g	1	0.3338(2)	0.21095(7)	$\frac{3}{4}$	0.0213(5)
Sn6	8f	1	$\frac{1}{2}$	0.12883(7)	0.58073(3)	0.0239(5)
Sn7	8f	1	0	0.15938(7)	0.67808(3)	0.0200(5)
Sn8	8f	1	0	0.91717(7)	0.69093(3)	0.0211(5)
Sn9	16h	1	0.7539(1)	0.97123(5)	0.72083(2)	0.0205(4)
Sn10	16h	1	0.2659(1)	0.03124(5)	0.56850(2)	0.0216(4)
Sn11	16h	1	0.2365(1)	0.97243(5)	0.62179(2)	0.0198(4)
Sn12	16h	1	0.2986(1)	0.91484(5)	0.53114(2)	0.0283(4)
Sn13	8f	1	0	0.07159(8)	0.49369(3)	0.0318(5)
Sn14	16h	1	0.1605(1)	0.82786(5)	0.62228(2)	0.0238(4)
Sn15	8f	1	0	0.02564(7)	0.65323(3)	0.0193(5)
Sn16	8f	1	$\frac{1}{2}$	0.14002(7)	0.66980(3)	0.0231(5)
Sn17	8f	1	$\frac{1}{2}$	0.90717(7)	0.69693(3)	0.0224(5)
Sn18	16h	1	0.2633(1)	0.11738(5)	0.70651(2)	0.0198(4)
Sn19	16h	1	0.2633(1)	0.29734(5)	0.56674(2)	0.0231(4)
Na1	4c	1	$\frac{1}{2}$	0.0579(5)	$\frac{3}{4}$	0.013(3)
Na2	16h	0.92(1)	0.2422(5)	0.1552(2)	0.6248(1)	0.032(3)
Sr2	16h	0.08(1)	0.2422(5)	0.1552(2)	0.6248(1)	0.032(3)
Na3	8f	1	0	0.9204(3)	0.5740(1)	0.017(2)
Na4	8f	1	$\frac{1}{2}$	0.9307(4)	0.4795(1)	0.036(3)
Na5	4c	1	0	0.8586(5)	$\frac{3}{4}$	0.034(4)
Na6	4c	1	0	0.0865(6)	$\frac{3}{4}$	0.041(4)
Na7	8f	1	$\frac{1}{2}$	0.8048(4)	0.6428(2)	0.043(3)
Na8	8f	1	$\frac{1}{2}$	0.9043(4)	0.5858(2)	0.042(3)
Na9	4c	1	$\frac{1}{2}$	0.8038(7)	$\frac{3}{4}$	0.069(5)
Na10	16h	1	0.2850(7)	0.2842(3)	0.6872(1)	0.045(2)
Na11	8f	0.5	$\frac{1}{2}$	0.247(1)	0.4788(4)	0.097(9)
Na12	16h	0.5	0.325(2)	0.279(1)	0.4875(3)	0.103(6)

(\*)  $U_{\text{eq}}$  is defined as one third of the trace of the orthogonalized  $U^{\text{ij}}$  tensor

**Table 5.3b** Atomic anisotropic displacement parameters ( $\text{\AA}^2$ ) for  $\text{Sr}_\delta\text{Na}_{5+x}\text{Sn}_{13}$  (standard deviation in parentheses)

Atom	$U_{11}$	$U_{22}$	$U_{33}$	$U_{12}$	$U_{13}$	$U_{23}$
Sn1	0.026(1)	0.018(1)	0.022(1)	–	–	-0.0013(8)
Sn2	0.022(1)	0.022(1)	0.019(1)	–	–	-0.0025(8)
Sn3	0.022(1)	0.019(1)	0.025(1)	–	–	-0.0014(8)
Sn4	0.027(2)	0.023(1)	0.025(1)	–	–	0.0003(8)
Sn5	0.026(2)	0.017(1)	0.020(1)	0.0020(9)	–	–
Sn6	0.025(1)	0.024(1)	0.023(1)	–	–	-0.0001(8)
Sn7	0.019(1)	0.018(1)	0.022(1)	–	–	0.0019(8)
Sn8	0.024(1)	0.016(1)	0.023(1)	–	–	-0.0003(8)
Sn9	0.020(1)	0.021(1)	0.021(1)	0.0011(6)	0.0005(6)	-0.0010(5)
Sn10	0.024(1)	0.018(1)	0.024(1)	-0.0008(6)	0.0028(6)	0.0012(5)
Sn11	0.019(1)	0.021(1)	0.020(1)	-0.0017(6)	0.0009(6)	-0.0030(5)
Sn12	0.038(1)	0.022(1)	0.024(1)	0.0003(7)	0.0060(6)	-0.0013(5)
Sn13	0.041(2)	0.035(1)	0.019(1)	–	–	0.0010(8)
Sn14	0.023(1)	0.021(1)	0.027(1)	0.0037(6)	-0.0040(6)	0.0033(6)
Sn15	0.020(1)	0.020(1)	0.018(1)	–	–	-0.0020(7)
Sn16	0.023(2)	0.021(1)	0.026(1)	–	–	0.0017(8)
Sn17	0.024(1)	0.018(1)	0.026(1)	–	–	-0.0010(8)
Sn18	0.020(1)	0.020(1)	0.020(1)	0.0005(6)	-0.0014(5)	-0.0001(6)
Sn19	0.021(1)	0.018(1)	0.030(1)	-0.0009(6)	-0.0007(6)	-0.0015(6)
Na1	0.002(9)	0.015(7)	0.021(6)	–	–	–
Na2	0.033(5)	0.033(4)	0.030(3)	0.006(3)	0.002(3)	0.001(2)
Sr2	0.033(5)	0.033(4)	0.030(3)	0.006(3)	0.002(3)	0.001(2)
Na3	0.005(6)	0.016(5)	0.031(5)	–	–	-0.005(4)
Na4	0.046(8)	0.040(6)	0.023(5)	–	–	-0.004(4)
Na5	0.05(1)	0.029(8)	0.024(7)	–	–	–
Na6	0.02(1)	0.06(1)	0.037(8)	–	–	–
Na7	0.039(8)	0.050(6)	0.039(5)	–	–	-0.001(5)
Na8	0.033(8)	0.042(6)	0.051(6)	–	–	-0.002(5)
Na9	0.09(1)	0.06(1)	0.054(9)	–	–	–
Na10	0.050(6)	0.032(4)	0.053(4)	-0.013(4)	-0.004(4)	0.005(3)
Na11	0.16(3)	0.08(2)	0.05(1)	–	–	0.014(1)
Na12	0.12(2)	0.12(2)	0.07(1)	-0.022(1)	-0.045(1)	0.003(1)

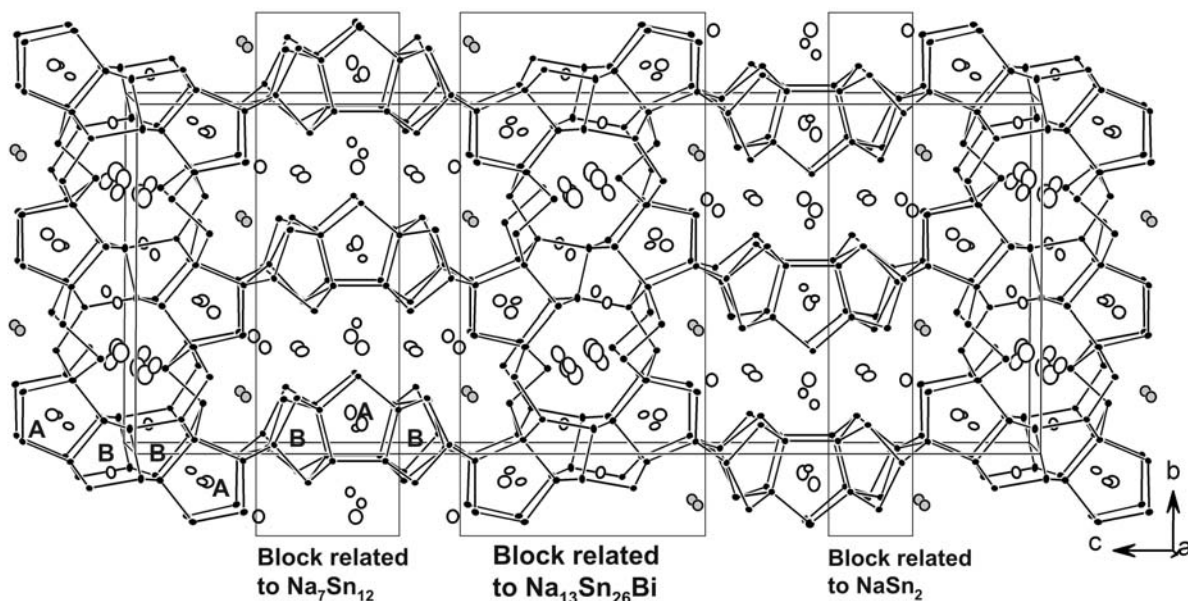


**Figure 5.1** Projection of the crystal structure of  $\text{Sr}_6\text{Na}_{5+x}\text{Sn}_{13}$  in the (100) plane showing its partition into blocks. Sn atoms black, Na opened circles, respectively.

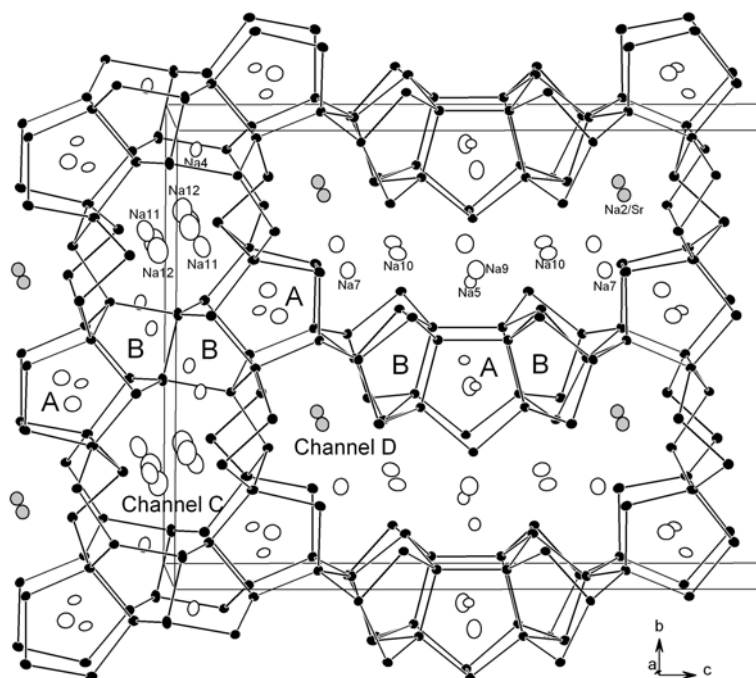


**Figure 5.2** A perspective view of a segment of  $\text{Sr}_6\text{Na}_{5+x}\text{Sn}_{13}$  structure with emphasis on largest channels C and D (with crescent-like shape). Sn atoms black, Na opened circles and Na/Sr mixed, grey. (Thermal ellipsoids at 50% probability level)

### 5.2.3 Description of the Structure of $\text{Sr}_{0.08(1)}\text{Na}_{5.67}\text{Sn}_{13}$

A detailed description of the structure of  $\text{Na}_5\text{Sn}_{13}$  can be found in reference [6]. For the novel  $\text{Sr}_{0.08}\text{Na}_{5.67}\text{Sn}_{13}$  a pictorial representation of the structure is given in Figure 5.1. It contains 19 independent tin and 12 sodium atomic positions. Only 10 atomic positions for sodium were found in  $\text{Na}_5\text{Sn}_{13}$ . At first glance, the structure of  $\text{Sr}_{0.08}\text{Na}_{5.67}\text{Sn}_{13}$  can be roughly divided into two blocks formed by two different building units. These building units are made up by two basic structural motifs, the  $\text{Sn}_5$  pentagon unit (forming the type A channel in Figure 5.2) and the realgar-like ring (forming the type B channel) and, they are both condensed in two different ways to form the building units of the compound that are in turn distributed into the two different alternating blocks in the structure.

The  $\text{Sn}_5$  pentagons are wrenched to achieve the interconnection with their apical atoms, and they contain four formally neutral 4-bonded tin (4b-Sn) atoms and a 3-bonded apex tin atom that is formally  $\text{Sn}^-$  (Figure 5.3b). The smaller ring forming the empty channels (type B) can be derived from the mineral Realgar,  $\beta\text{-As}_4\text{S}_4$ ,<sup>[11]</sup> or from Hittorf's phosphorus [ $\text{P}_8$ ] units.<sup>[12]</sup>

The first building unit has four condensed channels of two different types A and B that are condensed in the *c*-direction, with sequence ABBA (Figure 5.3a). A similar structural motif is found in  $\text{Na}_{13}\text{Sn}_{26}\text{Bi}$  (see § 5.3), but with some outstanding differences. In the second building unit, two rows of edge sharing tetrahedra sandwich one column of  $\text{Sn}_5$  pentagons in the way that each  $\text{Sn}_5$  pentagon is surrounded by four of such tetrahedra. The resulting structural component has three condensed channels of two types A and B with sequence BAB (Figure 5.4a). It is related to the building unit of  $\text{Na}_7\text{Sn}_{12}$  where the two types of rings are found with the sequence AB. The ring of the type B channel alone defines the basic motive of the compound  $\text{NaSn}_2$ . Sidewise bridging along *b*-direction of the basic component with channel sequence ABBA, through additional tri-coordinated Sn atoms that are positioned between them defines the large type C channel (Figure 5.2). On the other hand, the second basic component BAB is directly connected to the earlier, yielding in the largest type D channel with crescent-like shape. The type C channels are filled with two under-occupied Na positions, but are empty in  $\text{Na}_5\text{Sn}_{13}$ .

The shortest Sn–Sn distances (Table 5.4) in this compound are between 2.840(2) Å and 2.990(3) Å and are assumed to correspond to covalent bonds. The long contact

of 3.624(2) Å (Sn12–Sn12 in [Figure 5.3b](#)) between two  $\text{Sn}_5$  pentagons was assumed to be a single bond in  $\text{Na}_5\text{Sn}_{13}$  in order to be an electron precise Zintl phase. In  $\text{Sr}_\delta\text{Na}_{5+x}\text{Sn}_{13}$  two additional Na positions are found in the type C channel. Considering only the shortest Sn-Sn contacts (2.840(2) and 2.990(3) Å), an anionic network with six three bonded (3b) and seven 4b-atoms per formula unit results. The number of Na ought to be equal to that of 3b-Sn atoms in the structure, i.e. the phases with the composition  $\text{Sr}_\delta\text{Na}_{6-2\delta}\text{Sn}_{13}$  will correspond to electron precise Zintl phases and therefore, the actual composition,  $\text{Sr}_{0.08}\text{Na}_{5.67}\text{Sn}_{13}$ , indicates an electron-poor Zintl phase which is 0.17 electron short with respect to 8-N rule. The electron deficiency is most likely due to the defect (50% maximum occupancy) of two split cationic sites with very short Na-Na contacts (1.73 and 2.16 Å).

As might be expected from electrostatic arguments, the edges of the filled channels are nearly all defined by  $3\text{b-Sn}^-$  atoms, and the sodium cations are closest in proximity to the charged tin atoms rather than the formally neutral 4b-Sn ([Table 5.4](#)). The shortest Na-Sn interaction distance is 3.06(2) Å and the similar Na-Na distance is 3.16(4) Å. Both are in the range of those observed in other Na/Sn phases (see [Table 5.1](#)).

**Table 5.4** Atomic distances (< 3.6 Å) in  $\text{Sr}_{0.08(1)}\text{Na}_{5.67}\text{Sn}_{13}$  (standard deviations are in parentheses)

Atom pair	distance/ Å	Atom pair	distance/ Å	Atom pair	distance/ Å
Sn1 - Sn3	2.844(2)	Sn12 - Sn19	2.960(1)	Na3 - Sn19	3.224(5) x2
- Sn10	2.870(1) x2	- Sn10	2.961(1)	- Sn10	3.232(5) x2
- Sn13	2.918(2)	- Sn13	2.975(1)	- Sn14	3.356(6) x2
Sn2 - Sn16	2.863(2)	- Na4	3.187(6)	- Sn11	3.372(5) x2
- Sn11	2.874(1) x2	Sn13 - Sn13	2.857(3)	- Sn13	3.416(7)
- Sn17	2.891(2)	- Sn1	2.918(2)	- Sn12	3.448(4) x2
Sn3 - Sn1	2.844(2)	- Sn12	2.975(1) x2	- Sn1	3.655(7)
- Sn19	2.904(1) x2	Sn14 - Sn14	2.888(2)	Na4 - Sn12	3.187(6) x2
- Na11	3.12(2)	- Sn11	2.894(2)	- Sn4	3.230(8)
Sn4 - Sn6	2.859(2)	- Sn19	2.944(2)	- Sn6	3.251(7)
- Sn19	2.880(1) x2	- Na7	3.254(3)	- Sn10	3.293(6) x2
- Na11	3.06(2)	Sn15 - Sn8	2.840(2)	- Na4	3.40(2)
Sn5 - Sn18	2.920(1) x2	- Sn11	2.848(2) x2	- Sn12	3.550(7) x2
- Sn5	2.990(3)	- Sn7	2.888(2)	- Sn11	3.549(5)
- Na5	3.240(1)	Sn16 - Sn18	2.855(2) x2	Na5 - Sn9	3.189(4) x2
Sn6 - Sn4	2.859(2)	- Sn2	2.863(2)	- Sn5	3.238(9) x2
- Sn10	2.901(1) x2	- Na2	3.260(5)	- Sn9	3.445(7) x4
- Na2/Sr	3.251(5)	Sn17 - Sn9	2.868(1) x2	Na6 - Sn18	3.284(3) x4
Sn7 - Sn18	2.887(1) x2	- Sn2	2.891(2)	- Sn9	3.477(8) x4
- Sn15	2.888(2)	Sn18 - Sn16	2.855(2)	Na7 - Sn14	3.254(3) x2
- Na7	3.344(8)	- Sn7	2.887(1)	- Sn7	3.344(8)
Sn8 - Sn15	2.840(2)	- Sn5	2.920(2)	- Sn17	3.381(8)
- Sn9	2.877(2) x2	- Sn9	2.937(2)	- Na10	3.431(8)
- Na5	3.236(6)	Sn19 - Sn4	2.880(2)	- Sn3	3.489(8)
Sn9 - Sn17	2.868(1)	- Sn3	2.904(1)	Na8 - Sn11	3.267(6) x2
- Sn8	2.877(2)	- Sn14	2.944(2)	- Sn19	3.295(6) x2
- Sn18	2.937(2)	- Sn12	2.960(2)	- Sn12	3.305(7) x2
- Sn9	2.909(1)	Na1 - Sn9	3.197(5) x4	- Sn10	3.361(6) x2
- Na1	3.197(5)	- Sn18	3.269(4) x4	- Na7	3.46(1) x2
Sn10 - Sn1	2.870(1)	- Sn5	3.332(8) x2	- Sn3	3.586(8) x2
- Sn6	2.901(2)	Na2 - Sn6	3.251(5)	Na9 - Sn17	3.348(8) x2
- Sn11	2.933(2)	- Sn16	3.260(5)	- Sn5	3.504(7) x2
- Sn12	2.961(2)	- Sn3	3.324(5)	Na10 - Sn8	3.236(6)
- Na3	3.232(5)	- Sn7	3.463(5)	- Sn18	3.392(6)
Sn11 - Sn15	2.848(1)	- Sn14	3.473(5)	- Sn14	3.420(6)
- Sn2	2.874(1)	- Sn11	3.559(5)	- Na7	3.431(8)
- Sn14	2.894(2)	- Sn15	3.628(5)	- Sn5	3.499(6)
- Sn10	2.933(1)	Na12 - Na12	3.16(4)	- Sn16	3.518(6)
- Na8	3.267(6)	- Sn4	3.20(2)	- Sn17	3.541(6)
		- Sn19	3.21(2)	- Sn7	3.561(6)
		- Sn4	3.21(2)	Na11 - Sn4	3.06(2)
		- Sn13	3.44(2)	- Sn3	3.12(2)
		- Sn1	3.44(2)	- Sn1	3.36(2)
		- Sn12	3.61(2)	- Sn19	3.41(2) x2

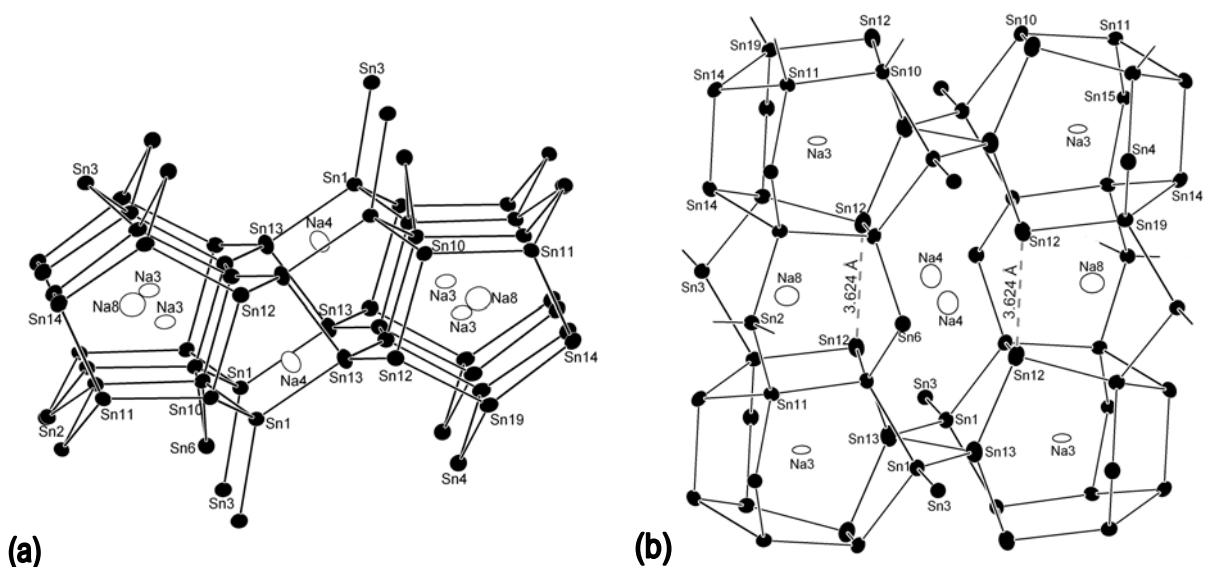


**Figure 5.3** (a) Top view and (b) side view of the four adjoining pentagonal stacks ABBA, parallel and perpendicular to  $a$ -direction, respectively. Sn–Sn contact at 3.624 Å is shown as broken lines. Sn black, Na opened circles (Thermal ellipsoids at 50% probability level)

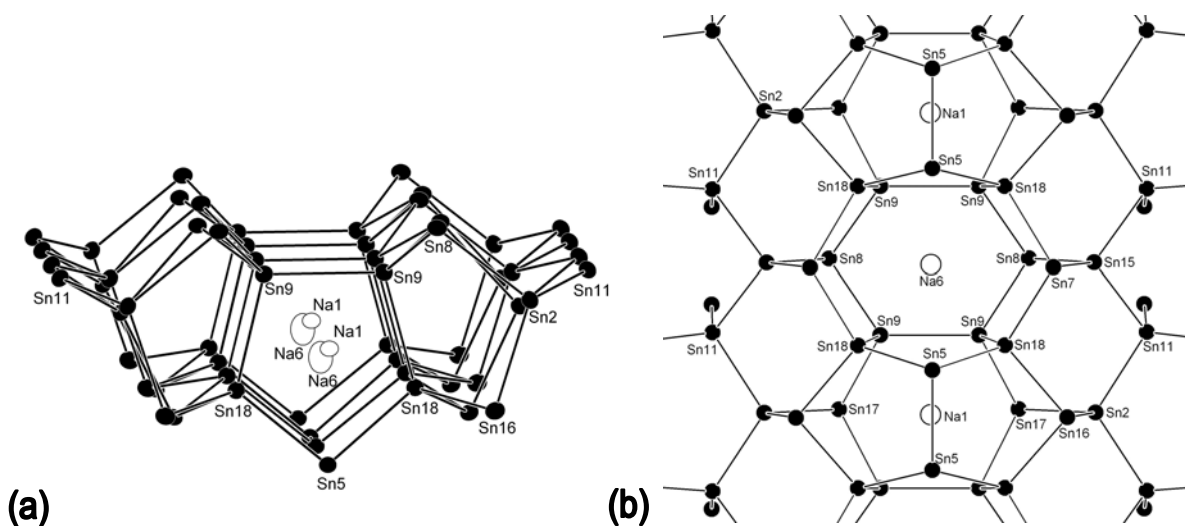


**Figure 5.4** (a) Top view and (b) side view of the three adjoining pentagonal stacks BAB, parallel and perpendicular to  $a$ -direction, respectively. Sn atoms black, Na opened circles.

### 5.3. Multicenter bonding in the novel Zintl phase $\text{Na}_{13-\delta}\text{Sn}_{26-\delta}\text{Bi}_{1+\delta}$ ( $\delta = 0.27$ )

#### 5.3.1 Synthesis and characterization

The compound  $\text{Na}_{13-\delta}\text{Sn}_{26-\delta}\text{Bi}_{1+\delta}$  was obtained from a mixture of elements Na:Sn:Bi with the composition 5:12:1. The mixture was heated at the rate of  $120^\circ\text{C}/\text{h}$  to  $650^\circ\text{C}$ , kept there for 12 h, then cooled at the rate of  $120^\circ\text{C}/\text{h}$  to  $270^\circ\text{C}$  where it is annealed for at least 5 days and, subsequently cooled to room temperature by turning off the oven. The product is air and moisture sensitive and crystallized as irregular silvery crystals. Most of the crystals appear to be twinned (multiple twinning) and not suitable for single crystal diffraction. The X-ray powder diagram of the product (Figure 5.5) compares very well with the theoretical diagram calculated from the structure solution crystal data (see below) however, with some unindexed peaks indicating additional yet unknown phases. The presence of the three elements Sn, Na and Bi was confirmed by EDX analysis, and no eventual contaminant was detected.

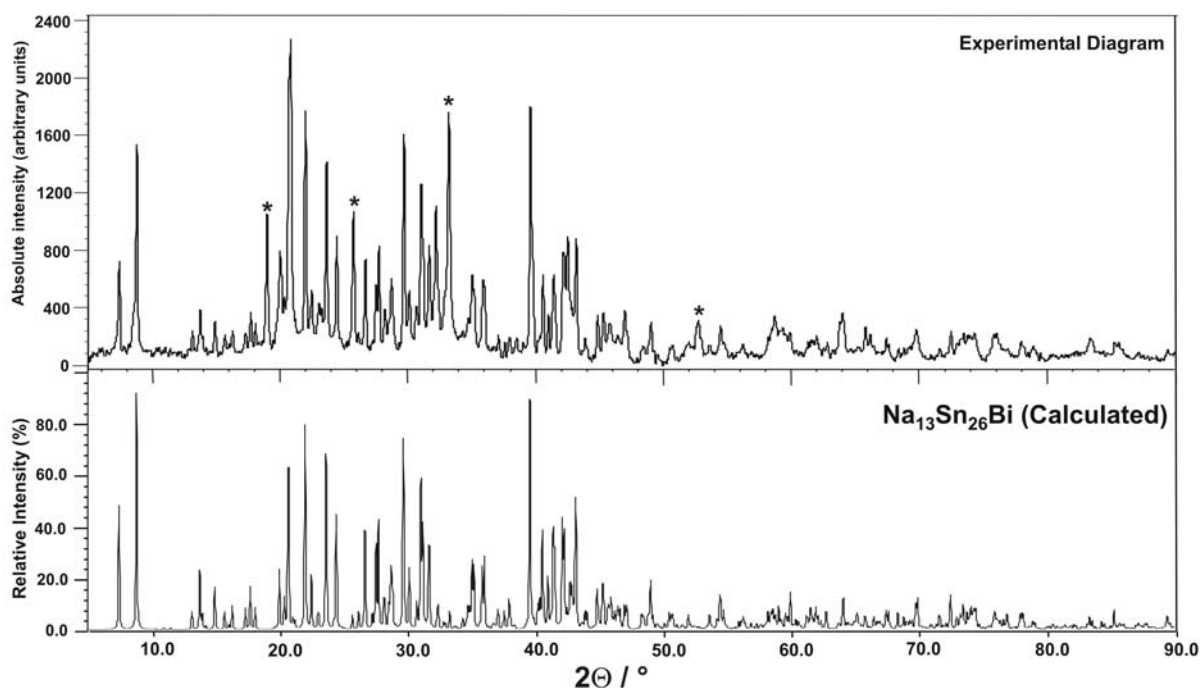


**Figure 5.5** Experimental powder diagram of the reaction product Na:Sn:Bi = 5:12:1 (top) and theoretical powder diagram calculated for  $\text{Na}_{13}\text{Sn}_{26}\text{Bi}$  (bottom). Strongest un-indexed reflections are labeled with stars (\*).

### 5.3.2 Determination of the crystal structure

Needle shape single crystals were selected from the product and checked for singularity. The best one was used for full data collection on the Enraf-Nonius CCD at room temperature with a crystal-detector distance of 40 mm. The crystallographic data as well as the structure refinement data are summarized in [Table 5.5](#) and the atomic positions and equivalent isotropic displacement parameters are listed in [Table 5.6a](#). The unit cell parameters were determined and refined using all the reflections from the 473 collected images. Systematically absent reflections were consistent with the triclinic unit cell, space group  $P\bar{1}$ . The structure was solved by direct method. Bi and Sn positions were assigned on the basis of peak height and atomic distances. Most of the Na positions were found in the difference Fourier map. The two bounded Sn1 shows small thermal ellipsoid with some residual electron density indicating possible Sn-Bi mixed occupancy. The refinement of the mixed occupancy at Sn1 position results in about 13% Bi occupancy. Partial defects were tested for all Na positions, giving significantly lower occupation factors for only two positions (Na2 and Na3) with a total of nearly 10% defect, suggesting a correlation with the Bi/Sn mixed occupied position. The two defect positions Na2 and Na3 are characterized by significantly larger ADPs. The final refinement was done assuming a correlation also because it is consistent with a charge balanced ideal phase  $\text{Na}_{13}\text{Sn}_{26}\text{Bi}$ . The final residual factor were  $R_1 = 0.033$  and  $wR_2 = 0.076$  for all data. The only faint indications of eventual crystallographic errors might be the slight asymmetry of the anisotropic thermal ellipsoid observed for Na1 and Bi1 (see [Table 5.6b](#)). As we will see next, these atoms have very unusual coordination geometry.

### 5.3.3 Structural description of $\text{Na}_{13-\delta}\text{Sn}_{26-\delta}\text{Bi}_{1+\delta}$

A projection of the structure of  $\text{Na}_{13-\delta}\text{Sn}_{26-\delta}\text{Bi}_{1+\delta}$  ( $\delta = 0.27$ ) is represented in [Figure 5.6](#). It forms a new structure type in the Zintl chemistry of Sn which is related to the structure of  $\text{Na}_{5+x}\text{Sn}_{13}$ .<sup>[6]</sup> The structure contains 13 independent Sn, 7 Na and only one Bi position. One Na atom (Na1, site *1b*) and Bi1 (site *1f*) are located on the inversion center. The shortest Sn–Sn contacts in the polyanion vary between 2.827(1) Å and 2.947(1) Å ([Table 5.7](#)). The Sn–Sn bond distances involving the Bi substituted Sn1 position are slightly longer (2.973(1) Å and 2.989(1) Å) as expected

from the bigger atomic size of Bi. Similar Sn–Sn distances are found in Na<sub>5+x</sub>Sn<sub>13</sub> (from 2.843(5) Å to 2.982(5) Å), Na<sub>7</sub>Sn<sub>12</sub> (from 2.827(2) Å to 3.088(2) Å) and NaSn<sub>2</sub> (from 2.833(1) to 2.975(2) Å). Bi1 atom has two contacts at 3.311(1) Å with the three-bonded Sn2 atoms, forming a Sn–Bi–Sn linear fragment. This interaction distance is a quite long when compared with other Bi–Sn single bond distances, like in Ba<sub>2</sub>K<sub>4</sub>(SnBi<sub>4</sub>) (2.927(1) Å) [13] or in K<sub>10</sub>(Sn<sub>2</sub>Bi<sub>6</sub>) (from 2.945(4) Å to 3.013(4) Å). [14] These Bi1–Sn2 contacts are close to the Bi–Sb contact (3.322(1) Å) found in Ba<sub>2</sub>BiSb<sub>2</sub> [15] which correspond to a non-classical multicenter bonding, suggesting a similar bond type within the linear trimer.

**Table 5.5** Crystallographic data and refinement parameters for Na<sub>13-δ</sub>Sn<sub>26-δ</sub>Bi<sub>1+δ</sub>

Empirical formula	Na <sub>12.73</sub> Sn <sub>25.73</sub> Bi <sub>1.27(1)</sub>
Formula weight	3611.29
Temperature	293(2) K
Crystal size	0.05×0.02×0.25 mm <sup>3</sup>
Mosaicity (°)	0.496(2)
Crystal color	Silvery
Diffractometer	Nonius CCD
Crystal system	Triclinic
Space group	<i>P</i> $\bar{1}$
Unit cell parameters	a = 9.0942(1) Å; $\alpha$ = 112.008(1)° b = 11.2637(2) Å; $\beta$ = 99.793(1)° c = 13.2573(2) Å; $\gamma$ = 101.455(1)°
Unit cell Volume	1188.46(3) Å <sup>3</sup>
Z	1
Density calculated	5.046 g/cm <sup>3</sup>
Absorption coefficient (Mo K $\alpha$ )	18.00 mm <sup>-1</sup> ( $\lambda$ = 0.71073 Å)
Absorption correction	empirical
F(000)	1532.0
Theta range	4.08° - 25.35°
Resolution range	5.00 - 0.83 Å
Index range	-10 ≤ h ≤ 10, -13 ≤ k ≤ 12, 0 ≤ l ≤ 15
Data completeness	100.0%
Integrated reflections	22869 (R $\sigma$ = 0.035)
Independent reflections	4324 (R <sub>int</sub> = 0.188)
Refinement method	Full-matrix least-squares on F <sup>2</sup>
Parameters / restraints	189 / 0
Goodness of fit on F <sup>2</sup>	1.060
Observed reflections [I > 2 $\sigma$ (I)]	3875
Final R indices	R <sub>1</sub> = 0.033, wR <sub>2</sub> = 0.073
Final R indices (all data)	R <sub>1</sub> = 0.040, wR <sub>2</sub> = 0.076
Extinction coefficient	0.00022(3)
Residual map (e <sup>-</sup> /Å <sup>3</sup> )	4.07 / -3.05

$$w = 1/[\sigma^2(F_o^2) + (0.0176 \times P)^2 + 27.98 \times P]$$

**Table 5.6a** Atomic coordinates and equivalent isotropic displacement parameters  $U_{eq}$  (standard deviation in parentheses)

Atom	Site	s.o.f	x	y	z	$U_{eq} / \text{\AA}^2$
Bi(1)	1f	1	1/2	0	1/2	0.0438(2)
Sn(1)	2i	0.863(5)	0.01386(7)	0.86940(6)	0.68553(5)	0.0147(3)
Bi	2i	0.137(5)	0.01386(7)	0.86940(6)	0.68553(5)	0.0147(3)
Sn(2)	2i	1	0.37174(8)	0.69873(7)	0.28736(5)	0.0122(2)
Sn(3)	2i	1	0.87401(8)	0.70635(7)	0.29733(6)	0.0137(2)
Sn(4)	2i	1	0.07058(8)	0.53143(7)	0.26005(6)	0.0111(2)
Sn(5)	2i	1	0.03463(8)	0.69258(7)	0.95552(6)	0.0112(2)
Sn(6)	2i	1	0.54012(8)	0.70189(7)	0.95306(6)	0.0105(2)
Sn(7)	2i	1	0.79763(8)	0.64567(7)	0.06119(6)	0.0122(2)
Sn(8)	2i	1	0.69957(8)	0.36218(7)	0.94810(6)	0.0117(2)
Sn(9)	2i	1	0.59032(8)	0.42799(7)	0.43411(6)	0.0133(2)
Sn(10)	2i	1	0.57461(8)	0.53006(7)	0.26212(6)	0.0111(2)
Sn(11)	2i	1	0.90774(8)	0.57093(7)	0.56843(6)	0.0120(2)
Sn(12)	2i	1	0.41195(8)	0.04932(7)	0.07881(6)	0.0161(2)
Sn(13)	2i	1	0.09878(8)	0.94152(7)	0.93199(6)	0.0140(2)
Na(1)	1b	1	0	0	1/2	0.034(2)
Na(2)	2i	0.935(5)	0.1933(7)	0.9180(6)	0.2346(5)	0.049(2)
Na(3)	2i	0.935(5)	0.3639(7)	0.0821(6)	0.7674(5)	0.046(2)
Na(4)	2i	1	0.2332(6)	0.7790(5)	0.5178(4)	0.035(1)
Na(5)	2i	1	0.3331(6)	0.2244(5)	0.4840(4)	0.033(1)
Na(6)	2i	1	0.7395(5)	0.7206(5)	0.7706(4)	0.030(1)
Na(7)	2i	1	0.2537(5)	0.7172(5)	0.7688(4)	0.028(1)

<sup>(1)</sup>  $U_{eq}$  is defined as one third of the trace of the orthogonalized  $U^{\dagger}$  tensor

**Table 5.6b** Atomic anisotropic displacement parameters (standard deviation in parentheses)

Atom	$U_{11}$	$U_{22}$	$U_{33}$	$U_{12}$	$U_{13}$	$U_{23}$
Bi1	0.0323(4)	0.0571(5)	0.0822(6)	0.0241(4)	0.0282(4)	0.0608(5)
Sn1/Bi	0.0128(4)	0.0164(4)	0.0171(4)	0.0046(3)	0.0038(3)	0.0105(3)
Sn2	0.0124(3)	0.0115(3)	0.0103(3)	0.0030(3)	0.0019(3)	0.0027(3)
Sn3	0.0129(3)	0.0123(3)	0.0113(3)	0.0027(3)	0.0017(3)	0.0012(3)
Sn4	0.0114(3)	0.0105(3)	0.0096(3)	0.0023(3)	0.0014(3)	0.0033(3)
Sn5	0.0112(3)	0.0107(3)	0.0107(3)	0.0026(3)	0.0022(3)	0.0040(3)
Sn6	0.0112(3)	0.0098(3)	0.0099(3)	0.0024(3)	0.0020(3)	0.0041(3)
Sn7	0.0120(3)	0.0147(3)	0.0115(3)	0.0045(3)	0.0031(3)	0.0068(3)
Sn8	0.0107(3)	0.0145(3)	0.0104(3)	0.0039(3)	0.0025(3)	0.0058(3)
Sn9	0.0119(3)	0.0158(4)	0.0120(3)	0.0034(3)	0.0026(3)	0.0063(3)
Sn10	0.0120(3)	0.0112(3)	0.0090(3)	0.0032(3)	0.0021(3)	0.0033(3)
Sn11	0.0107(3)	0.0141(3)	0.0116(3)	0.0038(3)	0.0025(3)	0.0059(3)
Sn12	0.0141(4)	0.0140(4)	0.0188(4)	0.0033(3)	0.0026(3)	0.0066(3)
Sn13	0.0118(3)	0.0127(3)	0.0159(4)	0.0036(3)	0.0032(3)	0.0044(3)
Na1	0.077(5)	0.009(3)	0.013(3)	0.005(3)	0.004(3)	0.008(3)
Na2	0.059(4)	0.030(3)	0.036(3)	0.028(3)	0.010(3)	0.004(3)
Na3	0.045(3)	0.037(3)	0.047(3)	-0.010(3)	0.003(3)	0.008(3)
Na4	0.043(3)	0.026(3)	0.034(3)	0.009(2)	0.019(2)	0.007(2)
Na5	0.033(3)	0.025(2)	0.028(2)	0.001(2)	-0.006(2)	0.008(2)
Na6	0.022(2)	0.038(3)	0.030(3)	0.004(2)	0.011(2)	0.015(2)
Na7	0.022(2)	0.037(3)	0.021(2)	0.013(2)	0.001(2)	0.008(2)

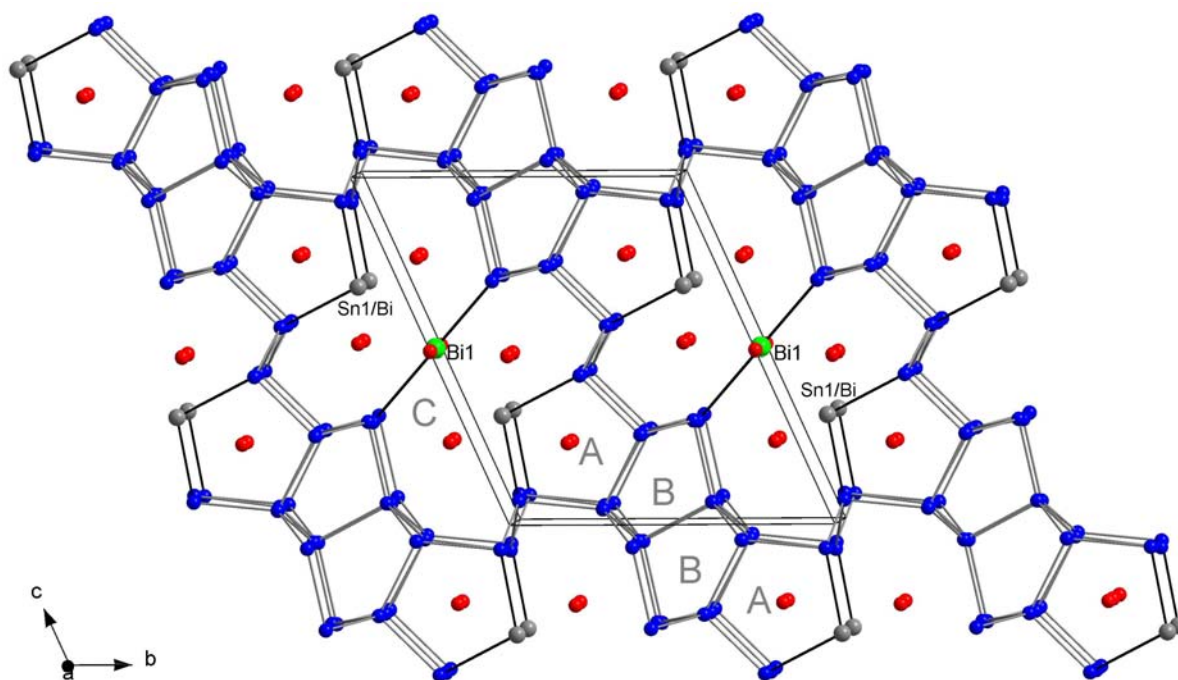
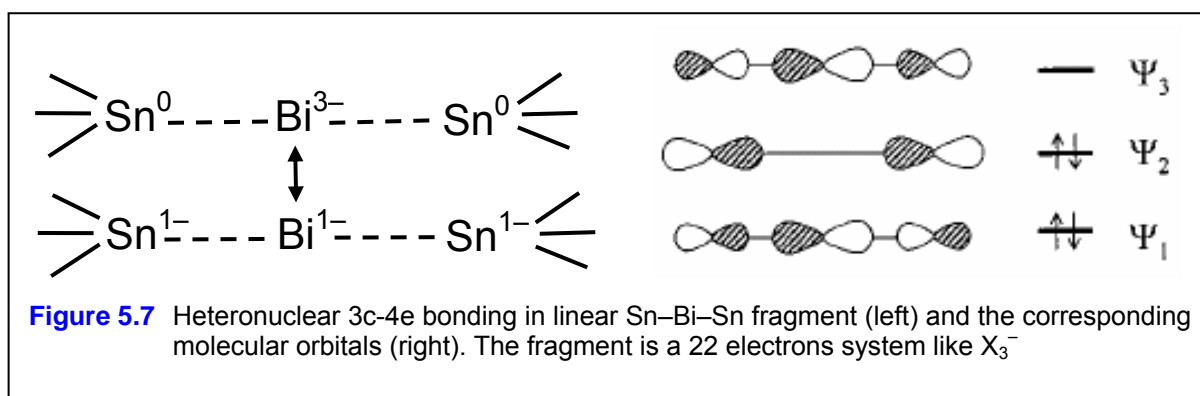


**Figure 5.6** Perspective view of the crystal structure of  $\text{Na}_{13-\delta}\text{Sn}_{26-\delta}\text{Bi}_{1+\delta}$ . Sn atoms blue, Na red and Bi1 green. Grey spheres represent the Sn1/Bi mixed position. The letters A, B and C mark the different channels of the structure as discussed in the text.

For electron counting purposes, the ideal structure  $\text{Na}_{13}\text{Sn}_{26}\text{Bi}$  is first considered with neither the Sn/Bi mixed occupancy, nor the Na defects. If one assumes that the short Sn–Sn distances represent single bonds, this gives per formula unit 16 (4b)Sn, 6 (3b)Sn, 2 (2b)Sn and 2 (3b)Sn and one additional interaction with Bi1 (2b, 3b and 4b denote two-, three- and four-bonded atoms). The shortest non-bonding Sn–Sn distance is 4.044(2) Å. Assuming charge transfer from Na to the Sn/Bi anionic network according to the Zintl concept and neglecting the Bi1–Sn2 contacts in the linear trimer, we can write  $\text{Na}_{13}\text{Sn}_{26}\text{Bi}$  as  $(\text{Na}^+)_{13}[(4\text{b})\text{Sn}^0]_{16}[(3\text{b})\text{Sn}^{1-}]_8[(2\text{b})\text{Sn}^{2-}]_2(\text{Bi}^{1-})$  where atomic charges denote formal oxidation state. This results in isolated  $\text{Bi}^{1-}$  (instead of the expected  $\text{Bi}^{3-}$ ), meaning that the compound is two electrons short from a closed shell phase. Alternatively, if we consider that Bi1–Sn2 contacts are single bonds, a different picture emerged in  $(\text{Na}^+)_{13}[(4\text{b})\text{Sn}^0]_{18}[(3\text{b})\text{Sn}^{1-}]_6[(2\text{b})\text{Sn}^{2-}]_2[(2\text{b})\text{Bi}^{1-}]$ , meaning that we now have two unaccounted electrons ( $13^+$  versus  $11^-$ ). This is a picture of a 3-center–4-electron bonding (3c-4e bonding) as found in  $\text{X}_3^-$  (X = halogen) or in  $\text{XeF}_2$  triatomic units.<sup>[16]</sup> The Sn–Bi interaction distance is in the range of delocalized bonds and the linear fragment Sn–Bi–Sn with three exo-bonded Sn atoms is isoelectronic with other hypervalent bonded trimer like  $\text{X}_3^-$  or  $\text{Pn}_3^{7-}$  (Pn = P, As, Sb, Bi) described in the  $\text{Ca}_{14}\text{AlSb}_{11}$ -type compounds.<sup>[17]</sup> Thus, we can assume

that  $\text{Na}_{13}\text{Sn}_{26}\text{Bi}$  is a charge optimized compound. It features in its structure the sidewise interconnected  $[\text{Sn}_{26}]^{12-}$  polyanion as building unit that interacts with the anion  $\text{Bi}^{1-}$  through 3c-4e bonding. The idea of electron-rich three-center bonding in so called ‘hypervalent molecule’ was proposed independently by Pimentel [18] and Rundle. [19] It invokes a delocalized three-center  $\sigma$ -bonding scheme as shown in Figure 5.7: three p-orbitals combine to give one bonding, one nonbonding and one antibonding molecular orbital (MO); the two lower-lying orbitals are occupied.



The partial replacement of the 2b-Sn1 by Bi correlates with Na under-occupancy which is significant at only two positions. To remain a charge balanced phase, the partial substitution and the Na defects have to be correlated. The exact formulation  $\text{Na}_{13-\delta}\text{Sn}_{26-\delta}\text{Bi}_{1+\delta}$  ( $\delta = 0.27$ ) accounts on the mixed-occupancy at the two bonded Sn position (Sn1). It is no surprise that the Sn/Bi mixed-occupancy occurs only at the two bounded Sn position because of the stronger relativistic effect in the heavier Bi atom that makes it reluctant to  $sp^3$  hybridation. Indeed, the lone pair effect is accompanied by the decrease availability of the valence electrons for covalent bonding. As a result, heavier main group elements have a marked tendency for low valence states. This means that the element Bi prefers atomic sites with the lowest number of covalent bonds.

Furthermore, the three-dimensional network of  $\text{Na}_{13}\text{Sn}_{26}\text{Bi}$  consists of tin polyanions that define three types of channels (labeled A, B and C) on which two are occupied by Na (type A) or Bi and Na (type C) atoms. The complex Sn polyanion  $\text{Sn}_{26}^{12-}$  is the repeating unit and features four condensed pentagonal channels as noticeable characteristics. The channels run parallel to the  $a$ -direction and are of two types (labeled A and B in Figure 5.6). The larger channels A are built up of  $\text{Sn}_5$  units and

are filled with Na atoms. The smaller type B channels are empty. The pentagonal  $\text{Sn}_5$  units are made up by four formally neutral 4-bonded tin (4b-Sn) atoms and one 2-bonded apical Sn atom that is formally  $\text{Sn}^{2-}$ . Vacancies at the apical position are alternatively observed every second unit (Figure 5.8). These flat pentagonal units  $\text{Sn}_5$  are stacked eclipsed on top of each other in the  $a$ -direction in a way that a pair of pentagon columns are linked at their basal atoms to 4-membered flat zigzag chains of Sn atoms running roughly parallel to the  $[011]$  direction and positioned between four pentagon units (Figure 5.8b). This linkage defines two smaller channels of type B and results in the one dimensional Sn polyanions  $\text{Sn}_{26}^{12-}$  as the repeating unit. The structure of this  $\text{Sn}_{26}^{12-}$  polyanion can therefore be rationalized by a partition into two types of adjoining channels with the sequence ABBA (Figure 5.8a). This structural motif is also found in the previously described  $\text{Sr}_3\text{Na}_{5+x}\text{Sn}_{13}$  and it results from closely related atomic connectivity but with slight differences. The  $\text{Sn}_{26}^{12-}$  polyanionic units are subsequently directly inter-connected in the  $bc$  plane through the lateral Sn atom of the pentagon units to form the three dimensional Sn network of the structure. The interconnection in the  $bc$  plane defines the largest channels C with shamrock-like shape that are filled with four rows of Na cations and one central row of alternating Bi and Na atoms (Figure 5.9).

The highest coordination number of Na by Sn atoms is observed in channel A (with 9 closer Sn atoms) where the shortest Na-Sn interaction distances range from 3.293(4) Å to 3.542(5) Å. In channel C, the shortest Na-Sn interaction distances are from 3.253(5) Å to 3.539(6) Å.

Bi1 atoms in channel C are surrounded by 8 Na atoms in distorted square prism geometry (Figure 5.10a). The interaction distances of Bi1 with Na4 and Na5 positions which show no noticeable defect are short (3.221(5) Å and 3.249(5) Å), but longer interaction distances are found with Na2 and Na3 positions (3.771(6) Å and 3.799(6) Å) which are slightly under-occupied. Na1 has a very particular square planar coordination sphere (Figure 5.10b), with strong similarities to that of Bi1. The interaction distances of Na1 with Sn are shorter (3.203(1) Å and 3.303(1) Å) in a square planar geometry. The shortest Na–Na interaction distance is 3.549(7) Å, in agreement with distances found in other Na-Sn binary systems (see Table 5.1).

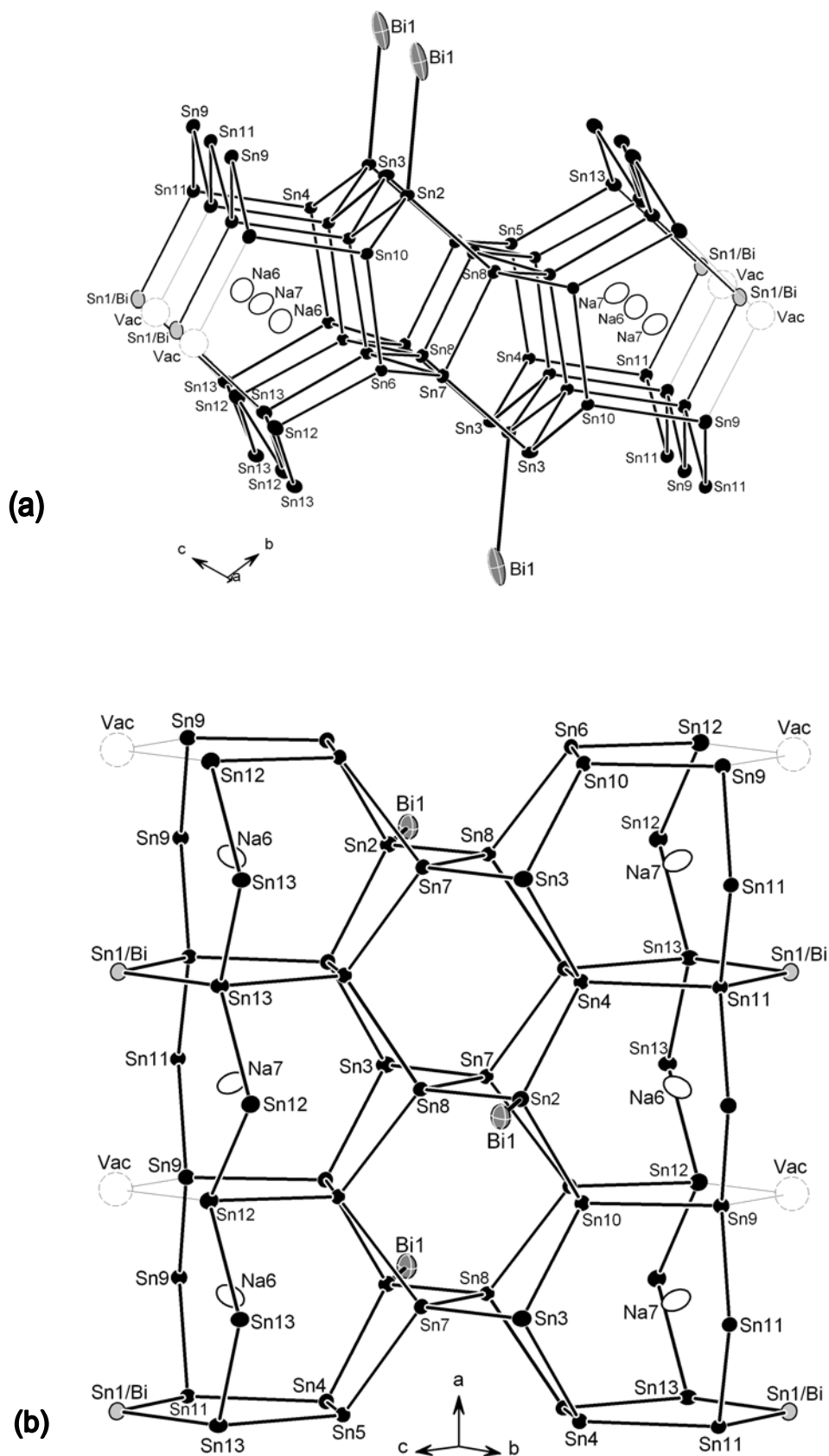


**Figure 5.8** Side view (top) and top view (bottom) of the structure of the Sn polyanion  $\text{Sn}_{26}^{12-}$ . Opened circles denote Na atoms, black and crossed grey spheres Sn and Bi atoms, respectively (Vac = 2b-Sn vacancies). Thermal ellipsoids are at 50% probability level.

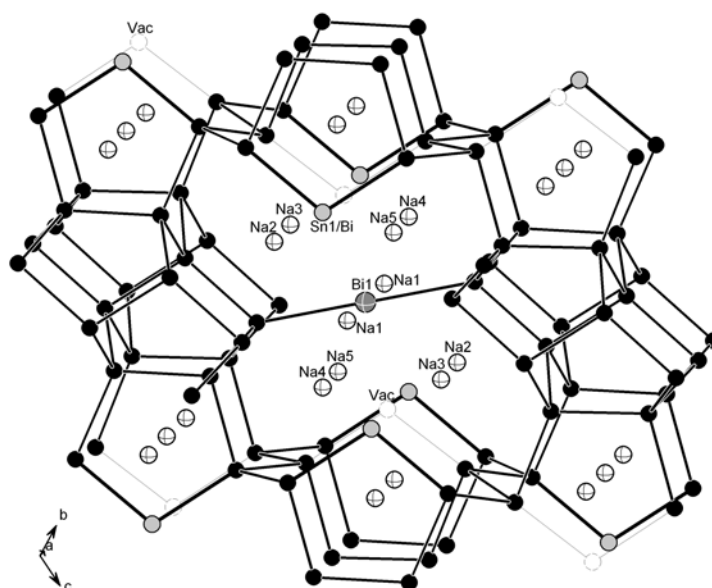


**Figure 5.9** A segment of the structure of  $\text{Na}_{13}\text{Sn}_{26}\text{Bi}$  highlighting the largest channel C with shamrock-like shape. Crossed circles denote Na, larger crossed grey sphere is Bi1, black and grey spheres are Sn and Sn1/Bi, respectively. (Vac = vacancies)

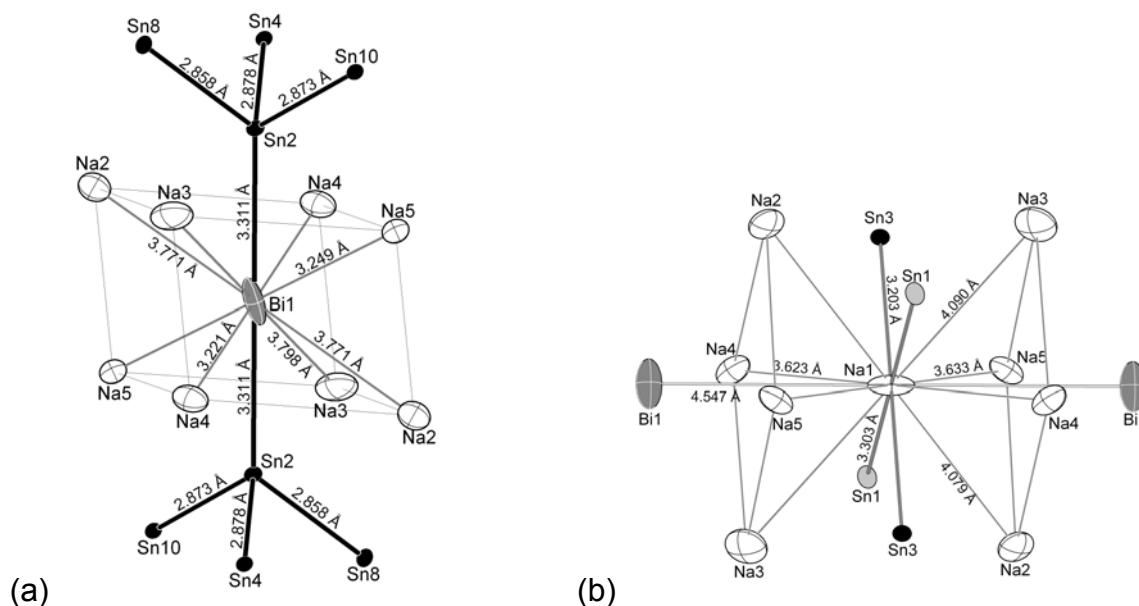


**Figure 5.10** The coordination of Bi1 atoms in the crystal structure of  $\text{Na}_{13}\text{Sn}_{26}\text{Bi}$  with Sn–Bi–Sn linear interaction (left). Na1 has a square planar coordination by Sn atoms (right). The coordination sphere of Na1 shows strong similarity with that of Bi1. Thermal ellipsoids are at 50% probability level.

**Table 5.7** Atomic distances (< 3.65 Å) in Na<sub>13</sub>Sn<sub>26</sub>Bi (standard deviations are in parentheses)

Atom pair	distance/ Å	Atom pair	distance/ Å	Atom pair	distance/ Å
Bi1 - Na4	3.221(5) x2	Sn9 - Sn9	2.880(1)	Na1 - Sn3	3.203(1) x2
- Na5	3.249(5) x2	- Sn11	2.890(1)	- Sn1/Bi	3.303(1) x2
- Sn2	3.311(1) x2	- Sn10	2.909(1)	- Na4	3.623(5) x2
- Na3	3.771(6) x2	Sn10 - Sn2	2.872(1)	- Na5	3.633(5) x2
- Na2	3.799(6) x2	- Sn3	2.881(1)	Na2 - Sn1/Bi	3.310(6)
Sn1/Bi - Sn13	2.973(1)	- Sn6	2.893(1)	- Sn2	3.428(6)
- Sn11	2.989(1)	- Sn9	2.909(1)	- Sn5	3.448(6)
Sn2 - Sn8	2.858(1)	Sn11 - Sn9	2.890(1)	- Na5	3.570(8)
- Sn10	2.873(1)	- Sn4	2.905(1)	- Sn12	3.594(7)
- Sn4	2.878(1)	- Sn11	2.931(1)	- Sn8	3.616(6)
- Bi1	3.311(1)	- Sn1/Bi	2.989(1)	Na3 - Sn1/Bi	3.303(5)
Sn3 - Sn7	2.867(1)	Sn12 - Sn12	2.875(2)	- Sn6	3.424(6)
- Sn4	2.880(1)	- Sn13	2.889(1)	- Sn2	3.461(5)
- Sn10	2.881(1)	- Sn6	2.947(1)	- Sn12	3.539(6)
Sn4 - Sn5	2.856(1)	Sn13 - Sn12	2.889(1)	- Na4	3.549(7)
- Sn2	2.878(1)	- Sn5	2.893(1)	- Sn8	3.610(5)
- Sn3	2.880(1)	- Sn13	2.912(1)	- Sn3	3.752(6)
- Sn11	2.905(1)	- Sn1/Bi	2.973(1)	- Bi1	3.798(6)
Sn5 - Sn8	2.827(1)	Na6 - Sn6	3.301(4)	Na4 - Bi1	3.221(5)
- Sn7	2.832(1)	- Sn9	3.316(5)	- Sn1/Bi	3.253(5)
- Sn4	2.856(1)	- Sn1/Bi	3.319(5)	- Sn9	3.266(5)
- Sn13	2.893(1)	- Sn12	3.326(5)	- Sn4	3.337(5)
Sn6 - Sn8	2.837(1)	- Sn11	3.378(5)	- Sn2	3.380(5)
- Sn7	2.840(1)	- Sn10	3.433(4)	- Na3	3.550(7)
- Sn10	2.893(1)	- Sn13	3.442(5)	- Sn11	3.549(5)
- Sn12	2.947(1)	- Sn5	3.464(5)	Na5 - Bi1	3.249(5)
Sn7 - Sn5	2.832(1)	- Sn4	3.542(5)	- Sn1/Bi	3.257(4)
- Sn8	2.840(1)	Na7 - Sn9	3.293(4)	- Sn9	3.270(5)
- Sn6	2.840(1)	- Sn12	3.316(4)	- Sn10	3.290(5)
- Sn3	2.867(1)	- Sn1/Bi	3.318(4)	- Sn2	3.389(5)
Sn8 - Sn5	2.826(1)	- Sn6	3.332(4)	- Sn9	3.530(5)
- Sn6	2.836(1)	- Sn13	3.377(4)	- Na2	3.567(7)
- Sn1/Bi	2.840(1)	- Sn10	3.382(4)		
- Sn2	2.858(1)	- Sn11	3.389(5)		
		- Sn5	3.485(5)		
		- Sn4	3.496(5)		

## 5.4 Discussions

The combination of alkali metal and tin leads to an astonishing large number of compounds and structures, even if the one restricted itself to the example of Na/Sn binary system. Solely in dependency on the atomic ratio, a large variety of chemical bond types ranging from localized two-electron–two-center (2e-2c) bonds to purely metallic bonds are established. On the Na-rich side, the charge transfer from Na to Sn is often enough to allow the Sn anions to achieve the octet as isolated species. But in the Sn-rich side, the transferred electrons are not enough to achieve the octet as isolated anions and the Sn atoms are forced to form bonds to each other, resulting

in a myriad polyanionic networks with various connectivity and bond types. Localized 2e-2c bonds are predominant in the formally Zintl phases  $\text{NaSn}$ ,  $\text{Na}_7\text{Sn}_{12}$  and  $\text{NaSn}_2$ . The non-stoichiometric phase  $\text{Sr}_8\text{Na}_{5+x}\text{Sn}_{13}$ , with localized 2e-2c bonds, doesn't obey the 8-N rule, but shows electron deficiency. A similar electron deficient phase is the chiral clathrate  $\text{K}_{6+x}\text{Sn}_{25}$  (for  $x = 0$ ) [20-21] with a three-dimensional covalent framework of tin polyhedra, which are filled with K atoms. The electron deficiency in these two phases is most probably due to the difficulty to find enough room in the lattice for all the cations that would be necessary to achieve the charge optimization. This suggests that, when it is impossible to find a room for all cations necessary to optimize the electron count in a particular structure, the phase stability has to be eventually achieved in consideration of other factors like Madelung energies between cations and the anionic network. The problem of filling space in an efficient way in a three-dimensionally bonded network is more complex than in systems with discrete clusters or low dimensional networks; the combined problems of lattice stability, size match and optimal bonding interactions in such 3D nets set up situations where the valence closure in some instances may be only approximately achieved.

For  $\text{K}_{6+x}\text{Sn}_{25}$ , the corresponding charge balance phase could be rationalized as  $\text{K}_6\text{Sn}_{23}\text{Bi}_2$ , [20] isostructural with the earlier. Thus, similarly we expected for  $\text{Na}_{5+x}\text{Sn}_{13}$  that the corresponding charge balance phase may be  $\text{Na}_5\text{Sn}_{12}\text{Bi}$  and will be isostructural to  $\text{Na}_{5+x}\text{Sn}_{13}$ . But here, the result was quite unexpected because the phase  $\text{Na}_{13}\text{Sn}_{26}\text{Bi}$  is obtained instead, with a lessening of the structure complexity on one hand, but a more complex bonding including localized 2e-2c covalent bonds and multicenter 4e-3c bond on the other hand. The occurrence of the weaker 4e-3c bond may be ascribed, to the smaller degree of charge transfer from Na to the anionic Sn/Bi network as compared with more electropositive K atom, and also to the stronger relativistic effects in Bi atom which is intimately related to the stability of the non-classical three-center bonded system.

The multicenter bonded Sn–Bi–Sn fragment in the structure of  $\text{Na}_{13}\text{Sn}_{26}\text{Bi}$  represents a rare example of heteronuclear three-center bonded system in the solid state. [16] Homonuclear triatomic anions with delocalized electron-rich 4e-3c bond have been observed in solid state only for the later p-block heavier elements (group 15, 16 and 17) in form of anions. Heteronuclear units are known, like  $\text{XeF}_2$ . All these linear trimers are 22 electrons systems and, if we consider the three exo-bonds of the two terminal Sn atoms in the Sn–Bi–Sn fragment and its -3 overall charge, we come out

with the same number of valence electrons. The 3c-4e bond in the Sn–Bi–Sn fragment is further stabilized with regard to the highly charged homonuclear  $\text{Bi}_3^{7-}$  trimer by the lower negative charge which eases the destabilization due to repulsion of  $p_\pi$  lone pairs.<sup>[16]</sup>

The occurrence of the phase  $\text{Na}_{13}\text{Sn}_{26}\text{Bi}$  shows that it is possible to stabilize novel tin frameworks by addition of a heteroatom (here Bi) at very low level. The chemical integrity of the Sn framework is almost preserved giving that the extent of Sn/Bi mixed-occupancy is very low. The interactions within the extended Sn framework involve strong localized covalent bonds, while those between  $\text{Sn}_{26}^{12-}$  polyanion and the hetero atom Bi involve weaker delocalized bond. This compound illustrates the versatility of the Zintl-Klemm formalism not only to help understand, but also to control a structure via the electron count and the bonding characteristic of the constituent main-group elements.

The pentagon is the basic structural motif of many Sn compounds with zeolithe-like extended structure, featuring condensed polyhedra or fragment of pentagon-dodecahedra.<sup>[8]</sup> The structures of the tin networks in compounds of the Na-Sn binary system can be described from three basic structural motifs, the  $\alpha$ -Sn tetrahedral fragment, the pentagonal ring and the realgar type cage. The different types of structure emerge from fragments made up by the condensation of the  $\text{Sn}_5$  pentagon based channel (type A) and the realgar-type ring based channel (type B) with different sequences. Direct interconnection of condensed fragments with AB sequence is found in  $\text{Na}_7\text{Sn}_{12}$  and, of only B ring in  $\text{NaSn}_2$ . Direct interconnection of condensed fragments with ABBA sequence form the 3D anionic network in  $\text{Na}_{13}\text{Sn}_{26}\text{Bi}$  and, a combination of BAB and ABBA fragments form the complex 3D network of  $\text{Na}_{5+x}\text{Sn}_{13}$  where they are interconnected directly and indirectly through tetrahedral  $\alpha$ -Sn fragment. Finally, the Sn richest phase  $\text{NaSn}_5$  features additionally the structure motif of  $\beta$ -Sn. This implies that pure metallic contacts also exist between Sn atoms in the structure.<sup>[7]</sup>

## 5.5 Literature

- [1] Guérin, F.; Richeson, D. *J. Chem. Soc., Chem. Commun.* **1994**, 2213.
- [2] Müller, W.; Volk, K. *Z. Naturforsch.* **1978**, 33b, 275.
- [3] Müller, W.; Volk, K. *Z. Naturforsch.* **1977**, 32b, 709.
- [4] Fässler, T. F.; Hoffmann, S. *Inorg. Chem.* **2003**, 42, 5474.
- [5] Dubois, F.; Fässler, T. F. *Inorg. Chem.* **2005**, 44, 477-479.
- [6] Vaughey, J. T.; Corbett, J. D. *Inorg. Chem.* **1997**, 36, 4316.
- [7] Fässler, T. F.; Kronseder, C. *Angew. Chem.* **1998**, 110, 1641.
- [8] Fässler, T. F.; Hoffmann, S. *Z. Kristallogr.* **1999**, 11, 722-734.
- [9] Hoffmann S. *Dissertation*, ETH Zürich, **2002**.
- [10] Fässler, T. F.; *Chem. Soc. Rev.* **2003**, 32, 80-86.
- [11] Mullen, D. J. E.; Nowacki, W. *Z. Kristallogr.* **1972**, 136, 48.
- [12] Thurn, H.; Krebs, H. *Acta Crystallogr.* **1969**, B25, 125.
- [13] Eisenmann, B.; Rössler, U. *Z. Anorg. Allg. Chem.* **2000**, 626, 1373-1379.
- [14] Asbrand, M.; Eisenmann, B. *Z. Kristallogr.* **1993**, 205, 323-324.
- [15] Ponou, S.; Fässler, T.F. *Inorg. Chem.* **2004**, 43, 6124-6126.
- [16] Munzarová, M.L.; Hoffmann, R. *J. Am. Chem. Soc.* **2002**, 124, 4787-4795.
- [17] Hach, R.; Rundle, R. E. *J. Am. Chem. Soc.* **1951**, 73, 4321.
- [18] Pimentel, G. C. *J. Chem. Phys.* **1951**, 19, 446.
- [19] Cordier, G.; Schäfer, H.; Stelter, M. *Z. Anorg. Allg. Chem.* **1984**, 519, 183.
- [20] Fässler, T. F.; Kronseder, C. *Z. Anorg. Allg. Chem.* **1998**, 624, 561-568.
- [21] Zhao, J.-T.; Corbett, J. D. *Inorg. Chem.* **1994**, 35, 5721.

## 6. Substitution effects on the Zintl phases of the Ba/Sn system

### 6.1 Overview

Several binary tin rich phases of tin and alkaline-earth metals (Ae) are known. The AeSn phases (Ae = Ca to Ba) crystallize in the CrB structure type. The structure contains linear zigzag chains  $\infty[\text{Sn}^{2-}]$ .<sup>[1]</sup> Exclusively two-fold bonded Sn atoms are expected from the 8–N rules. The compounds fulfill the valence rules (tin-tin separation of 2.9 Å). However, planar zigzag chains are found in the CrB type, while helical chains are found in the related element structures. By increasing the tin content, Ae<sub>3</sub>Sn<sub>5</sub> phases are described for Ae = Sr and Ba.<sup>[2]</sup> The tin atoms form five-atom clusters with weak interactions between them. In this case the Zintl concept can be extended by the introduction of the electron counting scheme according to Wade's rules. Electron transfer from the Ae atoms to tin leads to the polyanion  $[\text{Sn}_5]^{6-}$ , which indeed has an *arachno*-type structure and derives from a pentagonal bipyramid by removing two adjacent cluster vertices. However, band structure calculations (and conductivity measurements) show that these compounds are metallic and this fact may seem to deny their strict classification as Zintl (valence) compounds.<sup>[2]</sup> At higher tin content the binary phases BaSn<sub>3</sub>,<sup>[3]</sup> SrSn<sub>3</sub>,<sup>[4]</sup> SrSn<sub>4</sub>,<sup>[5]</sup> and BaSn<sub>5</sub><sup>[6]</sup> are structurally characterized. They are metallic and even superconducting at temperatures below 2.4 K (BaSn<sub>3</sub>), 5.4 K (SrSn<sub>3</sub>), 4.8 K (SrSn<sub>4</sub>) and 4.4 K (BaSn<sub>5</sub>).

BaSn<sub>3</sub> can be regarded as a compound at the borderline of structures, which derive from close packing of spheres and Zintl phases with localized chemical bonds. The structures can be described as distorted hexagonal closest atom packing as it is known for a variety of intermetallic compounds of the composition M'M<sub>3</sub>. Formal electron transfer from Ba to tin atoms leads to the formula  $[\text{Sn}_3]^{2-}$  and gets another perspective on the structure. The closest packing contains tri-membered rings of tin atoms, and the structures can be broken down to the polyanionic Zintl-anionic unit  $[\text{Sn}_3]^{2-}$  with an aromatic 2π-electron system that is isoelectronic with the aromatic cyclopropenium, C<sub>3</sub>H<sub>3</sub><sup>+</sup>.<sup>[3]</sup> Interactions between these units through their π-electron systems are strong and almost equal intra- and inter-ring contacts are observed. SrSn<sub>3</sub> possesses both molecular and metallic structural motives as the molecular anionic units  $[\text{Sn}_3]^{2-}$  are observed (like in BaSn<sub>3</sub>) in hexagonal slabs with Ni<sub>3</sub>Sn-type, alternating with metallic slabs consisting of cubic close-packing of atoms with a AuCu<sub>3</sub>-type and, leading to a *hhcc* stacking isotyp with the *h*-PuGa<sub>3</sub> structure type.<sup>[4]</sup>

$\text{SrSn}_4$  shows a unique structure motive in tin chemistry. The atoms that are covalently bonded by the two shortest Sn-Sn distances (2.900 Å and 3.044 Å) form a two-dimensional net consisting of hexagons of tin atoms with boat conformation. Further tin atoms connect the two-dimensional net of Sn hexagons at longer distances which are consistent with metallic interactions.  $\text{SrSn}_4$  can be derived from one to one intergrowth structure of 'molecular' valence substructure and metallic slab. <sup>[5]</sup>

Finally, in the tin-richest phase  $\text{BaSn}_5$  tin atoms form graphite-like layers (honeycombs). Two such layers built a slab of hexagonal prisms, which are centered by additional Sn atoms. The central tin atom has 12 nearest neighbours of tin atoms and represents the first case of a tin atom with such high coordination number. The slabs are separated by Ba atoms above and below the center of each tin hexagon. <sup>[6]</sup>

In the Ba/Sn binary phase, both  $\text{BaSn}_3$  and  $\text{Ba}_3\text{Sn}_5$  can be considered at the border between Zintl phase and intermetallics. Therefore, in assessing the transition from Zintl phases to intermetallics in the Ba/Sn system, we have studied the effects of Sn for Bi partial substitution on both the metallic  $\pi$ -system  $\text{BaSn}_3$  and the cluster compounds  $\text{Ba}_3\text{Sn}_5$ . This means an increase of the VEC whose effect depends on how dominant is the electron count factor on the stability of the parent structures.

## 6.2 Sn for Bi partial substitution in $\text{Ba}_3\text{Sn}_5$ – Synthesis and Characterization of the phases $\text{Ba}_3\text{Sn}_{4-y}\text{Bi}_{1+y}$ ( $y \leq 1$ )

### 6.2.1 Introduction

The  $\text{Pu}_3\text{Pd}_5$  structure type [7] is well known to be adopted by many polar intermetallics of the early p-block elements (groups 13–14). [8] Alkaline-earth and rare-earth tetrel systems, such as  $\text{Ba}_3\text{Pb}_5$ ,  $\text{Sr}_3\text{Sn}_5$ ,  $\text{Ba}_3\text{Sn}_5$ , [2]  $\text{La}_3\text{Sn}_5$  [9-10] and the corresponding triel systems, such as  $\text{La}_3\text{In}_5$  and  $\beta\text{-Y}_3\text{In}_5$  [11] have been structurally characterized. They contain square pyramidal cluster of the main group elements  $\text{E}_5^{n-}$ . Among this family of compounds,  $\text{La}_3\text{In}_5$  and  $\text{Y}_3\text{In}_5$  are metallic but electron precise according to Wade's rule. The  $\text{In}_5^{9-}$  here would be classified as *nido*-cluster ( $2n+4$ ) with 15 skeletal electrons and a charge of  $9^-$ , thereby matching the expected contribution from three rare-earth metal atoms and making this salts structurally Zintl phases. The relatively few cations in those phases appear to allow short intercluster contacts and, the metallic conduction is probably due to band broadening and overlapping. On the other hand, high charge (up to  $-9$ ) might also be important for rule violation.

In the tetrel group, extended Hückel, LMTO and ELF analysis indicated that the HOMO of  $\text{Sn}_5^{6-}$  is antibonding and the two electrons therefore delocalized, so that the clusters can alternatively be described as *nido*- $\text{Sn}_5^{4-} + 2e^-$  (or  $5e^-$  in  $\text{La}_3\text{Sn}_5$ ). [9] These compounds are 'metallic Zintl phases' because conductivity arises from the presence excess of electrons which referred to the idea of 'submerged continent' of Nesper. [12] The larger charge excess in  $\text{La}_3\text{Sn}_5$  (with formally  $\text{Sn}_5^{9-}$  cluster) is accommodated by the increase of the so called "*lattice covalency*" due to the contribution  $\text{La}^{3+}$  5d orbitals in bonding, [8] an analogous effect to the well known "*cage orbitals*" with Li cations. [12]

Thus, the compound  $\text{Ba}_3\text{Sn}_5$  seems to be interesting to probe the influence of VEC in the phase stability at the Zintl border. In the course of our present work we restricted our investigations on the effect of an increase of the VEC on phase stability of Zintl phases at the border to polar intermetallics. In other words, what happens if a fraction of Sn is substituted by electron richer element like bismuth?

### 6.2.2 Synthesis and characterization

The reaction mixtures of pure elements with nominal composition  $\text{Ba}_3\text{Sn}_{5-x}\text{Bi}_x$  where  $x = 1.5$  and  $2$  (only known phases like  $\text{BaSn}_3$  was found from reaction products with  $x \leq 1$ ), were loaded into sealed niobium ampoules. The mixtures were heated at  $150 \text{ K/h}$

to 800 °C for 6 hours, then cooled to 500 °C then annealed for 120 h at this temperature, and subsequently cooled down to room temperature at 120 K/h. All products obtained were crystalline and exhibited a grey colour and metallic luster. Phase analysis by X-ray powder diffraction (Figure 6.1) revealed the new compound  $\text{Ba}_3\text{Sn}_{4-y}\text{Bi}_{1+y}$  ( $y < 1$ ) as a major phase but, with small amounts of other unidentified phases.

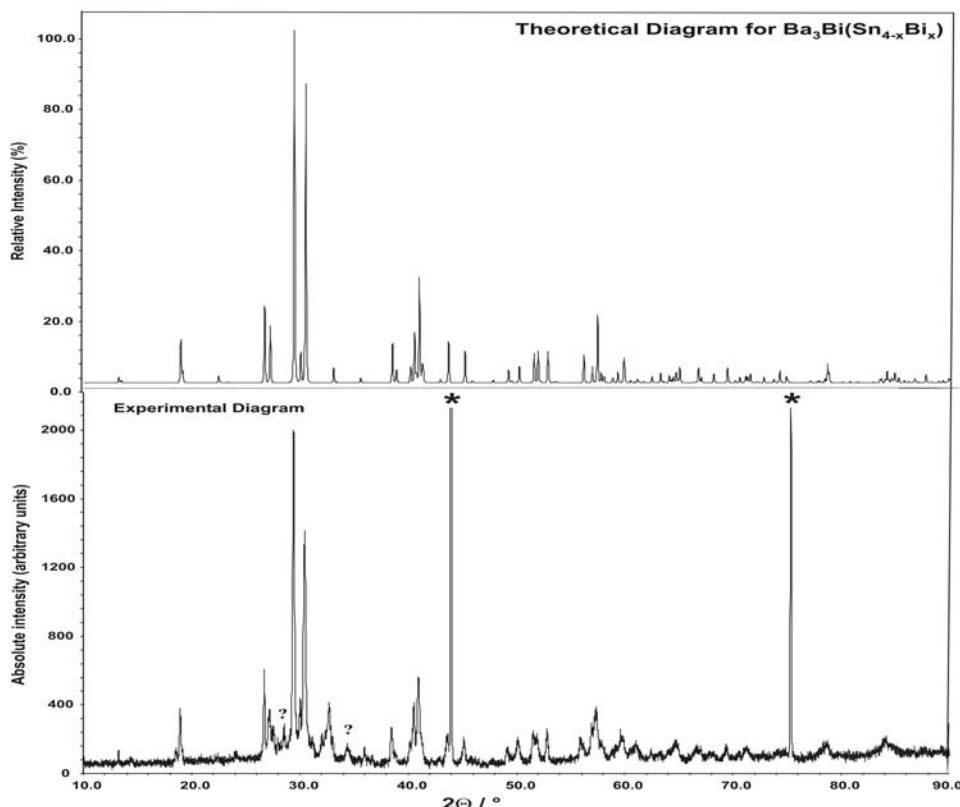


**Figure 6.1** Experimental powder diagram for reaction product (bottom) and theoretical (top) powder diagram of  $\text{Ba}_3\text{Sn}_{5-x}\text{Bi}_x$  calculated from single crystal refinements data. Diamond peaks (used as internal standard) are marked by stars and stronger unindexed peaks with question marks.

### 6.2.3 Crystal structure determination

Several single crystals were selected from different starting mixtures. The crystals were checked for singularities and diffraction data were collected for the best one at room temperature on Enraf-Nonius CCD and Stoe IPDS diffractometers, both at a window of a rotating anode. The data were corrected for absorption and the structure solved by direct method and refined on  $F^2$ . The tetragonal unit cell was determined and refined using all the integrated peaks from the recorded frames. Systematic

absent reflections indicate the space group *I4/mcm* (Nr. 140). The crystallographic data as well as the structure refinement data are summarized in Table 6.1 and the atomic positions and equivalent isotropic displacement parameters are listed in Tables 6.2 and 6.3. Structure solution revealed four atomic positions. The site 4c was assigned to Bi judging from peak heights, and the sites 16l, 8h and 4a to Sn1, Ba1 and Ba2 respectively, judging from bond distances and peak heights. The refinement of Sn/Bi mixed occupancy show significant Bi amount at Sn1 position (site 16l). This model leads to the best residuals, e.g.  $R_1 = 0.026$  and  $wR_2 = 0.074$  for all data. We could not obtain good crystals from reaction mixtures with higher Bi content ( $x > 2$ ).

**Table 6.1** Crystallographic data and refinement parameters for Ba<sub>3</sub>Sn<sub>4-y</sub>Bi<sub>1+y</sub> ( $y \leq 1$ )

Empirical formula	Ba <sub>3</sub> Sn <sub>3.07</sub> Bi <sub>1.93(4)</sub> ( $y = 0.93$ )	Ba <sub>3</sub> Sn <sub>3.16</sub> Bi <sub>1.84(3)</sub> ( $y = 0.84$ )
Formula weight	1179.28	1172.5075
Temperature	293(2) K	293(2) K
Crystal size	0.05×0.15×0.20 mm <sup>3</sup>	0.05×0.05×0.15 mm <sup>3</sup>
Mosaicity (°)	–	0.453(2)
Crystal color and shape	Black Silvery, block	Black Silvery, needle
Diffractometer	Stoe IPDS II	Nonius CCD
Crystal system	Tetragonal	Tetragonal
Space group	<i>I4/mcm</i> (Nr. 140)	<i>I4/mcm</i> (Nr. 140)
Unit cell parameters (Å)	$a = 9.263(1)$ ; $c = 13.327(2)$	$a = 9.248(1)$ ; $c = 13.323(3)$
Unit Cell Volume	1143.6(2) Å <sup>3</sup> , $Z = 4$	1139.5(3) Å <sup>3</sup> , $Z = 4$
Density calculated	6.849 g/cm <sup>3</sup>	6.835 g/cm <sup>3</sup>
Absorption coefficient (Mo K $\alpha$ )	46.189 mm <sup>-1</sup> ( $\lambda = 0.71073$ Å)	45.363 mm <sup>-1</sup> ( $\lambda = 0.71073$ Å)
Absorption correction	numerical	semi-empirical
F(000)	1926	1916
Max. / Min transmission	0.0111 / 0.0875	–
Theta range	4.36° - 29.20°	4.37° - 25.33°
Resolution range	4.67 Å – 0.72 Å	5.00 Å - 0.83 Å
Index range	$-12 \leq h \leq 12$ , $-11 \leq k \leq 12$ , $-18 \leq l \leq 18$	$-11 \leq h \leq 11$ , $-11 \leq k \leq 11$ , $-15 \leq l \leq 15$
Data completeness	99.5%	100%
Integrated reflections	10204 ( $R_\sigma = 0.055$ )	9466 ( $R_\sigma = 0.027$ )
Independent reflections	441 ( $R_{int} = 0.128$ )	300 ( $R_{int} = 0.036$ )
Refinement method	Full-matrix least-squares on	F <sup>2</sup> (SHELXTL)
Parameters	17	17
Goodness of fit on F <sup>2</sup>	1.018	1.154
Observed reflections [ $I > 2\sigma(I)$ ]	348	293
Final R indices	$R_1 = 0.027$ / $wR_2 = 0.046$	$R_1 = 0.025$ / $wR_2 = 0.073$
Final R indices (all data)	$R_1 = 0.045$ / $wR_2 = 0.048$	$R_1 = 0.026$ / $wR_2 = 0.074$
Extinction coefficient	0.00031(3)	0.0014(2)
Residual map (e <sup>-</sup> /Å <sup>3</sup> )	2.08 / -1.56	1.19 / -1.09

$$w = 1/[\sigma^2(Fo^2) + (0.0470 \times P)^2 + 9.71 \times P]$$

**Table 6.2a** Atomic coordinates and equivalent isotropic displacement parameters for  $\text{Ba}_3\text{Sn}_{3.16}\text{Bi}_{1.84(3)}$ 

Atom	Site	s.o.f	x	y	z	$U_{\text{eq}} / \text{\AA}^2$
Ba1	8h	1	0.3366(1)	0.1634(1)	1/2	0.022(1)
Ba2	4a	1	0	0	1/4	0.027(1)
Sn1	16l	0.79(1)	0.1388(1)	0.3612(1)	0.3087(1)	0.027(1)
Bi1	16l	0.21(1)	0.1388(1)	0.3612(1)	0.3087(1)	0.027(1)
Bi2	4c	1	0	0	0	0.026(1)

$U_{\text{eq}}$  is defined as one third of the trace of the orthogonalized  $U^{\text{J}}$  tensor

**Table 6.2b** Atomic coordinates and equivalent isotropic displacement parameters for  $\text{Ba}_3\text{Sn}_{3.07}\text{Bi}_{1.93(4)}$ 

Atom	Site	s.o.f	x	y	z	$U_{\text{eq}} / \text{\AA}^2$
Ba1	8h	1	0.3365(1)	0.1635(1)	1/2	0.022(1)
Ba2	4a	1	0	0	1/4	0.030(1)
Sn1	16l	0.77(1)	0.1379(1)	0.3621(1)	0.3091(1)	0.029(1)
Bi1	16l	0.23(1)	0.1379(1)	0.3621(1)	0.3091(1)	0.029(1)
Bi2	4c	1	0	0	0	0.026(1)

$U_{\text{eq}}$  is defined as one third of the trace of the orthogonalized  $U^{\text{J}}$  tensor

**Table 6.3a** Anisotropic displacement parameters ( $\text{\AA}^2$ ) for  $\text{Ba}_3\text{Sn}_{3.16}\text{Bi}_{1.84(3)}$ 

Atom	$U_{11}$	$U_{22}$	$U_{33}$	$U_{23}$	$U_{13}$	$U_{12}$
Ba1	0.0207(5)	$U_{11}$	0.0242(7)	-	-	0.0002(3)
Ba2	0.0277(6)	$U_{11}$	0.0252(8)	-	-	-
Sn1/Bi1	0.0284(5)	$U_{11}$	0.0247(6)	0.0037(2)	$-U_{23}$	-0.0025(3)
Bi2	0.0238(4)	$U_{11}$	0.0296(6)	-	-	-

**Table 6.3b** Anisotropic displacement parameters ( $\text{\AA}^2$ ) for  $\text{Ba}_3\text{Sn}_{3.07}\text{Bi}_{1.93(4)}$ 

Atom	$U_{11}$	$U_{22}$	$U_{33}$	$U_{23}$	$U_{13}$	$U_{12}$
Ba1	0.0194(4)	$U_{11}$	0.0265(5)	-	-	0.0008(4)
Ba2	0.0311(5)	$U_{11}$	0.0273(8)	-	-	-
Sn1/Bi1	0.0312(4)	$U_{11}$	0.0258(4)	0.0045(2)	$-U_{23}$	-0.0032(3)
Bi2	0.0232(4)	$U_{11}$	0.0329(6)	-	-	-

#### 6.2.4 Structural description of $\text{Ba}_3\text{Sn}_{4-y}\text{Bi}_{1+y}$

The space group and atom positions for  $\text{Ba}_3\text{Sn}_{4-y}\text{Bi}_{1+y}$  ( $y \leq 1$ ) reveal the isostructural relationship with the compound  $\text{La}_3\text{In}_4\text{Ge}$ .<sup>[13]</sup>  $\text{Ba}_3\text{Sn}_{4-y}\text{Bi}_{1+y}$  is isopointal with inverse  $\text{Cr}_5\text{B}_3$  family<sup>[14]</sup> and belongs to the  $\text{In}_5\text{Bi}_3$ -type subfamily which is characterized by a small  $c/a$  ratio of about 1.45, while larger values of around 1.85 are found for the  $\text{Cr}_5\text{B}_3$  aristotyp.<sup>[15]</sup> This  $c/a$  ratio is about 1.44 for  $\text{Ba}_3\text{Sn}_{4-y}\text{Bi}_{1+y}$  phases. A projection of the crystal structure is represented in Figure 6.2. The structure of  $\text{Ba}_3\text{Sn}_{4-y}\text{Bi}_{1+y}$  contains four crystallographic sites (Table 6.4). It can be described as a ABA'B' stacking of planar and puckered nets which alternate along [001]: planar  $3^2434$  nets of Ba1, centered by larger planar  $4^4$  nets of Bi2 are found at  $z = 0$  and puckered  $48^2$

nets (by projection of all Sn1/Bi atoms in their mean plane) of Sn1/Bi, centered by larger planar 4<sup>4</sup> nets of Ba2 at  $z = 0.25$ . Bi2 and Ba2 form linear chain along  $c$  axis. The coordination of Bi2 atoms by Ba1 and Ba2 defines a distorted octahedron with four Bi2–Ba1 contacts (3.4601(6) Å) in the waist and two shorter Bi2–Ba2 distances (3.3308(7) Å) in the axial direction. In fact, these compressed octahedra share corners to form a  $\infty^3$ [Ba<sub>6/2</sub>Bi] framework of twisted octahedra with an inverse ReO<sub>3</sub>-like distorted structure (Figure 6.3). The shortest distances between Sn1/Bi atoms of the puckered layers running in the  $ab$  plane and Ba atoms are 3.631(1) Å (Ba1–Sn1) and 3.6628(6) Å (Ba2–Sn1), meaning that Sn1/Bi network is quite apart from the [Ba<sub>6/2</sub>Bi] framework. The Sn1/Bi substructure corresponds to one of the four types of corrugated layers of homogeneous sphere packings with tetragonal symmetry that are illustrated in Figure 6.4. The Sn1/Bi atoms have two shorter contacts at 3.007(1) Å resulting into 4-member units with a ‘*bodyless butterfly*’ geometry, (Figure 6.2a) which are in term interconnected by longer contact of 3.302(2) Å, forming corrugated nets with wrenched quadrangles (Figure 6.2b) which are better described with the symbol of the Shubnikov nets  $4_c(8+2)^2$ . [16]

The shortest Sn–Sn distance within the 4-member units is in the range of atom-atom separations of elemental  $\alpha$ -Sn (2.81 Å) and  $\beta$ -Sn (3.02 and 3.18 Å) and may be considered as localized bond, while the distance between the 4-member units are much longer than expected for localized Sn–Sn bonds. Similar bond distances distribution is found in SrSn<sub>4</sub> [5] with localized bonds of 2.900(1) Å and 3.044(1) Å, as well as longer contacts of 3.287(1) Å and 3.302(1) Å, presumably metallic.

**Table 6.4a** Interatomic distances for Ba<sub>3</sub>Sn<sub>3.16</sub>Bi<sub>1.84(3)</sub>

Atomic pair		distance /Å	
Sn1/Bi1	– Sn1/Bi	3.007(1)	×2
	– Sn1/Bi	3.302(2)	
Bi2	– Ba2	3.331(1)	×2
	– Ba1	3.460(1)	×4
Ba2 – Bi2		3.331(1)	×2
– Sn1/Bi1		3.663(1)	×8
Ba1	– Bi2	3.460(1)	×2
	– Sn1/Bi1	3.631(1)	×2
– Sn1/Bi1		3.789(1)	×3

**Table 6.4b** Interatomic distances for Ba<sub>3</sub>Sn<sub>3.07</sub>Bi<sub>1.93(4)</sub>

Atomic pair		distance /Å	
Sn1/Bi1	– Sn1/Bi	3.002(1)	×2
	– Sn1/Bi	3.332(2)	
Bi2	– Ba2	3.332(1)	×2
	– Ba1	3.465(1)	×4
Ba2 – Bi2		3.332(1)	×2
– Sn1/Bi1		3.674(1)	×8
Ba1	– Bi2	3.465(1)	×2
	– Sn1/Bi1	3.638(1)	×2
– Sn1/Bi1		3.784(1)	×3

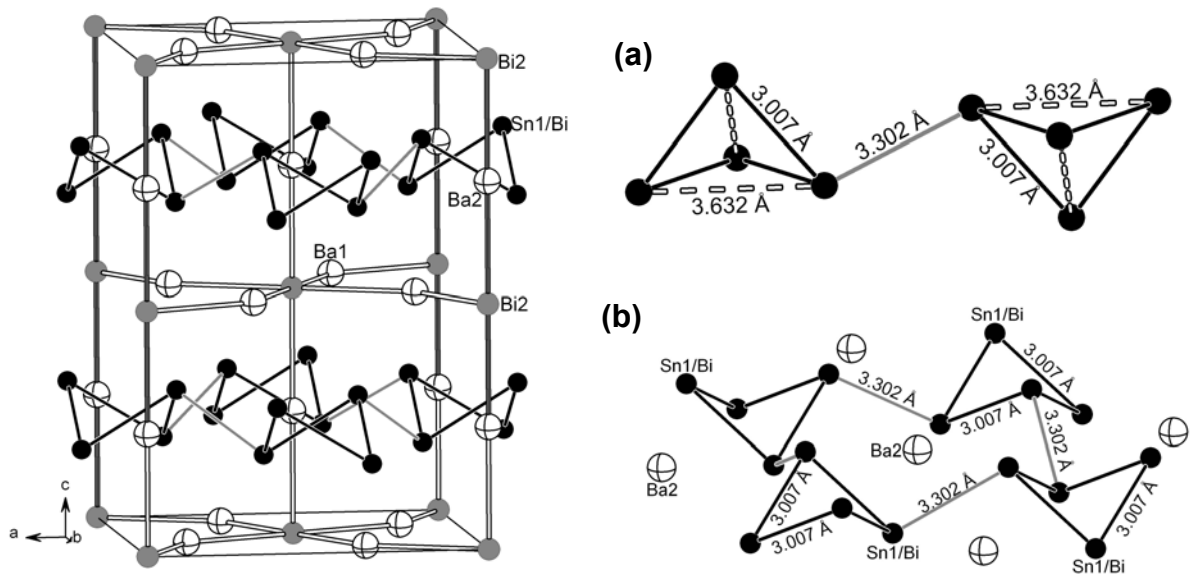


**Figure 6.2** Perspective view of the crystal structure of  $\text{Ba}_3\text{Sn}_{4-y}\text{Bi}_{1+y}$ : Sn1/Bi, black sphere; Bi, grey; Ba white crossed. (a) Geometry of the 'butterflies'  $\text{Sn}_4$  units showing on their relation to tetrahedron: the dashed lines denoted missing contacts. (b) The corrugated Sn1/Bi layers centered by Ba2.

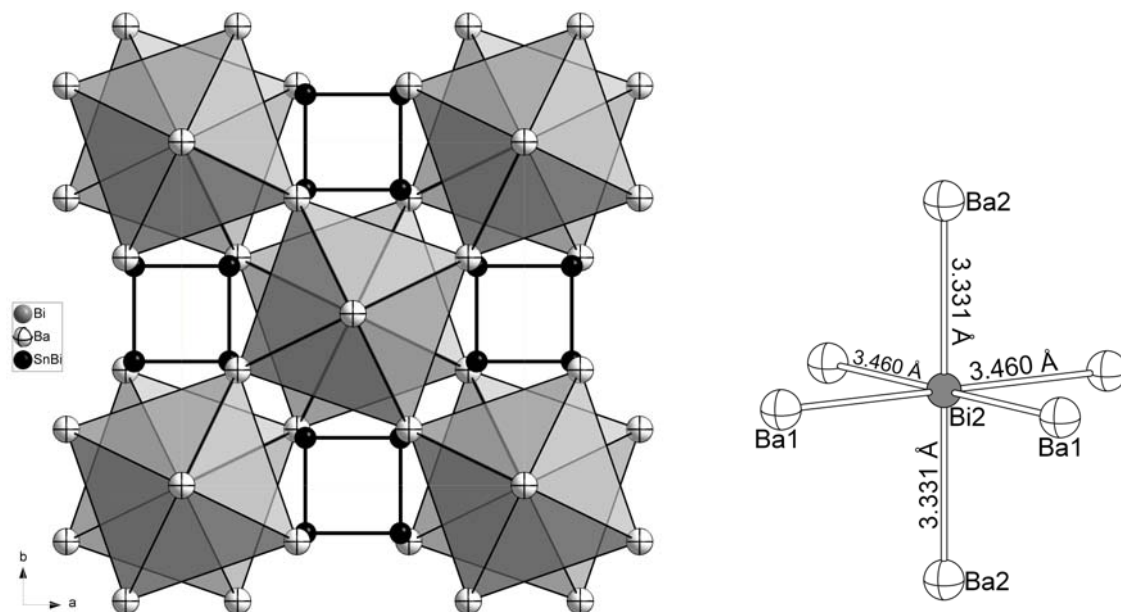


**Figure 6.3** Projection of the structure of  $\text{Ba}_3\text{Sn}_{4-y}\text{Bi}_{1+y}$  along [001]. The  $\frac{3}{\infty}[\text{Ba}_{6/2}\text{Bi}]$  octahedral framework corresponds to an anti-perovskite framework where the octahedra are turned alternately clockwise and anti-clockwise along the c-axis. (right) A closer view of the Bi coordination by  $\text{Ba}_6$  octahedron with the interaction distances.

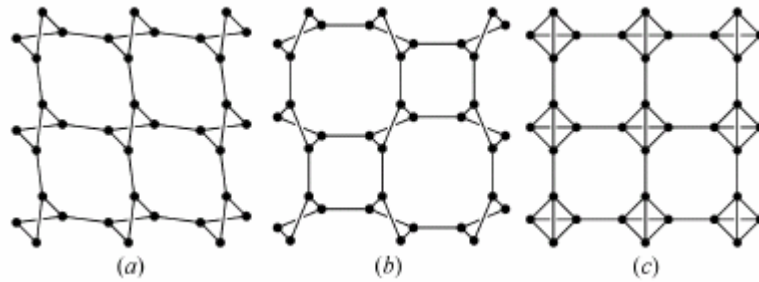


**Figure 6.4** The three tetragonal types of sphere packing with layer-like subunits corresponding to non-planar nets after ref. [16]. The symbols of the respective Shubnikov nets are: (a)  $4_c(8+2)^2$  layer, (b)  $4_c8(8+4)$  layer, (c)  $4_t8^2$  layer.

Within the Zintl-Klemm concept, a charge transfer from electropositive Ba to the anionic part may be assumed in the formulation  $3\text{Ba}^{2+}[\text{Bi}^{3-}(\text{Sn}_{4-y}\text{Bi}_y)^{3-}]$  where the isolated Bi2 atoms would be assigned a formal charge of -3. Taking account of the two substructures, we can write  $[\text{Ba}_{6/2}\text{Bi}]^{3+}[\text{Sn}_{4-y}\text{Bi}_y]^{3-}$ . For  $y = 1$ , the anions  $(\text{Sn}_3\text{Bi}_1)^{3-}$  is obtained and is isoelectronic with  $[\text{Sn}_4]^{4-}$ . The earlier should then form isolated tetrahedra or alternatively a 2D net of three-bonded atoms with similar bond length. The refined Bi occupancies at Sn1 position were  $y = 0.84(3)$  from starting mixtures with  $x = 1.5$  and  $y = 0.93(4)$  from  $x = 2$ . The low Bi occupancy ( $y < 1$ ) observed on refinement of X-ray data in the Sn1/Bi slab implies that both phases are electron deficient. Consequently, the Sn1/Bi sublattice is intermediate between isolated tetrahedra and regular 2D net of three bonded atoms. The long contact between Sn1/Bi 4-member ring units here is presumably originated from the electron deficiency. Therefore, the optimum Bi content ( $y = 1$ ) in the  $\text{Sn}_4$  layer should lead to the shortening of the intracluster distance, along with the increase of the intercluster distance. However, the refinements of Bi occupancy in  $\text{Sn}_4$  layer with increasing Bi content show only a modest trend in the expected direction. It is possible that somekind of bonding frustration may arise from packing effect, giving some more degree of freedom to the structure to accommodate for electron deficiency.

### 6.2.5 Electronic Structure

The band structure was calculated along the main directions of the reciprocal lattice for the hypothetical fully ordered variant  $\text{Ba}_3\text{BiSn}_4$  (which is formally one electron deficient) within the tight binding LMTO-ASA code, to gain a more deep insight view of bonding in the apparently 'electron deficient' compound, in order to have some useful clarifications of the problem.

The density of states (DOS) plot is represented in [Figure 6.5](#). As expected, the Fermi level ( $E_F$ ) is very near to a deep minimum (pseudo-gap) in the DOS, which would correspond to the ‘right’ Zintl count. Due to relativistic effects included in the DFT level, the energy separation between the band with mainly Bi-6s character (at the bottom of energy scale) and those associated with Bi-6p is very high. The energy of the bands with Sn-5s character are intermediate between the two former and those associated with Sn-5p overlap with the Bi-6p bands. It is clear from the DOS diagram and band structure that  $\text{Ba}_3\text{BiSn}_4$  is metallic.

The LMTO-band structure of  $\text{Ba}_3\text{BiSn}_4$  ([Figure 6.6](#)) shows flat bands with narrow dispersion crossing the Fermi level  $E_F$  (IDOS =  $54e^-$  /cell). Since  $E_F$  intersects bands along directions both parallel and perpendicular to  $c^*$ , the electrical conductivity is three-dimensional. The Fermi Level cuts the density of states at the flank of a local maximum; this relatively high DOS at  $E_F$  arises mainly from the flat band sections along symmetry lines  $\Gamma \rightarrow X$  and close to X, at the Fermi energy and along  $Z \rightarrow \Gamma$  close to  $\Gamma$ . These bands lying across the Fermi level are mainly contributed by the 5p- and 6p-orbitals of Sn and Bi atoms, respectively. Interestingly, in the band structure plot the very narrow band gap is opened at about +0.36 eV above  $E_F$  ([Figure 6.7](#)) and is equivalent to an integrated DOS of  $56 e^-$ /cell, as in  $\text{Ba}_3\text{Sn}_3\text{Bi}_2$  (i.e.  $y = 1$ ), predicting the electron count to be optimized at that point (some of the small densities of states in [Figure 6.5](#) may be related to inherent approximations in the LMTO-ASA program). Fat band analysis ([Figure 6.7](#)) shows that the band of higher energy, below the narrow gap, which crosses the Fermi level in the symmetry line  $\Gamma \rightarrow X$  has mainly Bi-6p character. These suggest that the electron deficiency is not associated only with the  $\text{Sn}_4$  slab, but also with  $[\text{Ba}_{6/2}\text{Bi}]$  substructure. In addition, the projected DOS showing strong Bi-6p character to the states below  $E_F$ ; this contribution of Ba to the filled part of the density of states is even higher than that of Bi between -3 eV and -1 eV, indicating a very large contribution of Ba to the covalent bonding in this phase. Significant Ba states that are hybridized with the conduction band indicate that the electron transfer from Ba to Bi is not effective enough and the Barium atoms play the role of carrier donor to the anionic network, allowing charge transfer between the two substructures.

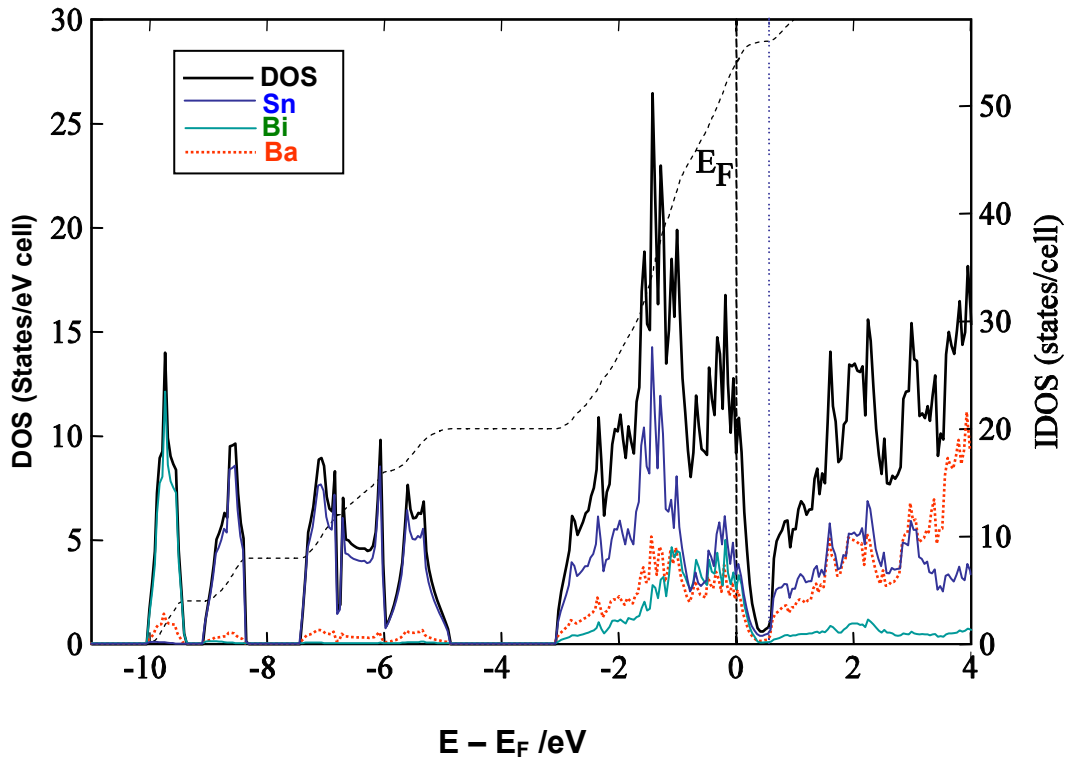


**Figure 6.5** DOS plot of the hypothetical phase  $\text{Ba}_3\text{BiSn}_4$  and its integration (dashed line). The pseudo-gap corresponds to an electron count of  $56 e^-/\text{cell}$  as in  $\text{Ba}_3\text{Bi}[\text{Sn}_3\text{Bi}]$

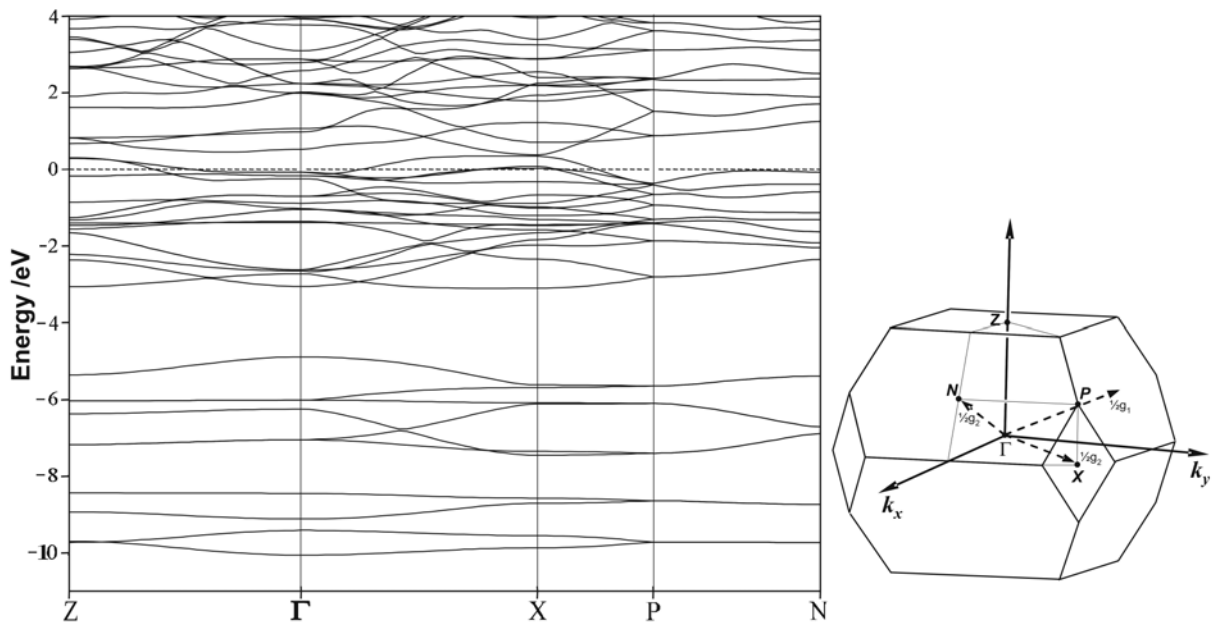


**Figure 6.6** Band structure of the hypothetical phase  $\text{Ba}_3\text{BiSn}_4$  along the high symmetry directions of the tetragonal body centered Brillouin zone (right)

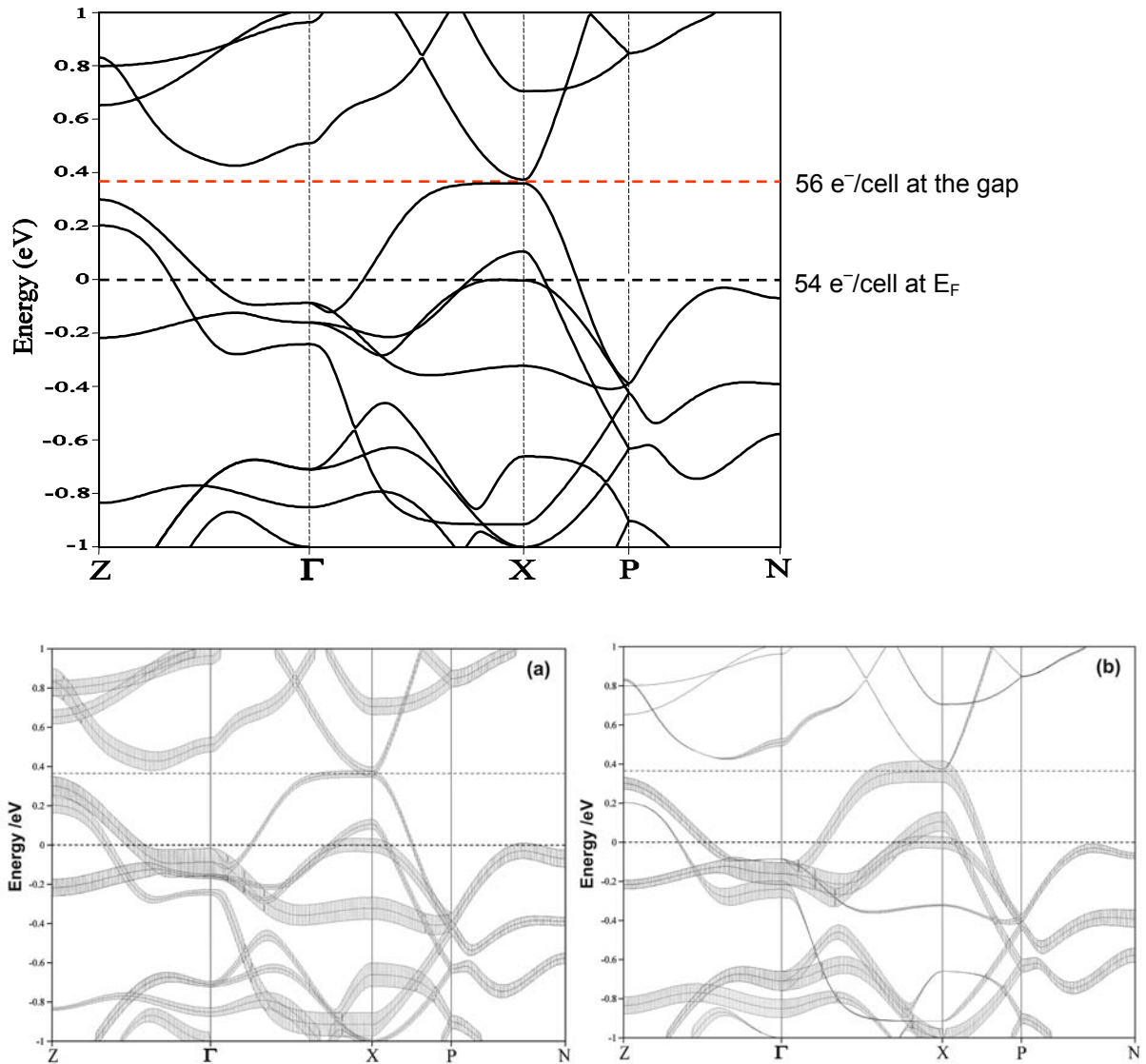


**Figure 6.7** (Top) Band dispersion at the vicinity of  $E_F$  in the hypothetical phase  $\text{Ba}_3\text{BiSn}_4$ . The gap corresponds to an IDOS of  $56 \text{ e}^-/\text{cell}$  as in the solid solution  $\text{Ba}_3\text{Bi}[\text{Sn}_3\text{Bi}]$ . (Bottom) Fat band plot:  $p_x$ -,  $p_y$ - and  $p_z$ -orbitals contributions of (a) Sn and (b) Bi atoms.

The strength of pairwise Sn–Sn interactions between atoms can be better quantified by crystal overlap Hamiltonian population (COHP) analyses as a function of energy. The COHP curves of the Sn–Sn bonds are represented in [Figure 6.8](#). The integrated COHP (-icohp) values of Sn–Sn interactions in the hypothetical phase are about  $0.217 \text{ eV}/\text{bond}$  for the contacts at  $3.007 \text{ \AA}$  and  $0.142 \text{ eV}/\text{bond}$  for  $3.302 \text{ \AA}$  contact. This clearly indicates that the butterflies are interconnected by significantly weaker bond, compared to the intrabonds. The analysis of the different bonding interactions show that all bonding levels filled up to  $E_F$  for the electron count of  $54 \text{ e}^-/\text{cell}$ . For the Sn–Sn contact at  $3.007 \text{ \AA}$ , some non-bonding Sn levels at or above  $E_F$  are not

completely filled. This means that the flat bands at  $E_F$  have essentially non-bonding character and, therefore the predominant character of the missing two electrons would have been non-bonding. This band characteristic (lone pairs at  $E_F$ ) have been observed in polar intermetallic alloys like  $\text{BaSn}_3$ ,  $\text{SrSn}_3$ ,  $\text{SrSn}_4$  and  $\text{BaSn}_5$  and was likened to their superconducting properties.<sup>[17]</sup> The Sn–Sn contact at 3.302 Å is slightly antibonding at  $E_F$  which is consistent with a metallic interaction. An electron count of  $56 e^-/\text{cell}$  will be necessary to fill those non-bonding levels. Thus, the phase  $\text{Ba}_3\text{Bi}[\text{Sn}_3\text{Bi}]$  ( $y = 1$ ) ought to correspond to the charge balance phase and would be isoelectronic with the phase  $\text{Ba}_3\text{Ge}_4\text{X}$  ( $X = \text{O}$  or  $\text{C}_2$ )<sup>[18-19]</sup> which contains  $\text{Ge}_4^{4-}$  tetrahedral units, forming to the Shubnikov net  $4_48^2$ <sup>[16]</sup> in which the wrenched quadrangles are replaced by isolated tetrahedra.

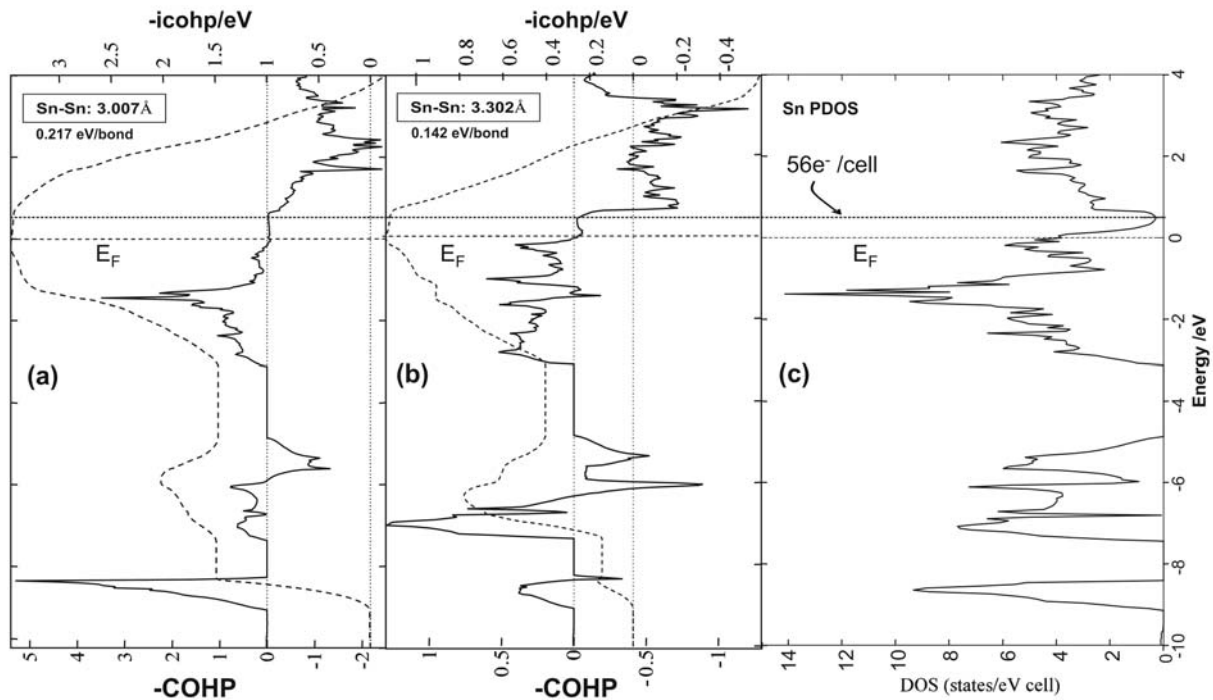


**Figure 6.8** -COHP plots of Sn–Sn interactions in the hypothetical fully ordered phase  $\text{Ba}_3\text{BiSn}_4$  (a) Sn–Sn = 3.007 Å and (b) Sn–Sn = 3.302 Å with their corresponding integration curves (-icohp) represented by dashed line. (c) Projected DOS of Sn showing strong Sn states around  $E_F$ . In all cases the Fermi level is taken as point of zero energy.

## 6.2.6 Discussions

In the structure of the solid solutions  $\text{Ba}_3\text{Sn}_{4-y}\text{Bi}_{1+y}$  ( $y < 1$ ) the Sn1/Bi corrugated net is intermediate between that in the formally Zintl phase  $\text{Ba}_3\text{Ge}_4\text{O}$  with  $\text{Ge}_4$  tetrahedra and that of the hypothetical  $\text{Ba}_3\text{Sn}_3\text{Bi}_2$  ( $y = 1$ ), where the Sn1/Bi layer may adopt a

corrugated layer of 3 bonded Sn with similar bond distances (alternative to isolated tetrahedra). The formal electron deficiency in  $\text{Ba}_3\text{Sn}_{4-y}\text{Bi}_{1+y}$  ( $y < 1$ ) is accommodated in the Sn1/Bi sub-lattice by bond isomerism leading to shorter bonds within the 4-membered ring units, which are in term interlinked by longer (metallic) contacts, corresponding to the Shubnikov net  $4_c(8+2)^2$ . The classical Zintl phase limit for this structure,  $\text{Ba}_3\text{Sn}_3\text{Bi}_2$ , may also form isostructural structure with  $\text{Ba}_3\text{Ge}_4\text{X}$  with tetrahedral geometry for the corresponding  $[\text{Sn}_3\text{Bi}]^{3-}$  anion. But the fact that the effective charge transfer from Ba to Bi is not optimal and, perhaps other factors in structure selection like packing efficiency and Madelung's energy, may hamper the transition to the ideal Zintl structure like in the phases  $\text{Ba}_3\text{Ge}_4\text{X}$  in which the cation-anion interactions are much more ionic.

The stabilities of diverse ionic cluster salts in solid are clearly often influenced by packing as well as electronic effects. Chemical modifications of the sizes of the cations or partial substitutions in the anionic substructure along with the formal charge on either can lead to new structure types, although these perhaps more often lead to instability of the cluster species. For example, electron poorer Ga for Sn substitution in  $\text{La}_3\text{Sn}_4\text{Ga}$  [8] keeps the cluster geometry and structure of the parent  $\text{La}_3\text{Sn}_5$  in which nominally five free metallic electrons remain beyond  $\text{Sn}_5^{4-}$  *nido*-clusters. But, in the particular example of the  $\text{Ba}_3\text{Sn}_5$  investigated in the present work, in which only two nominally free metallic electrons remain beyond  $\text{Sn}_5^{4-}$  *nido*-clusters, electron richer Bi for Sn substitution in  $\text{Ba}_3\text{Sn}_5$  leads to cluster instability and results in  $\text{Ba}_3\text{Sn}_{4-y}\text{Bi}_{1+y}$  phases, exactly in the same way than in  $\text{La}_3\text{In}_4\text{Ge}$ . [13] The latter derived from Ge for In substitution in the electron precise  $\text{La}_3\text{In}_5$ .  $\text{La}_3\text{In}_4\text{Ge}$  is isoconfigurational with  $\text{Ba}_3\text{Sn}_{4-y}\text{Bi}_{1+y}$ , but not isoelectronic as the former is formally three electrons deficient from a classical view of close shell compounds. The existence of a phase range in  $\text{Ba}_3\text{Sn}_{4-y}\text{Bi}_{1+y}$  as well as in the substitution variants  $\text{La}_3\text{Ge}(\text{In}_{4-y}\text{Sn}_y)$  ( $y \leq 3$ ) [8] indicates the remarkable flexibility of this structural type. The effect of Bi substitution at lower rate (starting mixtures with  $x \leq 1.0$ ) on  $\text{Ba}_3\text{Sn}_5$  is still to be investigated. For a more comprehensive study of the stability of the phases  $\text{Ae}_3\text{Sn}_5$  ( $\text{Ae} = \text{Sr}, \text{Ba}$ ), it would be also interesting to investigate the effect of a decrease of VEC on their stability, through for instance partial substitution of Sn atom by electron poorer element like the triel (Ga, In, Tl).

### 6.3 Sn for Bi substitution effects in $\text{BaSn}_3$ – The homologous series



#### 6.3.1 Introduction

Hexagonal and cubic close packing of atoms are among the most important structure motives of metals and intermetallic compounds. Among the polar intermetallics with divalent/trivalent metal cations (Ae) and anions of the group 12 – 14 elements (E), certain compounds with the composition  $\text{AeE}_3$  are particularly interesting because both atom size and electronic effects play important roles in structure selection. In their extremes, those adopt the  $\text{AuCu}_3$  ( $\text{Pm}\bar{3}\text{m}$ ) and the  $\text{Ni}_3\text{Sn}$  ( $\text{P6}_3/\text{mmc}$ ) structure types with Kagome nets of E atoms being packed in analogy to cubic and hexagonal close packing variant, respectively.<sup>[20-22]</sup> The different patterns give rise to octahedra of E atoms in both structures, yet with different connectivity of the octahedra. In the  $\text{AuCu}_3$ -type, the octahedra share corners along all three directions, whereas in the  $\text{Ni}_3\text{Sn}$ -type they share faces along the 6-fold axis to form chains that may or may not be connected through interchain (or intercluster) bonds perpendicular to the chain axis. Combinations of the two packing patterns result in intermediate structures, in which the cubic sequence in their structure types increases in the order of  $\text{Ni}_3\text{Sn}$  (*hhh*) <  $\text{BaPb}_3$  (*hhc*) <  $\beta\text{-HfNi}_3$  (*hhchc*) <  $\text{TiNi}_3$  (*hchc*) =  $\text{PuGa}_3$  (*hhcc*) <  $\beta\text{-HoAl}_3$  (*hchcc*) <  $\beta\text{-PuAl}_3$  (*hcc*) <  $\text{AuCu}_3$  (*ccc*).<sup>[21-23]</sup>

On the one hand, this structural series seems to be related to the size of the cations in such a way that smaller cations generate the  $\text{AuCu}_3$ -type structure whereas the  $\text{Ni}_3\text{Sn}$ -type structure occurs with larger cations. The examples of the  $\text{AeTt}_3$  phases ( $\text{Tt} = \text{Sn, Pb}$ ) are very illustrative.  $\text{BaPb}_3$  has a *hhc* stacking<sup>[24]</sup> whereas  $\text{SrPb}_3$  crystallizes in the  $\text{AuCu}$ -type (homeotyp of  $\text{AuCu}_3$ -type) with *cc* stacking.<sup>[25]</sup>  $\text{BaSn}_3$  has a  $\text{Ni}_3\text{Sn}$ -type (*hh*),<sup>[3]</sup> but the Sr homologue  $\text{SrSn}_3$  has *hhcc* stacking with  $\text{PuGa}_3$ -type.<sup>[4]</sup> On the other hand, the electron count i.e. the formal VEC is also very important in structure selection. The  $\text{AuCu}_3$ -type shows large variation of the formal VEC from 5 (e.g.  $\text{AePd}_3$ ) to 14 (e.g.  $\text{RTt}_3$ , R = Rare-earth) indicating a remarkable flexibility of the structure.<sup>[20]</sup> Here, the electron deficiency or excess is accommodated simply by changing overall anion–anion bond distances in triangular rings in the Kagome nets, which are all equivalent in the cubic symmetry.<sup>[26]</sup> But the  $\text{Ni}_3\text{Sn}$ -type seems to have another way to adjust their structures to the number of valence electrons. When these compounds have a maximum of 9 electrons per  $\text{E}_3$ , the inter- and the intra-chain distances are almost the same in a three-dimensional anionic network.<sup>[22-23]</sup> However,

when the vec per  $E_3$  unit is 12 or higher, the anionic structure becomes one dimensional, with much longer inter-chain distances. In this case, the inter-chain bonds are broken and lone-pair formation accommodates the electron abundance, as in  $\text{BaSn}_3$ .<sup>[3]</sup> No systematic study on the transition from  $\text{Ni}_3\text{Sn}$ -type to  $\text{AuCu}_3$ -type or vice-versa was reported to the best of our knowledge. Recent investigations on cations size effects in  $\text{Ba}_{1-x}\text{Sr}_x\text{Sn}_3$  have been done, but only in relation to the superconducting properties of the phases  $\text{BaSn}_3$  and  $\text{SrSn}_3$ .<sup>[27-21]</sup> After Kronseder,<sup>[27]</sup> we have studied in the present work, the effect of the valence electron concentration (VEC) on the structure and bonding in  $\text{BaSn}_{3-x}\text{Bi}_x$  solid solutions.

### 6.3.2 Synthesis and Characterization

The reaction mixtures of pure elements with nominal composition  $\text{BaSn}_{3-x}\text{Bi}_x$  where  $x = 0.5, 0.75$  and  $1$ , were loaded in sealed niobium ampoules. The mixtures were heated at  $150 \text{ K/h}$  to  $800 \text{ }^\circ\text{C}$  for 3 hours, then cooled to  $400 \text{ }^\circ\text{C}$  at  $150 \text{ K/h}$ , annealed for 120 hours at this temperature and, subsequently cooled down at  $60 \text{ K/h}$  to room temperature. All products obtained were crystalline and exhibited a silvery colour and metallic luster.

#### 6.3.2.1 Thermal analysis

Differential Thermal Analysis (DTA) was used to study the thermal behavior of two reaction products  $\text{BaSn}_{3-x}\text{Bi}_x$  ( $x = 0.5$  and  $x = 0.75$ ). About 200 mg of the reaction products were loaded in niobium crucibles that were subsequently weld-sealed. The samples were heated under a continuous argon flux from room temperature at the rate of  $10 \text{ K/min}$  to  $1000^\circ\text{C}$  and, cooled down at the same rate back to room temperature. Two successive loops were done for each sample.

The DTA curves of the mixture  $\text{BaSn}_{3-x}\text{Bi}_x$  with  $x = 0.5$ , (Figure 6.8) on heating reveal six noticeable peaks. The first endothermic peak ① (not visible in the second loop) with very weak magnitude at about  $237.5^\circ\text{C}$  corresponds to unreacted tin. This is followed by two overlapping small endothermic peaks ② and ③ at about  $411^\circ\text{C}$  ( $T_{\text{onset}} 403^\circ\text{C}$ ) and  $429^\circ\text{C}$  ( $T_{\text{onset}} 422^\circ\text{C}$ ). The peak ② indicates the presence of a new phase which is assigned to  $\text{Ba}_4\text{Sn}_{9-y}\text{Bi}_{3-y}$  (see §6.3.3) and, the peak ③ (peak ③ on cooling) may be assigned to  $\text{BaSn}_5$ . This is because some single crystals of  $\text{BaSn}_5$ <sup>[6]</sup> could be found in the mixture and previous thermal analysis of a stoichiometric mixture

suggests that the melting point of  $\text{BaSn}_5$  is around  $420^\circ\text{C}$ ; [21] on the other hand, the phase  $\text{Ba}_4\text{Sn}_{9-y}\text{Bi}_{3-y}$  could be synthesized only at  $400^\circ\text{C}$ . The peak ② corresponds on cooling to a shoulder below  $400^\circ\text{C}$  and almost disappeared in the second loop. On heating, the next two overlapping endothermic peaks ④ and ⑤ occurring at  $517^\circ\text{C}$  ( $T_{\text{onset}} 511^\circ\text{C}$ ) and  $536^\circ\text{C}$  ( $T_{\text{onset}} 529^\circ\text{C}$ ) correspond to the two exothermic peaks on cooling to peak ④ occurring at about  $490^\circ\text{C}$  ( $T_{\text{onset}} 494^\circ\text{C}$ ) and peak ⑤ at  $503^\circ\text{C}$  ( $T_{\text{onset}} 509^\circ\text{C}$ ) respectively, with significant temperature hysteresis which indicates a possible heterogeneous (liquid–solid) phase transitions.

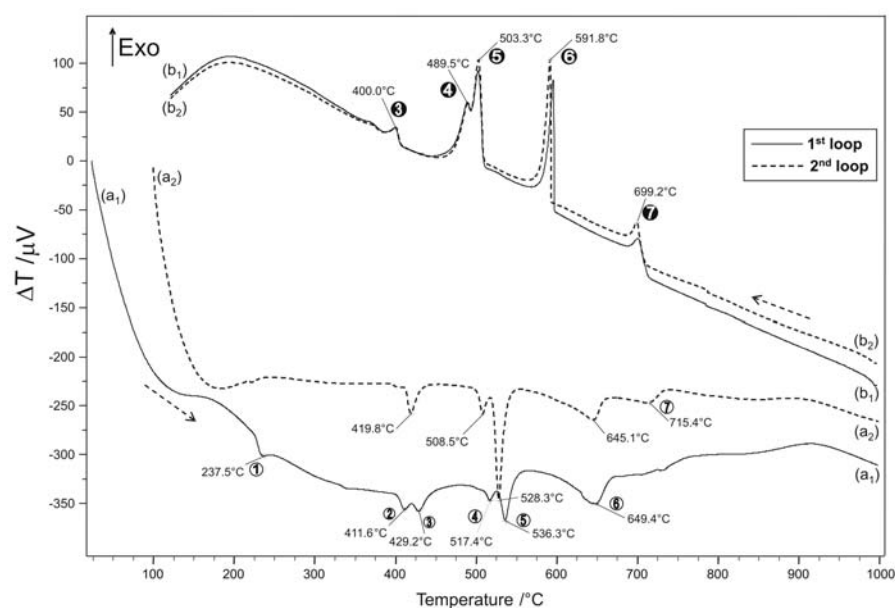


**Figure 6.8** DTA curves of the reaction product of  $\text{BaSn}_{3-x}\text{Bi}_x$  with  $x = 0.5$  annealed at  $400^\circ\text{C}$ . (a<sub>1</sub>) heating and (b<sub>1</sub>) cooling

To assess these two peaks, the reaction of  $\text{BaSn}_{3-x}\text{Bi}_x$  with  $x = 0.5$  was repeated with higher annealing temperature of  $500^\circ\text{C}$  instead of  $400^\circ\text{C}$ , to favour the thermally most stable phases. Single crystal diffraction and HRTEM indicates that varying the annealing temperature that way leads to a different reaction product at  $500^\circ\text{C}$ . Here, the main phase is identified as  $\text{Ba}_{13}\text{Sn}_{30+y}\text{Bi}_{9-y}$  (see §6.3.4) with almost the same composition as  $\text{Ba}_4\text{Sn}_{9-y}\text{Bi}_{3-y}$  and, HRTEM indicate the presence of closely related other phases (see below). Phase analysis by X-ray powder diffraction was very difficult and only single crystal diffraction was used for structural characterizations.

To assign the endothermic broad peak ⑥ at  $649^\circ\text{C}$  ( $T_{\text{onset}} 630^\circ\text{C}$ ), the same approach i.e. re-doing the reaction with annealing at  $600^\circ\text{C}$  produced mainly the compounds  $\text{Ba}_3\text{Sn}_{5-x}\text{Bi}_x$  (see § 6.2), suggesting that this peak may be due to the peritectical decomposition of that phase. The last endothermic peak ⑦ at  $715^\circ\text{C}$  ( $T_{\text{onset}} 702^\circ\text{C}$ ) appears more clearly in the second loop and may be assigned to  $\text{BaSn}_3$  and other phases  $\text{BaSn}_{3-\delta}\text{Bi}_\delta$  containing less than 5% Bi that were also revealed by HRTEM observations.

For the reaction product of the starting mixture Ba:Sn:Bi = 1:4:1 which yielded the substituted phase  $\text{BaSn}_{3-x}\text{Bi}_x$  with  $x = 0.75$ , the DTA pattern (Figure 6.9) is less complex with four endothermic peaks on heating, all with significant temperature hysteresis with regard to the corresponding peaks on cooling. The first endothermic peak ① at  $236^\circ\text{C}$  may be assigned to unreacted tin (use in excess) and corresponds to the exothermic peak ③ at about  $216^\circ\text{C}$ . The major exothermic incident on cooling, the sharp peak ⑤ at  $469^\circ\text{C}$  ( $T_{\text{onset}} 464^\circ\text{C}$ ), corresponding on heating to a very broad peak ④ at  $492^\circ\text{C}$  ( $T_{\text{onset}} 472^\circ\text{C}$ ), probably originates from incongruent decomposition of the main phase, identified as  $\text{Ba}_5\text{Sn}_{9+y}\text{Bi}_{6-y}$  (see §6.3.5). The second endothermic peak ② at  $339^\circ\text{C}$  (on heating) which corresponds to the exothermic peak ⑦ at  $296^\circ\text{C}$  on cooling, is quite weak and is assigned to not yet identified phases. The other weak peak ③ at  $410^\circ\text{C}$  ( $T_{\text{onset}} = 402^\circ\text{C}$ ), corresponding to peak ⑥ at  $365^\circ\text{C}$  on cooling, may indicate some amount of other  $\text{BaSn}_{3-x}\text{Bi}_x$  substituted phases, probably  $\text{Ba}_4\text{Sn}_{9-y}\text{Bi}_{3-y}$ . The peak which appears only on cooling at about  $442^\circ\text{C}$  is most probably an artifact.

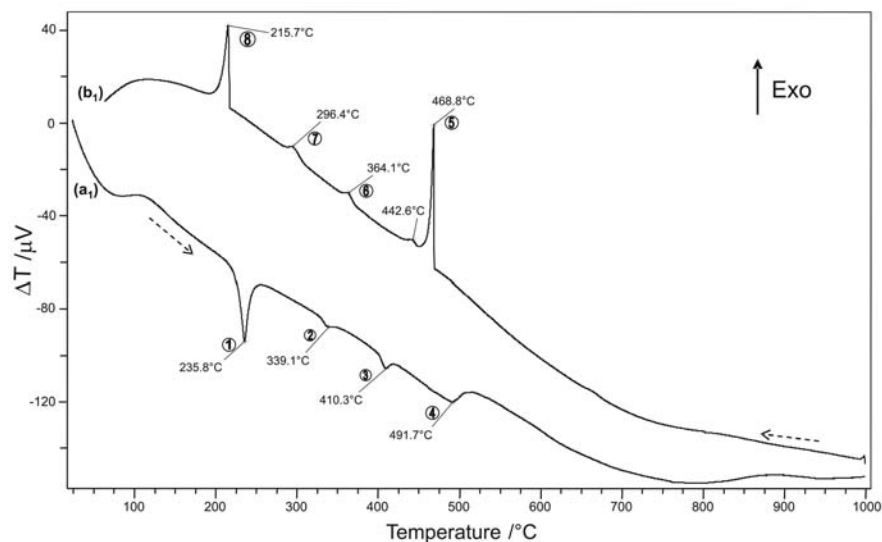


**Figure 6.9** DTA curves of the reaction product of Ba:Sn:Bi = 1:4:1 at  $400^\circ\text{C}$ ; (a) heating and (b) cooling

### 6.3.2.2 HTREM observations and some implications

The reaction product at 500°C of the mixture corresponding to  $x = 0.5$  was analyzed by the mean of electron microscopy. The application of the High Resolution Transmission Electron Microscopy (HRTEM) has made possible the observation of several additional stacking sequences in this sample, that have not yet been revealed by other techniques.

The compositions of the particle which contain only Ba-Bi-Sn vary significantly. Some of the investigated particles contain only small amount of Bi (ca. 5 at%). Oxygen is not an integral part of the crystals. The particles decompose quickly in electron beam under the condition of the HRTEM. As inhomogeneity doesn't allow one to work fast, the particles have to be examined with EDX first. But, more homogenous samples could possibly minimize this problem. However, under the conditions of the selected area electron diffraction range this problem does not occur. By this method we were able to prove the complex ordering variant that was revealed by X-ray measurements earlier (Figure 6.10,  $d_{003} \sim 36 \text{ \AA}$ ). Additionally, other variants – either simpler (Figure 6.10,  $d_{003} \sim 22 \text{ \AA}$ ), or even more complex (Figure 6.10,  $d_{003} \sim 50 \text{ \AA}$ ) – were detected. There are clear indications that these different variants coexist in a single microcrystal, meaning formation of domains with different ordering variants. These seem to indicate that the different ordering variants originate from different stacking of (001) layers not as different polytyps, but in the sense of a periodic sequence of structurally different layers (homologous series). In some cases significant diffuse diffraction fractions along  $[001]^*$  indicate a 1D disorder of the structures.

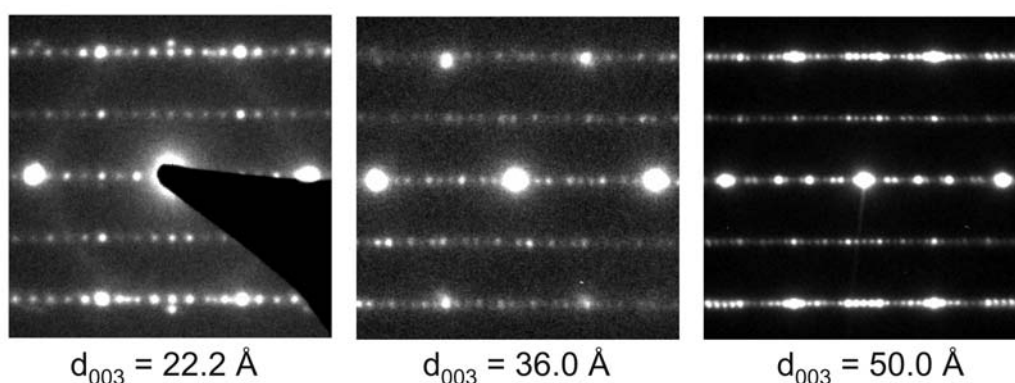


**Figure 6.10** Experimental patterns of selected area electron diffraction (SAED) along  $[001]^*$  direction of different particles from the reaction product  $\text{BaSn}_{3-x}\text{Bi}_x$  with  $x = 0.5$  at 500°C.

### 6.3.3 $\text{Ba}_4\text{Sn}_{9+y}\text{Bi}_{3-y}$ – The 8H structure of $\text{BaSn}_{3-x}\text{Bi}_x$ ( $x \sim 0.5$ )

#### 6.3.3.1 Crystal structure determination

Single crystal data collection was done on the Nonius DIP diffractometer with image plate detector, using the best crystal selected from the crushed of reaction product of Ba:Bi:Sn = 2:1:5 at 400°C. The crystallographic and refinement data are summarized in [Table 6.5](#) and the atomic parameters in [Tables 6.6](#). The compound crystallized in a hexagonal primitive unit cell with  $a = 7.271(1)$  Å and  $c = 22.165(4)$  Å ( $c/a = 2 \times 1.524$ ). On the basis of systematic absent reflections, the structure was solved in the space group  $P6_3/mmc$ , which is adopted by the parent  $\text{BaSn}_3$ . The unit cell parameters are also related to those of the parent structure  $\text{BaSn}_3$  as the  $a$ ,  $b$  parameters are in the same range (7.256(3) Å for  $\text{BaSn}_3$ ) for both compounds and the  $c$  parameter is nearly four time that of the parent ( $4 \times 5.492(3)$  Å), taking in account the small increase due to bigger size of Bi atom. All atomic positions were found during structure solution by direct methods. The refinement of the structure model with anisotropic atomic displacement parameters gives satisfactory residuals, but with electron density holes at Bi occupied position (site 6g) in the residual map, indicating possible mixed occupancy. No Bi occupancy was revealed in the two Sn positions on refinement. The final refinement with Bi/Sn mixed occupancy at site 6g yields about 42.2% Sn occupancy and leads to a good agreement between the refined composition  $\text{BaSn}_{2.57}\text{Bi}_{0.43(1)}$  and the nominal composition i.e.  $\text{BaSn}_{2.5}\text{Bi}_{0.5}$ . This model results in best final residuals of  $R_1 = 0.030$  and  $wR_2 = 0.094$  for all data with an essentially featureless residual map.

**Table 6.5** Crystallographic data and refinement parameters for Ba<sub>4</sub>Sn<sub>9+y</sub>Bi<sub>3-y</sub> (y ~ 1.3)

Empirical formula	Ba <sub>4</sub> Sn <sub>10.27</sub> Bi <sub>1.73(3)</sub>
Formula weight	2129.39
Temperature	293(2) K
Crystal size	0.05×0.05×0.2 mm <sup>3</sup>
Mosaicity (°)	0.398
Crystal color	grey with metallic luster
Diffractometer	Nonius DIP
Crystal system, Space group	hexagonal, P6 <sub>3</sub> /mmc (Nr. 194)
Unit cell parameters	a = b = 7.271(1) Å ; c = 22.165(4) Å
Unit cell Volume, Z	1014.8(3) Å <sup>3</sup> , Z = 2
Density calculated	6.969 g/cm <sup>3</sup>
Absorption coefficient (Mo K <sub>α</sub> )	34.87 mm <sup>-1</sup> (λ = 0.71073 Å)
Absorption correction	semi-empirical
F(000)	1761.8
Theta range	1.84° – 27.69°
Index range	-9 ≤ h ≤ 9, -9 ≤ k ≤ 9, -28 ≤ l ≤ 28
Data completeness	99.4%
Collected reflections	14134 (R <sub>σ</sub> = 0.020)
Unique reflections	510 (R <sub>int</sub> = 0.065)
Structure solution and refinement	SHELXTL (Siemens) (direct method)
Refinement method	Full-matrix least-squares on F <sup>2</sup>
Parameters	24
Goodness of fit on F <sup>2</sup>	1.281
Observed reflections [I > 2σ(I)]	508
Final R indices	R <sub>1</sub> = 0.029, wR <sub>2</sub> = 0.077
Final R indices (all data)	R <sub>1</sub> = 0.030, wR <sub>2</sub> = 0.094
Weighting parameters	a = 0.0336 / b = 34.62
Extinction coefficient	0.00064(10)
Residual map (e <sup>-</sup> / Å <sup>3</sup> )	1.41 / -0.98

**Table 6.6a** Atomic coordinates and equivalent isotropic ADPs of Ba<sub>4</sub>Sn<sub>9+y</sub>Bi<sub>3-y</sub>

Atom	Wyck.	s.o.f.	x	y	z	U <sub>eq</sub> / Å <sup>2</sup>
Sn1	6h		0.0565(2)	0.5283(1)	¼	0.0160(4)
Sn2	12k		0.1942(1)	0.8058(1)	0.1249(1)	0.0179(3)
Bi1	6g	0.58(1)	½	½	½	0.0223(4)
Sn	6g	0.42(1)	½	½	½	0.0223(4)
Ba1	2b		0	0	¼	0.0164(5)
Ba2	4f		1/3	2/3	0.6340(1)	0.0158(4)
Ba3	2a		0	0	0	0.0183(5)

U<sub>eq</sub> is defined as one third of the trace of the orthogonalized U<sup>ij</sup> tensor

**Table 6.6b** Anisotropic thermal displacement parameters (Å<sup>2</sup>) of Ba<sub>4</sub>Sn<sub>9+y</sub>Bi<sub>3-y</sub>

Atom	U <sub>11</sub>	U <sub>22</sub>	U <sub>33</sub>	U <sub>12</sub>	U <sub>13</sub>	U <sub>23</sub>
Sn1	0.0156(7)	0.016(1)	0.016(1)	0.0078(3)		
Sn2	0.0177(4)	U <sub>11</sub>	0.018(1)	0.0084(4)	-U <sub>23</sub>	0.0005(2)
Bi1/Sn	0.0217(4)	U <sub>11</sub>	0.016(1)	0.0052(4)	-U <sub>23</sub>	-0.0001(2)
Ba1	0.0133(6)	U <sub>11</sub>	0.023(1)	0.0066(3)		
Ba2	0.0145(5)	U <sub>11</sub>	0.018(1)	0.0072(2)		
Ba3	0.0166(6)	U <sub>11</sub>	0.022(1)	0.0083(3)		

### 6.3.3.2 Structural description and relationship

The compound  $\text{BaSn}_{2.57}\text{Bi}_{0.43(1)}$ , which should be written  $\text{Ba}_4\text{Sn}_{10.27}\text{Bi}_{1.73(3)}$  to reflect the observed 8H stacking, may be viewed as a distorted substitution variant of a close-packing of spheres (Figure 6.11). It has a 8H structure, meaning that it crystallizes in hexagonal symmetry with 8 layers of close-packed atoms per unit cell. The translational symmetry along the c-axis arises from the stacking of three crystallographically different close packed layers of two types (six hexagonal (*h*) and two cubic (*c*) layers) alternating with the sequence ABABACAC... (Jagodzinski notation (*hhhc*)<sub>2</sub>). The structure shows an ordered atomic distribution on five of its six crystallographic sites, and a hexagonal symmetry arrangement of Ba atoms. Only the *ccp* layers contain the Bi1/Sn mixed occupied position (site 6g, 42.2% Sn occupancy).  $\text{Ba}_4\text{Sn}_{10.27}\text{Bi}_{1.73(3)}$  corresponds to  $m = 3$ ,  $n = 1$  and  $y = 1.27(3)$  in the general formula  $\text{Ba}_{m+n}\text{Sn}_{3m+y}\text{Bi}_{3n-y}$ , where  $y$  represents the amount of Sn in predominantly Bi occupied position in the cubic close packed layers (*ccp* layers);  $m$  and  $n$  are the numbers of layers with cubic and hexagonal symmetry, respectively. The two close packed layers with hexagonal symmetry (*hcp* layers) are fully ordered and contain Ba and Sn with the ratio of 1:3, as in  $\text{BaSn}_3$ . Like in  $\text{BaSn}_3$ , the Sn atoms in the *hcp* layers are shifted with respect to the ideal positions in a closest packed layer in a way that discrete triangular  $\text{Sn}_3$ -units result and are well separated by Ba atoms. The Sn–Ba separation distances within the *hcp* layers (in-plane distances) of 3.653(1) and 3.658(1) Å are observed (Table 6.7). The shortest bond distances are found within those Sn trimer units with Sn–Sn distances of 3.019(2) Å and 3.035(2) Å, which compare very well with the corresponding distance in  $\text{BaSn}_3$  (3.058(1) Å). The Sn1–Sn2 distance (3.278(1) Å) between two  $\text{Sn}_3$  rings in the c-direction (out-planes contacts) is relatively short, while the corresponding in-plane inter-trimer distances (within the layer) are essentially non-bonding (> 4.2 Å), meaning that the  $\text{Sn}_3$  triangular units are clearly separated within the *ab* plane, but they interact strongly in the c direction. The Bi–Sn distance between *hcp* and *ccp* layers is 3.386(1) Å.

The antiprismatic stacking of three triangular  $\text{Sn}_3$ -units along the c-axis results in two condensed Sn octahedra (face-sharing) which forms a block that is identical, in terms of composition and structure, to a fragment of one-dimensional chains found in  $\text{BaSn}_3$ .

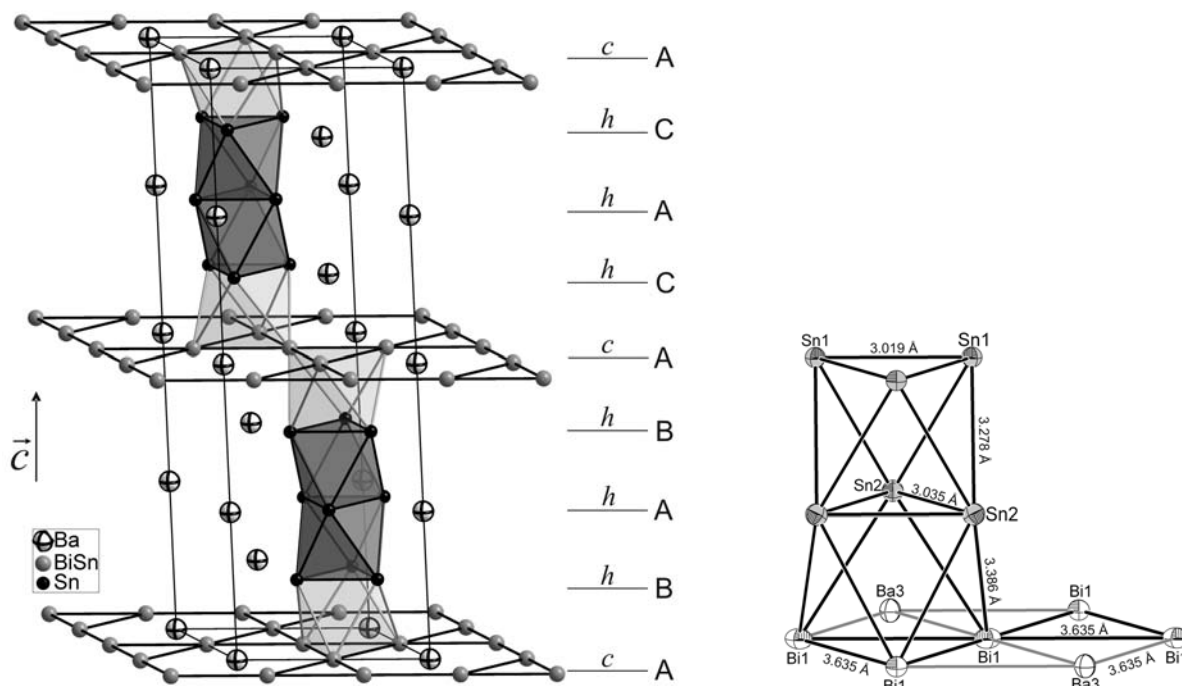


**Figure 6.11** Projection of the 8H crystal structure of  $\text{Ba}_4\text{Sn}_{10.27}\text{Bi}_{1.73(3)}$  with polyhedral representation showing two face-sharing Sn octahedra sandwiched between layers with cubic symmetry. (right) Fragment of the structure (thermal ellipsoids at 50% probability level) with some relevant interatomic distances.

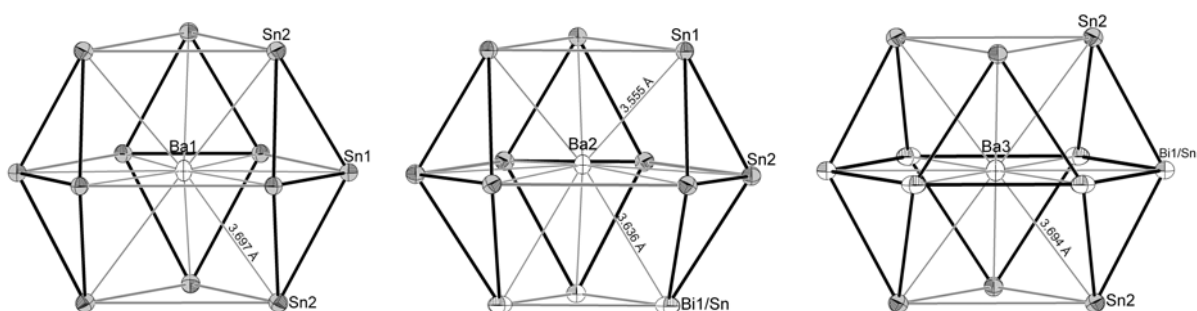


**Figure 6.12** Coordination polyhedra of Ba atoms in  $\text{Ba}_4\text{Sn}_{10.27}\text{Bi}_{1.73(3)}$  with thermal ellipsoids at 50% probability level: Ba(1) and Ba(2) Anticubeoctahedron, and Ba(3) Cubeoctahedron (black lines denoted shortest bonding distances)

**Table 6.7** Relevant Atomic distances in  $\text{Ba}_4\text{Sn}_{10.27}\text{Bi}_{1.73(3)}$  (standard deviation in parentheses)

Atomic pair	distance /Å		Atomic pair	distance /Å			
Sn1	-Sn1	3.019(2)	×2	Sn2	-Sn2	3.035(2)	×2
	-Sn2	3.278(1)	×4		-Sn1	3.278(1)	×2
	-Ba2	3.556(2)	×2		-Bi1/Sn	3.386(1)	×2
	-Ba1	3.653(1)	×2		-Ba2	3.658(1)	×2
Ba1	-Sn1	3.653(1)	×6	-Ba3	3.694(1)		
	-Sn2	3.698(1)	×6	Ba2	-Sn2	3.658(1)	×6
Bi1/Sn	-Sn2	3.386(1)	×4		-Sn1	3.556(2)	×3
	-Bi1/Sn	3.636(1)	×4		-Bi1/Sn	3.636(1)	×3
	-Ba3	3.636(1)	×2	Ba3	-Bi1/Sn	3.636(1)	×6
	-Ba2	3.636(1)	×2		-Sn2	3.694(1)	×6

In contrast to these “ $\text{BaSn}_3$ ” blocks, no distortion is observed in the *ccp* layers, in which Bi–Bi and Ba–Bi distances are all equal (3.636(1) Å). This indicates that these cubic layers correspond to ideal layers of cubic close packed of atoms, with no bond distance segregation which is consistent with mainly metallic interactions. In the binary phase  $\text{BaBi}_3$ ,<sup>[20]</sup> the Kagomé nets are slightly distorted because of the compression of the  $\text{Bi}_6$  octahedra, resulting in Bi–Bi separation of 3.658(1) Å and 3.668(1) Å and, Ba–Bi distance of 3.658(1) Å. Shorter inter-atomic distances within the *ccp* layers in  $\text{Ba}_4\text{Sn}_{10.27}\text{Bi}_{1.73(3)}$  is due to the smaller size of Sn atoms.

Thus,  $\text{Ba}_4\text{Sn}_{10.27}\text{Bi}_{1.73(3)}$  can be viewed as a recombination structure of the simple parents  $\text{BaSn}_3$  and  $\text{Ba}(\text{Bi},\text{Sn})_3$  that are periodically divided into blocks of  $\text{BaSn}_3$ -type and slabs of  $\text{BaBi}_3$ -type. The chains of two condensed Sn octahedra forming the  $\text{BaSn}_3$ -like blocks are sandwiched between two *ccp* layers through the tri-member Bi(1)/Sn ring of their Kagome-nets in a way that two additional (hetero-nuclear) octahedra are formed. The resulting chains of four elongated face-sharing octahedra, running parallel to the *c*-axis are connected exclusively by their corners in the *ccp* layers. The compression of the *c*-axis is reflected in the ratio  $c/a = 2 \times 1.524$  which is smaller than the value for the ideal closest packed structure ( $c/a = 1.633$ ) and this indicates that the interactions along the chains of four condensed octahedra are stronger than between those chains in the *ab* plane. Similar compression is observed in  $\text{BaSn}_3$  with  $c/a = 1.516$ .

Ba(1) and Ba(2) atoms in the *hcp* layers have anticubeoctahedral coordination geometry whereas Ba(3) atoms in the *ccp* layers have cubeoctahedral coordination geometry (Figure 6.12). The Ba2 atoms, which are positioned between hexagonal and cubic layers, are off-plane and shifted in a way that their interactions with the hexagonal layers are stronger than with the cubic layers. As a corollary, compared to in-plane distances, the Ba–Sn out-plane distances are shorter for Ba2–Sn1 (3.556(2) Å) but, longer for Ba1–Sn2 (3.698(1) Å). This may be ascribed to the mostly ionic type of Ba–Sn interactions in the hexagonal layers in contrast to rather metallic interactions in the cubic layers.

A filled variant of the 8H structure of  $\text{Ba}_4\text{Sn}_{10.27}\text{Bi}_{1.73(3)}$  can be found in the perovskites structures like  $\text{Ba}_4\text{Mn}_4\text{O}_{12}$ <sup>[28]</sup> with Sn and Bi at oxygen positions and the centers of the octahedra (Mn position in the perovskites) remain unoccupied [ $\text{Ba}_4\Box_4(\text{Sn},\text{Bi})_{12}$ ]. By analogy with  $\text{BaSn}_3$ , we can assume that a charge transfer from Ba to Sn results in

the formulation  $\text{Ba}^{2+}[\text{Sn}_3]^{2-}$  in the *hcp* layers, whereas the  $\text{Ba}(\text{Bi},\text{Sn})_3$  solid solution forming *ccp* layers where no significant bond segregation is observed, represent pure intermetallic slabs. Then, if only the shortest Sn–Sn contacts are considered to be bonding, the tin atoms forming the blocks of condensed octahedra may be regarded as  $[\text{Sn}_3]^{2-}$  anions that are isoelectronic with aromatic  $2\pi$ -electron cyclopropenyl cations ( $\text{C}_3\text{R}_3^+$ ), the simplest aromatic hydrocarbon. The antiprismatic stacking of these triangular units allows strong interactions between their  $\pi$ -systems and results in chains of two condensed octahedra that are sandwiched between two typical intermetallic layers ( $\text{AuCu}_3$ -type). This description implies that the 8H structure of  $\text{Ba}_4\text{Sn}_{10.27}\text{Bi}_{1.73(3)}$  possesses the structural motives of both charge balance and pure intermetallic compounds. This bonding picture, in which a structure is partitioned in two alternating slabs of ‘molecular’ closed-shell and typical intermetallic phases, was applied in other phases like  $\text{SrSn}_3$  and  $\text{Ca}_5\text{In}_9\text{Sn}_6$  [29] that can also be viewed as distorted and substituted close-packed structures.

### 6.3.4 $\text{Ba}_{13}\text{Sn}_{30+y}\text{Bi}_{9-y}$ – The 39R structure of $\text{BaSn}_{3-x}\text{Bi}_x$ ( $x \sim 0.5$ )

#### 6.3.4.1 Crystal structure determination

Single crystal data collection was done on the Enraf-Nonius CCD diffractometer at the window of a rotating anode, using the best crystal selected from the crushed of reaction product  $\text{Ba}:\text{Bi}:\text{Sn} = 2:1:5$  at  $500^\circ\text{C}$ . The crystallographic and refinement data are summarized in [Table 6.8](#) and the atomic parameters in [Tables 6.9](#). The compounds crystallize in a rhombohedra unit cell with  $a = 7.273(1) \text{ \AA}$ ,  $c = 108.04(2) \text{ \AA}$  ( $c/a = 10 \times 1.486$ ) in hexagonal setting. The unit cell is related to that of the parent structure of  $\text{BaSn}_3$  with the very long  $c$  axis being nearly 20 times longer. On the basis of systematic absence conditions, the structure was solved in the space group  $R\bar{3}m$ . All atomic positions were found during structure solution by direct methods. The refinement of all atomic positions and anisotropic atomic displacement parameters gives satisfactory residuals. All possible mixed occupancies were checked, and no Bi occupancy was found neither in Sn(1) nor in Sn(2) positions on refinement, but two atomic positions (sites 9e and 18h) show Bi/Sn mix occupancy with about 36% Sn and 35.2% Sn respectively, and resulting in a refined chemical composition that is in good agreement with the starting composition i.e.  $\text{BaSn}_{2.553}\text{Bi}_{0.447(4)}$  which is close to that of the previous *hhhc* homologue  $\text{BaSn}_{2.57}\text{Bi}_{0.43(1)}$ . To reflect the observed 39R structure, the compound should be formulated as  $\text{Ba}_{13}\text{Sn}_{33.19}\text{Bi}_{5.81(4)}$ . This gives the best final residuals of  $R_1 = 0.037$  and  $wR_2 = 0.065$  for all data and, the residual electron density map shows no significant feature.

#### 6.3.4.2 Structural description and relationship

The structure of  $\text{Ba}_{13}\text{Sn}_{33.19}\text{Bi}_{5.81(4)}$  ([Figure 6.13](#)) shows an intergrowth of hexagonal and cubic close-packed layers of atoms with a more complex stacking sequence compared to the previous 8H homologue  $\text{Ba}_4\text{Sn}_{10.27}\text{Bi}_{1.73(3)}$ . While the  $a$ ,  $b$  unit cell parameters are similar to those of the previous *hhhc* homologue, quite long range ordering emerges in the translational symmetry along  $c$ -axis arising from a record 39 layers stacking with the sequence ABABACACACBCBCACACBCBCBABABCBCBA-BABACACA... (Jagodzinski notation  $(hhhc)_2hhhhc$ ) giving a very long  $c$  parameter of  $108.05(2) \text{ \AA}$ . The formulation  $\text{Ba}_{13}\text{Sn}_{33.19}\text{Bi}_{5.81(4)}$  corresponds to the member  $m = 10$ ,  $n = 3$  and  $y = 3.19(4)$  of the homologous series  $\text{Ba}_{m+n}\text{Sn}_{3m+y}\text{Bi}_{3n-y}$ . Here, the stacking sequence derives from the previous *hhhc* homologue by adding one hexagonal layer

at every third BaSn<sub>3</sub>-like block. This results in one thicker BaSn<sub>3</sub>-like block which contains 3 condensed tin octahedra, alternating with two blocks of two face-sharing tin octahedra. Also the smaller ratio of  $c/a = 10 \times 1.486$ , compared to that of the *hhhc* phase, indicates stronger interaction between the layers, which is consistent with the increase of the BaSn<sub>3</sub>-like hexagonal layers. Interestingly, the refined chemical composition BaSn<sub>2.553</sub>Bi<sub>0.447(4)</sub> is closed to that of the previous *hhhc* homologous phase BaSn<sub>2.57</sub>Bi<sub>0.43(1)</sub> which is even virtually Sn-richer. The formation of one additional BaSn<sub>3</sub>-like hexagonal layer goes together with the decrease of Sn amount in the BaBi<sub>3</sub>-like cubic layers so that the overall composition doesn't change significantly in the two homologous phases.

**Table 6.8** Crystallographic and refinement data of Ba<sub>13</sub>Sn<sub>30+y</sub>Bi<sub>9-y</sub> ( $y \sim 3.2$ )

Empirical formula	Ba <sub>13</sub> Sn <sub>33.19</sub> Bi <sub>5.81(4)</sub>
Formula weight	6938.92
Temperature	293(2) K
Crystal size	0.1×0.1×0.3 mm <sup>3</sup>
Mosaicity (°)	0.340(1)
Crystal color	Silvery
Diffractometer	Enraf-Nonius CCD
Crystal system, Space group	Trigonal, R $\bar{3}$ m (Nr. 166)
Unit cell parameters	$a = b = 7.273(1) \text{ \AA}$ ; $c = 108.04(2) \text{ \AA}$
Unit cell Volume, Z	4949.9(1) Å <sup>3</sup> , Z = 3
Density calculated	6.983 g/cm <sup>3</sup>
Absorption coefficient (Mo K $\alpha$ )	35.317 mm <sup>-1</sup> ( $\lambda = 0.71073 \text{ \AA}$ )
Absorption correction	empirical
F(000)	8628.0
Theta range	1.02°-25.35°
Resolution range	20.00-0.83 Å
Index range	$-8 \leq h \leq 8$ , $-8 \leq k \leq 8$ , $-127 \leq l \leq 129$
Data completeness	99.9%
Collected reflections	23243 ( $R_\sigma = 0.0762$ )
Unique reflections	1281 ( $R_{\text{int}} = 0.1989$ )
Structure solution and refinement	SHELXTL (Siemens) (direct method)
Refinement method	Full-matrix least-squares on F <sup>2</sup>
Parameters	64
Goodness of fit on F <sup>2</sup>	1.130
Observed reflections [ $ I  > 2\sigma(I)$ ]	1112
Final R indices	$R_1 = 0.027$ , $wR_2 = 0.062$
Final R indices (all data)	$R_1 = 0.037$ , $wR_2 = 0.065$
Extinction coefficient	0.000053(4)
Residual map (e <sup>-</sup> /Å <sup>3</sup> )	2.03 / -2.50

$$w = 1/[\sigma^2(F_o^2) + (0.00 \times P)^2 + 23.68 \times P]$$

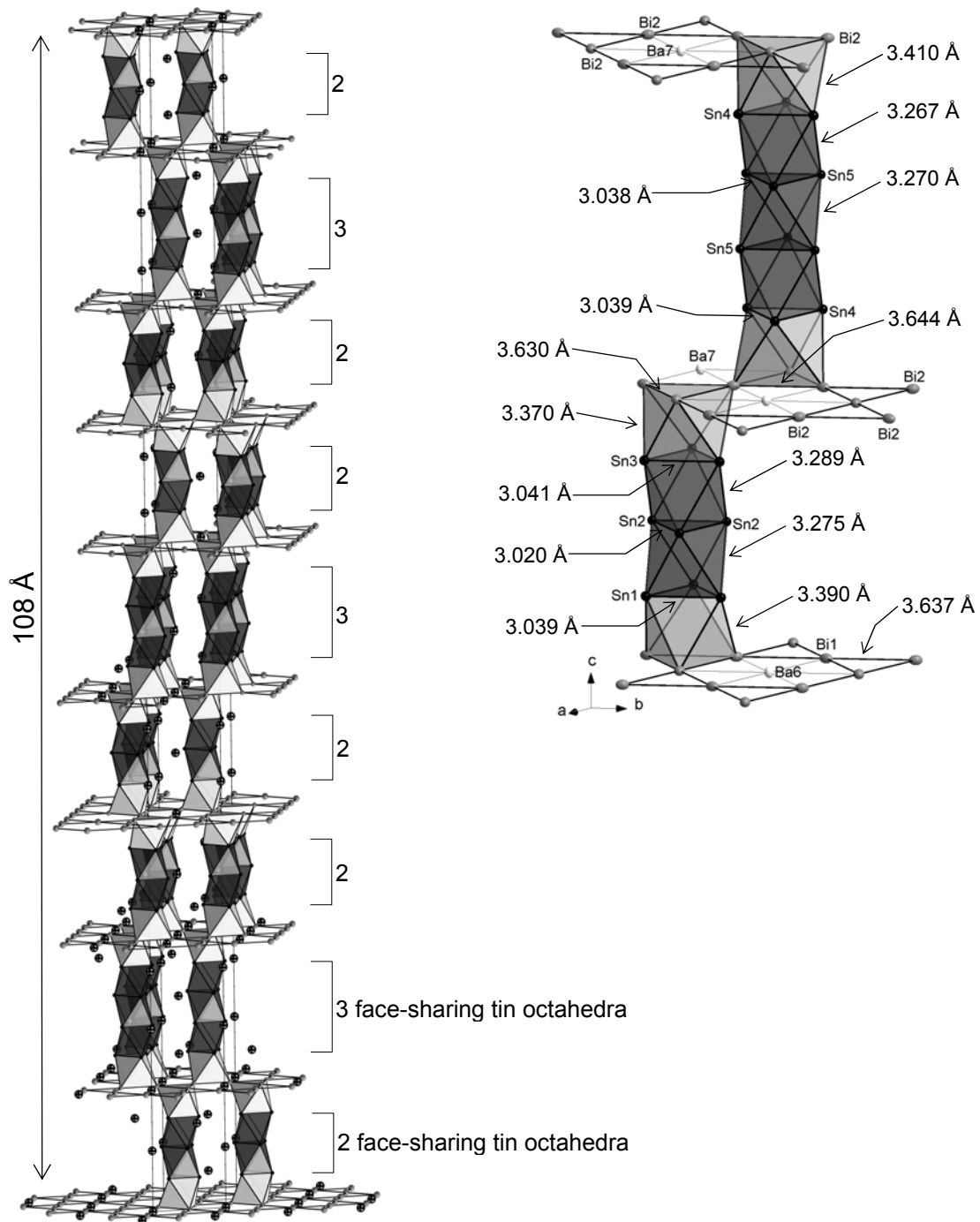


**Figure 6.13** (left) Projection of the structure of  $\text{Ba}_{13}\text{Sn}_{30+y}\text{Bi}_{9-y}$  with polyhedral representation showing the stacking of alternating chains of face sharing tin octahedra (two or three condensed tin octahedra), separated by typical intermetallic *ccp* layers. (right) Fragment of the structure of  $\text{Ba}_{13}\text{Sn}_{30+y}\text{Bi}_{9-y}$  with atom labeling and some interatomic distances.

**Table 6.9a** Atomic coordinates and equivalent isotropic displacement parameters

Atom	Wyck.	s.o.f.	x	y	z	U <sub>eq</sub> /Å <sup>2</sup>
Sn1	18h	1	0.4726(1)	$\bar{x}$	0.35899(1)	0.0180(2)
Sn2	18h	1	0.6101(1)	2 $\bar{x}$	0.38462(1)	0.0158(2)
Sn3	18h	1	0.4727(1)	$\bar{x}$	0.41040(1)	0.0179(2)
Sn4	18h	1	0.1393(1)	2x	0.53828(1)	0.0179(2)
Sn5	18h	1	0.8608(1)	$\bar{x}$	0.51277(1)	0.0151(2)
Ba1	6c	1	0	0	0.36079(1)	0.0155(3)
Ba2	6c	1	2/3	1/3	0.38471(1)	0.0165(3)
Ba3	6c	1	0	0	0.40845(1)	0.0158(3)
Ba4	6c	1	1/3	2/3	0.46333(1)	0.0155(3)
Ba5	6c	1	2/3	1/3	0.48763(1)	0.0154(3)
Ba6	3a	1	2/3	1/3	1/3	0.0179(3)
Ba7	6c	1	2/3	1/3	0.43608(1)	0.0175(3)
Bi1	9e	0.641(6)	1/6	1/3	1/3	0.0241(3)
Sna	9e	0.359(6)	1/6	1/3	1/3	0.0241(3)
Bi2	18h	0.648(5)	0.16700(3)	0.33399(7)	0.43585(0)	0.0244(2)
Snb	18h	0.352(5)	0.16700(3)	0.33399(7)	0.43585(0)	0.0244(2)

U<sub>eq</sub> is defined as one third of the trace of the orthogonalized U<sup>ij</sup> tensor

**Table 6.9b** Anisotropic thermal Atomic displacement parameters (Å<sup>2</sup>) for Ba<sub>13</sub>Sn<sub>33.19</sub>Bi<sub>5.81(4)</sub>

Atom	U <sub>11</sub>	U <sub>22</sub>	U <sub>33</sub>	U <sub>12</sub>	U <sub>13</sub>	U <sub>23</sub>
Sn1	0.0177(3)	U <sub>11</sub>	0.0180(4)	0.0083(3)	-U <sub>23</sub>	-0.0007(1)
Sn2	0.0154(3)	U <sub>11</sub>	0.0163(4)	0.0077(2)	-3U <sub>23</sub>	-0.0001(1)
Sn3	0.0175(3)	U <sub>11</sub>	0.0179(5)	0.0082(3)	-U <sub>23</sub>	0.0003(1)
Sn4	0.0174(3)	0.0192(4)	0.0177(4)	0.0096(2)	½U <sub>23</sub>	-0.0014(3)
Sn5	0.0150(3)	U <sub>11</sub>	0.0152(5)	0.0074(3)	-U <sub>23</sub>	-0.0002(1)
Ba1	0.0146(3)	U <sub>11</sub>	0.0174(6)	0.0073(2)		
Ba2	0.0135(3)	U <sub>11</sub>	0.0224(6)	0.0068(2)		
Ba3	0.0146(3)	U <sub>11</sub>	0.0182(6)	0.0073(2)		
Ba4	0.0147(3)	U <sub>11</sub>	0.0172(6)	0.0074(2)		
Ba5	0.0128(3)	U <sub>11</sub>	0.0205(6)	0.0064(2)		
Ba6	0.0156(4)	U <sub>11</sub>	0.0225(9)	0.0078(2)		
Ba7	0.0153(3)	U <sub>11</sub>	0.0218(7)	0.0077(2)		
Bi1/Sn	0.0235(3)	0.0348(4)	0.0178(5)	0.0174(2)	½U <sub>23</sub>	0.0008(3)
Bi2/Sn	0.0241(3)	0.0353(3)	0.0176(4)	0.0177(2)	½U <sub>23</sub>	-0.0007(2)

Among the 13 crystallographic positions (Table 6.9a), 7 are occupied by Ba atoms with 5 being in the ordered hexagonal layers together with Sn atoms and, 2 in partially ordered cubic layers together with Bi/Sn mixed occupied crystallographic sites.

The Sn atoms in the *hcp* layers are again shifted with respect to the ideal position in a hexagonal closest packed layer resulting in isolated Sn<sub>3</sub> triangular units that are well separated within the plane by long Ba–Sn contacts (from 3.653 Å to 3.659 Å). The shortest Sn–Sn contacts (Table 6.10) are found within the triangular units and range

from 3.020(1) Å to 3.039(1) Å. Contacts between those trimers in the *c* direction range from 3.270(1) Å to 3.289(1) Å. Further Sn–Sn in-plane contacts are longer than 4.2 Å and represent non bonding interactions. On the other hand, the Bi–Sn contacts between cubic and hexagonal layer range from 3.370(1) Å to 3.390(1) Å. One over two cubic layers is slightly distorted giving Bi2–Bi2 contacts of 3.630(1) Å and 3.644(1) Å and intermediate Bi2–Ba7 distance of 3.637(1) Å. It is worth noting that the undistorted cubic layers are situated between two chains with three stacked triangular Sn-units, while the distorted are between chains with four and three Sn trimers. This means that the slight distortion in one *ccp* layer may be due mainly to packing effects. The Bi1–Bi1 and Bi1–Ba6 distances within the undistorted cubic layers are similar (3.637(1) Å).

**Table 6.10** Some relevant inter-atomic distances in  $\text{Ba}_{13}\text{Bi}_{9-y}\text{Sn}_{30+y}$  (standard deviation in parentheses)

Atomic pair	distance /Å	
Sn1	–Sn1	3.039(1) ×2
	–Sn2	3.275(1) ×2
	–Bi1	3.390(1) ×2
	–Ba1	3.658(1) ×2
Sn3	–Sn3	3.041(1) ×2
	–Sn2	3.289(1) ×2
	–Bi2	3.370(1) ×2
	–Ba3	3.659(1) ×2
Sn5	–Sn5	3.038(1) ×2
	–Sn4	3.267(1) ×2
	–Sn5	3.270(1) ×2
	–Ba5	3.653(1) ×2
	–Ba5	3.654(1) ×2
Ba1	–Sn1	3.658(1) ×6
	–Sn2	3.559(1) ×3
	–Bi1/Sn	3.635(1) ×3
Ba2	–Sn2	3.654(1) ×6
	–Sn3	3.698(1) ×3
	–Sn1	3.701(1) ×3
Ba3	–Sn2	3.558(1) ×3
	–Bi2/Sn	3.632(1) ×3
	–Sn3	3.659(1) ×6
Ba5	–Sn5	3.653(1) ×6
	–Sn5	3.654(1) ×3
	–Sn4	3.716(1) ×3

Atomic pair	distance /Å	
Sn2	–Sn2	3.020(1) ×2
	–Sn1	3.275(1) ×2
	–Sn3	3.289(1) ×2
	–Ba2	3.654(1) ×2
Sn4	–Sn4	3.039(1) ×2
	–Sn5	3.267(1) ×2
	–Bi2	3.410(1) ×2
	–Ba4	3.657(1) ×2
Bi1/Sn	–Sn1	3.390(1) ×4
	–Bi1/Sn	3.637(1) ×4
	–Ba6	3.637(1) ×2
	–Ba1	3.635(1) ×2
Bi2/Sn	–Sn3	3.370(1) ×2
	–Sn4	3.410(1) ×2
	–Bi2/Sn	3.630(1) ×2
	–Ba7	3.637(1) ×2
Ba4	–Bi2/Sn	3.644(1) ×2
	–Sn5	3.556(1) ×3
	–Bi2/Sn	3.634(1) ×3
Ba6	–Sn4	3.657(1) ×6
	–Bi1/Sn	3.637(1) ×6
	–Sn1	3.697(1) ×6
Ba7	–Bi2/Sn	3.637(1) ×6
	–Sn3	3.697(1) ×3
	–Sn4	3.695(1) ×3

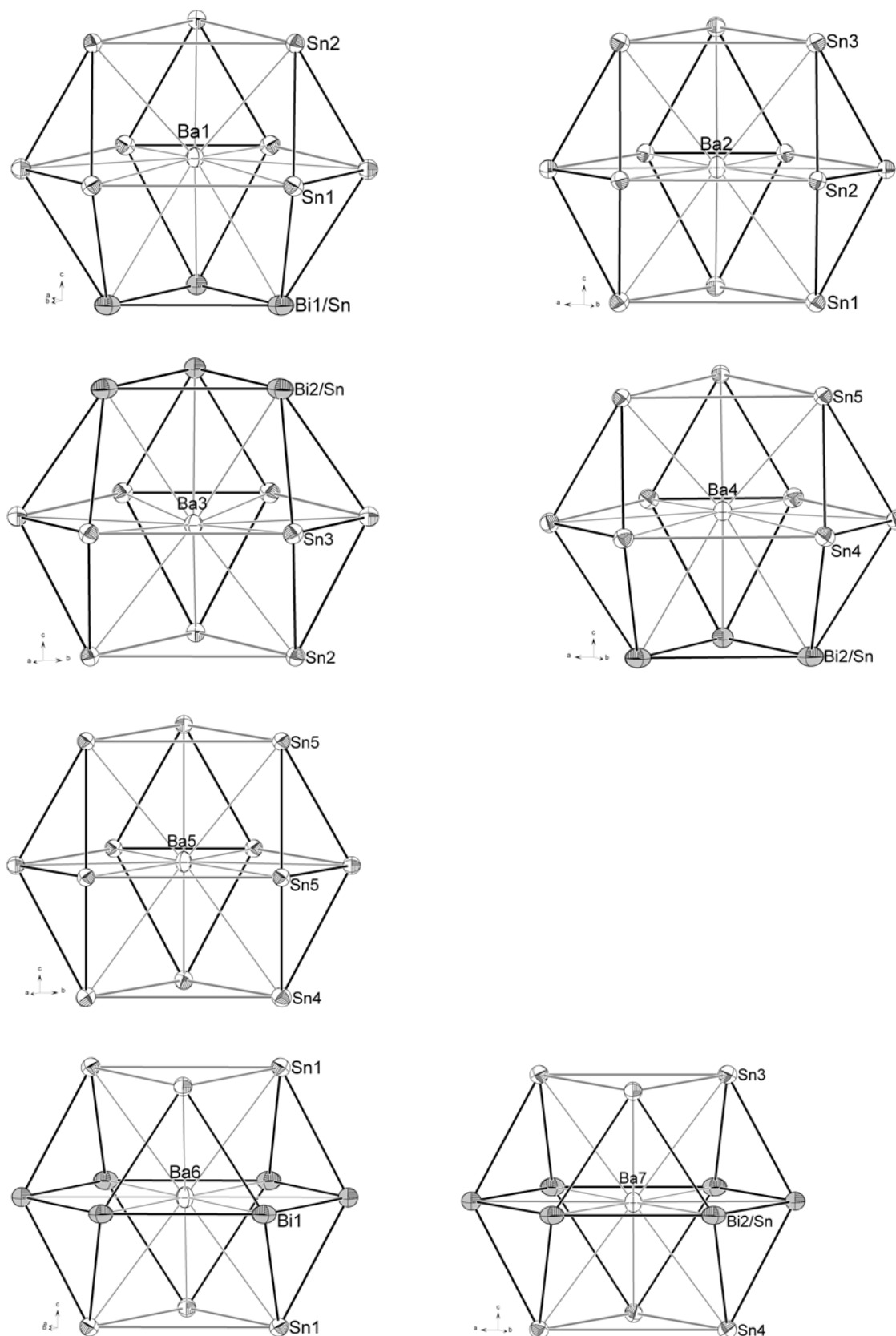


**Figure 6.14** Coordination polyhedra of Ba atoms in  $\text{Ba}_{13}\text{Bi}_{9-y}\text{Sn}_{30+y}$ : Ba1, Ba2, Ba3, Ba4 and Ba5 Anticubeoctahedron, Ba6 and Ba7 cubeoctahedron (black lines denoted shortest interatomic distances); thermal ellipsoids at 50% probability level

The Ba1, Ba2, Ba3, Ba4 and Ba5 atoms in the *hcp* layers have anticubeoctahedral coordination geometry whereas Ba6 and Ba7 atoms in the *ccp* layers have beoctahedral coordination geometry (Figure 6.14). When compared to in-plane distances (Table 6.10), the Ba–Sn out-plane distances are shorter for Ba1, Ba3 and Ba4 which are positioned between hexagonal and cubic layers, but longer for Ba2, Ba5 atoms which are positioned between two hexagonal layers. In the former group, the Ba atoms are always off-plane and shifted in the direction of the hexagonal layers which indicates stronger interaction with the lone pair of  $\text{Sn}_3$  units, originate from the stronger ionic effects in the hexagonal layers. Similar observations were can be made in the *hhc* homologous compound described above.

Similarly to the previous homologous member  $\text{Ba}_4\text{Sn}_{10.27}\text{Bi}_{1.73(3)}$  we can assume that a charge transfer from Ba to Sn results in the formulation  $\text{Ba}^{2+}[\text{Sn}_3]^{2-}$  in the *hcp* layers, whereas in the *ccp* layers, which correspond to the solid solution  $\text{Ba}(\text{Bi},\text{Sn})_3$ , are more typical intermetallic. Here, we have two different blocks of face-sharing Sn octahedra in ratio 2 to 1; one block containing 3 face-sharing octahedra and two blocks with 2 face-sharing octahedra that are separated by the *ccp*-layers. Two successive blocks with two condensed Sn octahedra  $[\text{Sn}_9]^{6-}$  alternate with one block of three condensed Sn octahedra  $[\text{Sn}_{12}]^{8-}$ , building up an intergrowth structure with two closed-shell blocks and one intermetallic layer as components.

### 6.3.5 Synthesis and Crystal structure of $\text{Ba}_5\text{Sn}_{9+y}\text{Bi}_{6-y}$ – The 10H structure of $\text{BaSn}_{3-x}\text{Bi}_x$ ( $x \sim 0.75$ )

#### 6.3.5.1 Synthesis

The reaction mixture of pure elements with nominal composition  $\text{BaSn}_{3-x}\text{Bi}_x$  for  $x = 0.75$  was loaded in a sealed niobium ampoule. Some excess of Sn was necessary to obtain good single crystals which were found in the mixture  $\text{Ba}:\text{Bi}:\text{Sn} = 1:1:4$ . The mixtures were heated at  $150 \text{ K/h}$  to  $800 \text{ }^\circ\text{C}$  for 3 hours, then cooled to  $400 \text{ }^\circ\text{C}$  at  $150 \text{ K/h}$ , annealed for 120 h and, subsequently cooled down at  $-60 \text{ K/h}$  to room temperature. All products obtained were crystalline and exhibited a silvery colour and metallic luster.

#### 6.3.5.2 Crystal structure determination

Single crystal data collection was done on the Enraf-Nonius CCD diffractometer, using the best crystal (platy black shiny crystal) selected from the crushed of reaction product. The crystallographic data and refinement parameters are summarized in [Table 6.11](#) and the atomic parameters in [Tables 6.12](#). The compound crystallizes in a hexagonal primitive unit cell. On the basis of systematic absence conditions, the structure was successfully solved in the space group  $P6_3/\text{mmc}$ . The structure was successfully solved by direct methods. The refinement of all atomic positions and anisotropic atomic displacement parameters gives satisfactory residuals. All possible Sn/Bi mixed occupancies were checked, but only one atomic position (site 18k) shows refineable Bi/Sn mixed occupancy with about 39% Sn atoms. No Bi occupancy was found in hcp layers at Sn(1) or Sn(2) positions during refinement. This gives a good agreement between the refined composition  $\text{Ba}_5\text{Sn}_{11.34}\text{Bi}_{3.66(6)}$  ( $y = 2.34(6)$ , i.e.  $x = 0.73$ ) and the nominal composition  $\text{BaSn}_{3-x}\text{Bi}_x$  ( $x = 0.75$ ). This results in the best final residuals for all data of  $R_1 = 0.039$  and  $wR_2 = 0.094$  for 26 refined parameters.

**Table 6.11** Crystallographic data and refinement parameters for Ba<sub>5</sub>Sn<sub>9+y</sub>Bi<sub>6-y</sub> (y = 2.34(6))

Empirical formula	Ba <sub>5</sub> Sn <sub>11.34</sub> Bi <sub>3.66(6)</sub>
Formula weight	2797.51
Temperature	293(2) K
Crystal size	0.10×0.10×0.02 mm <sup>3</sup>
Mosaicity (°)	0.651(1)
Crystal colour	Silvery
Diffractometer	Enraf-Nonius CCD
Crystal system, Space group	hexagonal, P6 <sub>3</sub> /mmc (Nr. 194)
Unit cell parameters	a = b = 7.274(1) Å, c = 27.943(6) Å
Unit cell Volume, Z	1280.4(4) Å <sup>3</sup> , Z = 2
Density calculated	7.256 g/cm <sup>3</sup>
Absorption coefficient (Mo K <sub>α</sub> )	43.401 mm <sup>-1</sup> (λ = 0.71073 Å)
Absorption correction	semi-empirical
F(000)	2302
Theta range	1.46° – 25.35°
Index range	-8 ≤ h ≤ 8, -8 ≤ k ≤ 8, -33 ≤ l ≤ 33
Data completeness	100%
Collected reflections	17061 (R <sub>σ</sub> = 0.093)
Unique reflections	508 (R <sub>int</sub> = 0.026)
Structure solution and refinement	SHELXTL (Siemens) (direct method)
Refinement method	Full-matrix least-squares on F <sup>2</sup>
Parameters	26
Goodness of fit on F <sup>2</sup>	1.240
Observed reflections [I > 2σ(I)]	496
Final R indices	R <sub>1</sub> = 0.038, wR <sub>2</sub> = 0.093
Final R indices (all data)	R <sub>1</sub> = 0.039, wR <sub>2</sub> = 0.094
Residual map (e/Å <sup>3</sup> )	4.17 / -1.46

Weighting scheme:  $w = 1/[\sigma^2(F_o^2) + (0.0359 \times P)^2 + 51.39 \times P]$

**Table 6.12a** Atomic coordinates and equivalent isotropic displacement parameters for Ba<sub>5</sub>Sn<sub>9+y</sub>Bi<sub>6-y</sub>

Atom	Wyck.	s.o.f.	x	y	z	U <sub>eq</sub> / Å <sup>2</sup>
Sn(1)	6h	1	0.8052(1)	$\bar{x}$	¼	0.0147(4)
Sn(2)	12k	1	0.5280(1)	2x	0.1504(1)	0.0176(4)
Ba(1)	2c	1	1/3	2/3	¼	0.0149(6)
Ba(2)	4e	1	0	0	0.1578(1)	0.0150(4)
Ba(3)	4f	1	1/3	2/3	0.0563(1)	0.0184(5)
Bi(1)	12k	0.61(1)	0.8343(1)	$\bar{x}$	0.0511(1)	0.0257(4)
Sn	12k	0.39(1)	0.8343(1)	$\bar{x}$	0.0511(1)	0.0257(4)

U<sub>eq</sub> is defined as one third of the trace of the orthogonalized U<sup>ij</sup> tensor

**Table 6.12b** Anisotropic thermal displacement parameters (Å<sup>2</sup>) for Ba<sub>5</sub>Sn<sub>9+y</sub>Bi<sub>6-y</sub>

Atom	U <sub>11</sub>	U <sub>22</sub>	U <sub>33</sub>	U <sub>12</sub>	U <sub>13</sub>	U <sub>23</sub>
Sn(1)	0.015(1)	U <sub>11</sub>	0.014(1)	0.0081(6)		
Sn(2)	0.017(1)	0.019(1)	0.017(1)	0.0096(3)	-0.0006(2)	-0.0013(4)
Ba(1)	0.013(1)	U <sub>11</sub>	0.020(1)	0.0063(4)		
Ba(2)	0.015(1)	U <sub>11</sub>	0.016(1)	0.0073(3)		
Ba(3)	0.018(1)	U <sub>11</sub>	0.019(1)	0.0092(3)		
Bi(1)/Sn	0.025(1)	U <sub>11</sub>	0.017(1)	0.0048(4)	-U <sub>23</sub>	0.0024(2)

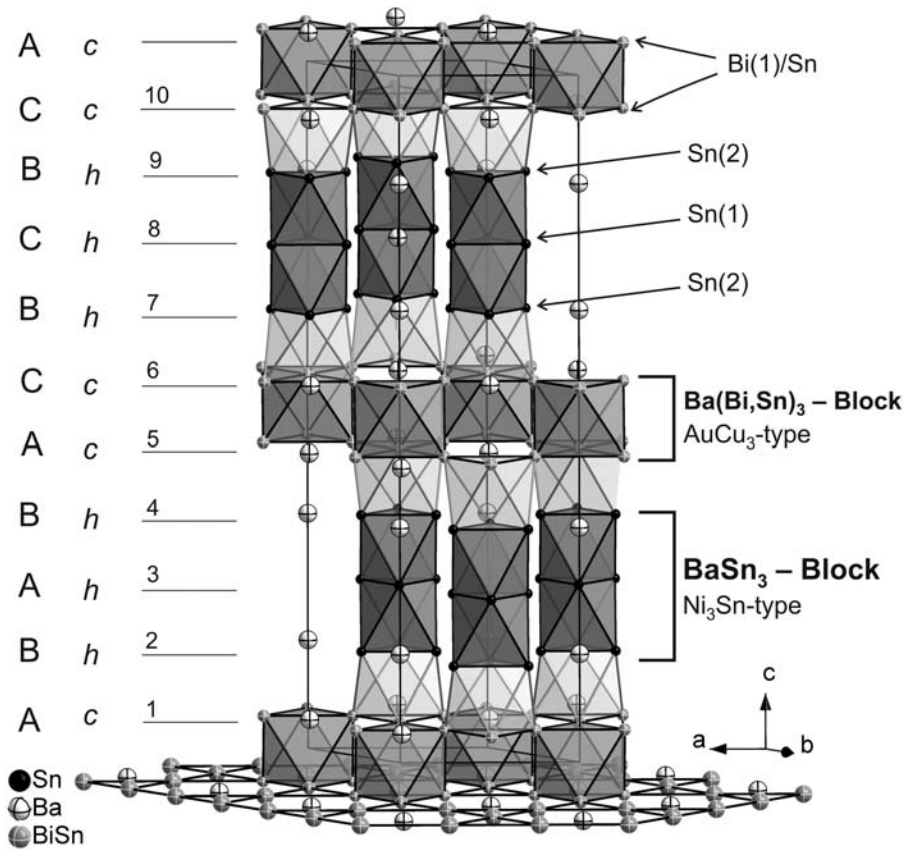


**Figure 6.15** Projection of the crystal structure of  $Ba_5Sn_{9+y}Bi_{3-y}$  showing the 10H stacking of hexagonal  $BaSn_3$ - and cubic  $BaBi_3$ -like layers

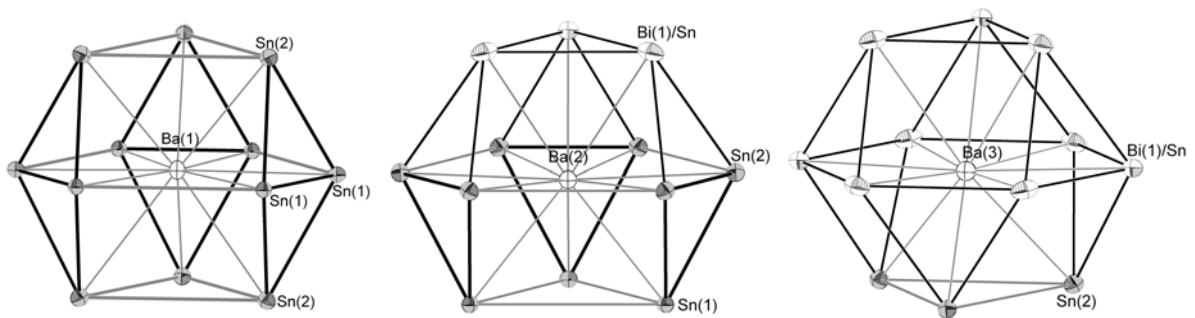


**Figure 6.16** Coordination polyhedra of Ba atoms in  $Ba_5Sn_{9+y}Bi_{3-y}$ : Ba(1) Anticubeoctahedron, Ba(2) and Ba(3) Cubeoctahedron (black lines denoted shortest interatomic distances); thermal ellipsoids at 50% probability level

### 6.3.5.3 Structural description and relationship

The formulation  $\text{Ba}_5\text{Sn}_{11.34}\text{Bi}_{3.66(6)}$  corresponds to  $m = 3$ ,  $n = 2$  and  $y = 2.34$  in the homologous series  $\text{Ba}_{m+n}\text{Sn}_{3m+y}\text{Bi}_{3n-y}$ . In the 10H structure of  $\text{Ba}_5\text{Sn}_{11.34}\text{Bi}_{3.66(6)}$  (Figure 6.15) the translational symmetry along the  $c$ -axis arises from 10 layer-stacking of cubic (4 layers) and hexagonal (6 layers) close packed layers of atoms with the sequence ABABACBCBC... (Jagodzinski notation  $(hhhcc)_2$ ). There are six different crystallographic sites from which five are ordered. Again, a mixed occupied Bi/Sn position (site 12k) is found in the layers with cubic symmetry (39% Sn occupancy). The structure derives from the previously described 8H homologous structure, by adding one more  $\text{Ba}(\text{Bi},\text{Sn})_3$ -like cubic layers to form thicker blocks with cubic symmetry which comprises two layers instead of only one observed in the Bi poorer 8H structure. The hexagonal layers are fully ordered and still identical in composition and structure to that of  $\text{BaSn}_3$ . The shortest Sn–Sn contacts correspond to the intra-trimer bond distances of 3.023(3) Å for Sn(1)–Sn(1) and 3.017(2) Å for Sn(2)–Sn(2) (Table 6.13). The in-plane Sn–Ba distances in the hexagonal layers are significantly long (3.654(1) Å and 3.660(1) Å). The Sn(1)–Sn(2) inter-trimer distance between two hexagonal layers is 3.285(1) Å, shorter than the corresponding in-plane inter-trimer distances ( $> 4.2$  Å). The Bi–Sn2 contact between cubic and hexagonal layers is 3.396(1) Å.

The cubic layers are slightly distorted with in-plane Bi–Bi contacts of 3.617(2) Å and 3.657(1) Å and, a Bi–Ba3 distance of 3.640(1) Å. Out-planes Bi–Bi contacts between two cubic layers are shorter (3.536(2) Å). Ba(1) and Ba(2) atoms have an anticubeoctahedral coordination geometry of exclusively Sn atoms for the former and of Sn and Bi for the latter while, Ba(3) are found in cubeoctahedral coordination geometry of Bi and Sn (Figure 6.16). The Ba2 atoms that are positioned between  $c$ - and  $h$ -layers are off-plane and shifted in the direction of the  $h$ -layer; this indicates stronger interactions with the lone-pair of the  $\text{Sn}_3$  trimer in  $h$ -layers.

The structure of  $\text{Ba}_5\text{Sn}_{11.34}\text{Bi}_{3.66(6)}$  contains strings of two condensed (face-sharing) Sn octahedra that are fragments of the infinite chain found in  $\text{BaSn}_3$ . These strings are sandwiched between 2D layers of edge sharing Bi/Sn octahedra (fragment of  $\text{BaBi}_3$ -type structure) to form a recombination structure of the two simple parents  $\text{BaSn}_3$  and  $\text{BaBi}_3$ .

Like in the previous homologous phases, we can assume that a charge transfer from Ba to Sn results in the formulation  $\text{Ba}^{2+}[\text{Sn}_3]^{2-}$  in the  $hcp$  layers, whereas the

$Ba(Bi,Sn)_3$  solid solution in the *ccp* layers are typical intermetallic slabs. Here, the block with hexagonal symmetry (face sharing Sn octahedra) is similar to that in the *hhhc* homologue, but the block with cubic symmetry (edge sharing octahedra) is doubled as a result of the increase of the Bi content, so that the structure and the composition of the  $BaSn_3$ -like block is preserved. This clearly indicates that the hexagonal layers are not affected by the increase of Bi rate; the system reacts to higher amounts of Bi by creating more of the  $BaBi_3$ -like *ccp*-layers.

**Table 6.13** Relevant Atomic distances in  $Ba_5Sn_{9+y}Bi_{6-y}$  (standard deviation in parentheses)

Atomic pair				distance /Å						
Sn1	-Sn1	3.023(3)	×2	Sn2	-Sn2	3.027(2)	×2			
	-Sn2	3.285(1)	×4		-Sn1	3.285(1)	×2			
	-Ba2	3.558(2)	×2		-Bi1/Sn	3.396(1)	×2			
	-Ba1	3.654(1)	×2		-Ba3	3.596(2)	×2			
Ba1	-Sn1	3.654(1)	×6	-Ba2	3.660(1)	×2	Ba2	-Sn2	3.660(1)	×6
	-Sn2	3.709(1)	×6	-Sn1	3.558(2)	×3		-Bi1/Sn	3.642(2)	×3
Bi1/Sn	-Sn2	3.396(1)	×2	Ba3	-Sn2	3.596(2)	×3			
	-Bi1/Sn	3.536(2)	×2		-Bi1/Sn	3.640(1)	×6			
	-Bi1/Sn	3.617(2)	×2		-Bi1/Sn	3.668(2)	×3			
	-Bi1/Sn	3.657(2)	×2							
	-Ba3	3.640(1)	×2							
	-Ba3	3.668(2)	×2							

### 6.3.6 Synthesis and Crystal structure of $Ba_2Sn_{3+y}Bi_{3-y}$ – The 12R structure of $BaSn_{3-x}Bi_x$ ( $x \sim 1$ )

#### 6.3.6.1 Synthesis

The reaction mixture of pure elements with nominal composition  $BaSn_{3-x}Bi_x$  for  $x = 1$  was loaded in sealed niobium ampoule. The mixtures were heated at 150 K/h to 800 °C for 3 hours, then cooled to 400 °C at 150K/h, then annealed for 120 h at this temperature, and subsequently cooled down at 60 K/h to room temperature. The reaction product was crystalline and exhibited a silvery colour and metallic luster.

#### 6.3.6.2 Crystal structure determination

Single crystal data collection was done on the Enraf-Nonius CCD diffractometer, using the best crystal (platy black shiny crystal) selected from the crushed of the reaction product. The crystallographic and refinement data are summarized in [Table](#)

6.14 and, the atomic parameters in Tables 6.15. BaSn<sub>2.0</sub>Bi<sub>1.0(2)</sub> crystallizes in a trigonal rhombohedra unit cell. On the basis of systematic absence conditions, the structure was successfully solved in the space group  $R\bar{3}m$ ,  $a = b = 7.276(1)$  Å and  $c = 33.713(7)$  Å ( $c/a = 3 \times 1.545$ ). All atomic positions were found with direct method. The refinement of all atomic positions and anisotropic atomic displacement parameters gives satisfactory residuals. Each atomic position was checked for possible mixed occupancy, but only one site (Wyck. 18h) gives significant Bi/Sn mixed occupancy with about 34% Sn atoms on refinement. This leads to a very good agreement between the refined and the nominal chemical compositions and gives the best final residuals for all data of  $R_1 = 0.061$  and  $wR_2 = 0.152$ , in which strong absorption problems are reflected ( $R_{\text{int}} = 28.1\%$ ).

**Table 6.14** Crystallographic data and refinement parameters for **Ba<sub>2</sub>Sn<sub>3+y</sub>Bi<sub>3-y</sub>** ( $y \sim 1$ )

Empirical formula	Ba <sub>2</sub> Sn <sub>4.03(4)</sub> Bi <sub>1.97(4)</sub>
Formula weight	1167.40
Temperature	293(2) K
Crystal size	0.05×0.2×0.2 mm <sup>3</sup>
Mosaicity (°)	0.490(2)
Crystal color	Silvery
Diffractometer	Enraf-Nonius CCD
Crystal system	Trigonal
Space group	$R\bar{3}m$ (Nr. 166)
Unit cell parameters	$a = b = 7.276(1)$ Å; $c = 33.713(7)$ Å
Unit cell Volume, Z	1545.6(4) Å <sup>3</sup> , Z = 6
Density calculated	7.525 g/cm <sup>3</sup>
Absorption coefficient (Mo K <sub>α</sub> )	50.98 mm <sup>-1</sup> ( $\lambda = 0.71073$ Å)
Absorption correction	semi-empirical
F(000)	2868.0
Theta range	1.00°– 25.35°
Resolution range	20.40 – 0.83 Å
Index range	$-8 \leq h \leq 8$ , $-8 \leq k \leq 8$ , $-40 \leq l \leq 40$
Data completeness	100%
collected reflections	11116 ( $R_\sigma = 0.056$ )
Unique reflections	401 ( $R_{\text{int}} = 0.281$ )
Structure solution and refinement	SHELXTL (Siemens) (direct method)
Refinement method	Full-matrix least-squares on F <sup>2</sup>
Parameters	21
Goodness of fit on F <sup>2</sup>	1.231
Observed reflections [ $I > 2\sigma(I)$ ]	376
Final R indices	$R_1 = 0.058$ , $wR_2 = 0.149$
Final R indices (all data)	$R_1 = 0.061$ , $wR_2 = 0.152$
Extinction	0.00018(5)
Residual map	Highest peak 6.44 [0.87 Å from Bi(1)] Deepest hole -2.61 [1.09 Å from Bi(1)]

$$w = 1/[\sigma^2(F_o^2) + (0.0764 \times P)^2 + 105.82 \times P]$$

**Table 6.15a** Atomic coordinates and equivalent isotropic displacement parameters

Atom	Wyck.	x	y	z	s.o.f	U <sub>eq</sub> / Å <sup>2</sup>
Bi(1)/	18h	0.1670(1)	2x	0.12437(3)	0.66(1)	0.0296(7)
Sn	18h	0.1670(1)	2x	0.12437(3)	0.34(1)	0.0296(7)
Sn(1)	18h	0.1373(2)	$\bar{x}$	-0.04182(4)		0.0231(6)
Ba(1)	6c	$\frac{1}{3}$	$\frac{2}{3}$	0.03616(7)		0.0212(7)
Ba(2)	6c	$-\frac{1}{3}$	$\frac{1}{3}$	0.11974(7)		0.0235(7)

U<sub>eq</sub> is defined as one third of the trace of the orthogonalized U<sup>ij</sup> tensor

**Table 6.15b** Anisotropic thermal displacement parameters (Å<sup>2</sup>) for Ba<sub>2</sub>Sn<sub>3+y</sub>Bi<sub>3-y</sub> (y ~ 1)

Atom	U <sub>11</sub>	U <sub>22</sub>	U <sub>33</sub>	U <sub>12</sub>	U <sub>13</sub>	U <sub>23</sub>
Bi(1)/Sn	0.025(1)	0.039(1)	0.030(1)	0.0193(5)	$\frac{1}{2}U_{23}$	0.0030(4)
Sn(1)	0.018(1)	U <sub>11</sub>	0.033(1)	0.0090(7)	-U <sub>23</sub>	-0.0004(3)
Ba(1)	0.016(1)	U <sub>11</sub>	0.031(1)	0.0081(4)		
Ba(2)	0.019(1)	U <sub>11</sub>	0.033(1)	0.0094(5)		

### 6.3.6.3 Structural description and relationship

The formulation Ba<sub>2</sub>Sn<sub>4</sub>Bi<sub>2</sub> corresponds to m = 1, n = 1 and y = 1 in the homologous series Ba<sub>m+n</sub>Sn<sub>3m+y</sub>Bi<sub>3n-y</sub>. The phase BaSn<sub>2</sub>Bi crystallizes in a 12R structure with four atomic positions distributed in two crystallographic layers that can be described as a substitution variant of a close packed layer of atoms. It represents the yet Bi richest phase of the homologous series Ba<sub>m+n</sub>Sn<sub>3m+y</sub>Bi<sub>3n-y</sub>. The stacking of the 12 close packed layers of atoms, six hexagonal and six cubic, along the c-axis with the sequence ABCACABCBCAB... (Jagodzinski notation (hhcc)<sub>3</sub>) gives a quite long c parameter of 33.7126 Å (Figure 6.17). The structure derives from an intergrowth of BaSn<sub>3</sub>-like and BaBi<sub>3</sub>-like blocks in an equal 2:2 proportion. One atomic position in the cubic layer is mixed-occupied with Sn and Bi. The Table 6.16 contains some relevant interatomic distances. The hexagonal layers are fully ordered and contain the triangular Sn<sub>3</sub>-unit in which Sn–Sn contact are shortest (2.999(3) Å) and they are well separated by Ba atoms with longer in-plane Ba1–Sn contacts of 3.662(1) Å. The Sn–Sn distance between two hexagonal layers is 3.309(1) Å whereas the in-plane distance between two trimers units is 4.277(2) Å, meaning non-bonding interaction. The Sn–Bi distance between hexagonal and cubic layers 3.396(2) Å. The cubic layers are only slightly distorted giving the in-plane Bi–Bi distances of 3.632(2) Å and 3.644(2) Å and, the Ba2–Bi distance of 3.641(1) Å. The Bi–Bi distance of 3.538(2) Å between two cubic layers is significantly shorter than the corresponding in-plane contacts (Figure 6.17).

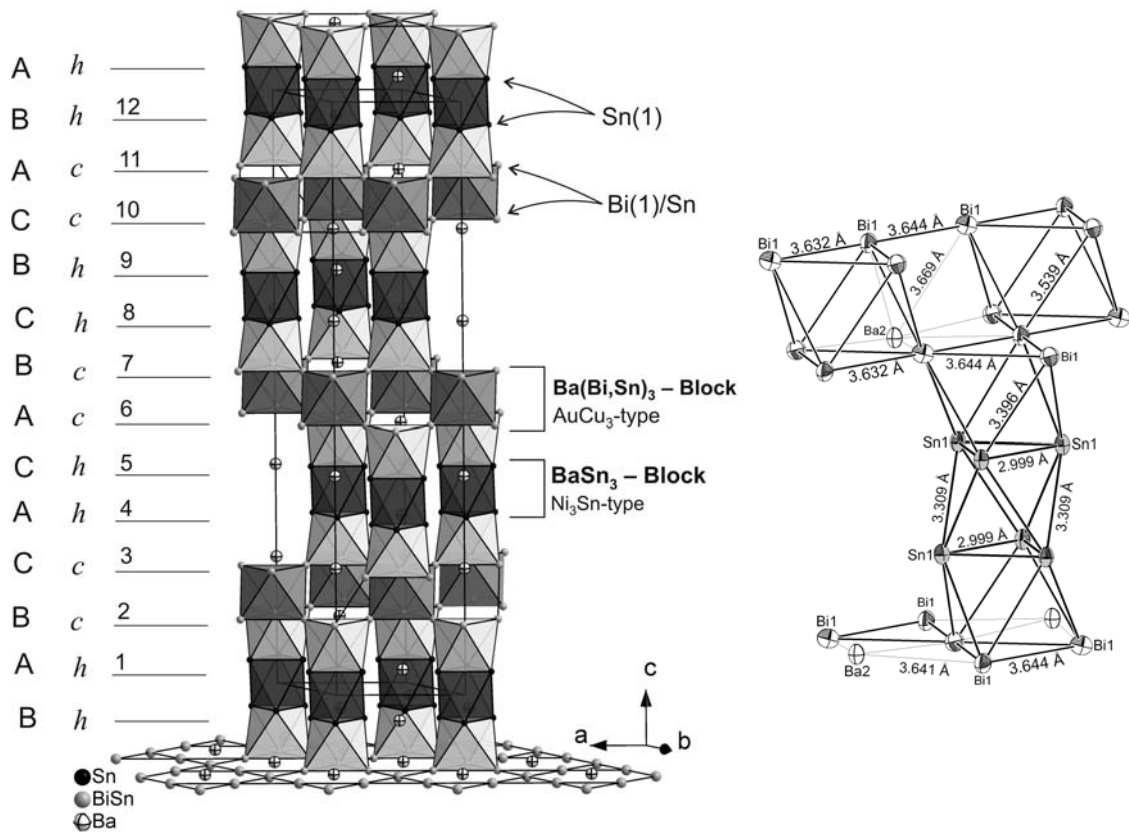


**Figure 6.17** Projection of the crystal structure of  $Ba_4Sn_{10.27}Bi_{1.73(3)}$ . (right) Fragment of the structure (thermal ellipsoids at 50% probability level) with some relevant interatomic distances.

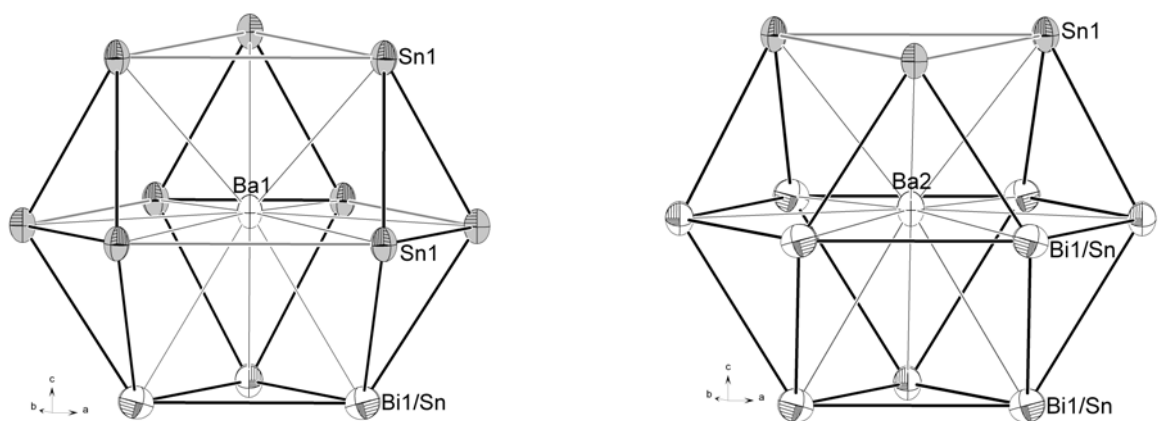


**Figure 6.18** Coordination polyhedra of Ba atoms in  $BaBiSn_2$ : Ba(1) Anticubeoctahedron, Ba(2) Cubeoctahedron (black lines denoted shortest interatomic distances); thermal ellipsoids at 50% probability level

**Table 6.16** Relevant Atomic distances in  $\text{BaBiSn}_2$  (standard deviation in parentheses)

Atomic pair	distance /Å	n	Atomic pair	distance /Å	n	
Sn1	-Sn1	2.999(3)	Bi1/Sn	-Sn1	3.396(1)	
	-Bi1/Sn	3.396(1)		-Bi1/Sn	3.539(2)	
	-Ba2	3.606(2)		-Bi1/Sn	3.632(2)	
	-Ba1	3.609(2)		-Bi1/Sn	3.644(2)	
	-Ba1	3.662(1)		-Ba1	3.637(2)	
Ba1	-Sn1	3.609(2)	-Ba2	3.641(1)	×2	
	-Bi1/Sn	3.637(2)	Ba2	-Sn1	3.606(2)	×3
	-Sn1	3.662(1)	-Bi1/Sn	3.641(1)	×6	
			-Bi1/Sn	3.669(1)	×3	

The Ba atoms are surrounded by 12 Sn and Bi atoms in either anticuboctahedra (Ba1) or cuboctahedra (Ba2) coordination geometry (Figure 6.18). The Ba2 atoms are again off-plane and shifted towards the hexagonal layer, due to the stronger interactions with the lone pair of the  $\text{Sn}_3$  triangular units.

A similar atomic distribution was recently described in  $\text{SrSn}_3$  which represents a fully ordered variant.<sup>[4]</sup> Other isotypic alloys, albeit poorly described, are the phases  $\text{Mg}_3\text{In}$ <sup>[30]</sup> and  $\text{h-PuGa}_3$ .<sup>[31]</sup> Furthermore, the filled variants of the 12R structure of  $\text{BaSn}_2\text{Bi}$  are found in the hexagonal perovskite family like  $\text{BaCrO}_3$ <sup>[32]</sup> or Elpasolith minerals (e.g.  $\text{Cs}_2\text{NaCrF}_6$ ,  $\text{Cs}_2\text{NaFeF}_6$ ),<sup>[33]</sup> where Ba or Cs are at Ba positions and O or F at Sn/Bi positions, respectively. The respective Cr-, Fe- and Na-positions are unoccupied in the alloy and this can be written as  $\text{Ba}\square(\text{Sn}_2\text{Bi})$ .

#### 6.4 Discussions on the homologous series $\text{Ba}_{m+n}\text{Sn}_{3m+y}\text{Bi}_{3n-y}$

The  $\text{BaSn}_3$  phases derive from a hexagonal closed packing of Sn atoms by replacing every fourth Sn atom by Ba in each hexagonal layer, under maintenance of  $\text{Sn}_3$  triangles (distorted Kagomé net). The partial substitutions of Sn by electron richer Bi atom in the anionic substructure of the electron precise phase  $\text{BaSn}_3$  have revealed several new phases that have previously unknown intermediate structures resulting from the combination of the cubic and hexagonal closed packing patterns structures, in which the cubic character in their structure types increases with increasing Bi content. The following general observations can be made:

- The structure of  $BaSn_3$  is not stable toward an increase of VEC and the system reacts to the addition of Bi atoms by creating ccp-layers that are partially disordered with Bi/Sn site occupation.
- Variation of the hexagonal closest packing and cubic closest packing along the c-axis is realized, generating a homologous series  $Ba_{m+n}Sn_{3m+y}Bi_{3n-y}$  where y is the amount of Sn atoms in the predominantly Bi occupied cubic layers. The members of the homologous series crystallize in a hexagonal structure in space group  $P6_3/mmc$  or rhombohedra  $R\bar{3}m$  with almost similar a, b unit cell parameters but varying c parameter.
- Their crystal and electronic structures can be described as recombination structure of the simple parents  $BaSn_3$  and  $BaBi_3$  that are periodically divided into blocks with hexagonal close packing of atoms that are identical in structure and composition to the electron precise phase  $BaSn_3$  without a phase width and, slabs of the typical alloys  $Ba(Bi/Sn)_3$  with cubic close packing of atoms that are structurally related to  $BaBi_3$  structure and have noticeable phase width.

The above defined formula describes the homologous series of structures that are constructed according to the same principle. The substitution procedure occurs only within the ccp layers. The composition and the structure of the layers are very close in all structures. The only structural characteristic that discriminate one structure type to another is the relative thickness of the two block components.

The crystal structures of the first four members of the homologous series  $Ba_{m+n}Bi_{3n-y}Sn_{3m+y}$  have been determined by single crystal diffraction (see [Table 6.17](#)) and HRTEM and DTA analysis clearly indicate that more homologous phases exist and are still to be structurally characterized.

**Table 6.17** Current members of the homologous series  $Ba_{m+n}Sn_{3m+y}Bi_{3n-y}$

Bi rate (x)	Sn rate in c-layer	Space groupe	Unit Cell dimensions, Å		Cell type - Jagodzinski notation	Perovskite analogue
			a, b	c		
$BaSn_3$ (n = 0)	–	$P6_3/mmc$	7.253	5.496	2H – (hh)	$BaNiO_3$
$Ba_4Sn_{9+y}Bi_{3-y}$ (y = 1.3 )	42%	$P6_3/mmc$	7.271	22.165	8H - (hhhc) <sub>2</sub>	$BaMnO_3$
$Ba_{13}Sn_{30+y}Bi_{9-y}$ (y = 3.2 )	35 - 36%	$R\bar{3}m$	7.273	108.04	39R - (hhhchhhchhhhc) <sub>3</sub>	?
$Ba_5Sn_{9+y}Bi_{6-y}$ (y = 2.3)	39%	$P6_3/mmc$	7.274	27.943	10H - (hhhcc) <sub>2</sub>	?
$Ba_2Sn_{3+y}Bi_{3-y}$ (y = 1.0)	34%	$R\bar{3}m$	7.276	33.713	12R - (hhcc) <sub>3</sub>	$BaCrO_3$
$BaBi_3$ (m = 0)	–	$P4/mmm$	5.188	5.157	3C- (ccc)	$CaTiO_3$

It is not clear if the amount of Sn in the predominantly Bi occupied cubic layers is determined by either electronic factors or by matrix requirements to match the almost regular cubic layers with the distorted hexagonal layers. In fact, the inclusion of Sn atoms in cubic layers leads to shorter interatomic distances within the corresponding Kagomé net and, subsequently reduces the difference of atomic separation between the cubic and the hexagonal type of layers.

These results address important issues concerning the bonding and properties of main group intermetallic compounds of the  $\text{Ni}_3\text{Sn}$ -type that have not yet been systematically studied. They suggest that the optimum electron count in the  $\text{AE}_3$  phase of the  $\text{Ni}_3\text{Sn}$ -type family is 14 electrons per  $\text{E}_3$  unit. An increase of the VEC will result in the formation of the  $\text{AuCu}_3$ -type layers. Recent results in our group show that the anionic structure remains one-dimensional, when Sn is partially substituted by electron poorer Tl atoms.<sup>[34]</sup> Taking this and other results from the literature<sup>[20,23,26]</sup> in account and disregarding the role of the cation, we can assume that for the  $\text{Ni}_3\text{Sn}$ -type, when compounds  $\text{AE}_3$  have no more than nine valence electrons per  $\text{E}_3$ , the inter- and intrachain distances are almost the same in a three-dimensional anionic network; significant distortion of the anionic Kagomé net occurs with more than 9 valence electrons per  $\text{E}_3$ . When the VEC per  $\text{E}_3$  is between 12 and 14, the anionic structure becomes one-dimensional, with much longer interchain distances. In these cases, the interchain bonds are broken and lone-pair formation accommodates the electron abundance as in the  $[\text{Sn}_3]^{2-}$  in  $\text{BaSn}_3$  or the homologous  $[\text{In}_3]^{5-}$  in  $\text{Ca}_5\text{In}_9\text{Sn}_6$ . The antiprismatic staking of the trimer results in the formation of condensed (face-sharing octahedra) with strong interactions between  $2\pi$ -electron systems parallel to the chain that explain the metallic or even the superconducting properties.

Concerning the size effect, the one can imagine intuitively that the cation size should be big enough to keep apart the condensed octahedra chain to achieve the hexagonal type structure. Thus, it would be interesting to study also the size effect through for instance partial substitution in the cationic substructure of the phase  $\text{BaSn}_3$ , i.e.  $\text{Ba}_{1-x}\text{Sr}_x\text{Sn}_3$  or  $\text{Ba}_{1-x}\text{Ca}_x\text{Sn}_3$ .

## 6.5 Literature

- [1] Eckerlin, P.; Meyer, H. J.; Wölfel, E. *Z. Anorg. Allg. Chem.* **1955**, 307, 145.
- [2] Zürcher, F.; Nesper, R.; Hoffmann, S.; Fässler, T. F. *Z. Anorg. Allg. Chem.* **2001**, 627, 2211.
- [3] Fässler, T. F.; Kronseder, C. *Angew. Chem., Int. Ed. Engl.* **1997**, 36, 2683.
- [4] Fässler, T. F.; Hoffmann, S. *Z. Anorg. Allg. Chem.* **2000**, 626, 106-112.
- [5] Hoffmann, S.; Fässler, T. F. *Inorg. Chem.* **2003**, 42, 8748-8754.
- [6] Fässler, T. F.; Hoffmann, S.; Kronseder, C. *Z. Anorg. Allg. Chem.* **2001**, 620, 2486-2492.
- [7] Cromer, D. *Acta Crystallogr.* **1976**, B32, 1930.
- [8] Corbett, J.D. In *Chemistry, Structure and Bonding in Zintl Phases and Ions*; Kauzlarich, S., Ed.; VCH: New York, **1996**; Chapter 3.
- [9] Klem, M.T.; Vaughey, J.T.; Harp, J.G.; Corbett, J.D. *Inorg. Chem.* **2001**, 40, 7020-7026.
- [10] Borzone, G.; Borsese, A.; Ferro, R. *Z. Anorg. Allg. Chem.* **1983**, 501, 199.
- [11] Zhao, J.-T.; Corbett, J. D. *Inorg. Chem.* **1995**, 34, 378.
- [12] Nesper, R. *Prog. Solid State Chem.* **1990**, 20, 1.
- [13] Pearson, W. B. *The Crystal Chemistry and Physics of Metals and Alloys*; Wiley-Interscience: New York, 1972.
- [14] Schewe, I.; Böttcher, P.; von Schnering, H.G. *Z. Kristallogr.* **1989**, 188, 287.
- [15] Fischer W. *Acta Cryst.* **2005**, A61, 435-444
- [16] Fässler, T. F. *Chem. Soc. Rev.* **2003**, 32, 80-86.
- [17] Curda, J.; Carrillo-Cabrera, W.; Schmeding, A.; Peters, K.; Somer, M.; von Schnering, H. G. *Z. Anorg. Allg. Chem.* **1997**, 623, 929-936
- [18] Wenger, S. Dissertation, ETH Zürich, **1997**.
- [19] Guloy, A.; Corbett, J. D. *Inorg. Chem.* **1996**, 35, 2616-2622.
- [20] Villars, P.; Calvert, L. D. *Pearson's Handbook of Crystallographic Data for Intermetallic Phases*, 2nd ed.; American Society of Metals: Metals Park, OH, **1991**.
- [21] Hoffmann S. Dissertation, ETH Zürich, **2002**.
- [22] Müller, U. in *Inorganic Structural Chemistry*, John Wiley & Sons, **1993**.
- [23] Seo, D-K.; Corbett, J. D. *J. Am. Chem. Soc.* **2002**, 124, 3, 415.
- [24] Sands, D. E.; Wood, D. H.; Ramsey W. J. *Acta Cryst.* **1964**, 17, 986.
- [25] Zintl, E.; Neumayr, S. *J. Less. Common Met.* **1966**, 11, 308
- [26] Vajenine, G.; Hoffmann, R. *J. Am. Chem. Soc.* **1998**, 120, 4200.
- [27] Kronseder C. Dissertation, ETH Zürich, **1998**.
- [28] Potoff, A.D.; Chamberland, B.L.; Katz, L. *J. Solid State Chem.* **1973**, 8, 234.
- [29] Xu, Z.; Guloy, A. M. *J. Am. Chem. Soc.* **1998**, 120, 7349.
- [30] Schubert, K.; Gauzzi, F.; Frank, K. *Z. MetallKde.* **1963**, 54, 422.
- [31] Larson, A. C.; Cromer, D. T.; Stambaugh, C. K. *Acta Cryst.* **1957**, 10, 443.
- [32] Chambarland, B. L. *Inorg. Chem.* **1966**, 8, 286.
- [33] Babel D.; Haegele R. *J. Solid State Chem.* **1976**, 18, 39.
- [34] Müller, N. Diploma Thesis, ETH Zürich, **1998**.

## 7. Heteronuclear Zintl Anions at the Border to Intermetallics – Synthesis, Characterization and Electronic Structure of Ba<sub>5</sub>In<sub>4</sub>Bi<sub>5</sub>

### 7.1 Introduction

The semiconducting properties of the elements of group 14 have long been compared to that of the isoelectronic binaries of groups 13/15 and groups 12/16. Thus, it occurs to us that another way to probe the importance of electronic effects on the stability of Zintl phases of the Ba/Sn binary system at the border to intermetallics is to prepare isoelectronic phases that are based on heteronuclear anionic substructures. In the previous chapter, Sn for Bi partial substitutions in two borderline Zintl phases BaSn<sub>3</sub> and Ba<sub>3</sub>Sn<sub>5</sub> clearly show that both structures aren't stable towards an increase of the VEC. With this in mind, we have investigated the ternary system Ba–Bi–In, on the basis of isoelectronic relationships to the binary stannides BaSn<sub>3</sub> and Ba<sub>3</sub>Sn<sub>5</sub>. The same approach was recently used in the synthesis of the heteroatomic cluster [In<sub>4</sub>Bi<sub>5</sub>]<sup>3-</sup>,<sup>[1]</sup> isoelectronic to the *nido*-cluster [Tt<sub>9</sub>]<sup>4-</sup> (Tt = Si, Ge, Sn, Pb). Indium and bismuth were chosen because they can be distinguished by X-ray diffraction and they satisfy some important requirements like relatively similar electronegativities (Pauling's), 1.7 vs 1.9, and comparable covalent radii, 1.42 vs. 1.51 Å,<sup>[2]</sup> respectively. They are also capable of forming clusters on their own and, as heavy elements, have an inert s pair of electrons in the outer shells. Indeed, the anion In<sub>3</sub><sup>5-</sup> was described in Ca<sub>5</sub>In<sub>9</sub>Sn<sub>6</sub> and is isosteric and isoelectronic with aromatic π-system Sn<sub>3</sub><sup>2-</sup>. On the other hand, the Wade's *nido*-cluster [In<sub>5</sub>]<sup>9-</sup> and the *Arachno*-cluster [Sn<sub>5</sub>]<sup>6-</sup> are isosteric but not isoelectronic and, they are found in isotypic phases La<sub>3</sub>In<sub>5</sub> and Ba<sub>3</sub>Sn<sub>5</sub>, respectively.

Therefore, the hypothetical phases Ba<sub>2</sub>In<sub>3</sub>Bi<sub>3</sub> and Ba<sub>6</sub>In<sub>5</sub>Bi<sub>5</sub> should be isoelectronic with the phases BaSn<sub>3</sub> and Ba<sub>3</sub>Sn<sub>5</sub>, respectively. Attempts have been made to prepare such compounds, but always result with the same new phase Ba<sub>5</sub>In<sub>4</sub>Bi<sub>5</sub>.

### 7.2 Synthesis and Characterization

Two different reaction mixtures using molar ratio Ba:In:Bi = 6:5:5 and Ba:In:Bi = 2:3:3 were heated at 800°C for 5 hours, cooled down to 400°C with a rate of 60 °C/h, and held at that temperature for five days before cooling down to room temperature. Both reactions yield only the new phase Ba<sub>5</sub>In<sub>4</sub>Bi<sub>5</sub>. Very regular shape single crystal was found in the reaction products. The new phase could latter be prepared quantitatively

from a stoichiometric mixture according to powder X-ray diffraction diagram (Figure 7.1). The compound is air-sensitive and crystallizes as needle- or rod-shape crystals with silverish color and metallic luster. EDX analysis confirms the presence of all three elements and absence of possible niobium impurities or any other elements.

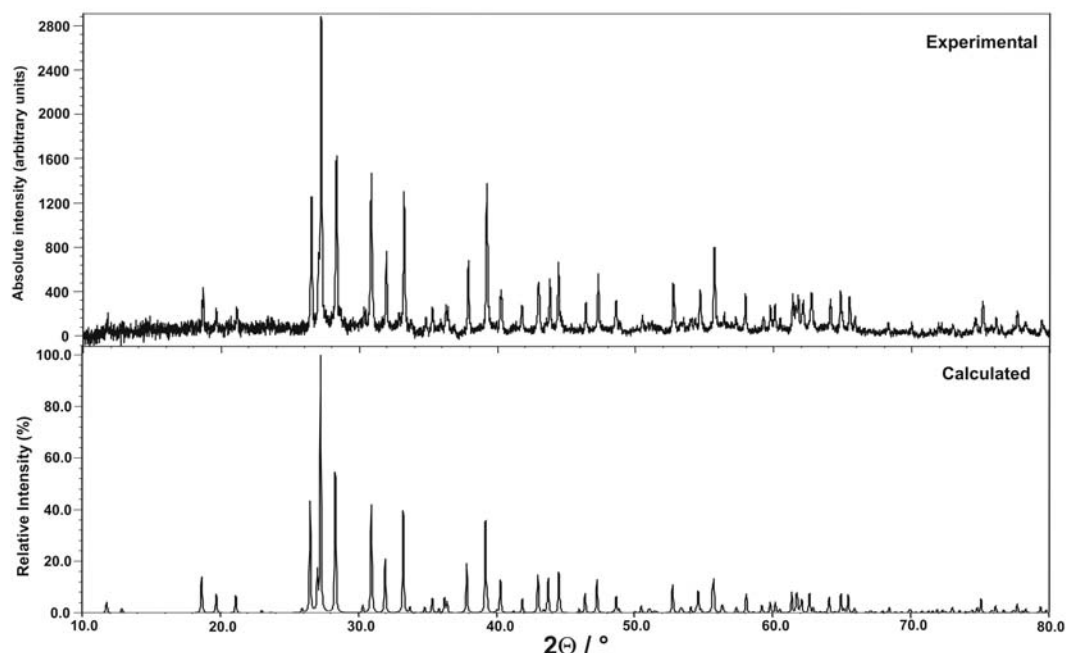


**Figure 7.1** Powder diffraction diagram of the reaction products of the stoichiometric mixture  $\text{Ba}:\text{In}:\text{Bi} = 5:4:5$  at and calculated diagrams of  $\text{Ba}_5\text{In}_4\text{Bi}_5$  (below) in tetragonal  $P4nc$  system.

### 7.3 Crystal structure determination

Crystal structure investigations were performed on single crystal by X-ray diffraction. Single crystals of  $\text{Ba}_5\text{In}_4\text{Bi}_5$  were selected, mounted in thin-wall glass capillaries, and checked for singularity. The best one, a needle-shaped single crystal ( $0.40 \times 0.167 \times 0.05$  mm), was used for data collection at room temperature with a Stoe IPDS. A total of 180 frames were recorded with exposure time of 7 min/frame, angular range of  $3.8^\circ < 2\theta < 55.7^\circ$ ,  $\omega$ -scans,  $\Delta\omega = 1^\circ$ . The crystal detector distance was 120 mm. The unit cell was indexed and refined with all the 8234 integrated peaks. Numerical absorption correction was applied using the program X-shape from STOE. The Laue class  $4/mmm$  was based on the intensity statistics, the satisfactory averaging and, the acentric space group  $P4nc$  was found to be correct based on successful structure solution. All the five atomic positions of the structure were found during structure solution by direct methods and no mixed-occupancy was found, indicating a fully ordered phase. A summary of the crystallographic and refinement data is given in Table 7.1 and the atomic parameters in Tables 7.2.

**Table 7.1** Crystallographic data and structure refinement of Ba<sub>5</sub>In<sub>4</sub>Bi<sub>5</sub>

Chemical formula	Ba <sub>5</sub> In <sub>4</sub> Bi <sub>5</sub>
formula weight	2190.88
space group	<i>P4nc</i> (n°104)
Temperature	293(2)K
Diffractometer	Stoe IPDS II
radiation, λ (Å)	Mo Kα, 0.71073
a (Å)	10.620(1)
c (Å)	9.009(2)
Unit cell volume	1016.0(3) Å <sup>3</sup> , Z = 2
ρ <sub>calc</sub> (g/cm <sup>3</sup> )	7.161
μ (cm <sup>-1</sup> )	570.39
F(000)	1782
crystal size (mm <sup>3</sup> )	0.30 × 0.15 × 0.05
2θ range for data collection	3.8° – 55.7°
index ranges	-13 ≤ h ≤ 13, -13 ≤ k ≤ 13, -11 ≤ l ≤ 11
Collected reflections	8204
independent reflections	1137
observed reflections [I > 2σ]	1046
R <sub>int</sub> / R <sub>σ</sub>	0.058 / 0.034
absorption correction	numerical
min /max Trans.	0.0135 / 0.0967
Nr. of parameters	35
goodness-of-fit on F <sup>2</sup>	1.219
R <sub>1</sub> /wR <sub>2</sub> <sup>[*]</sup> , I > 2σ	0.024 / 0.070
R <sub>1</sub> /wR <sub>2</sub> , all data	0.027 / 0.084
Flack parameter	-0.07(1)
extinction parameter	0.0067(3)
largest diff peak and hole (e <sup>-</sup> / Å <sup>3</sup> )	3.32 / -2.64

$$^{\dagger} w = 1/[\sigma^2 (F^2_o) + (0.0382 \times P)^2 + 28.60 \times P]$$

**Table 7.2(a)** Atomic Coordinates and Isotropic Equivalent Displacement Parameters for Ba<sub>5</sub>In<sub>4</sub>Bi<sub>5</sub>

Atom	site	x	y	z	U <sub>eq</sub> / Å <sup>2</sup>
Bi1	8c	0.3906(1)	0.1908(1)	0.6903(1)	0.0175(3)
Bi2	2a	½	½	0.3180(2)	0.0123(4)
Ba1	8c	0.6057(2)	0.1884(2)	0.3740(2)	0.0170(4)
Ba2	2a	½	½	0.7001(3)	0.0210(6)
In1	8c	0.1834(2)	0.0720(2)	0.5316(2)	0.0200(4)

**Table 7.2(b)** Anisotropic displacement parameters (Å<sup>2</sup>) for Ba<sub>5</sub>In<sub>4</sub>Bi<sub>5</sub>

Atom	U <sub>11</sub>	U <sub>22</sub>	U <sub>33</sub>	U <sub>23</sub>	U <sub>13</sub>	U <sub>12</sub>
Bi1	0.0138(4)	0.0186(4)	0.0201(4)	-0.0010(4)	0.0004(3)	-0.0044(3)
Bi2	0.0129(5)	0.0129(5)	0.0110(5)			
Ba1	0.0146(6)	0.0166(6)	0.0197(6)	-0.0002(5)	-0.0001(4)	0.0027(5)
Ba2	0.0144(7)	0.0144(7)	0.0101(9)			
In1	0.0194(7)	0.0160(7)	0.0245(7)	-0.0042(6)	-0.0100(6)	-0.0005(5)

#### 7.4 Description of the Structure of $\text{Ba}_5\text{In}_4\text{Bi}_5$

According to single crystal structure determination, the new compound  $\text{Ba}_5\text{In}_4\text{Bi}_5$  crystallizes in the non-centrosymmetric space group  $P4nc$  with a new structure type. The structure contains square pyramids with four exo-bonds at the square base (idealized  $C_{4v}$  symmetry). The latter is made of the four indium atoms in the formula while the four exo-bonded atoms (Bi1) and the apex of the pyramid (Bi2) are the five bismuth atoms (Figure 7.2).

The In–Bi exo-bond distance of 2.912(2) Å is quite normal for a single bond between these elements. It compares well, for example, with the observed range of distances in  $\text{Cs}_7\text{In}_4\text{Bi}_6$ , 2.896(3) – 3.105(3) Å.<sup>[3]</sup> The In–In distance in the square, 2.958(2) Å, is also close to a single-bond distance when compared with 2.976(4) and 3.004(5) Å observed between indium atoms coordinated by bismuth in  $\text{Cs}_7\text{In}_4\text{Bi}_6$ . Nevertheless, it is somewhat longer than the Pauling's distance for a single bond, 2.84 Å.<sup>[2]</sup>

The remaining four In–Bi distances in the pyramid, i.e. those to the apical Bi, are quite long for a single bond, 3.322(2) Å, and suggest rather delocalized bonding. They compare better with the intercluster distances of 3.376(2) Å that occur between the exo-bonded bismuth atoms and indium atoms of four neighbouring pyramids (Table 7.3). This suggests that the interactions between the pyramids can not be disregarded. Thus, the clusters should not be considered as isolated units but rather as parts of an extended network as shown in Figure 7.3. The exo-bonded square pyramids are stacked in columns along the  $c$ -axis and the columns are connected via the intercluster In–Bi contacts. The columns are shifted by  $c/2$  and twisted by approximately  $16.4^\circ$  around the  $c$ -axis with respect to the surrounding columns. The rotation reduces the overall symmetry of the cell from body-centered to the current tetragonal primitive unit cell. The occurrence of such a rotation most likely originates from a strong need of the clusters to interlink to each other.

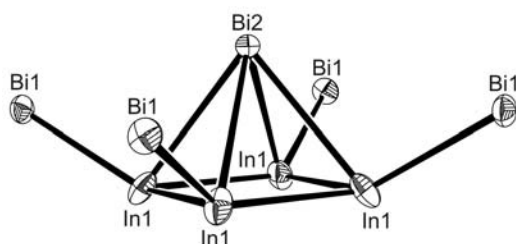


**Figure 7.2** Ortep plot of the  $[\text{In}_4\text{Bi}_5]$  cluster in  $\text{Ba}_5\text{In}_4\text{Bi}_5$  (thermal ellipsoids at 70% probability level)

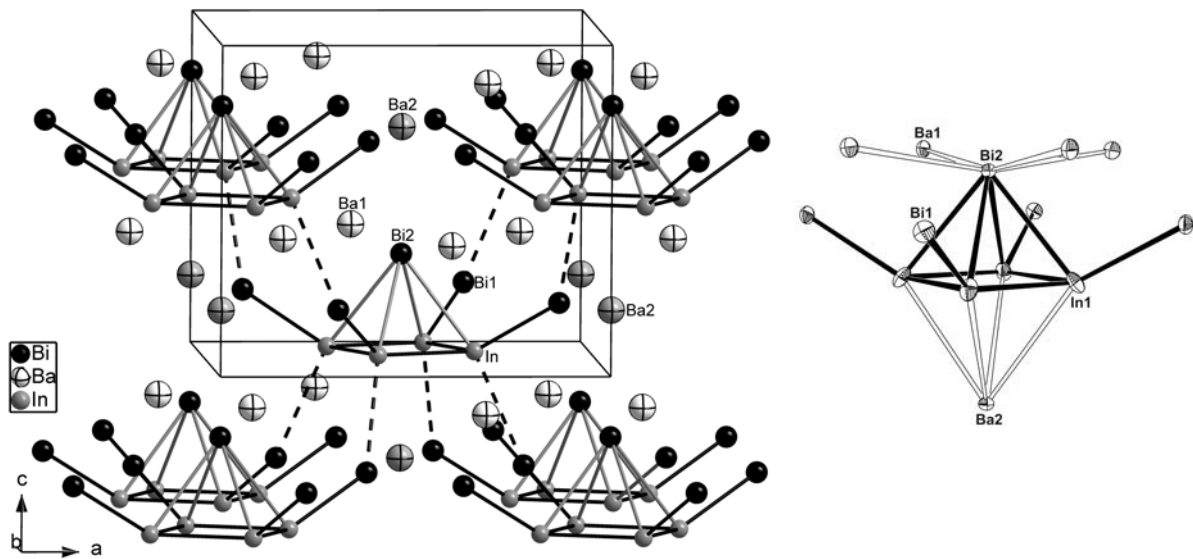


**Figure 7.3** The structure of  $\text{Ba}_5\text{In}_4\text{Bi}_5$  with the unit cell outlined (Ba1 - crossed ball, Ba2 - grey crossed, Bi - black, In - grey). The square pyramidal clusters with four In–Bi1 exo bonds are stacked along the c-axis. They are inter-connected via longer Bi–In distances shown as black dashed lines. **Right:** Ortep plot of the asymmetric unit in  $\text{Ba}_5\text{In}_4\text{Bi}_5$  (thermal ellipsoids at the 50% probability level)

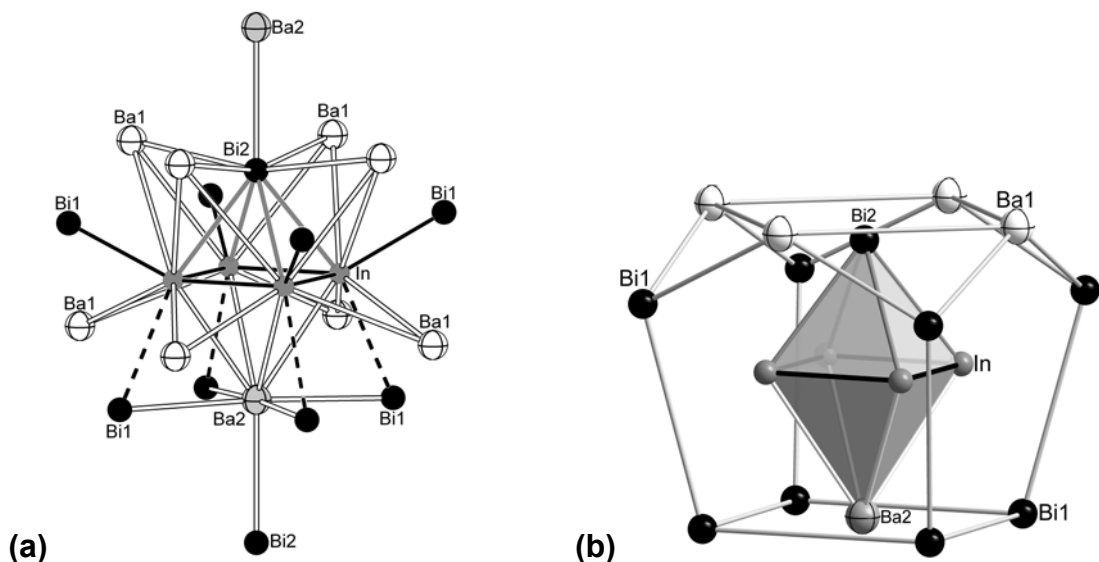


**Figure 7.4** (a) A closer view of the coordination around  $[\text{In}_4\text{Bi}_5]$  showing an octahedron-like formation capped by Ba2 and Bi1 that resembles  $\text{M}_6\text{X}_{16}$  clusters (Bi - black; Ba1 – crossed; Ba2 - grey crossed; In1 - grey). All Ba–In and Ba–Bi interactions are shown with open bonds. The similarity of the coordinations of Ba2 and Bi2 is clearly visible. (b) The 12 closest atoms around  $[\text{BiIn}_4\text{Ba}]$  octahedra define a polyhedron closed to a “staggered” cuboctahedron where the ‘waist’ atoms Bi1 are shifted to the ‘chest’.

**Table 7.3** Selected interatomic distances (Å)

Bi1	-In1	2.912(2)	In1	-In1	2.958(2) ×2
	-In1	3.376(2)*		-Ba1	3.707(2)
	-Ba1	3.653(2)		-Ba1	3.830(2)
	-Ba1	3.655(2)		-Ba1	3.864(2)
	-Ba1	3.679(2)		-Ba1	4.084(2)
	-Ba1	3.682(2)	Ba2	-Bi1	3.484(1) ×4
	-Ba1	4.171(2)		-In1	3.647(2) ×4
Bi2	-In1	3.322(2) ×4			
	-Ba2	3.442(3)			
	-Ba1	3.531(2) ×4			

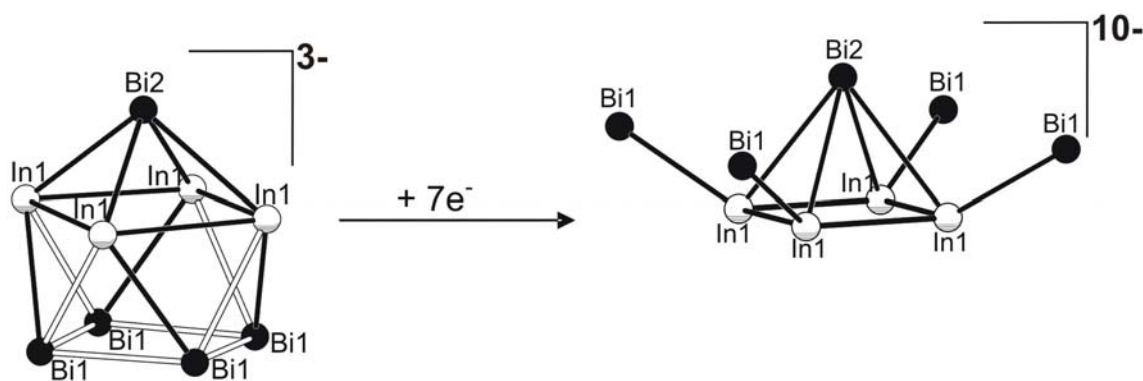
(\*) Inter-cluster bonds

The five barium cations in the formula occupy two different positions. Ba2 caps the square base of the In<sub>4</sub>Bi pyramid (opposite to the Bi apex) with Ba–In distances of 3.647(2) Å. Its coordination environment is very similar to that of the capping bismuth atom, Bi2, and resembles a pseudo-octahedron in which one of the vertices is replaced by the In<sub>4</sub> square (Figure 7.4). Thus, the nearest neighbours of Bi2 and Ba2 are 4Ba1 + Ba2 +  $\eta^4$ -In<sub>4</sub> and 4Bi1 + Bi2 +  $\eta^4$ -In<sub>4</sub>, respectively. It is perhaps these structural reciprocities that give rise to the observed substantial contribution of barium in the calculated electronic structure of the compound (below). Also, if we consider Ba2 as part of the cluster, we obtain an octahedral unit surrounded by Bi and Ba atoms that bridge edges and cap faces and resemble the coordination topology of the well-known M<sub>6</sub>X<sub>18</sub> transition metal halide clusters (Figure 7.4a). The 12 closer Bi and Ba atoms around BiIn<sub>4</sub>Ba octahedra give a coordination geometry which is related to a “staggered cuboctahedron” where the four ‘waist’ atoms (Bi1) are shifted to the ‘chest’ (Figure 7.4b). This emphasizes the relation of the Ba<sub>5</sub>In<sub>4</sub>Bi<sub>5</sub> structure with the cubic close-packed systems. Ba1, on the other hand, has 10 neighbors (Bi2 + 5Bi1 + 4In1) at distances between 3.653(2) Å and 4.084(2) Å (see Table 7.3) with no outstanding coordination geometry, an indication for less directional interactions.

Full electron transfer from barium to the more electronegative indium and bismuth as prescribed by the Zintl-Klemm concept would result in a charge of 10<sup>-</sup> for the exo-bonded pyramid, i.e. [In<sub>4</sub>Bi<sub>5</sub>]<sup>10-</sup>. The species can be viewed as composed of a deltahedral *nido*-cluster with  $2n + 4 = 14$  skeletal bonding electrons, four 2-center–2-electron exo-bonds, one lone pair of electrons at the apical bismuth, and four exo-bonded bismuth atoms that need another 6 electrons each in order to satisfy the octet

rule. This totals  $14 + 8 + 2 + 24 = 48$  electrons of which only 37 are provided by the four In (3 electrons each) and 5 Bi (5 electrons each) atoms. Thus, a closed-shell species should have a charge of  $-11$  instead, i.e.  $[\text{In}_4\text{Bi}_5]^{11-}$ , and therefore  $[\text{In}_4\text{Bi}_5]^{10-}$  is formally one electron short.

It should be pointed out here that the previously known deltahedral cluster with the same stoichiometry  $[\text{In}_4\text{Bi}_5]^{3-}$  has substantially different charge and very different geometry.<sup>[1]</sup> It is a closed-shell *nido*-cluster of nine atoms with the shape of a monocapped square antiprism as shown in the left of Scheme 4. With respect to this, the new species  $[\text{In}_4\text{Bi}_5]^{10-}$  can be viewed as its inverted, opened version, almost as the blossomed flower from its bud of  $[\text{In}_4\text{Bi}_5]^{3-}$ . This "process" during which some In–Bi and Bi–Bi interactions are formally removed is clearly caused by the substantial reduction with 7 additional electrons (8 electrons for a closed-shell unit of  $[\text{In}_4\text{Bi}_5]^{11-}$ ) which would fill four empty antibonding levels of the cluster. This, as can be expected, leads to a major reorganization of the delocalized bonding within the cluster that is expressed in the removal of the four Bi–Bi interactions at the open square face of  $[\text{In}_4\text{Bi}_5]^{3-}$  as well as four of the associated Bi–In bonds, while reinforcing the four remaining Bi–In bonds. The four bismuth atoms are then shifted upwards and also tangentially away from one of the two indium atoms to which they are bonded. Apparently, this tangential displacement of the bismuth atoms is not complete, and the bismuth atoms are not perfectly radial with respect to the cluster but are rather  $7.4^\circ$  off of the vertical plane through In–Bi2–In. Thus, although the  $\text{In}_4\text{Bi}$  pyramid has exact  $C_{4v}$ -symmetry the symmetry of the whole unit  $[\text{In}_4\text{Bi}_5]^{10-}$  is reduced to  $C_4$ .



Scheme 4.

## 7.5 Electronic Structure of $\text{Ba}_5\text{In}_4\text{Bi}_5$ and Discussions

In order to gain some insight into the factors behind the stability of this apparently one-electron deficient compound, LMTO calculations were carried out. The calculated band structure along the main symmetry lines of the tetragonal Brillouin zone is represented in [Figure 7.5](#). The most interesting features of the band structure are the flat bands with very little dispersion (less than 0.1 eV) that intercept the Fermi level as we move across the faces of the Brillouin zone. There is no steep band crossing the Fermi level in the electronic system. The Fermi level passes through the four flat bands (and the bottom of the dispersed band) and makes them partially filled. They would have been completely filled with two additional electrons in a hypothetical, electronically-balanced compound " $\text{Ba}_{11}\text{In}_8\text{Bi}_{10}$ " (note that the unit cell contains two formula units). The continuum of states at and around the Fermi level is consistent with the observed metallic properties.<sup>[4]</sup>

Further analysis of the electronic structure of  $\text{Ba}_5\text{In}_4\text{Bi}_5$  was done based on the calculated total DOS of the compound and the separate contributions from the constituting elements ([Figure 7.6](#)). As expected the Fermi energy is right at a sharp spike (maximum of DOS) and very close to a narrow band gap which is consistent with a half filled band. The four peaks with the lowest energies in the DOS are the bismuth (around -10 eV) and indium *s*-orbitals (between -6 and -3 eV). The continuous region following them (-3.0 to +0.2eV) contains predominantly contributions from the *p*-orbitals of Bi and In, but also strong participation of Ba. As a matter of fact, the latter is larger than that of indium. In this section the In, Bi and Ba contributions have very similar shapes (the curves follow each other) and indicate good Bi–In and Ba–Bi orbital mixing and bonding interactions (but no noticeable bonding Ba–In interactions). The remaining one-third of the block is dominated by the bismuth *p*-orbitals, particularly from *p<sub>z</sub>*-orbitals. The sharp spike right at the Fermi level has almost purely bismuth *p<sub>z</sub>*-orbitals character, mostly from Bi1, that would have been filled if two additional electrons were available. This peak is made of the four flat bands discussed above and has essentially non bonding character and, therefore, the predominant character of the "missing" two electrons would have been non-bonding.

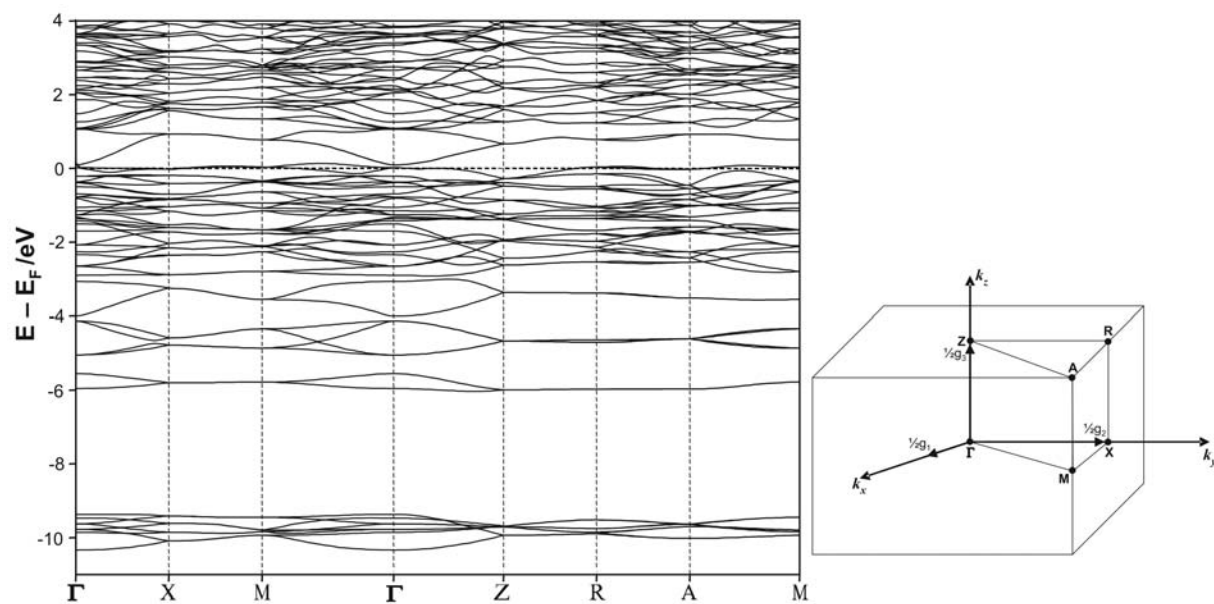


**Figure 7.5** Calculated band structure for  $\text{Ba}_5\text{In}_4\text{Bi}_5$  along the high symmetry directions of the tetragonal P Brillouin Zones (right):  $\Gamma = (0, 0, 0)$ ;  $X = (\frac{1}{2}, 0, 0)$ ;  $M = (\frac{1}{2}, \frac{1}{2}, 0)$ ;  $Z = (0, 0, \frac{1}{2})$ ;  $R = (\frac{1}{2}, 0, \frac{1}{2})$ ;  $A = (\frac{1}{2}, \frac{1}{2}, \frac{1}{2})$ , in units of the tetragonal reciprocal lattice vectors.

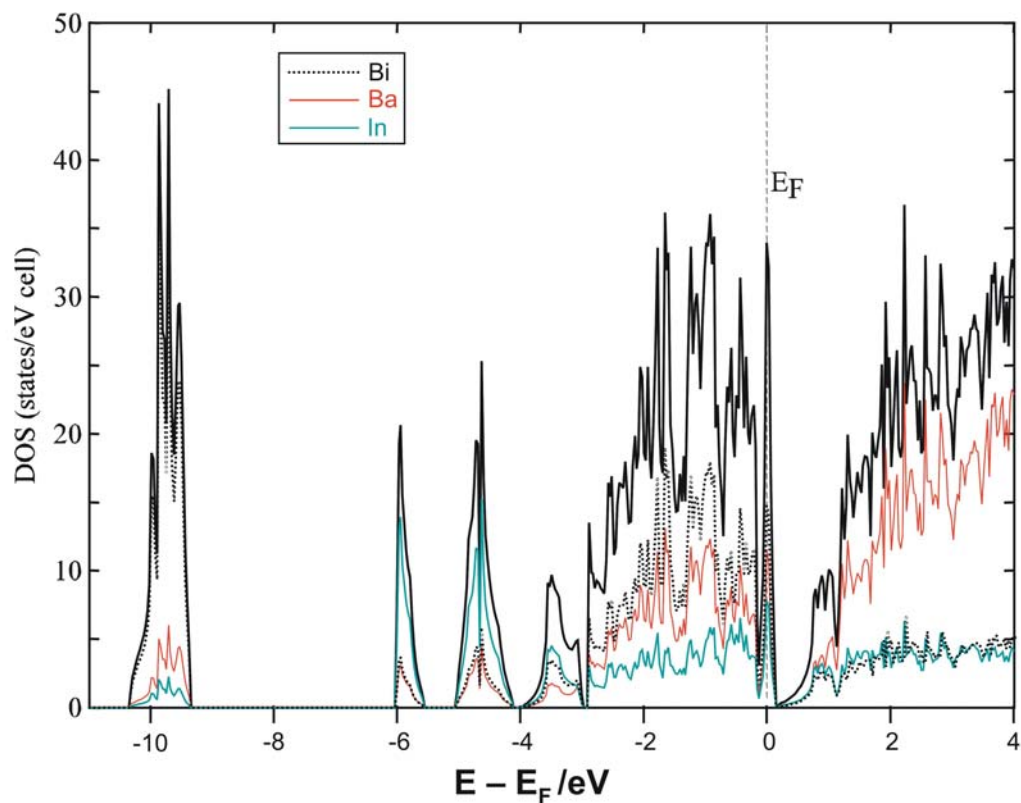


**Figure 7.6** Total and projected density of states of  $\text{Ba}_5\text{In}_4\text{Bi}_5$ .

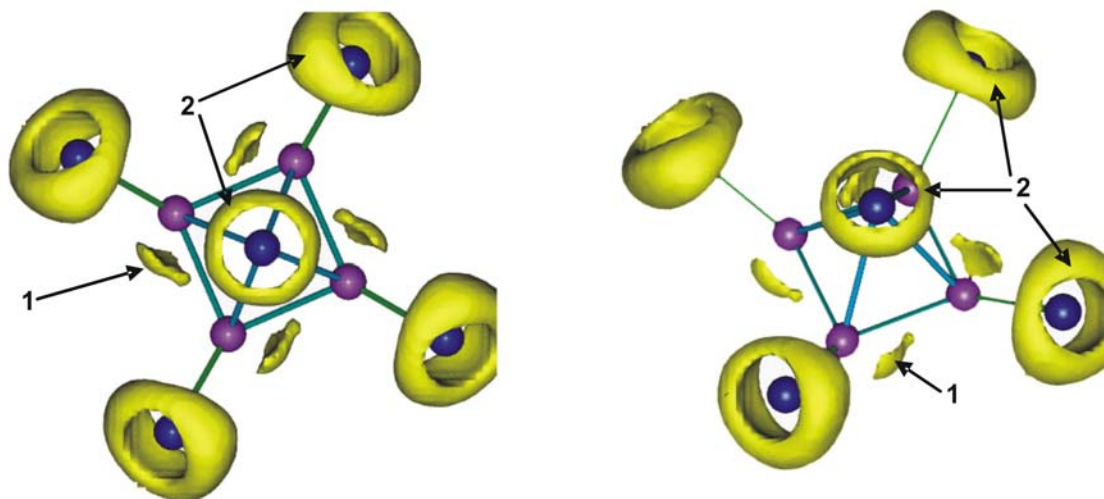


**Figure 7.7** Three-dimensional ELF representations of the valence electron density of  $\text{In}_4\text{Bi}_5$  cluster in  $\text{Ba}_5\text{In}_4\text{Bi}_5$ . The surfaces correspond to the constant ELF value of 0.8; ① and ② designate bonding and non-bonding electron pairs, respectively.

The nature of the chemical bond was additionally analyzed by the means of the electron localization function (ELF). The ELF characterizes electron regions in space, which can be associated with localized chemical bonds and enables the partition of the real space in localization domains even in intermetallic compounds. [5]

The images in Figure 7.7 show three-dimensional iso-surfaces of the ELF, calculated from the valence electrons. It clearly indicates the direction of free electron pairs ② at exo bonded Bi1 and apical Bi2 in form of a torus-type three-dimensional domain. It shows also an area ① which represents a localized bond between two indium atoms. Surprisingly, no domain of the covalent bond ELF attractor was found between In and the exo-bonded Bi1, even by lowering the ELF value down to  $\text{ELF} = 0.3$ . This may be due to strong relativistic effects in Bi which induce the expansion of the valence 6p-orbitals as a result of the shielding phenomenon by the contracted s-orbital.

As already discussed,  $\text{Ba}_5\text{In}_4\text{Bi}_5$  presents a very well packed structure with matching positioning for the five barium and five bismuth atoms with respect to each other as well as with respect to the indium square. Thus, barium atoms are in positions that allow optimum interactions with the non-bonding lone pairs of both the capping Bi2 as well as the four exo-bonded Bi1 atoms. Therefore, although the anionic part of the structure, i.e. Bi–In, does not have enough electrons to fill the relatively high lying levels (mostly Bi) near the Fermi level, the overall structure, i.e. Ba–In–Bi, compensates this by switching on relatively strong Ba–Bi bonding interactions and

thus stabilizing a considerable portion of the filled DOS. The present study suggests that, if it is impossible to find room for all cations necessary for electron balancing in a particular structure, the system finds such a distribution of the available cations that would maximize their participation in the covalent bonding of the structure and thus compensate for the electron "deficit".

The fact that the Fermi level passes near a maximum in the density of states suggests that the compound could be superconducting. However, all tests at temperatures as low as 2 K and various fields on both field cooled and zero-field cooled samples gave negative results and did not show superconducting transitions. But the measurement of the temperature dependency of the resistivity shows that  $\text{Ba}_5\text{In}_4\text{Bi}_5$  is a highly conducting compound.<sup>[4]</sup>

Many formations with various sizes and dimensions are known for heteroatomic anions involving atoms of groups 13 (triels, Tr = Al, Ga, In, Tl) and 15 (pnictogens, Pn = P, As, Sb, Bi),  $[\text{Tr}_m\text{Pn}_n]^{q-}$ .<sup>[6]</sup> One of the most common motifs is  $\text{TrPn}_4$ , a tetrahedrally coordinated triel atom. Known are isolated tetrahedra,  $[\text{TrPn}_4]^{9-}$ , dimers of edge-bridged tetrahedra,  $[\text{Tr}_2\text{Pn}_6]^{12-}$ , chains of corner-shared tetrahedra,  ${}^\infty[\text{TrPn}_3]^{6-}$ , chains of edge-shared tetrahedra,  ${}^\infty[\text{TrPn}_2]^{3-}$ , layers and 3D-frameworks of corner- and edge-shared tetrahedra and many other combinations of variously shared tetrahedra.<sup>[6-9]</sup> Often the tetrahedra are connected via Pn–Pn bonds<sup>[8-9]</sup> and very rarely even by Tr–Tr bonds.<sup>[10]</sup> Triangular-planar coordination  $\text{TrPn}_3$  is also known and the units have been found as isolated  $[\text{TrPn}_3]^{6-}$ , edge-sharing in dimers of  $[\text{Tr}_2\text{Pn}_4]^{6-}$ , and corner-sharing in a ring-like trimer of  $[\text{Tr}_3\text{Pn}_6]^{9-}$ .<sup>[6]</sup> These anions are typical Zintl anions that are characterized by covalent bonds; multicenter bonding was described only in the Wade's cluster  $[\text{In}_4\text{Bi}_5]^{3-}$ .

The present compound  $\text{Ba}_5\text{In}_4\text{Bi}_5$  is the first 'electron deficient' phase featuring heteronuclear  $[\text{Tr}_m\text{Pn}_n]^{q-}$  anion. Apparently such electron "shortages" with respect to the classical closed-shell bonding schemes can develop when other factors such as Madelung energy and packing efficiency become perhaps more important than charge optimization.  $\text{Ba}_5\text{In}_4\text{Bi}_5$  presents the first such an example that involves a heteronuclear framework.

## 7.6 Literature

- [1] Xu, L.; Sevov, S. C. *Inorg. Chem.* **2000**, *39*, 5383.
- [2] Pauling, L. "*The Nature of the Chemical Bond*" Cornell Univ. Press, Ithaca, NY, **1960**.
- [3] Bobev, S.; Sevov, S. C. *Inorg. Chem.* **1999**, *38*, 2672
- [4] Ponou, S.; Fässler, T. F.; Tobías, G.; Canadell, E.; Cho, A.; Sevov, S. C., *Chem. Eur. J.* **2004**, *10*, 3615.
- [5] Fässler, T. F. *Chem. Soc. Rev.* **2003**, *32*, 80.
- [6] Eisenmann, B.; Cordier G. in *Chemistry, Structure and Bonding of Zintl Phases and Ions*, (Ed.: S. M. Kauzlarich), VCH, Weinheim, **1996**, p. 61.
- [7] Gascoin, F.; Sevov, S. C. *Inorg. Chem.* **2002**, *41*, 2292.
- [8] Cordier, G.; Ochmann, H.; Schafer, H. *Mater. Res. Bull.* **1986**, *21*, 331.
- [9] (a) Bobev, S.; Sevov, S. C. *Inorg. Chem.* **1999**, *38*, 2672. (b) Bobev, S.; Sevov, S. C. *J. Solid State Chem.* **2002**, *163*, 436. (c) Gascoin, F.; Sevov, S. C. *Inorg. Chem.* **2001**, *40*, 6254.
- [10] (a) Kim, S.-J.; Kanatzidis, M.G. *Inorg. Chem.* **2001**, *40*, 3781. (b) Park, S.-M.; Kim S.-J.; Kanatzidis, M. G. *J. Solid State Chem.* **2003**, *174*, 310.

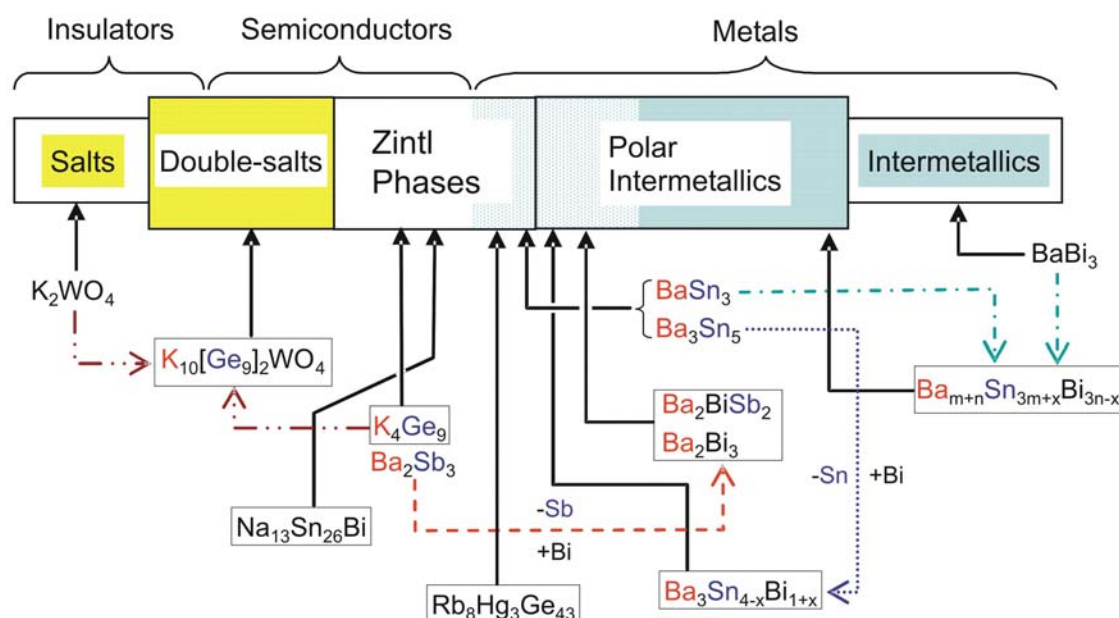
## 8. Summary and Final Discussions

This work was dedicated to the rational design of compounds within and beyond the Zintl concept. Zintl phases are salt-like compounds that are formed by combination of nonnoble metals (alkali, alkaline-earth, and rare earth metals) with post-transition metals. They are intermediate compounds that can be positioned between salts and intermetallic compounds in which metallic, ionic and covalent bonds exist. Zintl phases are expected to be semiconducting but they can also be metallic (Scheme 5). The rational design and structural characterization of new tetrelide-tungstate double-salts involving nine-atom clusters of the tetrel group ( $Tt_9$ ) and oxometallate anions of transition metal like tungstates, using the Zintl concept was our first goal. This would extend the Zintl phases into more ionic region (see Scheme 5). The second goal was to study of effects of electronic fluctuations on Zintl polyanionic networks, particularly those on the border with intermetallics, using the partial substitution approach. Thus, the transition from electron precise Zintl phases to typical intermetallic compounds was investigated, focusing on the change in the structures and their chemical bonding. Here, the Structure-composition-property inter-relationships which go beyond the grasp of the Zintl concept could be studied by theoretical band structure calculations.

In the course of this work, the new compounds  $K_{10}[Ge_9]_2WO_4$ ,  $Rb_{10}[Ge_9]_2WO_4$ , and  $Cs_{10}[Ge_9]_2WO_4$  which are exciting intergrowth of the Zintl phases  $A_4Ge_9$  and the tungstates  $A_2WO_4$  were obtained. Additionally, some simple binary or pseudo-binary phases were obtained during the synthesis of the double-salts. Thus, the binary phase  $K_4Ge_9$  whose crystal structure was still missing could be successfully refined. Also, using a mercury oxide in the starting mixtures, a new mercury containing clathrate-I,  $Rb_8Hg_3Ge_{43}$  was obtained and its structure successfully refined by single crystal diffraction data. Substituting Bi for the homologous Sb in the classical Zintl phase  $Ba_2Sb_3$  lead to the new isostructural polar intermetallic phases  $Ba_2Bi_3$ ,  $Ba_2BiSb_2$  as well as the solid solutions  $Ba_2Bi_{1+y}Sb_{2-y}$ . The phase  $BaBi_2$  was obtained as a by-product during the thermal analysis of  $Ba_2Bi_3$ . The new phases  $Sr_\delta Na_{5+x} Sn_{13}$  ( $x = 0.7$ ) and  $Na_{13-\delta} Sn_{26-\delta} Bi_{1+\delta}$  ( $\delta = 0.27$ ) were prepared by partially substituting Sr for Na and Bi for Sn respectively, in the compound  $Na_5Sn_{13}$ . Similarly, the effects of the partial substitution of Bi for Sn in the Ba/Sn system were investigated on the two phases  $Ba_3Sn_5$  and  $BaSn_3$ . The former yielded the novel phases  $Ba_3Sn_{4-y}Bi_{1+y}$  ( $y < 1$ ),

and the latter revealed the new homologous series of compounds  $\text{Ba}_{m+n}\text{Sn}_{3m+y}\text{Bi}_{3n-y}$  whose first four members were structurally characterized by single crystal diffraction:  $\text{Ba}_4\text{Sn}_{9+y}\text{Bi}_{3-y}$  (8H structure),  $\text{Ba}_{13}\text{Sn}_{30+y}\text{Bi}_{9-y}$  (39R structure),  $\text{Ba}_5\text{Sn}_{9+y}\text{Bi}_{6-y}$  (10H structure),  $\text{Ba}_2\text{Sn}_{3+y}\text{Bi}_{3-y}$  (12R structure). Finally, the compound  $\text{Ba}_5\text{In}_4\text{Bi}_5$  was obtained from reactions which were originally designed to produce phases with heteronuclear polyanions that are isoelectronic with the Ba stannates  $\text{Ba}_3\text{Sn}_5$  and  $\text{BaSn}_3$ .

All these new compounds could be positioned in the spectrum from insulating salts, through semiconducting Zintl phases to intermetallics, according to their properties as schematically drawn in [Scheme 5](#).



Scheme 5.

The compounds  $\text{A}_{10}[\text{Ge}_9]_2\text{WO}_4$  ( $\text{A} = \text{K}, \text{Rb}, \text{Cs}$ ) are the first examples of double-salts with a group 14 nine-atom cluster and an oxometallate of a transition metal. They crystallize in a hierarchical cluster replacement of the  $\text{Al}_2\text{Cu}$  prototype with  $[\text{Ge}_9]^{4-}$  clusters at the Al position,  $\text{WO}_4^{2-}$  anions at the Cu position and the cations occupying the tetrahedral voids of the structure. They are rather unimaginable phases featuring the tungstate anion  $\text{WO}_4^{2-}$  in which W ( $d^0$ ) atom has the formal oxidation state of +6, beside the oxidable Zintl anion  $[\text{Ge}_9]^{4-}$  with multicenter bond. The synthesis and structural characterization of these double-salts,  $\text{A}_{10}[\text{Ge}_9]_2\text{WO}_4$ , provide one of the most impressive experimental proof of the validity of the Zintl concept, and meanwhile

a big step forward in the preparation of new types of composite materials combining intermetallic phases and non-conducting materials, which are predicted to have a bright future in technology (ref. [22] in §1.4). These results clearly demonstrate that the Zintl-Klemm concept can be used for the rationale design of new classes of compounds with high application potential in fields like nanoscale materials or optics.

The binary phase  $K_4Ge_9$  can be described as a hierarchical cluster replacement derivative of the  $Cr_3Si$  structure in which both Cr and Si atoms are replaced by  $Ge_9^{4-}$  cluster with the  $K^+$  cations as spacers occupying the tetrahedral holes of the lattice. It crystallizes in the rhombohedra (pseudo cubic) polar space group  $R3c$ . Its structure represents the much symmetrical  $Cr_3Si$ -analogous packing of  $E_9$  clusters in the phases  $A_4E_9$  with only two independent  $Ge_9$  clusters.

In the new clathrate-I  $Rb_8Hg_3Ge_{43}$ , the framework of the tetrahedrally coordinated Ge atoms is substituted by electron poorer Hg atoms (two valence electrons less). Four Hg atoms are necessary to achieve an electronically balanced phase. The Rb cations in the cage provide eight electrons, but only six are needed for the three Hg atoms in the framework; thus,  $Rb_8Hg_3Ge_{43}$  has two extra electrons and represents a 'metallic Zintl phase'.

The second part of this work dealt with substitution effects in Zintl phases. The smooth transition from covalent to metallic bonds through hypervalent bonds, defines a diffuse region where a competition between localized and delocalized bonds, and between directed and non-directed bonds is observed. The theory appears to be essential in order to develop a description of these complex electronic structures that disregard the classical chemical ideas for electron precise compounds.

$Ba_2Bi_3$  and the substituted phases  $Ba_2Bi_{1+y}Sb_{2-y}$  crystallize in the  $W_2CoB_2$  structure type with Ba at the W position, one Bi at the Co position and the other Bi and/or Sb at the B position. They contain planar  $(4.6.4.6)(4.6^2)_2$  anionic nets of three- and four-bonded Bi and/or Sb atoms that interact through electron-rich multicenter bonding and are separated by Ba cations. In the anionic layers of the substituted phases, the Sb atoms have a strict site preference for the three-bonded position. The observed transition, at a constant valence electron concentration, from the electron precise Zintl phase  $Ba_2Sb_3$  to the borderline polar intermetallics  $Ba_2BiSb_2$  and  $Ba_2Bi_3$ , by a

continuous increase in the Bi content nicely shows the importance of some atomic properties like electronegativity and relativistic effects in the structure and bonding of Zintl phases and polar intermetallic compounds. These atomic properties influence the extent of charge transfer from the active metal to the anionic substructure which in turn determines the nature of the chemical bonding in the system. A reformulation of the Zintl concept to account for the electron-rich multicenter bonding, as well as band structure calculations suggest that the phases have one extra electron which fills Bi–Bi antibonding states. The strict site preference of Sb atoms indicates atomic site with enhance properties for electron localization. A partitioning of the total electronic energy into site energy and bond energy creates two components to the colouring problem, allowing us to explain, with simple chemical arguments, the strict site preference of Sb atoms.

The partial substitution of Sr for Na in the formally one electron deficient phase  $\text{Na}_5\text{Sn}_{15}$  yields an electron richer composition,  $\text{Sr}_{0.08}\text{Na}_{5+x}\text{Sn}_{13}$  ( $x = 0.7$ ). Two additional Na occupied positions have been found in this structure compared to the previously reported. The phase  $\text{Sr}_{0.08}\text{Na}_{5+x}\text{Sn}_{13}$  is still about 0.2 electron short with respect to the classical view of close shell compounds. The electron deficiency is most likely due to the defects in two split cationic sites (50% maximum occupancy) with very short Na–Na contacts in the case of full occupancy.

In an attempt to substitute a fraction of Sn atoms by Bi in the same  $\text{Na}_5\text{Sn}_{15}$  compound, a new phase  $\text{Na}_{13-\delta}\text{Sn}_{26-\delta}\text{Bi}_{1+\delta}$  ( $\delta = 0.27$ ) with an extended Sn framework was obtained.  $\text{Na}_{13}\text{Sn}_{26}\text{Bi}$  can be viewed as a charge optimized compound featuring the covalently bonded  $[\text{Sn}_{26}]^{12-}$  Zintl polyanion as a building unit that interacts with the anion  $\text{Bi}^{1-}$  through 3c-4e bonding. Similar multicenter bond is described in the so called ‘hypervalent’ molecules like  $\text{I}_3^-$  or  $\text{XeF}_2$ . The multicenter bonded Sn–Bi–Sn fragment in the structure of  $\text{Na}_{13}\text{Sn}_{26}\text{Bi}$  represents a rare example of a heteronuclear three-center bonded system in the solid state.

The structure of  $\text{Ba}_3\text{Sn}_{4-y}\text{Bi}_{1+y}$  ( $y < 1$ ) contains a  ${}^3_{\infty}[\text{Ba}_{6/2}\text{Bi}]$  framework of twisted octahedra with an inverse  $\text{ReO}_3$ -like distorted structure hosting Bi substituted puckered layers of covalently bonded  $\text{Sn}_4$  units with a ‘bodyless butterfly’ like structure. These units are interconnected by weaker (metallic) bonds. The simple application of the Zintl concept indicates that the phases  $\text{Ba}_3\text{Sn}_{4-y}\text{Bi}_{1+y}$  are electron

deficient when  $y < 1$ , and band structure calculations predict the electron count to be optimized for  $y = 1$  which corresponds to the phase  $\text{Ba}_3\text{Bi}(\text{Sn}_3\text{Bi})$ .

The new homologous series of structures  $\text{Ba}_{m+n}\text{Sn}_{3m+y}\text{Bi}_{3n-y}$  crystallize in the hexagonal space group  $P6_3/mmc$  or rhombohedral  $R\bar{3}m$ . Their structures are constructed from the stacking of close packed layers of atoms with  $\text{AuCu}_3$ -like cubic (c) or  $\text{Ni}_3\text{Sn}$ -like hexagonal (h) symmetry, alternating with different sequences. The first structurally characterized members are:  $\text{Ba}_4\text{Sn}_{9+y}\text{Bi}_{3-y}$  ( $y = 1.3$ ) hhhc,  $\text{Ba}_{13}\text{Sn}_{30+y}\text{Bi}_{9-y}$  ( $y = 3.2$ ) (hhhc)<sub>2</sub>hhhhc, for  $\text{Ba}_5\text{Sn}_{9+y}\text{Bi}_{6-y}$  ( $y = 2.3$ ) hhhcc and  $\text{Ba}_2\text{Sn}_{3+y}\text{Bi}_{3-y}$  ( $y = 1.0$ ) hhcc. The hexagonal layers are fully ordered and are identical in terms of structure and composition to a fragment of the structure of  $\text{BaSn}_3$ . However, the cubic layers are partially ordered with Bi/Sn mixed occupancy and are structurally identical to a fragment of the structure of  $\text{BaBi}_3$  where the Bi position is partially substituted by Sn. Thus, the new homologous series of structures  $\text{Ba}_{m+n}\text{Sn}_{3m+y}\text{Bi}_{3n-y}$  is defined by an intergrowth of block corresponding to an electron precise (Zintl) phase  $\text{BaSn}_3$  with no phase width and, slaps corresponding to a typical intermetallic phase  $\text{BaBi}_3$  showing noticeable phase width and metallic (delocalized) interactions. What is still not clear is whether the amount of Sn in the predominantly Bi occupied cubic layers is determined by electronic factors or by matrix requirements to match the larger cubic layers with the distorted hexagonal layers.

The new ternary phase  $\text{Ba}_5\text{In}_4\text{Bi}_5$  forms a non-centrosymmetric structure of a new type (tetragonal,  $P4nc$ ). The structure contains interconnected heteroatomic clusters of  $\text{In}_4\text{Bi}_5$  square pyramids having a  $\text{In}_4$ -base with four exo-bonded bismuth atoms and a capping Bi atom. According to Wade's rules and band structure calculations, the compound is one electron-deficient per cluster, i.e.  $[\text{In}_4\text{Bi}_5]^{10-}$  instead of the expected  $[\text{In}_4\text{Bi}_5]^{11-}$  for a closed-shell species. The clusters were discussed also in light of the known heteroatomic deltahedral clusters with the same composition but different charge,  $[\text{In}_4\text{Bi}_5]^{3-}$ . The band structure calculations suggest substantial participation of barium in the overall bonding of the structure that "accounts" for the electron shortage. Moreover, the investigation of the chemical bonding with the help of the electron localization function (ELF) shows that localized covalent bonds beside delocalized bonds coexist in  $\text{Ba}_5\text{In}_4\text{Bi}_5$ .

Among many other interesting findings that emerge from the second part of this study, it is worth noting that how atoms arrange themselves in extended solid state structures depends on the number of valence electrons and the differences in electrochemical potentials, which are related to electronegativity, size, and the types of valence electronic structure the atoms bring to the compound.

Also, the occurrence of many compounds that violate the stability rule indicates that, while in classical valence compounds (Zintl phases) the electron count almost exclusively governs their structural stability, in borderline polar intermetallics all the three criteria for phase stability (electron count, Madelung energy and packing efficiency) are intimately related. Therefore, the mutual optimization of Madelung energy and space filling can even override the usually dominating factor of electron count, giving rise to unusual electronic and physical properties. Hence, the existence of open shell compounds like  $\text{Na}_{5+x}\text{Sn}_{13}$  and  $\text{Ba}_5\text{In}_4\text{Bi}_5$  suggests that, when it is impossible to find room for all cations necessary to optimize the electron count in a particular structure, the phase stability can be achieved by considering other factors like Madelung energies between cations and the anionic network.

## 9. List of publications

---

Parts of the results presented in this thesis were published in following papers:

1. *Synthesis, Characterization and Electronic Structure of  $Ba_5In_4Bi_5$ , an Acentric and One-Electron Deficient Phase*  
Ponou S., Fässler T. F., Tobías G., Canadell E., Cho A., Sevov S. C. *Chem. Eur. J.* **2004**, *10*, 3615-3621.
2. *Non-classical bonding in the novel structure of  $Ba_2Bi_3$  and unexpected site preference in the coloring variant  $Ba_2BiSb_2$*   
Ponou S., Fässler T.F. *Inorg. Chem.* **2004**, *43*, 6124-6126.
3.  *$KBi_{2-x}Pb_x$  ( $x \leq 1$ ): A zintl phase evolving from a distortion of the cubic laves-phase structure*  
Ponou S., Müller N., Fässler T.F., Häussermann U. *Inorg. Chem.* **2005**, *44*, 7423-7430

## Curriculum Vitae

Name: Ponou  
Surname: Simeon  
Date of birth: 01.01.1970  
Place of birth: Yaounde – Cameroon  
Citizenship: Cameroonian

### Education

1976 - 1982 Primary school Ekoudou in Yaounde  
1982 - 1986 Secondary school at C.E.S Ngoa-Ekelle in Yaounde  
1986 - 1989 Bilingual High school of Yaounde, Baccalauréat in June 1989

### University background

1989 - 1993 University of Yaounde, Bachelor in Chemistry in June 1993  
1993 - 1995 University of Yaounde I, Master's in Solid State Chemistry, June 1995  
1995 - 2000 Teaching Assistant at the Faculty of Science of the University of Yaounde I  
2000 - 2001 Diplôme d'Etudes Approfondies (DEA), Université de Nancy 1 – France  
2001 - 2002 Graduate College «*Kinetik und Mechanismus von Ionen Reaktionen*» at Eduard Zintl Institute, Technische Universität Darmstadt  
2002 - 2003 Beginning of the PhD program in Prof. Thomas Fässler group at the Eduard Zintl Institute, Technische Universität Darmstadt  
October 2003 Move to the “Technische Universität München” with Prof. T. F. Fässler

### Languages:

1. French (educational language)
2. English (2<sup>nd</sup> educational language)
3. German (Z-DAF)

My Mother language: Ngoma'lah